Volcanism in Modern Back-arc Regimes and Their Implications for Ancient Greenstone Belts

Marc Lorin Fassbender

A thesis submitted in partial fulfillment of the requirements for the Doctorate in Philosophy degree in Earth Sciences

Department of Earth and Environmental Sciences
University of Ottawa

© Marc Lorin Fassbender, Ottawa, Canada, 2023

Table of Contents

Table of Figures ..... **VII**

List of Tables ..... **X**

Abbreviations ..... **XI**

Abstract ..... **XIII**

Résumé ..... **XIV**

Acknowledgements ..... **XVI**

Statement of original contribution ..... **XVII**

Chapter 1: Introduction **1**

1.1 Background 2

1.2 Research objectives and overview of methods 3

1.3 Thesis organization 4

References 5

Figures 7

Chapter 2: Geochemical Signatures of Felsic Volcanic Rocks in Modern Oceanic Settings and Implications for Archean Greenstone Belts **10**

Abstract 11

2.1 Introduction 12

2.2 Occurrence of Modern Submarine Felsic Volcanic Rocks 13

2.2.1 Mid-ocean ridge assemblages 13

2.2.2 Ocean-island assemblages 14

2.2.3 Intraoceanic arc and back-arc assemblages 15

2.2.4 Intracontinental arc and back-arc assemblages 16

2.3 Data Sources 17

2.4 Whole-Rock Compositions and Melt Generation 18

2.5 Methods and Analysis 21

2.5.1 PCA and unsupervised hierarchical clustering 21

2.5.2 Training a new classifier 26

2.6 Discussion 29

2.6.1 Petrogenetic significance of the hierarchical clusters 29

2.6.2 Comparison with Archean felsic volcanic rocks 32

2.6.3 Implications for the F-classification scheme 37

Conclusions 40

Acknowledgments 41

References 42

Figures 54

Tables 74

Chapter 3 Geochemical Signatures of Mafic Volcanic Rocks in Modern Oceanic Settings and Implications for Archean Mafic Magmatism 78

Abstract 79

3.1 Introduction 80

3.2 Petrogenesis of Modern Oceanic Mafic Volcanic Rocks 81

3.2.1 Mid-ocean ridge basalts 81

3.2.2 Ocean island basalts 82

3.2.3 Intraoceanic arc and back-arc basalts 82

3.2.4 Boninites 83

3.3 Data Sources 84

3.4 Approach and Methods 86

3.4.1 Principal components analysis 86

3.4.2 Agglomerative hierarchical clustering 87

3.4.3 Training a classifier 88

3.5 Results 90

3.6 Discussion 92

3.6.1 A case study of the Lau basin 94

3.6.2 Comparison with Archean mafic volcanic rocks 97

Conclusions 100

Acknowledgments 101

References 102

Figures 114

Tables 139

Chapter 4: Highly Episodic Growth of the Niuafo'ou Microplate, NE Lau Basin, from Ar-Ar Dating: Implications for Crustal Growth in Greenstone Belts 142

Abstract 143

4.1 Introduction 144

4.2 Emergence of the Niuafo'ou Microplate 146

4.3 Samples 149

4.4 Methodology 151

4.5 Results and interpretation 152

4.6 Discussion 155

4.6.1 Possible implications for crustal growth in greenstone belts 159

Conclusion 160

Acknowledgements 161

References 162

Figures 169

Tables 189

Chapter 5: Summary and Conclusions 191

5.1 Chapter highlights 192

5.2 Comparison between modern oceans and the AGB 194

5.3 Future directions 196

Appendix A 199

Appendix B 215

Appendix C 235

Table of Figures

Figure 1.1: Global map of oceanic felsic volcanic rocks compiled for this study. 7

Figure 1.2: Global map of mafic volcanic rock samples from the oceans compiled for this study. 8

Figure 1.3: Geologic map of the Abitibi greenstone belt showing the volcanic assemblages and locations of mafic volcanic rock samples compiled for this study 9

Figure 2.1: Global map of oceanic felsic volcanic rocks compiled for this study. 54

Figure 2.2: Major and trace element plots showing the geochemical signatures of modern felsic volcanic rocks 56

Figure 2.3: Primitive mantle-normalized trace element plots of modern oceanic felsic volcanic rocks. 59

Figure 2.4: Principal components plot of the major and trace element geochemistry of modern oceanic felsic volcanic rocks. 61

Figure 2.5: Plot of the "Mean Decrease Gini" value for individual elements in the classification of a sample into the target class or "cluster". 63

Figure 2.6: Schematic illustration of the geodynamic settings of dry versus wet melting in the example of the Lau Basin 64

Figure 2.7: Locations of felsic volcanic rocks sampled in the northern Lau Basin and primitive mantle-normalized trace element plot of Lau Basin felsic volcanic rocks 65

Figure 2.8: Chondrite-normalized La/Yb versus Yb plot of felsic volcanic rocks from the Abitibi Greenstone Belt (AGB) superimposed on the fields of the F-classification after Hart et al. (2004). 68

Figure 2.9: Chondrite-normalized La/Yb versus Yb plot of modern oceanic felsic volcanic rocks superimposed on the fields of the F-classification of Archean felsic volcanic rocks (after Hart et al., 2004). 70

Figure 2.10: Primitive mantle-normalized trace element plots of felsic volcanic rocks of the Abitibi Greenstone Belt (AGB) compared to modern oceanic felsic volcanic rocks. 71

Figure 2.11: Results of the random forest classification of Abitibi felsic volcanic rocks according to target classes. 73

Figure 3.1: Global map of mafic volcanic rock samples from the oceans compiled for this study. 114

Figure 3.2: Major and trace element plots showing the geochemical signatures of modern oceanic mafic volcanic rocks. 116

Figure 3.3: Examples of geochemical and tectonic affinity diagrams for mafic volcanic rocks showing the classifications of modern oceanic basalts. 118

Figure 3.4: Primitive mantle-normalized trace element plot comparing a subset of mafic volcanic rocks from mid-ocean ridges, ridge-hotspot intersections and ocean islands 122

Figure 3.5: Principal components plots of the major and trace element geochemistry of modern oceanic mafic volcanic rocks. 123

Figure 3.6: Summary of hierarchical clustering classification overlain on PC1-PC2. Different clusters of samples from the hierarchical cluster analysis are outlined by the labelled polygons (C1-C7). 125

Figure 3.7: Plot of the "Mean Decrease Gini" value for individual elements for the classification of a sample into a target class or "cluster" 126

Figure 3.8: Selected trace element ratios for samples assigned to each target cluster (C1-C7). 128

Figure 3.9: Regional bathymetric map of the Lau back-arc basin (Ryan et al., 2009) showing spreading ridges, spreading rates and rates of retreat of the active arc 130

Figure 3.10: Spatial distribution of selected trace element ratios in mafic volcanic rocks of the northern Lau Basin illustrating enrichment and depletion patterns in Ba, Nb, Yb, and Th. 132

Figure 3.11: Schematic illustration of general mantle flow at microplate edges and terminating back-arc spreading centers as in the NE Lau Basin. 133

Figure 3.12: Map showing the locations of basalt belonging to different target classes in the northern Lau Basin. 134

Figure 3.13: Geological assemblage map of the Abitibi Greenstone Belt showing the locations of mafic volcanic rock samples compiled for this study and contoured probabilities of different target classes of mafic volcanic rocks derived from the random forest classifier 136

Figure 3.14: Primitive mantle–normalized trace element plot of representative mafic volcanic rocks from Matagami, Noranda, and Val-d'Or. 138

Figure 4.1: Regional bathymetric map of the Lau back-arc basin (from Stewart et al., 2022) showing spreading ridges, spreading rates, rates of retreat of the active arc (in mm/yr), and radiometric ages 169

Figure 4.2: Assemblage map of the Lau Basin (from Stewart et al., 2022). 171

Figure 4.3: Magnetic anomaly map of the Lau Basin from the two-dimensional (2-D) magnetic inversions (from Zellmer and Taylor, 2001) showing the sample locations of this study..... 173

Figure 4.4: Bathymetric map of the southern FRSC, northern ELSC, CLSC and the proposal Central Lau "nanoplate" (CLNP of Conder and Wiens, 2011) in the south of the Niuafo'ou Microplate showing the location and results of Ar-Ar radiometric ages. 174

Figure 4.5: Representative photomicrographs of SO267 DR48-1B.. 175

Figure 4.6: Representative photomicrographs of SO267 DR49-1. 176

Figure 4.7: Representative photomicrographs of SO267 DR49-1. 177

Figure 4.8: Representative photomicrographs of SO267 DR60-1B.. 178

Figure 4.9: Representative photomicrographs of SO267 DR65-1G. 179

Figure 4.10: Representative photomicrographs of SO267 DR69-2A. 180

Figure 4.11: Representative photomicrographs of SO267 DR77-4A. 181

Figure 4.12: Major and trace-element plots of the Ar-Ar samples showing their geochemical signatures and Lau Basin samples for reference. 182

Figure 4.13: Results of high-resolution incremental heating Ar-Ar analyses for the SO267 basaltic volcanic rocks showing cumulative Ar-release and variable K/Ca ratios during the step heating process..... 185

Figure 4.14: Schematic illustration of the Lau Basin opening and the sequence of eruption of lavas sampled for this study 188

List of Tables

Table 2.1. Summary table of felsic rock compositions in modern oceanic settings illustrating geochemical differences in different lithotectonic assemblages. 74

Table 2.2. Summary Table of geochemical indicators of lithotectonic assemblages of felsic volcanic rocks (see text for discussion and references). 76

Table 2.3. Summary of target classes in the hierarchical clustering of modern oceanic felsic volcanic rock compositions according to tectonic setting and principal components analysis (PCA). 77

Table 3.1. Summary characteristics of mafic volcanic rock compositions in modern oceanic settings. 139

Table 3.2. Interpreted significance of trace element indicators of mafic volcanic rocks from different modern oceanic settings (see text for details and references). 140

Table 3.3. Summary attributes of the target classes of oceanic mafic volcanic rocks according to tectonic setting. 141

Table 4.1. Whole rock geochemistry of the Ar-Ar samples. 189

Table 4.2. Summary of Ar-Ar ages from the southern Niuafo'ou microplate (this study). 190

Table 5.1. Summary table of features in major Lau assemblages and similar AGB assemblages. 198

Abbreviations

AGB: Abitibi Greenstone Belt

CLR: Centred-Log Ratio

CLSC: Central Lau Spreading Center

ELSC: Eastern Lau Spreading Center

ER: Eastern Rifts

FRSC: Fonualei Rift and Spreading Center

HFSE: High Field Strength Element

HREE: Heavy Rare Earth Element

IDW: Inverse Distance Weighted

LILE: Large Ion Lithophile Element

LREE: Large Rare Earth Elements

MOR: Mid-Ocean Ridge

MORB: Mid-Ocean Ridge Basalt

MSC: Manus Spreading Center

MTJ: Mangatolu Triple Junction

NELSC: Northeastern Lau Spreading Center

NVZ: Northern Volcanic Zone

NWLSC: Northwestern Lau Spreading Center

ODP: Ocean Drilling Program

OIB: Ocean Island Basalt

PER: Pearce Element Ratio

PR: Peggy Ridge

PC: Principal Component

PCA: Principal Component Analysis

REE: Rare Earth Element

RF: Random Forest

RR: Rochambeau Rifts

SMOTE: Synthetic Minority Oversampling Technique

STEP: Subduction Transform Edge Propagator

SVZ: Southern Volcanic Zone

TVZ: Taupo Volcanic Zone

VFR: Valu Fa Ridge

VMS: Volcanogenic Massive Sulphide

Abstract

Greenstone belts are dominated by volcanic rocks with lithogeochemical characteristics that reflect a range of possible geodynamic settings. Many analogies with modern tectonic settings have been suggested. Increasing exploration and comprehensive sampling of volcanic rocks in modern oceans provides the unique opportunity to characterize different melt sources from intraoceanic settings. This thesis examines geochemical data from more than 2850 submarine mafic and more than 2200 submarine felsic volcanic rocks, representing a wide range of settings. The results show significant geochemical variability spanning the full range of compositions of volcanic rocks found in ancient greenstone belts. This diversity reflects complex rift and spreading regimes, variations in crustal thickness, dry melting versus wet melting, mantle mixing and crustal contamination. Highly variable melting conditions are thought to be related to mantle heterogeneities, complex mantle flow regimes and short-lived tectonic domains, such as those caused by diffuse spreading, multiple overlapping spreading centers and microplate breakouts.

Systematic differences in the volcanic rocks are revealed by a combination of principal components analysis and unsupervised hierarchical clustering. Rocks from most arc-backarc systems have strongly depleted mantle signatures and well-known subduction-related chemistry. This contrasts with rocks in Archean greenstone belts, which show no, or at least weaker, subduction-related chemistry and stronger mantle enrichment resulting from a less-depleted mantle, less wet-melting, and variable crustal contamination. The geochemistry of the modern volcanic rocks reflects lower mantle temperatures, thinner crust and subduction-related processes of present-day settings. However, rocks that are geochemically identical to those in Archean greenstone belts occur in many modern back-arc basins, such as the Lau Basin. Crustal growth and area-age relationships in the Lau Basin are similar to observed ages and compositions of volcanic assemblages in greenstone belts, such as the Blake River Group of the Abitibi Greenstone Belt. Such settings are recognized as favorable locations for volcanogenic massive sulfide (VMS) deposits, and therefore the particular geochemical signatures of the volcanic rocks are important for enhanced area selection in base and precious metal exploration.

Résumé

Les ceintures de roches vertes sont principalement constituées de roches volcaniques, dont les caractéristiques géochimiques peuvent refléter des domaines géodynamiques différents. De nombreuses analogies avec les contextes tectoniques modernes ont été proposées. Une exploration des fonds océaniques toujours plus poussée et un échantillonnage de plus en plus important offrent une opportunité unique de mieux caractériser et comprendre quelles sont les possibles sources des magmas à l'origine des roches volcaniques intra-océaniques. Dans cette thèse, les données géochimiques de roches volcaniques sous-marines comprenant plus de 2850 roches mafiques et plus de 2200 roches felsiques, qui représentent un large panel de contextes géodynamiques, ont été étudiées. Les résultats montrent une variabilité géochimique significative correspondant à l'ensemble des compositions de roches volcaniques trouvées dans les anciennes ceintures de roches vertes. Cette diversité reflète les régimes complexes de rift et d'accrétion, les variations d'épaisseur de la croûte, la fusion anhydre par rapport à la fusion saturée en eau, le mélange du manteau et la contamination crustale. Les conditions de fusion très variables sont probablement liées aux hétérogénéités du manteau, aux régimes complexes de la convection mantellique et aux micro-plaques tectoniques de courte durée, tels que celles crées dans les zones d'accrétion diffuse, comme les multiples zones de recouvrement (Overlapping Spreading Center) ou les ruptures de micro-plaques.

Les variations systématiques au sein des roches volcaniques ont été étudiées par une combinaison d'analyses des composants principaux avec le regroupement hiérarchique non supervisé. Les roches de la plupart des systèmes arc/arrière-arc ont des signatures de manteau fortement appauvries et une chimie liée à la subduction. Cela contraste avec les roches des ceintures de roches vertes archéennes, qui ne présentent aucune chimie liée à la subduction, ou du moins une plus faible, et un enrichissement du manteau plus fort résultant d'un manteau moins appauvri, d'une fusion plus sèche et d'une contamination crustale variable. La géochimie des roches volcaniques modernes reflète des températures de manteau plus basses, une croûte plus mince et une contribution des phénomènes de subduction, tels qu'ils sont décrits aujourd'hui. Cependant, des roches géochimiquement identiques à celles des ceintures de roches vertes archéennes se trouvent dans de nombreux bassins d'arrière-arc modernes, tels que le bassin de Lau. La croissance crustale

et les relations entre les différents domaines et l’âge dans le bassin de Lau sont similaires aux âges et compositions observés au sein d’assemblages volcaniques de certaines ceintures de roches vertes, comme le groupe de Blake River de la ceinture de roches vertes de l'Abitibi. Ces régions sont reconnues comme des emplacements favorables pour les gisements de sulfures massifs volcanogènes (VMS), et par conséquent, les signatures géochimiques spécifiques des roches volcaniques se révèlent être importantes pour une meilleure sélection des zones d'exploration des métaux de base et précieux.

Acknowledgements

First and foremost, I would like to particular acknowledge the support and patience of my supervisor and mentor Mark Hannington.

This research is a product of the Metal Earth Project funded by the Canada First Research Excellence Fund (CFREF), the Natural Sciences and Engineering Research Council of Canada (NSERC), and the Marine Mineral Resources Group at the GEOMAR-Helmholtz Centre for Ocean Research Kiel. CFREF, NSERC, and the Helmholtz Association are acknowledged for their support.

Thanks to the Mineral Exploration Research Centre (MERC) and all members of the VMS-thematic subproject of the Canadian Metal Earth program and the iMAGE-CREATE (Collaborative Research and Training Experience Program). This is contribution MERC-ME-2023-20.

Thank you to my thesis examiners Prof. Dr. Pierre-Simon Ross, Prof. Dr. Eric Grunsky, Prof. Dr. Brian Cousens and Prof. Dr. Brian O'Driscoll, and the reviewers of the manuscripts.

This project would not have been possible without all the help I received over the years, professionally and personally. Many people supported and influenced me and this project and had their part in this. This includes mainly people from the University of Ottawa, Canada and the GEOMAR Helmholtz Centre for Ocean Research in Kiel, Germany. I would like to specifically acknowledge the contributions of David Diekrup and Alan Baxter.

Thanks to all my friends in Canada, Germany and elsewhere and family which supported me during the various stages of this project.

Thank you, Ina, thank you for all your support and thank you for sharing this adventure with me.

Statement of original contribution

This thesis is the summary of original research undertaken at the University of Ottawa by Marc Lorin Fassbender under the supervision of Prof. Mark Hannington. The project was planned and executed by Marc Lorin Fassbender, with primary funding from a NSERC Discovery grant awarded to Mark Hannington, the CFREF Metal Earth Project at Laurentian University, the iMAGE-CREATE projects, and a Society of Economic Geologists research fund awarded to Marc Lorin Fassbender for Ar-Ar radiometric dating.

Chapter 1: Introduction

- Written by M. L. Fassbender with editorial corrections by M. Hannington.

Chapter 2: Geochemical Signatures of Felsic Volcanic Rocks in Modern Oceanic Settings and Implications for Archean Greenstone Belts

M.L. Fassbender, M. Hannnington, M.S. Stewart, P.A. Brandl, A.T. Baxter, D. Diekrup

- Written by M. L. Fassbender with editorial corrections by M. Hannington.
- Marc L. Fassbender – compiled the sample database, conducted the data analysis and machine learning, and wrote the manuscript
- Mark D. Hannington – helped initiate the project, oversaw the analysis at all stages, and edited the manuscript
- Margaret S. Stewart – helped initiate the project and oversaw the analysis
- Philipp A. Brandl – participated in the data analysis
- Alan T. Baxter – assisted with the Modern/Archean comparison
- David Diekrup – assisted with the Modern/Archean comparison

This article was published in Economic Geology in 2023:

Fassbender, M.L., Hannington, M., Stewart, M.S., Brandl, P.A., Baxter, A.T., and Diekrup, D., 2023, Geochemical signatures of felsic volcanic rocks in Modern oceanic settings and implications for Archean greenstone belts: Economic Geology, v. 118, p. 319-345.

Aspects of this work were presented orally:

Fassbender, M.L., Hannington, M., Stewart, M.S., Brandl, P.A., Baxter, A.T., and Diekrup, D., 2021, Geochemical signatures of felsic volcanic rocks in Modern oceanic settings and implications for Archean greenstone belts: 100th Anniversary Society of Economic Geology Conference, Canada, Whistler, 17th September.

Chapter 3: Geochemical Signatures of Mafic Volcanic Rocks in Modern Oceanic Settings and Implications for Archean mafic magmatism

M.L. Fassbender, M. Hannington, A.T. Baxter, D. Diekrup, M.S. Stewart, P.A. Brandl

- Marc L. Fassbender – compiled the sample database, conducted the data analysis and machine learning, and wrote the manuscript
- Mark D. Hannington – helped initiate the project, oversaw the analysis at all stages, and edited the manuscript
- Alan T. Baxter – helped initiate the project and assisted with the Modern/Archean comparison
- David Diekrup – assisted with the Modern/Archean comparison
- Margaret S. Stewart – helped initiate the project
- Philipp A. Brandl – participated in the data analysis

This manuscript is in review in Economic Geology:

Fassbender, M.L., Hannington, M., Baxter, A.T., Diekrup, D., Stewart, M.S., and Brandl, P.A., 2023, Geochemical signatures of mafic volcanic rocks in Modern oceanic settings and implications for Archean mafic magmatism: Economic Geology, in review.

Aspects of this work were presented during poster sessions:

Fassbender, M.L., Hannington, M., Brandl, P.A. Stewart, M., Baxter, A.T., Diekrup, D., 2020, Geochemical evolution of back-arc spreading regimes – a multivariate analysis of Lau Basin volcanic rocks: Student Minerals Colloquium at the, Prospectors and Developers Association of Canada, Conference, Toronto, 1st-4th March.

Fassbender, M.L, Hannington, M., Stewart, M., 2019, Volcanic Rock Geochemistry of the Lau Basin: Unexpected Complexity of Active Back-arc Spreading Centers: Student Minerals Colloquium at the Prospectors and Developers Association of Canada, Conference, Toronto, 3rd-6th March.

Chapter 4: Highly Episodic Growth of the Niuafo'ou Microplate, NE Lau Basin, from Ar-Ar Dating: Implications for Crustal Growth in Greenstone Belts

M.L. Fassbender, M. Hannington, A.T. Baxter, D. Diekrup, M.S. Stewart, P.A. Brandl

- Written by M. L. Fassbender with editorial corrections by M. Hannington
- Marc L. Fassbender – compiled the sample database, conducted the data analysis, and wrote the manuscript
- Mark D. Hannington – helped initiate the project, oversaw the analysis at all stages, and edited the manuscript
- Alan T. Baxter – assisted with the Modern/Archean comparison
- David Diekrup – assisted with the Modern/Archean comparison
- Margaret S. Stewart – helped initiate the project
- Philipp A. Brandl – participated in the data analysis

This manuscript is in preparation for submission

Fassbender, M.L., Hannington, M., Baxter, A.T., Diekrup, D., Stewart, M.S., and Brandl, P.A., 2023, Highly Episodic Growth of the Niuafo'ou Microplate, NE Lau Basin, from Ar-Ar Dating: Implications for Crustal Growth in Greenstone Belt.

Chapter 5: Summary and Conclusion

- Written by M. L. Fassbender with editorial corrections by M. Hannington.

Chapter 1

Introduction

1.1 Background

Volcanic rocks are the dominant rock type in the modern oceans and in ancient greenstone belts. Their widespread occurrence and diverse geochemical signatures make them ideal to investigate different geotectonic environments through space and time. They also host seafloor massive sulfides and their ancient analogs, volcanogenic massive sulfide deposits. In this thesis, geochemical signatures of mafic and felsic rocks from modern intraoceanic settings were classified and compared to similar rocks from ancient greenstone belts. A combination of principal components analysis, agglomerative hierarchical clustering, and random forest was used to compare the volcanic suites.

By far most volcanic rocks are being produced at mid-ocean ridges, back-arc spreading centers, arc volcanoes, and ocean islands (Perfit and Davidson, 2000). Despite their importance for global volcanism, sampling of all of these settings has been difficult. This is changing with increased exploration of the oceans and greater availability of high precision analytical data from modern submarine environments. However, some settings are better represented than others. Most research has been conducted at the mid-ocean ridges with much less sampling in arc and back-arc settings, despite the great diversity of rock types in subduction-zone environments (Barker and Hill, 1980; Stern, 1987).

Although sampling has been limited, for over 40 years, the geochemical signatures of modern oceanic volcanic rocks have been used to infer possible geodynamic settings of ancient greenstone belts and their contained mineral deposits (e.g., Lesher et al., 1986; Paradis et al., 1988; Kerrich and Wyman, 1997; Hart et al., 2004; Piercey, 2011). Precise analogs of Archean plate tectonics in modern settings seem unlikely due to the hotter mantle temperatures in the Archean, thicker oceanic crust, a lack of continental basement, and subduction regimes that were either non-existent or in their infancy (e.g., Bédard et al., 2013; Wyman, 2013). However, detailed comparisons have been limited due to the lack of samples from modern arc and back-arc environments. In this thesis, geochemical signatures of felsic (**Figure 1.1**) and mafic (**Figure 1.2**) rocks from modern intraoceanic settings are classified and compared to similar rocks from the Archean Abitibi Greenstone Belt (AGB). The AGB is the largest intact Neoarchean greenstone belt and one of the most economically important volcanic terranes in the world (**Figure 1.3**). The volcanic and

sedimentary rocks are widely interpreted to be part of an intraoceanic arc-backarc system with similarities to modern oceanic microplate mosaics (Jackson et al., 1994; Percival et al., 2012; Wyman, 2013). However, other authors have suggested significant differences between Archean and post-Archean magmatism and tectonics, with some Archean terranes possibly having no modern analog (e.g., Bédard et al., 2013). Certain rock types thought to be uniquely associated with mineral endowment in the AGB (e.g., felsic volcanic rocks with flat rare earth element patterns, significant heavy rare earth element enrichment, and strong negative Eu anomalies: so-called FIIIb rhyolites) are also found in modern intraoceanic arc-backarc systems. Mafic volcanic rocks from modern back-arc spreading centers also share a number of attributes with AGB basalts, including derivation from a high-temperature mantle, mantle mixing and possible crustal contamination.

A type locality of modern back-arc basin opening is the Lau Basin. We compare the geochemistry of different volcanic suites in the Lau Basin to similar volcanic rocks from the AGB. However, interpretation of the growth history of the basin has been complicated by a lack of clearly defined magnetic data. We used Ar-Ar radiometric dating to investigate the age relationships of the rapidly opening Lau Basin and explore the progression of back-arc rifting.

1.2 Research objectives and overview of methods

The main research objectives of this thesis are to better classify modern submarine volcanic rocks in terms of whole rock geochemistry and to compare volcanic suites from modern and ancient submarine tectonic settings using a unique global data set purpose-built for the study. The approach aimed to characterize the geochemical signatures of mafic and felsic volcanic rocks from distinct lithotectonic environments using multivariate techniques such as principal components analysis and agglomerative hierarchical clustering. Particularly, we emphasize the usage of sub-sets of elements, that are selected based on their importance in different lithotectonic settings instead of simply using all data available which may potentially dilute the geochemical signals. Traditional methods of volcanic rock discrimination, such as the F-Classification or lithotectonic discrimination diagrams (e.g., Lesher et al., 1986; Hart et al., 2004; Pearce, 2014) become impractical for these datasets because of the large numbers of samples. Instead, we reassess the available data sets using purely data driven analysis and a machine learning approach (random

forest classification) that employs comprehensive linear combinations of correlated elements for classification rather than selected trace element ratios. Multivariate techniques have a proven track record and show great potential for systematic identification of distinct geochemical units (Grunsky et al., 1992; Harris and Grunsky, 2015). We suggest that a random forest classifier can accurately identify the similarities and differences between volcanic suites from different tectonic settings and similarly characterize volcanic rocks from the AGB. The classifier, trained on databases of felsic and mafic volcanic rocks from the global oceans, uses hundreds of decision trees to identify samples belonging to a specific target class (Breiman, 2001). We suggest that distinct geochemical signatures for each target class can be interpreted in terms of different petrogenesis and lithotectonic settings. We further propose that complex growth histories and mantle domains are reflected in the geochemical data. Details about methods are presented in each chapter and in the appendices.

1.3 Thesis organization

The geochemistry of felsic volcanic rocks is examined in Chapter 2, with an in-depth comparison of rocks that are found in both modern intraoceanic arc-backarc systems and in the AGB. In Chapter 3 the geochemistry of mafic volcanic rocks is similarly compared, and in Chapter 4 we explore crustal growth in the type locality of modern back-arc basin opening in the Lau Basin. The northern Lau Basin is an example of a microplate mosaic analogous to those inferred for some greenstone belts. New Ar-Ar ages challenge the view of basin opening as a linear progression from rifting to eventual spreading and instead provide evidence of ridge jumps, rift propagation into older crust, and diffuse extension throughout the basin development. The complexity of crustal growth during basin opening is strongly correlated to the whole-rock geochemistry. Age data and volcanic rock geochemistry from the AGB, show similar geochemical diversity and age ranges that may reflect a similarly complex growth history.

Appendices are included as digital supplements. They provide the data not included in the manuscripts, including entire geochemical datasets, QA/QC, additional details on the methodology and workflows.

References

Barker, P.F., and Hill, I.A., 1980, Asymmetric spreading in back-arc basins, Nature, v. 285, p. 652-654.

Bédard, J.H., Harris, L.B., and Thurston, P.C., 2013, The hunting of the snArc: Precambrian Research, v. 229, p. 20-48.

Breiman, L., 2001, Random Forests: Machine Learning, v. 45, p. 5-32.

Dubé, B., and Mercier-Langevin, P., 2020, Gold Deposits of the Archean Abitibi Greenstone Belt, Canada, in Sillitoe, R.H., Goldfarb, R.J., Robert, F., and Simmons, S.F., ed., Geology of the World's Major Gold Deposits and Provinces: Special Publications of the Society of Economic Geologists, p. 669-708.

Grunsky, E.C., Easton, R.M., Thurston, P.C., and Jensen, L.S., 1992, A Statistical approach to the characterization and classification of Archean volcanic rocks of the Superior Province: Ontario Geological Survey Special, v. 4, p.1397-1438.

Harris, J.R., and Grunsky, E.C., 2015, Predictive lithological mapping of Canada's North using Random Forest classification applied to geophysical and geochemical data: Computers and Geosciences, v. 80, p. 9-25.

Hart, T.R., Gibson, H.L., and Lesher, C.M., 2004, Trace element geochemistry and petrogenesis of felsic volcanic rocks associated with volcanogenic massive Cu-Zn-Pb sulfide deposits: Economic Geology, v. 99, p. 1003-1013.

Jackson, S.L., Fyon, A., and Corfu, F., 1994, Review of Archean supracrustal assemblages of the southern Abitibi greenstone belt in Ontario, Canada: Products of microplate interaction within a large-scale plate-tectonic setting: Precambrian Research, v. 65, p. 183-205.

Kerrich R., and Wyman, D.A., 1997, Review of developments in trace-element fingerprinting of geodynamic settings and their implications for mineral exploration: Australian Journal of Earth Sciences v. 44, p. 465-487.

Lesher, C.M., Goodwin, A.M., Campbell, I.H., and Gorton, M.P., 1986, Trace-element geochemistry of ore-associated and barren, felsic metavolcanic rocks in the Superior Province, Canada: Canadian Journal of Earth Sciences, v. 23, p. 22-237.

Monecke, T., Mercier-Langevin, P., Dubé, B., and Frieman, B.M., 2017, Geology of the Abitibi Greenstone Belt, Canada: Reviews in Economic Geology, v. 19, p. 7-49.

Paradis, S., Ludden, J., and Gelinas, L., 1988, Evidence of contrasting compositional spectra in comagmatic intrusive and extrusive rocks of the late Archean Blake River Group, Abitibi, Quebec: Canadian Journal of Earth Sciences, v. 25, p. 134-144.

Pearce, J.A., 2014, Immobile element fingerprinting of ophiolites: Elements v. 10, p. 101-108.

Percival, J. A., Skulski, T., Sanborn-Barrie, M., Stott, G. M., Leclair, A. D., Corkery, M. T., and Boily, M., 2012, Geology and tectonic evolution of the Superior Province, Canada, Tectonic styles in Canada: The Lithoprobe Perspective, Geological Association of Canada, Special Paper, 49, p. 321-378.

Perfit, M.R., and Davidson, J.P., 2000, Plate tectonics and volcanism, in Sigurdsson, H., Houghton, B.F., McNutt, S.R., Rymer, H., Stix, J., and Ballard, R.D., eds., Encyclopedia of volcanoes: San Diego, CA, Academic Press, p. 89-113.

Piercey, S.J., 2011, The setting, style, and role of magmatism in the formation of volcanogenic massive sulfide deposits: Mineralium Deposita, v. 46, p. 449-471.

Stern, T.A., 1987, Asymmetric back-arc spreading, heat flux and structure associated with the central volcanic region of New Zealand: Earth and Planetary Science Letters, v. 85, p. 265-276.

Thurston, P.C., Ayer, J.A., Goutier, J., and Hamilton, M.A., 2008, Depositional gaps in Abitibi greenstone belt stratigraphy: A key to exploration for syngenetic mineralization: Economic Geology, v. 103, p. 1097-1134.

Wyman, D.A., 2013, A critical assessment of Neoarchean “plume only” geodynamics: Evidence from the Superior Province: Precambrian Research, v. 229, p. 3-19.

Figures

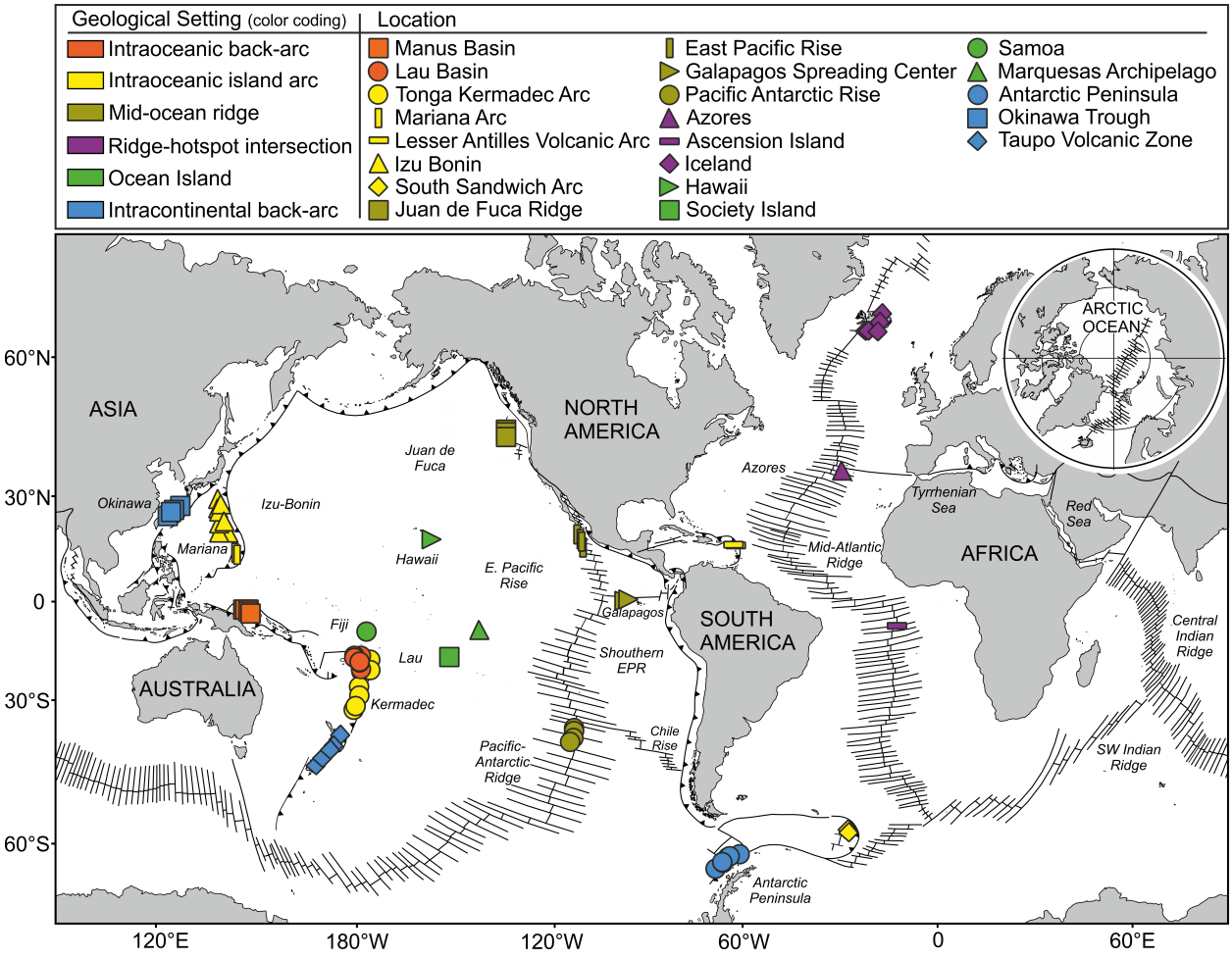


Figure 1.1: Global map of oceanic felsic volcanic rocks compiled for this study. Samples are included from intraoceanic back-arc basins (orange: Manus Basin, Lau Basin), intraoceanic island arcs (yellow: Tonga-Kermadec Arc, Mariana Arc, Lesser Antilles Volcanic Arc, Izu-Bonin Arc, South Sandwich Arc), mid-ocean ridges (olive: Juan de Fuca Ridge, East Pacific Rise, Galapagos Spreading Center, Pacific-Antarctic Rise), ridge-hotspot intersections (purple: Azores, Ascension Island, Iceland), ocean islands (green: Hawaii, Society Islands, Samoa, Marquesas Archipelago) and intracontinental arc-backarc basins (blue: Antarctic Peninsula, Okinawa Trough, Taupo Volcanic Zone). Details of the sample sources are provided in **Appendix A Table A1**.

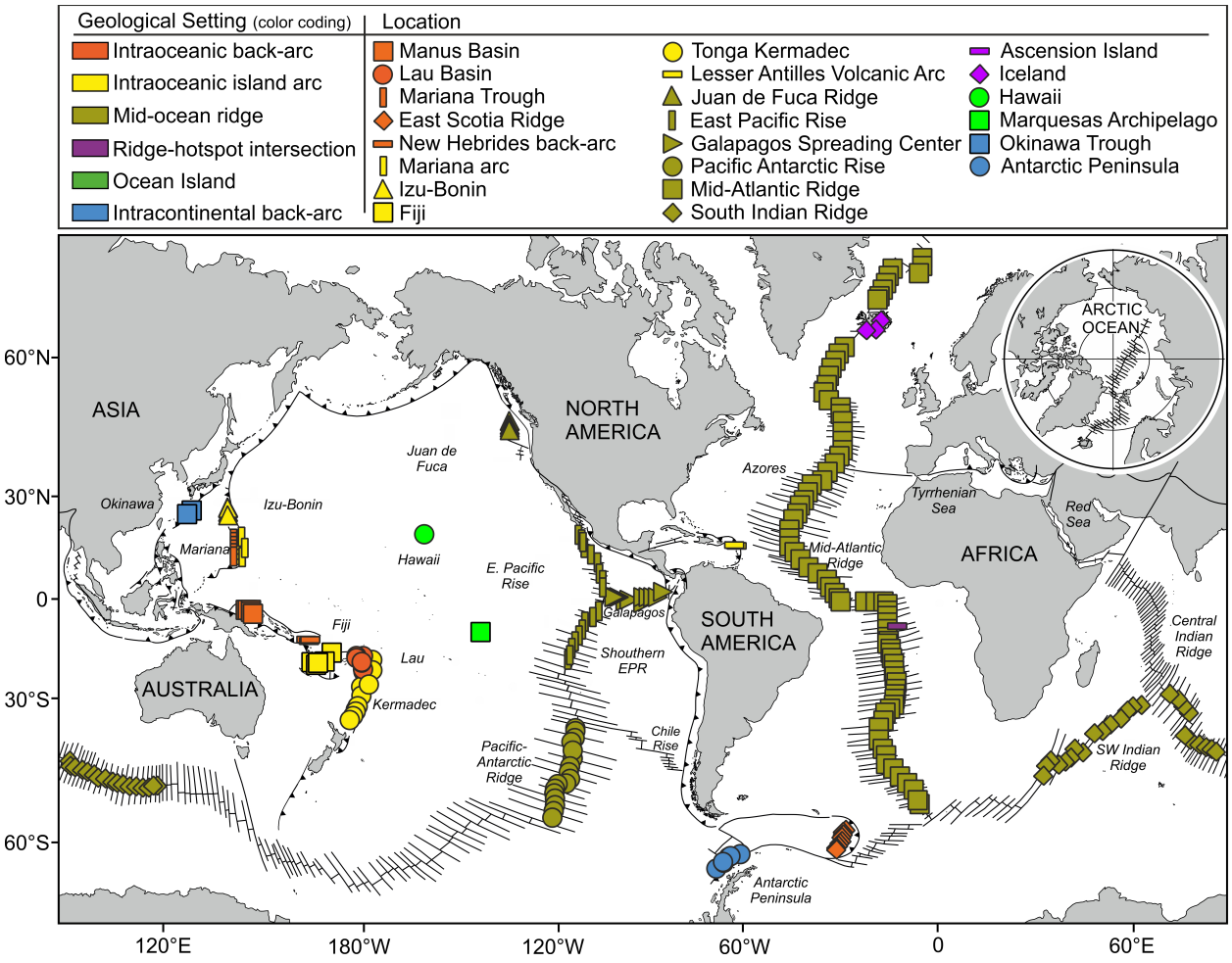


Figure 1.2: Global map of mafic volcanic rock samples from the oceans compiled for this study. Six different tectonic settings are represented including intraoceanic back-arc basins (orange: Manus Basin, Lau Basin, Mariana Trough, East Scotia Ridge, New Hebrides arc-backarc), intraoceanic island arcs (yellow: Mariana arc, Izu-Bonin, Fiji, Tonga Kermadec Arc, Lesser Antilles Volcanic Arc), mid-ocean ridges (olive: Juan de Fuca Ridge, East Pacific Rise, Galapagos Spreading Center, Pacific Antarctic Rise, Mid-Atlantic Ridge, South Indian Ridge), ridge-hotspot intersections (purple: Ascension Island, Iceland), ocean islands (green: Hawaii, Marquesas Archipelago) and intracontinental arc-backarc basins (blue: Antarctic Peninsula, Okinawa Trough). Details of the samples are provided in **Appendix B Table A1**.

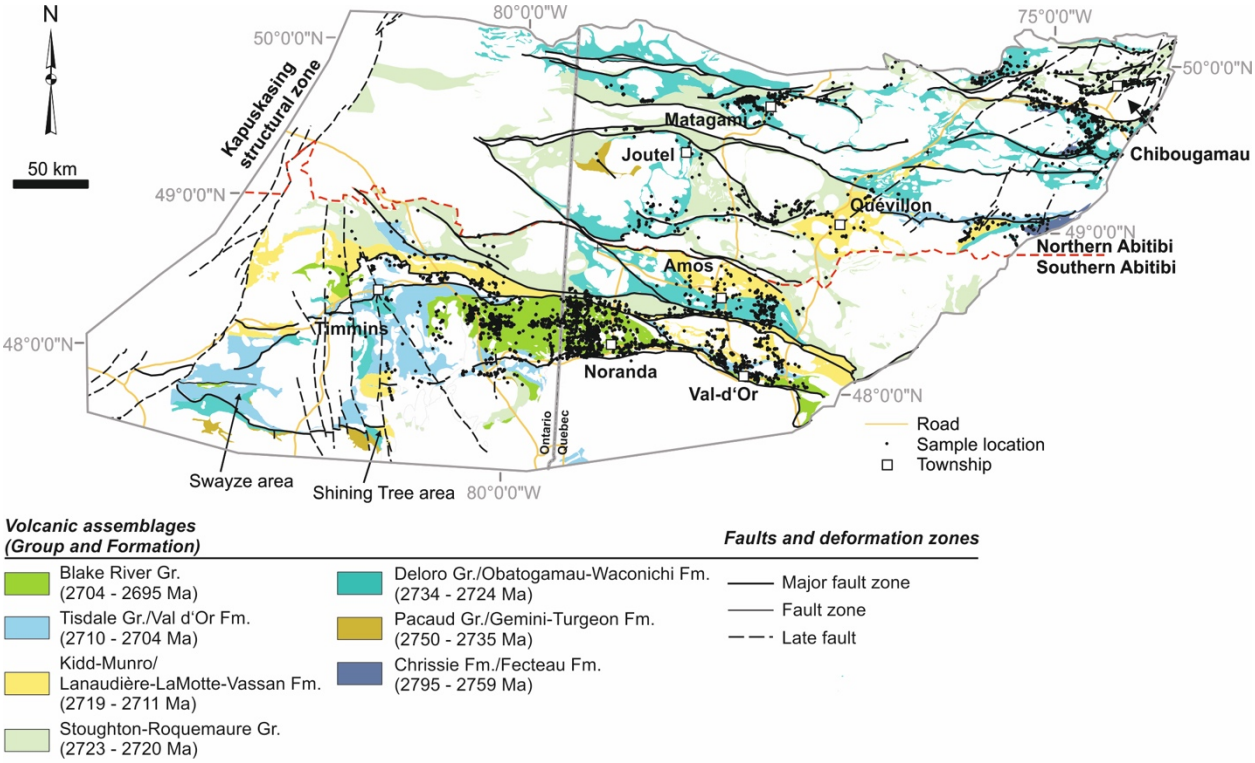


Figure 1.3: Geologic map of the Abitibi greenstone belt showing the volcanic assemblages and locations of mafic volcanic rock samples compiled for this study (modified from Thurston et al. (2008), Monecke et al. (2017a), and Dubé and Mercier-Langevin, (2020). Details of the samples are provided in **Appendix B Table A13**.

Chapter 2

Geochemical Signatures of Felsic Volcanic Rocks in Modern Oceanic Settings and Implications for Archean Greenstone Belts

Article published: Fassbender, M.L., Hannington, M., Stewart, M., Brandl, P.A., Baxter, A.T., and Diekrup, D., 2023, Geochemical Signatures of Felsic Volcanic Rocks in Modern Oceanic Settings and Implications for Archean Greenstone Belts: Economic Geology, v. 118, p. 319-345.

Abstract

Felsic volcanic rocks are abundant in ancient greenstone belts and important host rocks for volcanogenic massive sulfide (VMS) deposits. About half of all VMS deposits are hosted by dacite or rhyolite, an association that reflects anomalous heat flow during rifting, partial melting of basaltic crust, and fractional crystallization in high-level magma chambers. For over 30 years, geochemical signatures of these rocks (e.g., F-classification of Archean rhyolites) have been widely used to identify possible hosts for VMS deposits in ancient greenstone belts. However, comparisons with modern oceanic settings have been limited, owing to a lack of samples of felsic volcanic rocks from the seafloor. This is changing with increasing exploration of the oceans. In this study, we have compiled high-quality geochemical analyses of more than 2200 unique samples of submarine felsic volcanic rocks (>60 wt.% SiO_2) from a wide range of settings, including mid-ocean ridges, ridge-hotspot intersections, intraoceanic arc and back-arc spreading centers, and ocean islands. The compiled data show significant geochemical diversity spanning the full range of compositions of rhyolites found in ancient greenstone belts. This diversity is interpreted to reflect variations in crustal thickness, the presence or absence of slab-derived fluids (dry melting versus wet melting), and mantle anomalies. Highly variable melting conditions are thought to be related to short-lived microplate domains, such as those caused by diffuse spreading and multiple overlapping spreading centers. Systematic differences in the compositions of felsic volcanic rocks in the modern oceanic settings are revealed by a combination of principal components analysis, unsupervised hierarchical clustering and supervised random forest classification of the compiled data. Dacites and rhyolites from mid-ocean ridge settings have moderately depleted mantle signatures, whereas rocks from ridge-hotspot intersections and ocean islands reflect enriched mantle sources. Felsic volcanic rocks from arc-backarc systems have strongly depleted mantle signatures and well-known subduction-related chemistry (strong LILE enrichment in combination with strong negative Nb-Ta anomalies and low HREE). This contrasts with felsic volcanic rocks in Archean greenstone belts, which show HFSE and HREE enrichment (so-called FIIIb-type) due to a less depleted mantle, a lack of wet melting, and variable crustal contamination. The differences between modern and ancient volcanic rocks are interpreted to reflect the lower mantle temperatures, thinner crust and subduction-related processes in present-day settings. We suggest that the abundance of FIIIb-type felsic volcanic rocks in Archean greenstone belts is related to

buoyant microplate domains with thickened oceanic crust that was better preserved on emerging Archean cratons, whereas in post-Archean tectonic settings most of these rocks are subducted.

2.1 Introduction

In Archean greenstone belts, bimodal volcanic successions host the majority of volcanogenic massive sulfide (VMS) deposits (Barrie and Hannington, 1999; Franklin et al., 2005). A close association with felsic volcanic rocks is widely viewed as a consequence of rifting, during which large-scale hydrothermal systems were developed. Geochemical characterization of the felsic volcanic rocks has focused on their rare earth element (REE) and High Field Strength Element (HFSE) signatures, which have been interpreted to reflect different conditions of melting (e.g., temperature and depth) and led to the well-known F-classification of Archean rhyolite (Lesher et al., 1986; Hart et al., 2004), with felsic lavas as expressions of the high heat-flow environment. In developing the F-classification, a causal link was established between the cooling history of the subvolcanic magma chambers (at least partly driven by hydrothermal convection) and the formation of VMS deposits. However, attempts to assign the geochemical signatures of the felsic volcanic rocks to different geodynamic settings have had mixed success (Prior et al., 1999; Yang and Scott, 2003; Huston et al., 2010; Piercey, 2011; Yeats et al., 2017). It has been shown that REE signatures of felsic volcanic rocks differ significantly between Archean and post-Archean systems, complicating any comparisons (Lentz, 1998; Hart et al., 2004; Piercey, 2011). Early studies that compared Archean rhyolites with samples from modern oceanic settings were limited by the small numbers of samples available from the present-day ocean floor. However, in the last decades ocean exploration and seabed sampling have significantly improved. An important finding has been that felsic volcanic rocks are common in modern oceanic assemblages, and they have a remarkably large compositional range that reflects highly variable processes, including melting and assimilation of amphibole-bearing altered crust oceanic crust and fractional crystallization in a range of geodynamic settings (Brophy, 2008; Tamura et al., 2009; van der Zander et al., 2010; Wanless et al., 2010; Piercey, 2011; Freund et al., 2013; Embley and Rubin, 2018). With increased sampling, the different conditions of melt generation can now be comprehensively examined and compared to ancient analogs.

In this paper, we compiled data for more than 2200 unique samples of submarine felsic and intermediate lavas from 71 different locations at mid-ocean ridges, ridge-hotspot intersections, oceanic back-arc spreading centers, rifted island arcs, and intracontinental back-arc rifts (**Figure 2.1**). Using a combination of principal components analysis, unsupervised hierarchical clustering and supervised random forest classification we show consistent geochemical diversity between the different settings. These differences are compared to the compositions of felsic volcanic rocks from the Archean Abitibi Greenstone Belt (AGB) in the Superior Province of Canada. Although it is clear that the geochemical characteristics of rhyolites have changed due to the evolution of tectonic styles (e.g., Huston et al., 2019), the diversity of modern oceanic felsic volcanic rocks highlights a number of different processes that could explain the signatures of similar rocks in ancient greenstone belts.

2.2 Occurrence of Modern Submarine Felsic Volcanic Rocks

In modern oceanic settings, felsic volcanic rocks have been sampled from: i) propagating tips of mid-ocean ridge spreading centers (Wanless et al., 2010; Freund et al., 2013); ii) central volcanic complexes above mantle hot spots (Zellmer et al., 2008; Flude et al., 2010; van der Zander et al., 2010); iii) volcanic fronts of active island arcs (Hunter, 1998; Leat et al., 2007), and iv) arc-related rifts and back-arc spreading centers (Fretzdorff et al., 2006; Tamura et al., 2009) (**Figure 2.1** and **Table 2.1**). The complex chemistry and petrogenesis of the felsic magmas closely match the diversity of tectonic settings in which these rocks occur (**Tables 2.1** and **2.2**).

2.2.1 Mid-ocean ridge assemblages

Felsic lavas are now widely reported from mid-ocean ridges, including the East Pacific Rise, Galapagos Spreading Center, Juan de Fuca Ridge and the Pacific-Antarctic Rise (Wanless et al., 2010; Freund et al., 2013). The silicic lavas are associated with the propagating tips of overlapping spreading centers (OSCs: Perfit and Fornari, 1983), with ridge-hotspot intersections (Haase et al., 2005), and with ridge-transform intersections (Regelous et al., 1999). The melts are thought to be delivered as episodic injections caused by rift propagation or ridge-transform interactions, creating isolated magma chambers that undergo fractional crystallization. Such melts are found on the eastern limb of the overlapping spreading center at 9°N on the East Pacific Rise and at the

intersection of the Juan de Fuca Ridge with the Blanco Transform Zone (Wanless et al., 2010). Although the felsic lavas are erupted from small, isolated magma chambers, they are commonly found at or adjacent to axial highs where the largest volumes of melt reside in the crust (Haase et al., 2005). Assimilation of hydrothermally altered oceanic crust is also common at the propagating tips of the spreading centers (Wanless et al., 2010; Freund et al., 2013), further enhancing melting. Where influenced by a nearby hotspot or mantle plume, as at the Foundation hotspot near the Pacific-Antarctic Rise, the hotter mantle leads to increased melting, episodic magma replenishment, and a thicker crust. Under these conditions, more evolved melts develop in multiple magma reservoirs that are influenced by greater wall-rock assimilation and efficiently cooled by hydrothermal convection.

2.2.2 Ocean-island assemblages

Ocean-island dacites and rhyolites, such as those on Iceland, Ascension Island, and the Azores, are products of hotspot or plume-influenced magmatism (van der Zander et al., 2010; Jicha et al., 2013; Jeffery et al., 2016). The felsic magmas are produced by deep partial melting (van der Zander et al., 2010) or shallow fractional crystallization and differentiation (Jicha et al., 2013). The volcanic products belong to well-developed bimodal successions, such as the large central volcanoes and fissure-dike swarms of Iceland (Jónasson, 2007; Sigmarsson and Steinthórsson, 2007). The Krafla central volcano, situated in the North Iceland Rift Zone, for example, hosts numerous fissure-dike swarms occupied by doleritic and felsic intrusions (Thordarson and Larsen, 2007). Rhyolite lenses in the rift zone are interpreted to be products of partial melting of hydrothermally altered basalt (Zierenberg et al., 2013) or fractional crystallization with assimilation of crustal material (Brophy, 2009). Although Icelandic magmatism is largely tholeiitic, having originated from melting at low fO_2, calculated fH_2O values can be as high as those of oxidized island-arc melts (e.g., derived from 90% fractional crystallization: Portnyagin et al., 2012). Similarly, on Ascension Island (Chamberlain et al., 2016) and at the Marquesas Archipelago (Chauvel et al., 2012), closed system fractionation in shallow magma chambers leads to evolved melts with high H_2O concentrations. Cyclic eruptions of evolved melts at the Furnas Volcano in the Azores have been interpreted to reflect a stratified magma chamber (Jeffery et al., 2016). Shallow differentiation and deep hydrous melting produce tholeiitic and calc-alkaline

rhyolites in the late, shield-building stages of the Waianae volcano, Hawaii (Zander et al., 2010), whereas felsic volcanic rocks associated with the shield-building stage on Samoa are alkaline (Konter et al., 2012). The latter are similar to partial melts of deep-seated basaltic dike swarms at Huahine in the Society Islands (Harnois et al., 2006).

2.2.3 Intraoceanic arc and back-arc assemblages

Felsic volcanic rocks are common in modern intraoceanic arc and back-arc assemblages. Typically, the arc front is intruded by fluid-fluxed melt, whereas the back-arc basin is intruded by mantle rising into the back-arc spreading center in response to basin opening. At the volcanic front, devolatilization of the subducted slab enriches the mantle wedge in H_2O, resulting in abundant calc-alkaline melts (Grove et al., 2003; Tatsumi and Suzuki, 2009). These are commonly stalled in the upper arc crust and fractionate (Tamura et al., 2009; Deering et al., 2011). The erupted melts have variable chemistry, reflecting input of different slab-derived components and different melting and crystallization processes (Tamura et al., 2009; Haraguchi et al., 2017). For example, on the Izu-Bonin arc, intra-arc volcanism is due to remelting of the basaltic or andesitic crust and fractionation in high-level magma chambers, producing a range of bimodal rift-related volcanic rocks (e.g., in the Sumisu rift) and rhyolite-dominated submarine volcanoes (e.g., Myojin knoll: Shukuno et al., 2006; Tani et al., 2008; Tamura et al., 2009). Seismic profiles of the Izu-Bonin arc have confirmed that rhyolite-dominated volcanoes at the arc front are situated above thinned middle crust where partial melting occurred (Tamura et al., 2009). Bimodal volcanism at the front of the Tonga-Kermadec arc is related mostly to basalt fractionation with intrusions of mafic melts into the middle crust where they stagnate, fractionate and eventually rise to the surface (e.g., Raoul, Macauley, and Healy volcanoes: Turner et al., 2012; Barker et al., 2013). The sources of fluids that induce melting are variable. Volcanic rocks of the southern Kermadec arc show the influence of fluids derived from subducted sediments (e.g., Brothers volcano), whereas in the northern Kermadec arc, the melts have been influenced by fluids from altered oceanic crust (e.g., Healy: Haase et al., 2006). Rhyolites of the northern Tonga arc volcanoes (e.g., Fonualei volcano, Niuatoputapu volcano) and nearby rear-arc complexes (Niuatahi volcano) are mainly related to intra-arc rifting and basalt fractionation (Turner et al., 2012; Park et al., 2015). Felsic rocks of the Proctor Shoal in the South Sandwich arc are products of partial melting of basaltic crust within the

arc (Leat et al., 2007). Felsic melts of the Anatahan volcano in the Mariana arc are derived solely from fractional crystallization without any crustal contamination (Wade et al., 2005). In contrast, felsic rocks from the Soufriere Hills in the Lesser Antilles are products of complex multi-stage magmatism from partial melting of the mantle wedge, deep fractional crystallization and magma mixing and assimilation of crustal material (Zellmer et al., 2003).

Silicic magmatism in back-arc basins is focused at propagating rifts, overlapping spreading centers, and off-axis volcanoes (Fretzdorff et al., 2006; Beier et al., 2015). Active spreading centers in mature back-arc basin settings closely resemble mid-ocean ridges, and the felsic lavas are mostly related to fractional crystallization in isolated magma chambers, in some cases with local assimilation of hydrated crust. Enhanced cooling and fractionation of the melt lenses is promoted by stagnation in older and colder crust behind the propagating rift tips (Fretzdorff et al., 2006). This may be particularly common in areas of greater crustal thickness, as in the Manus Basin (e.g., Beier et al., 2015). Back-arc spreading centers that are located furthest from the arc are most similar to mid-ocean ridges, with the least influence of subduction-derived components (e.g., no Large Ion Lithophile Element (LILE) enrichment or negative Nb-Ta anomalies: see below). Felsic volcanic rocks in these settings have been sampled at the Central Lau Spreading Center (CLSC) and Northwestern Lau Spreading Center (NWLSC) in the Lau Basin and at the Manus Spreading Center (MSC) in the Manus Basin (Jenner et al., 2012; Lytle et al., 2012; Beier et al., 2015). In contrast, back-arc spreading centers located immediately behind the arc have significant subduction-derived components, as at the Valu Fa Ridge behind the Tofua arc and at Pual Ridge and SuSu Knolls in the Eastern Manus Rifts (Sinton et al., 2003; Zhang et al., 2018).

2.2.4 Intracontinental arc and back-arc assemblages

Felsic volcanic rocks are abundant in the early stages of rifting of continental crust, such as in the Taupo Volcanic Zone (TVZ). Magmatism in the TVZ, both onshore and offshore, is linked to faulting, diking, uplift and localized subsidence where the crust is most thinned (Parson and Wright, 1996; Rowland et al., 2010). The transition from andesitic to dominantly rhyolitic volcanism is associated with the onset of strong extension, allowing the felsic melts to rise into the upper crust (Deering et al., 2011). Felsic volcanic rocks in the Okinawa Trough back-arc basin are similarly associated with melting of continental crust that is passively rifting with anomalously

high heat flow (Shinjo and Kato, 2000). In both settings the melts show evidence of assimilation of crustal material and mixing of basaltic and more evolved magma (Shinjo and Kato, 2000; Deering et al., 2011). In contrast, felsic melts of the Bransfield Strait, an extending marginal basin of the West Antarctic Peninsula, are produced by fractional crystallization with minor crustal assimilation (Fretzdorff et al., 2004).

2.3 Data Sources

Geochemical analyses of silicic lavas (> 60 wt.% SiO_2) were compiled for each of the locations described above. From an original database of more than 2200 published analyses, we removed any samples analyzed by inappropriate methods, duplicate samples, results of duplicate analyses, and samples with location errors or incomplete descriptions. We also rejected samples with incomplete major and trace element data, so all results contain at least Si, Ti, Al, K, Y, Zr, Nb, Ba, La, Sm, Eu, Yb and Th. These elements were chosen based on their availability in the published data sets and because of their common use in lithotectonic discrimination diagrams. Every sample in the final data set was analyzed for each of these elements. No samples were included where the concentration of any element was equal to or below detection or exceeded the upper limits of detection or where the limits of detection were not specified. We further inspected the data by comparison with fresh rock compositions of whole-rock standards to minimize any alteration effects, including inspection of REE profiles and immobile element plots. We chose not to exclude potentially mobile elements from the analyzed data, such as K, Si, Ba and La, because they are important discriminators of rock type in unaltered samples. Pearce Element Ratio (PER) plots of these data (**Appendix A Figure A1**) show that the modern samples are not affected by alteration. **Figure 2.2** shows the range of felsic volcanic rock compositions in several common major and trace element discrimination diagrams that have been used for both basalt and rhyolite: a total alkali-silica plot (after Le Maitre, 1989), a Winchester and Floyd-type immobile element plot (after Pearce, 1996), and a magmatic affinity plot (after Ross and Bédard, 2009). The final database includes 404 high-quality analyses from modern oceanic settings (**Appendix A Table A1**) plus a comprehensive data set of 239 samples from the well-studied TVZ.

2.4 Whole-Rock Compositions and Melt Generation

The mid-ocean ridge felsic volcanic rocks from the East Pacific Rise, Galapagos Spreading Center, Pacific-Antarctic Rise and Juan de Fuca Ridge, include andesite, dacite and rhyolite (**Figure 2.2A** and **B**). Samples from ridge-hotspot intersections and ocean islands, such as Iceland, the Azores and Ascension Island, are mostly trachytes and low-alkali dacites and rhyolites. Samples from intraoceanic back-arc assemblages, such as the Lau Basin, are mainly andesites and dacites and plot in a strong linear array from low to high SiO_2 with increasing Na_2O+K_2O. Samples from the Manus Basin have a similarly large range of compositions from andesite to rhyolite. Samples from island-arc assemblages, such as Izu-Bonin, range from dacite to rhyolite and have a narrower range of Na_2O+K_2O. Felsic volcanic rocks from intracontinental arc-backarc assemblages, such as the Okinawa Trough, Western Antarctic Peninsula and TVZ, are mostly rhyolite and dacite. A number of the arc and back-arc samples plot outside the fields of andesite in Pearce (1996) (**Figure 2.2B**). The original Winchester and Floyd (1977) discrimination diagram is based on a limited number of samples and therefore the field boundaries for andesite and rhyolite do not reflect the full variation of data available today. Pearce (1996) addressed this using a more comprehensive dataset but increasing numbers of samples dredged from the modern ocean seafloor show that some boundaries may still need to be adjusted. Data for a selection of felsic rocks from the AGB (Hart et al., 2004; Gaboury and Pearson, 2008) are shown for comparison; as discussed further below, they are not meant to be classified by these plots.

Despite the diversity of sample sites, the major and trace element compositions of felsic volcanic rocks from different settings are remarkably uniform. The andesites and dacites from mid-ocean ridges have SiO_2 concentrations up to 68.0 wt.%, low K_2O (0.9-1.4 wt.%), high TiO_2 (0.6-1.9 wt%), flat REE profiles and high values of $Yb_{(CN)}$ (54.5-99.9, CN=chondrite normalized: **Table 2.1**). Felsic volcanic rocks from ocean islands have similar SiO_2 (60.3-68.1 wt.%), intermediate TiO_2 (0.1-1.8 wt.%) and high K_2O (2.8-6.0 wt.%), with slightly to strongly elevated Large Rare Earth Elements (LREE), compared to mid-ocean ridge samples, and intermediate $Yb_{(CN)}$ (6.3-37.7). The felsic volcanic rocks from ridge-hot spot intersections have a large range of SiO_2 concentrations (61.1-76.5 wt.%), high K_2O (1.9-5.9 wt.%) and REE concentrations that are slightly enriched with intermediate $Yb_{(CN)}$ (12.9-52.5). Felsic volcanic rocks from intraoceanic back-arc

rifts and spreading centers have SiO_2 concentrations up to 74.6 wt.% and higher K_2O (0.3-2.0 wt.%) than the felsic rocks from mid-ocean ridges, as well as low TiO_2 (0.3-2.1 wt.%), flat REE patterns and generally low $Yb_{(CN)}$ (8.6-79.7). Samples from intraoceanic island arcs have higher SiO_2 concentrations (up to 75.8 wt.%) than samples from back-arc spreading centers and consistently low $Yb_{(CN)}$ (9.80-24.05). Felsic volcanic rocks from intracontinental back-arc rifts and spreading centers have the highest SiO_2 (71.1-80.4 wt.%) and K_2O (2.1-4.9 wt.%), low TiO_2 (0.06-0.45 wt.%), slightly elevated $La/Yb_{(CN)}$ (4.22-8.64) and mostly low $Yb_{(CN)}$ (6.9-15.2). The trace and REE patterns of specific assemblages are summarized in **Figure 2.3**.

The origins of the silicic magmas in these different settings is debated (Haase et al., 2006; Brophy, 2008; Tamura et al., 2009; Wanless et al., 2010; Piercey, 2011). Although the dominant processes are thought to be partial melting of hydrated mafic crust and fractional crystallization in mafic magma chambers, there are important variations. Melting in the mantle to produce the precursor basalt can be influenced by geochemical heterogeneities caused by earlier partial melting, input of plume-derived material, or mantle mixing. Thus, variations in the composition of the mafic crust can have a major influence on the derived silicic magmas. This is monitored using trace elements that track enrichment and depletion of incompatible components (Hofmann, 2014). In subduction settings, melting in the mantle is enhanced by the presence of aqueous fluids released from the dehydrating slab (so-called "wet melting") (Pearce et al., 2005; Langmuir et al., 2006; Escrig et al., 2012). Fluids from the slab are highly enriched in LILE, while the less mobile HFSE remain behind. Thus, arc basalts derived from wet melting are enriched in LILE and significantly depleted in moderately incompatible elements such as Ti and Heavy Rare Earth Elements (HREE) (Kelemen et al., 2014). A diagnostic feature is a relative depletion of Nb and Ta, which are insoluble in aqueous fluids and are retained in the mantle wedge above the dehydrating slab (Briqueu et al., 1984; Baier et al., 2008). This is reflected in a negative Nb-Ta anomaly in normalized trace element plots of the basalts and any derived felsic volcanic rocks (see below). The high water contents of arc-related melts also suppress plagioclase fractionation, which results in less pronounced negative Eu anomalies, lower Ti and Fe concentrations, and higher Al concentrations compared to anhydrous melts (Danyushevsky, 2001; Tamura et al., 2005; Langmuir et al., 2006). The high water content also results in high oxygen fugacity (fO_2), suppressing sulfide saturation (Jenner et al., 2010).

"Dry melting" of the mantle occurs at mid-ocean ridges and at mature back-arc spreading centers in response to adiabatic decompression (Langmuir et al., 2006). The melts generally lack the negative Nb-Ta anomaly and show no LILE enrichment typical of wet melting, and they have pronounced negative Eu anomalies. When mafic melts rise into axial magma reservoirs and become isolated and fractionate, any differentiated products will similarly lack the Nb-Ta anomaly and LILE enrichment. Crustal thickness determines the temperature and pressure and therefore the stability of different phases (e.g., garnet or amphibole) during melting. High pressures associated with thicker crust stabilize garnet that concentrates HREE (Hart et al., 2004). At lower pressures, amphibole is the residual phase resulting in the enrichment of La over Yb in the melt. Melting at shallow crustal levels in the absence of garnet or amphibole fractionation results in flat REE patterns in the associated rocks (Hart et al., 2004).

A third process − assimilation of hydrothermally altered crust − can result in significant enrichment of HREE, owing to the presence of HREE-enriched hydrothermal amphibole in the melted material (Wanless et al., 2010). This is important at mid-ocean ridges, but appears to be less so in back-arc assemblages (Beier et al., 2015).

From the above, the characteristic features of silicic lavas at mid-ocean ridges (i.e., negative Eu anomalies, significant HREE enrichment, and flat REE patterns) may be related to: i) a lack of garnet fractionation during shallow/low-pressure melting causing flat REE patterns; ii) plagioclase fractionation under dry melting conditions leading to depletion of Eu; and iii) partial melting and assimilation of altered crust containing HREE-enriched hydrothermal amphibole. In contrast, in subduction settings, the felsic rocks have weak negative Eu anomalies, LILE enrichment, and strong Nb-Ta anomalies related to: i) the suppression of plagioclase fractionation under wet melting conditions; ii) enrichment of LILE by fluids from the dehydrating slab; and iii) the low solubility of Nb and Ta in the subduction fluids. In continental margin arcs, such as the Okinawa Trough and TVZ, the melt compositions additionally reflect variable assimilation of crustal material with high LILE, high Th, low HFSE and low HREE concentrations (Shinjo and Kato, 2000).

2.5 Methods and Analysis

2.5.1 PCA and unsupervised hierarchical clustering

We carried out a multivariate statistical analysis to determine whether the modern felsic volcanic rocks from different tectonic assemblages can be clearly distinguished in the whole-rock geochemical data. The analysis was performed with the R statistical software package (R Core Team, 2020). The workflow is presented in **Appendix A Figure A3** and can be replicated with the code and instructions provided in the **Appendix A** (**Appendix_Workflow_AI.knwf**). All data were recalculated to elemental concentrations in ppm, and centered-log ratio transformations were applied to overcome closure effects (Aitchison, 1982; see **Appendix A Table A2**). Principal components analysis (PCA) (Bartholomew, 2010) was conducted with all 13 elements (Si, Ti, Al, K, Y, Zr, Nb, Ba, La, Sm, Eu, Yb, Th) for all samples in the data set. PCA reduces the variables into a limited number of "components" that account for the largest variance in the data set. Each principal component (PC) is affected by all the variables and represents a fraction of the total variance; the first and second principal components, PC1 and PC2, account for most of the variance (54% and 31%, respectively; see **Appendix A Table A3**). The loadings of each element on each component describe how the different elements contribute individually to the variance (**Figure 2.4** and **Appendix A Table A4**). In **Figure 2.4**, the red element labels correspond to loadings for the entire data set. The plotted points for each sample are a linear combination of the loadings for Si, Ti, Al, K, Y, Zr, Nb, Ba, La, Sm, Eu, Yb, and Th plotted in PC1-PC2 space. The loadings for each sample are given in **Appendix A Table A5**. The analysis shows Yb and Y have strong positive loadings on PC1, whereas Th, La, and K have strong negative loadings. Zr, Nb, and Sm have strong positive loadings on PC2, whereas Si, Al, and Ba have strong negative loadings (**Figure 2.4** and **Table 2.3**). The PCA shows very consistent behaviour between elements that are commonly more mobile (e.g., K, Ba and La) and the immobile elements (Th and Al), suggesting that the results are reflecting primary melt compositions and not alteration. To determine if alteration of the samples has affected the results, we repeated the PCA using only Al, Nb, Ti, Th, Y, Yb, and Zr, which yielded nearly identical PC1 and PC2 scores (see **Appendix A Figure A2**).

We used an unsupervised agglomerative hierarchical clustering of the PCA data to identify geochemically distinct groups of samples in the data set. This type of cluster analysis applies a set of queries or algorithms to classify samples into different groups and maximize the differences between the groups. This is done using Ward's criterion, which is the sum of the squared distances of individuals from the center of the cluster. In our study, we performed a cluster analysis on the first 3 principal components from the PCA. They account for ~90% of the variance and the most important geochemical features in the data set. The cluster analysis was performed with the R statistical software using the unsupervised hierarchical clustering function "HCPC" (Husson et al., 2009). In this type of analysis, no pre-assigned groups or clusters are identified (i.e., the analysis is unsupervised), and the number of clusters is determined by a hierarchical procedure that builds the data tree (i.e., a dendrogram of decision steps that identify the different clusters). Agglomerative hierarchical clustering starts by assuming that every individual sample forms its own cluster, and then the statistical differences or "distances" from all other samples are calculated (e.g., using a proximity matrix). The two samples with the closest distance to each other form the next level of clusters. Ward's criterion calculates the center of each cluster and the distance between clusters. The smallest number of clusters representing all of the samples was determined using an iterative approach. **Figure 2.4A** shows 9 clusters (C1-C9) that were identified with clear separation of the samples based on the loadings of the different elements on PC1 and PC2. The elements with the greatest influence in identifying the individual clusters are: Nb, La and Zr (C1); Nb, La and Th (C2); Y, Yb, and Sm (C3); Ti, Eu and Al (C4); Si, Al, and Th (C5); Si, Al, and Ba (C6); Yb, Zr and Sm (C7); Th, La and Ba (C8); K, Ba and Th (C9). The clustering results and the cluster metadata are given in **Appendix A Tables A5** and **A6**.

Felsic volcanic rocks from ridge-hotspot intersections cluster in the field with negative loadings on PC1 and positive loadings on PC2 (C1 and C2), reflecting the incompatible element-enriched mantle source and high Nb and La of oceanic hotspot assemblages. Samples from mid-ocean ridges cluster in the field with positive loadings on PC1 and positive loadings on PC2 (C3), reflecting the significant enrichment in HREE due to assimilation of hydrated oceanic crust containing HREE-enriched hydrothermal amphibole. Felsic volcanic rocks from intraoceanic arc-backarc environments cluster in three distinct fields with small-to-large positive loadings on PC1 and slightly negative loadings on PC2 (C4, C5, C6), reflecting strong enrichment of elements that are

mobile in slab-derived fluids, such as Ba, and depletion of insoluble elements, such as Zr. A few samples from intraoceanic back-arc environments, such as the Manus Spreading Center in the Manus Basin, the Northwest Lau Spreading Center and the Central Lau Spreading Center in the Lau Basin, plot in the same cluster as mid-ocean ridge samples (C3). This reflects significant HREE enrichment due to assimilation of MOR-like crust. Felsic volcanic rocks from intracontinental arc-backarc systems, including the TVZ, mostly plot with a narrow range of positive to negative loadings on PC2 and a large range of positive to negative loadings on PC1 (C7, C8, C9), reflecting strong enrichment of elements in slab-derived fluids (Ba, K) and enrichment of Th due to crustal assimilation. Felsic volcanic rocks from the marginal back-arc basin of the West Antarctic Peninsula cluster in a field with positive loadings on PC1 and PC2 (C7) reflecting less enrichment of fluid-mobile elements (Ba, K) due to stalled subduction (see below).

The characteristics of each cluster and their relationship to specific lithotectonic assemblages are summarized in **Table 2.3** and **Figure 2.4A** (see also **Appendix A Figure A4**). Cluster C1 contains mainly samples from the Society Island group, Marquesas Archipelago, and the Azores, whereas cluster C2 contains mostly samples from Iceland and Ascension Island. Samples in C1 have higher Nb, Th and Zr concentrations and stronger pronounced negative Eu anomalies. The samples from the Society Islands are related to partial melting of deep-seated basalt with significant crustal contamination (Harnois and Stevenson, 2006), whereas the samples from the Azores are related to fractional crystallization of cyclically rejuvenated magma chambers with trachytic caps (e.g., at the Furnas volcano located at the Terceira Rift: Jeffery et al., 2016). The samples from Iceland in C2 have a transitional affinity, high La/Yb ratios and negative Eu anomalies related to the mantle plume and increased crustal thickness which causes more alkaline geochemical affinity. These rocks are products of near-solidus differentiation (Jónasson, 2007), partial melting of hydrothermally altered and metasomatized basalt and further fractional crystallization (Zellmer et al., 2008). Although Ascension Island is located 90 km west of the Mid-Atlantic Ridge, the felsic lavas erupted when Ascension was closer to, or at, the ridge axis. These samples occur in both C1 and C2, reflecting two different fractionation trends: one with increased Zr/Nb ratios due to ilmenite fractionation (i.e., partitioning Nb) and the other related to zircon/titanite fractionation (i.e., partitioning Zr: Jicha et al., 2013). Cluster C3 contains all of the mid-ocean ridge dacites from

the Pacific-Antarctic Rise, East Pacific Rise, Galapagos Spreading Center and the Juan de Fuca Ridge. These samples have anomalously high HREE concentrations, typical for assimilation of hydrothermally altered crust at mid-ocean ridge spreading centers. Cluster C3 also contains a number of samples from intraoceanic back-arc spreading centers, notably the Manus Spreading Center and the Northwest Lau and Central Lau spreading centers (NWLSC and CLSC: **Table 2.3**). These samples have flat REE patterns, mostly lack negative Nb-Ta anomalies, and show no LILE enrichment normally associated with subduction-related assemblages. Instead, they are located far from a subduction zone where the melts are influenced mainly by the mantle source and spreading regime. One sample from the West Antarctic Peninsula (Bransfield Strait, which is a failed intracontinental back-arc spreading center behind the South Shetland island arc), plots in the same cluster as mid-ocean ridge samples (C3), reflecting no enrichment of fluid-mobile elements (Ba, K) (see **Appendix A Figure A4**), despite its proximity to the continental margin. The subduction zone at Bransfield has stalled (Fretzdorf et al., 2004), resulting in a decrease in the contribution from a dehydrating slab and a rhyolite signature closer to that of the East Pacific Rise and Pacific-Antarctic Rise. Cluster C4 contains felsic volcanic rocks from the Raoul volcano of the Tonga-Kermadec arc and Sumisu Knoll at the volcanic front of the Izu-Bonin arc. These samples have strong arc signatures (e.g., deep negative Nb-Ta anomalies, LILE enrichment and weak negative Eu anomalies) and flat REE patterns, and they are less enriched in HREE than rhyolites from MOR or most back-arc spreading centers. An exception is the Valu Fa Rift and back-arc spreading center (VFR) of the Southern Lau Basin, which is propagating into arc crust of the Tofua volcanic arc. Samples from the VFR fall in cluster C4 (see **Appendix A Figure 4**) and share a strong arc signature resulting from fractional crystallization of mafic magma chambers with the addition of components from the nearby arc (Fretzdorff et al., 2006; Barker et al., 2013). The volcanic rocks at Sumisu Knoll are thought to be products of partial melting of the middle arc crust (Tamura et al., 2009; Haraguchi et al., 2017). Cluster C5 contains felsic volcanic rocks from the volcanic front of the Mariana Arc (Anatahan), the Lesser Antilles Arc (Montserrat), the Kermadec Arc (Brothers and Healy volcanoes) and the Niuatahi rear-arc volcanic complex behind the active Tofua Arc in the northern Lau Basin. Samples from arc-related rifts are also included in this cluster, namely from the Sumisu Rift and Myojin Rift behind the Izu arc, two samples from the Bransfield Strait and several samples from the Pual Ridge in the Manus Basin. All samples have strong arc signatures, including LILE enrichment, slight LREE enrichment and weak negative Eu anomalies

related to fractional crystallization and/or partial melting of the middle arc crust. They exhibit a negative Nb-Ta anomaly, but it is less pronounced than the samples belonging to cluster C4. Two samples from the Okinawa Trough also fall into cluster C5. Cluster C6 contains felsic volcanic rocks from the Fonualei and Niuatoputapu volcanic islands on the Tofua Arc, Macauley volcano on the Kermadec Arc, and Proctor shoal on the South Sandwich Arc. These samples have strong arc-like signatures similar to the samples in cluster C5 but with a slightly weaker negative Eu anomalies, stronger pronounced negative Nb-Ta anomalies and generally lower HFSE and REE concentrations. They are related to mafic melt lenses that were emplaced into the cold arc crust and underwent fractional crystallization (Turner et al., 2012; Barker et al., 2013). Cluster C6 also contains samples from the Bayonnaise Knoll, located in a back-arc depression behind the Izu volcanic arc, from rift-related assemblages at SuSu Knolls in the Manus Basin, and from the Torishima Rift and Aogashima Rift behind the Izu volcanic arc. These rocks, including samples from Pual Ridge in the Manus Basin, are also products of fractional crystallization of mafic melt lenses with minor contributions from assimilated crustal material or partially melted middle arc crust (Tamura et al., 2009; Beier et al., 2015). Samples from some locations (e.g., Macauley Volcano, Torishima Rift and Pual Ridge) plot both in Cluster C5 and C6, reflecting a transitional character. Cluster C7 is mainly defined by the felsic volcanic rocks from Hook Ridge in Bransfield Strait. However, it also contains four samples from back-arc rifts behind the Izu-Bonin Arc (Sumisu Rift and Myojin Rift) and two samples from the Mangatolu Triple Junction within the northern Lau back-arc basin. These rocks all have slight negative Nb-Ta anomalies, slight LILE enrichment, intermediate negative Eu anomalies, mostly flat REE patterns and slightly less HREE enrichment than mid-ocean ridge samples but reflecting limited input from the subduction zone compared to other arc-related samples (C4, C5, and C6). Clusters C8 and C9 contain mostly felsic rocks from the Okinawa Trough back-arc rift and the TVZ, which are enriched in LREE, alkali elements, and Th and have negative Nb-Ta anomalies. However, samples from the TVZ fall into two clusters, capturing both dry (i.e., cluster C8) and wet (i.e., cluster C9) melting conditions, as previously documented by Deering et al. (2008) (see discussion). A few samples from hot-spot volcanoes (Hawaii, Samoa, and Ascension Island) plot in C8 (**Figure 2.4A**) because of their low HREE concentrations and stronger alkaline signatures compared to other hotspot volcanoes. These samples are related to late-stage shield volcano development and deep hydrous crustal melting (van der Zander et al., 2010).

The cluster analysis illustrates the significant geodynamic control on the geochemical signatures of modern oceanic felsic volcanic rocks. Clusters C1 and C2 correspond mainly to hot-spot related assemblages; C3 corresponds to mid-ocean ridge-like assemblages; C4-C6 correspond to intraoceanic arc assemblages; C7 corresponds to arc-backarc assemblages with weak subduction-zone influence; and C8 and C9 correspond to intracontinental arc assemblages. In the following section we perform a supervised classification based on the identified clusters and conduct a blind test to determine if the classification scheme can accurately predict geodynamic influences in the felsic volcanic rock geochemistry.

2.5.2 Training a new classifier

Supervised classification is a machine-learning task that sorts samples into known classes identified using a "training" data set. The training is an iterative process by which a machine-learning classifier, such as random forest, learns what values are meaningful to achieve the best classification outcome and builds a model that can be used as a classification scheme. We used our database of 643 samples of modern felsic volcanic rocks to build the model. The steps involve initial processing of the data to create the training set, training of the classifier, and then evaluation of its prediction success. The initial input is a selection of parameters (i.e., analyzed elements) and predetermined clusters (i.e., target classes) for each sample. These are randomly divided into a training data set, used to build and validate the random forest classifier, and a blind test data set used to evaluate the prediction rate. Random forest (RF) has proven to be particularly useful for supervised classification based on multivariate input (Fernandez-Delgado et al., 2014). It functions using multiple decision trees with true or false outcomes (Breiman, 2001) (e.g., "are SiO_2 concentrations >73 wt. % ?"; if yes, the sample is a rhyolite; if not, the samples is a dacite). These decision points are commonly referred to as "nodes"; follow-on decision points are referred to as "child nodes". The cut-offs for each cluster are determined by the classifier's ability to separate the training data most efficiently. For example, if dacites and rhyolites are to be divided at a node based on their SiO_2 concentrations, a value of 73 wt. % correctly identifies all dacites and all rhyolites. The correct cut-off is identified through an iterative approach testing several SiO_2 concentrations until the best separation of the clusters is achieved, commonly referred to as "pure" separation. At every node, the "impurity" can be measured, corresponding to the probability of a

parameter falsely classifying a sample, and therefore a measure of the importance of the parameter in the decision making. This is commonly determined using the “Gini index”:

$$Gini(t) = \sum_{c=1}^{j} g_c(1 - g_c)$$

$$g_c = \frac{n_c}{n}$$

where “t” is the node in the decision tree (e.g., Ti), “c” is the target class (e.g., C1), “j” refers to the possible classes (e.g., C1-C9), and “g_c” is the relative frequency of classification, “n_c” is the number of samples belonging to target class “c”, and “n” is the total number of samples evaluated at this node. Nodes, or parameters (e.g., Ti), with a low Gini index have a high probability of correctly classifying a sample.

A single decision tree alone may be very sensitive to overfitting; it may work very well with the training data but performs poorly in blind tests. Random forest overcomes this problem by using a large number of uncorrelated decision trees operating as a “committee” that casts votes for each decision. Multiple decision trees (usually a thousand or more) are created by randomly selecting elements (i.e., the nodes) from a training data set. Each decision tree is then evaluated or "trained" with randomly chosen samples (equal to the total number of samples in the data base), a method commonly known as “bootstrapping”. Importantly, during this process samples can be picked multiple times, which leaves behind a pool of samples that were not picked and therefore not involved in some decision trees (so-called “out of bag” samples); typically about 1/3 of all samples. These “out of bag” samples are used to validate the classification (see below). To classify an unknown sample, each of the randomized decision trees casts a single “vote” for a single target class or cluster (C1-C9). The votes cast by all of the decision trees are given in percentages (summing to 100%), and RF uses the majority decision of these votes to finally classify a sample (Breiman, 2001). A disadvantage of the random forest classifier is that it will force a decision regarding the classification of a sample even if the sample does not match any of the target classes. Forced decisions do not receive a majority vote but rather a randomly distributed set of votes that can be investigated in the metadata.

We randomly selected 80% of our database to train and validate our RF classifier; the remaining 20% was used for a blind test (see below), which is a standard approach to validate the RF classifier. The target classes are the 9 clusters shown in **Figure 2.4**. The differences in the number of samples in the target clusters can create a class imbalance, which can lead to poor performance of the RF classifier. To overcome this, we equalized the number of samples for each cluster prior to the training process using the synthetic minority oversampling technique (SMOTE: Chawla et al., 2002). SMOTE "creates" new samples by slightly altering the geochemical composition of original samples until each class contains the same number of samples as the largest class, resulting in an artificial training set with 1440 samples. The data created by this process are given in **Appendix A Table A7**.

Building and testing our classifier was done using the R statistical software, in which a defined number of decision trees is selected and a minimum number of nodes, based on classification performance. Gini indexes were calculated to evaluate the performance of each node, which were ordered from their highest to their lowest predictive power. 1000 decision trees, each trained with 3 randomly selected elements yielded the highest predictive power in our classifier. To validate the model, we used the subset of samples remaining from the bootstrapping procedure (i.e., "out of bag" samples). These samples were separated from the original 643 samples and none were created via SMOTE. The method correctly classified 100% of the "out of bag" samples of all target classes C1-C9 (**Appendix A Table A8**). The impurity for each node averaged over the complete RF classification scheme is referred to as the Mean Decrease Gini. It corresponds to the probability of misclassification and identifies Al, Ba, Nb, Th, Yb, and Y as the most important variables in determining whether a sample is classified correctly (**Figure 2.5**). In contrast, nodes corresponding to Ti and Eu have low Mean Decrease Gini values and therefore less influence in the correct identification of a sample. We then conducted a blind test on the randomly selected samples that were not used in the training of the model (20% of our original database) to determine how well the classifier performs on new data. At least 3 samples were available for each target class in the blind test (see **Appendix A Table A9**). The test samples were correctly classified in almost every case for all target classes, reaching an overall accuracy of 96% (**Appendix A Table A10**).

2.6 Discussion

Using automated principal components analysis and hierarchical clustering, we have identified 9 target classes of felsic volcanic rock compositions in the modern oceans corresponding to distinct geodynamic settings and reflecting different melting conditions. Based on these target classes, we then constructed a RF classifier that accurately identifies rocks from those settings. Here, we discuss the petrogenetic significance of the target classes, and then assess the application of the RF classier to ancient volcanic rocks.

2.6.1 Petrogenetic significance of the hierarchical clusters

The most important geochemical characteristics of the target classes in our model include: high La/Sm in target class C1 and C2, indicating enriched mantle contributions to the source melts; flat and HREE-enriched REE patterns in target class C3, indicating assimilation of hydrothermally altered crust; negative Nb-Ta anomalies and LILE enrichments with low Th in target class C4, C5 and C6, related to subduction-zone processes in intraoceanic arc-backarc systems; and similar negative Nb-Ta anomalies and LILE enrichments but with high Th in target class C7, C8 and C9 reflecting contributions from continental crust. These characteristics correspond closely to the established petrogenesis of felsic volcanic rocks in different geodynamic settings described above and summarized in **Table 2.3**. However, no prior knowledge of the geodynamic settings of the samples has influenced the clustering described here.

The characteristics of felsic rocks in target class C1 are most consistent with an ocean island setting, with increased heat flow and enriched mantle sources of the hotspot environment (Zander et al., 2010; Chauvel et al., 2012; Konter et al., 2012). In addition to high La/Sm, they are characterized by intermediate to strongly negative Eu anomalies, no negative Nb-Ta anomaly and an alkaline affinity. Low Ti, Si and Al and high Nb and La result in negative loadings on PC1 and positive loadings on PC2. Felsic rocks in target class C2 also have enriched OIB-like mantle signatures, high La/Sm, intermediate to strongly negative Eu anomalies and no negative Nb-Ta anomalies, typical of ridge-hotspot intersections, but they have lower Nb, Th, and Al, more variable and higher Si, and are less alkaline than rocks from target class C1. This reflects shallower melting and a shift to tholeiitic affinity in rift regimes. Felsic rocks in target class C3 have

significant enrichment in HFSE with high total REE and flat REE patterns but no negative Nb-Ta anomalies and low potassium, typical of rocks from mid-ocean ridges. The pronounced negative Eu anomaly and lack of LILE enrichment reflect dry melting conditions. The characteristics of felsic volcanic rocks in this class overlap with felsic rocks from intraoceanic back-arc spreading centers far from any subduction zone or where subduction has stalled resulting in no dehydration of the downgoing slab. Felsic volcanic rocks in target classes C4, C5 and C6 have geochemical signatures reflecting a range of melting regimes in intraoceanic arc and back-arc systems. Felsic volcanic rocks in C4 and C6 have strong arc signatures with significant input from a dehydrating slab, as in arc-front volcanoes and arc-related rifts. These rocks are characterized by large negative Nb-Ta anomalies, slightly less HREE enrichment than target class C7, and small to intermediate negative Eu anomalies. Strong negative Eu anomalies, flat REE patterns and high HREE in target class C4 indicate drier melting conditions and a shallower melting regime than samples in target class C6. Felsic volcanic rocks in target class C5 also have strong arc signatures characterized by negative Nb-Ta anomalies, LREE enrichment and small to intermediate negative Eu anomalies observed at near-arc volcanoes and in related back-arc rifts. They are similar to rocks in target class C6 but with higher REE, Th, and HFSE and less pronounced Nb-Ta anomalies. Felsic volcanic rocks in target class C7 have weak arc signatures with low input from a dehydrating slab indicated by small negative Nb-Ta anomalies, less HREE enrichment than at mid-ocean ridges, and intermediate negative Eu anomalies, typical of felsic rocks in extended continental arc or back-arc crust. Felsic volcanic rocks in target class C8 and C9 have geochemical signatures mostly reflecting the role of continental crust with variable input from a dehydrating slab, as in intracontinental back-arc rifts and spreading centers. They are characterized by calc-alkaline affinity, negative Nb-Ta anomalies, intermediate negative Eu anomalies, LILE enrichment and high Th. Target class C8 has higher HREE, indicating drier melting conditions than target class C9.

The interpretations of the different classes are supported by isotopic data that confirm different conditions and sources of melting (Fretzdorff et al., 2006; Haase et al., 2006; Barker et al., 2013; Beier et al., 2015). In the case of ocean islands (target class C1) the felsic volcanic rocks are products of deep, low-degree mantle melting of anhydrous depleted mantle, whereas at ridge-hotspot intersections (target class C2) they result from shallow fractionation of melt lenses. The

latter have transitional alkaline to tholeiitic geochemical affinity but with plume-like signatures that are less pronounced than in ocean islands because of the additional influence of the spreading regime, including stagnation of melt lenses, assimilation of crustal material, and partial melting of crustal rocks (Brophy, 2009; Zierenberg et al., 2013). At MOR spreading centers (target class C3) the volcanic rocks are products of upwelling asthenospheric mantle, with felsic rocks derived from fractional crystallization of isolated magma chambers and assimilation of hydrated oceanic crust at overlapping spreading centers, propagating rift tips and transform boundaries. Felsic rocks from intraoceanic arc and back-arc systems (target classes C4, C5, C6, and C7) all show some influence of the arc and subducting slab, including high degrees of partial melting (e.g., approximately 20%) of the basaltic crust due to the strong volatile input (C4), volcanoes built on older arc or forearc crust with fractional crystallization occurring in stalled magma chambers (C5), or with highly variable influence of slab-derived fluids (C6 and C7). Felsic rock in continental margin arcs (target classes C8 and C9) all show evidence of crustal melting and the input of metasedimentary material.

At back-arc spreading centers there is commonly a transition from wet to dry melting with distance from the volcanic arc (Fretzdorff et al., 2004; Langmuir et al., 2006; Escrig et al., 2012). Back-arc basins that are characterized by diffuse spreading and multiple spreading centers, such as the NE Lau Basin (Stewart et al., 2021), experience a wide range of wet and dry melting conditions (Zhang et al., 2018), whereas volcanic rocks from back-arcs dominated by a single spreading center are geochemically less diverse (e.g., Mariana back-arc: Taylor and Martinez, 2003). These differences are illustrated schematically in **Figure 2.6**. Thermal convection below spreading centers causes mantle flow orthogonal to the ridge axis (Sparks et al., 1993). Because back-arc spreading centers are commonly asymmetric, rocks from across the basin commonly reflect a range of different melting conditions (Langmuir et al., 2006; Bézos et al., 2009) − the arc-proximal side influenced by wet melts, and the arc-distal side focusing drier mantle melts. Differences in the degree of partial melting are indicated by flat HREE-enriched and flat HREE-depleted end-members in close proximity (Tamura et al., 2005; Escrig et al., 2012) as observed in the northern Lau Basin (**Figure 2.7**). Felsic volcanic rocks from mature back-arc spreading centers, especially in the west of the Lau Basin, lack a negative Nb-Ta anomaly and have overall higher HFSE and REE concentrations and more pronounced negative Eu anomalies than observed in back-arc rifts closer to the arc, such as the VFR. Identical relationships are seen in the Manus Basin, with felsic volcanic rocks from

the Eastern Rift, located close to the arc, exhibiting strong negative Nb-Ta anomalies, low HSFE and HREE concentrations and weak negative Eu anomalies compared to spreading centers farther from the arc (e.g., at Pual Ridge). Felsic volcanic rocks from the mature Manus Spreading Center in the center of the basin are nearly identical to those from mid-ocean ridges. These differences correspond closely to the FIV-type arc-like signatures and FIIIb-type intraoceanic back-arc spreading signatures inferred for some Archean rhyolites (see below).

Greater crustal thickness, which causes deeper melting, is reflected in increasing $La/Yb_{(CN)}$, Th and K, as observed, for example in the Eastern Rifts in the Manus Basin (Beier et al., 2015), at the Healy and Brothers volcanoes of the Tonga-Kermadec arc (Barker et al., 2013), and some near-arc volcanoes in thickened crust of the NE Lau Basin (Niuatahi: Park et al., 2015). These variations are similar to what has been observed in ancient greenstone belts where thickened crust has been proposed (McKenzie et al., 1988).

2.6.2 Comparison with Archean felsic volcanic rocks

On average, Archean crust was more mafic than oceanic crust today (e.g., Palin et al., 2020), and the mafic melts were formed from mantle sources that required melting at very high temperatures (Prior et al., 1999; Piercey, 2011; Thurston, 2015). Felsic volcanic rocks in Archean greenstone belts occur in bimodal mafic-felsic volcanic successions in locally thickened crust. They were derived in part from differentiation of high-level magma chambers and by partial melting of the hydrated oceanic crust, as in the modern oceans (Hart et al., 2004). The volumes of felsic volcanic rocks are significantly greater than in modern intraoceanic settings (e.g., Franklin et al., 2005), probably reflecting the higher mantle temperatures, longer residence times of melt in the crust and more extensive fractionation. The source of the felsic melts is recorded in part by Zr/Y ratios, HFSE concentrations and, in particular, REE patterns that underpin the F-classification of Archean rhyolites (**Table 2.2** and **Figure 2.8**: Lesher et al., 1986; Barrie et al., 1993; Hart et al., 2004).

In the F-classification different types of Archean rhyolites were grouped according to the compatible-incompatible element behaviour of Zr, Y, LREE, HREE; the latter reflecting the strong partitioning of HREE into garnet and amphibole in the source regions of the rhyolitic melts. FI rhyolites have alkaline to calc-alkaline affinities and formed by low-degree partial melting at high pressure (i.e., in the stability field of garnet) with HREE depletion due to garnet fractionation at the source. They are interpreted to have formed from arc-related magmas at deep crustal levels. FII rhyolites have a calc-alkaline affinity and formed from high-degree partial melts with slightly depleted HREE. They are thought to have formed in continental arc and back-arc settings with melts originating at intermediate crustal depths. FIII rhyolites have tholeiitic affinity and formed by low-pressure partial melting of basalt with variable HREE enrichment (no residual garnet or amphibole). FIIIa rhyolites, which are thought to have formed in shallow melt lenses in rifted island arcs, have flat REE patterns and intermediate HREE concentrations. FIIIb rhyolites, which are interpreted to have formed in oceanic rifts, have flat REE patterns, significant HREE enrichment and strong negative Eu-anomalies caused by partial melting of hydrated mafic crust and plagioclase fractionation. FIV rhyolites have a tholeiitic affinity and are thought to have formed in juvenile volcanic arcs by low-pressure, moderate-degree partial melting of a LREE-depleted mantle source. Hart et al. (2004) considered FIV-type rhyolites to be restricted to post-Archean intra-arc assemblages associated with volatile-fluxed melting. **Figure 2.9** compares the trace element signatures of modern oceanic felsic volcanic rocks to the fields originally chosen for the F classification of Archean rhyolites. The major differences and similarities are discussed below, with reference to the felsic volcanic rocks of the Abitibi Greenstone Belt.

The AGB is the largest intact Neoarchean greenstone belt and economically one of the most important volcanic terranes in the world. Submarine volcanism produced six temporally distinct assemblages between 2795 and 2695 Ma, traditionally divided into the Northern and Southern Volcanic Zones (Monecke et al., 2017). They contain a number of mafic and felsic synvolcanic intrusive complexes, such as at Matagami and Noranda, and mafic-ultramafic successions such as in the Kidd-Munro Assemblage. Significant volcanogenic base metal sulfide deposits are associated with the felsic volcanic rocks at Matagami, Noranda, and Kidd Creek. The volcanic and sedimentary rocks of the AGB are widely interpreted to be part of an intraoceanic arc-backarc system with similarities to modern oceanic microplate mosaics (Jackson et al., 1994; Percival et

al., 2012; Wyman, 2013). However, a number of authors have suggested significant differences between Archean and post-Archean magmatism and tectonics, with some Archean terranes possibly having no modern analog (see below). We have used the RF classifier developed in this paper to test whether Archean felsic volcanic rocks of the AGB can be classified along the same geochemical lines as modern samples and thereby possibly interpreted in terms of processes like those observed in the modern oceans. We make no assumptions about the nature of Archean tectonics or the applicability of Phanerozoic systems to Archean geodynamics − which is a larger discussion beyond the scope of this paper.

Felsic volcanic rocks from 20 different locations in the AGB (see **Appendix A Table A**11) were examined with the RF classifier developed for the modern samples. We used data compiled by Gaboury and Pearson (2008) and the MRD085 data set from the Ontario Geological Survey (2001), which was also used by Hart et al. (2004). These data were selected because the samples were collected specifically to avoid altered rocks, which was confirmed by petrography, and any suspect samples were flagged for removal based on differences between mobile and immobile element behaviour. To mitigate any effects of alteration that were not already recognized and filtered out by Gaboury and Pearson (2001), we tested the data using Pearce Element Ratio (PER) plots [e.g., (Ca Na K)/Zr versus (Al Ca)/Zr: **Appendix A Figure A1**] and also ran the RF classifier with and without the mobile elements (see **Appendix A Tables A12** and **A13**). The RF classifier addresses the problem of alteration by failing to classify any samples for which the major or trace elements fall outside identified ranges for unaltered samples in the training sets. The samples included in the analysis are tholeiitic to calc-alkaline felsic volcanic rocks from the Selbaie area, Gemini-Turgeon, Geant-Dormant, Joutel, Normetal, Lac Herbert, Quevillon and Coniagas in the Northern Volcanic Zone (NVZ), as well as samples from the Hunter Mine Group, Val-d'Or, Noranda, Bousquet, the western Blake River Group, and the Timmins-Porcupine area, and dominantly tholeiitic rocks from the Matagami area, Kidd Creek, and Kamiskotia. 145 samples with >60 wt.% SiO_2 were selected for the final database, following the same QA/QC applied to the modern volcanic rocks (**Appendix A Table A11**).

The dacites and rhyolites from the AGB belt have generally higher SiO_2 (60.2-85.9 wt.%) than modern submarine felsic volcanic rocks and more variable K_2O (0.02-4.43 wt.%); Na_2O+K_2O concentrations are generally lower than in modern felsic volcanic rocks and span the entire TAS range (**Figure 2.2A**). They have low TiO_2 (0.05-0.81wt.%), flat to steeply dipping REE patterns and variable $Yb_{(CN)}$ (9.10-50.10) (**Figure 2.10**). Importantly, negative Nb-Ta anomalies and LILE enrichments, which are the dominant features of felsic volcanic rocks in modern submarine arcs, are found in every assemblage of the AGB. The RF classifier identifies the AGB rhyolites as belonging to four main target classes: C2, C3, C5, and C8 (**Appendix A Table A12** and **Figure 2.11**). However, 87 of the 145 samples were not classified (i.e., no single class received more than 50% of the votes). This indicates either fundamental differences from modern oceanic felsic volcanic rocks or geochemical variation due to alteration and metamorphism among these samples. The majority of samples that were not classified have high and variable K_2O that would suggest alteration (e.g., from Kidd Creek: **Appendix A Table A11**). The remaining 58 samples were assigned to one of the target classes (**Figure 2.11** and **Appendix A Table A12**). Al, Ba, Nb, Th and Yb had the greatest influence on the identification of a target class for the AGB samples. None of the samples were classified as belonging to target class C1 (e.g., with strong plume influence). However, 4 rhyolite samples from Kidd Creek were classified as belonging to C2, indicating similarities to ridge-hotspot intersections such as Iceland as previously suggested by Prior et al. (1999). Three samples from Matagami were assigned to target class C3, indicating similarities with modern mid-ocean ridges (FIIIb-type signatures: see below). The samples from Noranda show greater geochemical variability with one sample classified in C3, five samples in C5, one sample in C7 and one sample in C8, similar to rhyolites associated with rifting of thickened arc crust in the Eastern Manus Basin, as previously observed by Yang and Scott (2003). A high proportion of felsic volcanic rocks in the Southern Volcanic Zone of the AGB are classified as belonging to intraoceanic back-arc and arc-related rifts (e.g., target class C5). None of the samples are fully classified into C4 or C6, which contain mostly felsic volcanic suites from nascent back-arc rifts and volcanoes at the volcanic fronts of active arcs. Four samples from the Hunter Mine area and six samples from the Bousquet Formation were classified into C8 and C9, indicating geochemical similarities with rhyolites from the Taupo Volcanic Zone and Okinawa Trough (with FI to FII-type signatures: see below). Although there is no evidence of continental basement in the Hunter Mine and Bousquet areas, the Bousquet Formation is interpreted to have been deposited

on much older crust, as indicated by inherited zircon ages (Ayer et al., 2002; Mercier-Langevin et al., 2007). Samples from the Bousquet Formation have negative Nb-Ta anomalies, high Th concentrations, and negative Eu anomalies that are nearly identical to felsic volcanic rocks of the TVZ, although the La/Yb and Zr/Y ratios are slightly lower (**Figure 2.10B**). In **Appendix A Table A13**, we show the results for the AGB samples using the RF classifier including only immobile elements, which resulted in more samples being classified into C7 instead of C5.

The comparison with the classification of modern samples suggests that felsic magmas generated above the hot Archean mantle were geochemically most similar to those of modern back-arc spreading centers with MOR-like signatures, such as the Manus, Central Lau, and Northwest Lau spreading centers (target class C3) and the large dacitic lava flows recently documented in the Northeast Lau Basin (e.g., Niuatahi in target class C5). The voluminous eruption of dacite at Niuatahi is thought to be due to high upper mantle temperatures at this location (Embley and Rubin, 2018). An important difference is that the Abitibi felsic volcanic rocks have a weaker negative Nb-Ta anomaly than felsic volcanics erupted above modern subduction zones, implying little input from a dehydrating slab or simply a less depleted mantle. In **Figure 2.10A**, the geochemical signatures of the felsic volcanic rocks of Matagami and Kidd Creek are compared to Iceland and MOR-like dacites from the northern Lau Basin. In these plots, rhyolites from Kidd Creek and Matagami have the greatest similarity to felsic volcanic rocks from MOR-like back-arc spreading centers such as the NWLSC and Mangatolu Triple Junction (MTJ). In contrast, samples from Noranda bear a closer resemblance to felsic volcanic rocks from Niuatahi and Okinawa (**Figure 2.10D**). The close juxtaposition of diverse geochemical signatures in centers such as Noranda (Gaboury and Pearson, 2008) may reflect complex spreading regimes similar to modern, high heat-flow domains in the northern Lau Basin and Manus Basin (Lagabrielle et al., 1997; Yang and Scott, 2003; Karson, 2017). In particular, the complex microplate tectonics of these settings (Sleeper et al., 2016; Baxter et al., 2020) have been suggested as a possible modern analog of Archean greenstone terranes, citing the high heat flow and more abundant spreading centers (e.g., Stewart et al., 2021). The melting conditions at Matagami may have been similar to dry melting conditions and/or thickened crust at the Pacific-Antarctic Rise and Northwestern Lau Spreading Center in the Lau Basin today.

Arc-like geochemical signatures are common in the Abitibi (Ayer et al., 2002) but do not prove that volcanic arcs and subduction zones existed, as there could have been a number of different ways to produce the observed signatures (Bedard, 2013; Pearce, 2008; Mole et al., 2021). Because Archean rocks are not as depleted as modern volcanic rocks, many argue that modern plate tectonic processes could not have been the cause of negative Nb-Ta anomalies and high Th concentrations (Bedard et al., 2013; Thurston 2015). A number of alternative models of Archean greenstone belt evolution have been suggested that could account for the differences (e.g., "dome and keel" and "mantle wind" models: Sawyer et al., 1994; Bedard et al., 2013; Thurston, 2015; Mole et al., 2021). Some have invoked crustal contamination to create the arc-like signatures, which is consistent with the Th enrichment identified in the RF classification and with evidence of older crust beneath the AGB (e.g., Mole et al., 2021). Any process that introduced hydrated basalt to depth could have created conditions appropriate for generation of arc-like geochemical signatures (Pearce, 2008). In particular, negative Nb-Ta anomalies may be related to ilmenite fractionation and assimilation of amphibolite (seawater-altered crustal components: Haase et al., 2005), resulting in arc-like rocks without subduction. We show that the only places in the modern oceans where arc-like geochemical signatures exist in the absence of subduction are in the few felsic rocks from the Pacific Antarctic Rise (Haase et al., 2005; Freund et al., 2013) and dacites with negative Nb-Ta anomalies on Iceland (Willbold et al., 2009). The comparison with the AGB shows that very similar rocks, divided along clearly defined geochemical lines, existed in the Archean and perhaps for similar reasons.

2.6.3 Implications for the F-classification scheme

Attempts to identify modern analogs of FI-FIV rhyolites have had mixed results (e.g., Prior et al., 1999; Piercey, 2011; Huston et al., 2019). It is well established that geochemical characteristics of Archean rhyolites are not directly comparable to those in Phanerozoic belts, which are dominated by FII and FIV types (Lentz, 1998; Piercey et al., 2001; Hart et al., 2004). Piercey (2011) characterized felsic volcanic rocks from juvenile, mafic-dominated post-Archean settings as having tholeiitic FIV-like signatures with low HFSE and HREE, typical of modern forearc or intra-arc rifting. Felsic volcanic rocks from more mature arc-backarc systems, and especially those derived from partial melting of continental crust and sedimentary rocks were found to have

intermediate FII-to-FIII signatures with high HFSE and HREE and within-plate (A-type) to peralkaline affinity (Piercey, 2011).

Figure 2.8 shows the distribution of AGB rhyolites in FI-FIV space. Felsic volcanic rocks of the Bousquet Formation, with high Zr/Y and distinct negative Nb-Ta anomalies, have FI signatures similar to continental margin arc volcanics of the TVZ but are less enriched than hotspot volcanoes. Many of the AGB felsic volcanic rocks fall in the FII field, including samples from the Hunter Mine area and Lac Herbert, although this type of rhyolite is mainly found in post-Archean felsic volcanic centers (Hart et al., 2004). Felsic volcanic rocks from Noranda, Joutel, Normetal and Quevillon (**Appendix A Table A11** and **Figure 2.10**) overlap with the FII and FIIIa fields. The REE signatures of felsic volcanic rocks from Noranda are variable. They range from HFSE- and HREE-enriched suites (almost FIIIb) to HFSE- and HREE-depleted rocks (mostly FIIIa), similar to modern intraoceanic arc-backarc systems. In contrast, FIIIb-type rhyolites from Matagami and Kidd Creek have significantly higher $Yb_{(CN)}$. The enriched sources were most likely hot mantle material that is thought to be directly linked to the formation of largee VMS deposits in these areas. Prior et al. (1999) particularly compared FIIIb rhyolites from Kidd Creek to the rhyolites from plume-like sources in Iceland. Thus, Archean FIIIb rhyolites probably originated in extensional settings dominated by MOR-type spreading above an anomalous mantle, possibly in complex microplate mosaics like the northern Lau Basin today. Several authors have pointed to the lack of post-Archean FIIIb signatures as an indication of the decrease in mantle temperatures and shift in the depth of melting through time (e.g., Lesher et a., 1986; Lentz, 1998; Hart et al., 2004). FIV-like felsic volcanic rocks are rare or absent in the AGB, probably reflecting the lack of volatile-fluxed melting.

Felsic volcanic rocks from modern settings span almost the entire range of the F-classification (**Figure 2.9**). Those associated with alkaline hotspot magmatism and some calc-alkaline continental arcs overlap with the FI field. Felsic volcanic rocks from the TVZ, Myojin Rift (Izu-Bonin), rear-arc volcanoes such as Niuatahi (Lau Basin) and large arc volcanoes such as Montserrat (Lesser Antilles Arc) overlap with FII. These rocks are all characterized by weak calc-alkaline affinity and steep REE patterns due to amphibole fractionation. Increasing crustal thickness, from Niuatahi to the TVZ, is reflected in increasing La/Yb ratios. Some samples from

modern ridge-hotspot intersections (Iceland, Azores, Ascension Island) also have FII signatures, but with higher Zr/Y, La/Yb and total HREE concentrations than Archean FII-rhyolites. Those from transitional or continental margin arc-backarc systems, such as the Okinawa Trough, Western Antarctic Peninsula and the Eastern Rifts of the Manus Basin, overlap with FIIIa. Samples from intraoceanic arc-backarc systems, such as Izu-Bonin, the Mariana arc and volcanoes of the Tonga-Kermadec arc, also plot in FIIIa. The arc influenced suite is distinguished from FIIIb by lower $Yb_{(CN)}$ and significant negative Nb-Ta anomalies compared to more distant back-arc spreading centers (e.g., NWLSC, CLSC and the Manus Spreading Center: **Figure 2.3**). Samples from distant back-arc spreading centers, together with felsic volcanic rocks from mid-ocean ridges and ridge-hotspot intersections (e.g., Pacific-Antarctic Rise, East Pacific Rise, Galapagos Spreading Center, Juan de Fuca Ridge), overlap with FIIIb. They have flat REE patterns, slightly negative to absent Nb-Ta anomalies and significant HREE enrichment indicating assimilation of hydrated oceanic crust (Haase et al., 2005; Wanless et al., 2010). Propagating rift tips and overlapping spreading centers, in particular, which are characterized by episodic magma injections and melt fractionation without continuous replenishment (Wanless et al., 2010), appear to be ideal settings for the generation of FIIIb-type rhyolites today. These complex spreading regimes may be the surface expression of small and hot mantle convection cells, leading to localized mantle upwelling and enhanced melting (Rychert et al., 2020). Felsic volcanic rocks from intraoceanic arc volcanoes and arc rifts, such as the Aogashima Rift and Valu Fa Rift are FIV-type. They are characterized by lower HREE concentrations, smaller negative Eu anomalies and more pronounced negative Nb-Ta anomalies than the back-arc spreading centers (**Figure 2.3**), consistent with the influence of the subducting slab.

Although there is general agreement with many of the inferred geodynamic settings of the F-classification, it is clear that modern felsic volcanic rocks cross several different fields, and some fall completely outside the FI-IV classifications. Most Archean rhyolites show some degree of LREE enrichment due to the enriched mantle or greater crustal thickness (Lesher et al., 1986), whereas modern felsic volcanic suites have strongly depleted signatures. This, together with the numerous examples of alkali and peralkaline samples, accounts for many of the modern examples plotting outside the fields of Archean rhyolites (Hart et al., 2004; Piercey 2011; Hollis et al., 2015). Although some have suggested that the F-classification has outlived its usefulness with the

widespread availability of immobile trace element data, it has yet to be replaced with a rhyolite classification scheme involving more elements, as is the case for mafic volcanic rocks (e.g., Agrawal et al., 2008).

The geochemical differences between Archean and post-Archean submarine felsic volcanic rocks have been interpreted mainly in terms of crustal and mantle conditions (Hart et al., 2004). An important observation of this study is that modern FIIIb-like dacites and rhyolites are found in a number of different tectonic settings, including at the tips of propagating rifts and overlapping spreading centers on mid-ocean ridges, and at mature back-arc spreading centers such as the NWLSC in the Lau Basin and the Manus Spreading Center in the Manus Basin. In the modern oceans, this type of crust has a low preservation potential owing to eventual subduction. Thus, the limited occurrences of FIIIb-type felsic rocks in post-Archean assemblages might simply reflect limited preservation. Studies of ophiolites indicate that the likelihood of preservation of these different types of oceanic crust is strongly dependent on the age of the crust, its thickness, and the thermal state and geometry of the plate boundaries (Shervais, 2001; Dilek and Furnes, 2014). Although the characterization of Archean greenstone belts as obducted oceanic crust is debated (Furnes et al., 2015; Palin et al., 2020), the abundance of FIIIb-type felsic volcanic rocks in the Archean may indicate more complicated microplate architectures and increased probability of preservation in buoyant microplate domains (e.g., Wyman, 2013).

Conclusions

We compared the major and trace element geochemistry of modern submarine felsic volcanic rocks using PCA, hierarchical clustering and random forest to identify important similarities and differences between tectonic settings. Automated hierarchical clustering reveals significant geochemical diversity in felsic volcanic rocks from subduction-zone settings related to fluids from the subducting slab but also considerable variation related to local geodynamic influences. Mid-ocean ridge-like dacites found in the complex microplate mosaics of the northern Lau Basin and the Manus Basin are related to anomalous heat flow, rising asthenospheric mantle, and rift propagation especially at overlapping spreading centers. They have flat REE patterns, significant HREE enrichment, and strong negative Eu anomalies similar to Archean FIIIb rhyolites, such as felsic volcanic rocks from Matagami. Major differences in the abundance of Archean and post-

Archean felsic volcanic rocks of different types may be at least partly explained by their preservation potential. Modern mid-ocean ridges and mature back-arc spreading centers have low preservation potential, owing to the eventual subduction at basin margins. In contrast, the complex microplate mosaics of Archean greenstone belts might have been important settings for preservation of this type of crust, promoted by the thickness of the crust and high heat flow in the Archean. While they are not exact tectonic analogs, the geochemical evolution of felsic volcanic rocks in Archean greenstone belts may share many of the same influences observed in modern microplate breakouts, such as in the northern Lau Basin.

Felsic volcanic rocks from transitional arc-backarc systems, such as the eastern Manus Basin, are characterized by calc-alkaline to tholeiitic affinities with negative Nb-Ta anomalies, positive $La/Yb_{(CN)}$ ratios and variable HREE concentrations, similar to rhyolites of the Noranda Volcanic Complex. Felsic volcanic rocks at continental margin arcs, such as the Taupo Volcanic Zone and Okinawa Trough, are characterized by calc-alkaline affinities with negative Nb-Ta anomalies, positive $La/Yb_{(CN)}$ ratios and high Th concentrations, similar to the rhyolites of the Bousquet Formation. Dacites and rhyolites from high heat flow environments, mid-ocean ridges and distant spreading centers, characterized by tholeiitic affinity and flat REE patterns, are similar to rhyolites from Mattagami. Rhyolites from ridge-hotpot intersections, which have tholeiitic to weak alkaline affinity and flat REE patterns to slightly positive $La/Yb_{(CN)}$ ratios, are geochemically close relatives of rhyolites at Kidd Creek.

Acknowledgments

We thank Pierre-Simon Ross and Stephen Piercey for the helpful comments on the improvement of this manuscript and the comparisons with AGB felsic volcanic rocks. This research was funded through the Canada First Research Excellence Fund (CFREF, Metal Earth) and the Marine Mineral Resources Group at the GEOMAR Helmholtz Centre for Ocean Research Kiel. The Helmholtz Association, the Natural Sciences and Engineering Research Council of Canada (NSERC), and the German Ministry of Science and Education (BMBF, grant 03G0267) are acknowledged for the support of this work through research grants to the authors. The project is also supported by the NSERC Collaborative Research and Training Experience program (iMAGE-CREATE) on Marine Geodynamics and Georesources. This is contribution MERC-ME-2022-12.

References

Agrawal, S., Guevara, M., Verma, S.P., 2008, Tectonic discrimination of basic and ultrabasic volcanic rocks through log-transformed ratios of immobile trace elements: International Geology Review, v. 50, p. 1057-1079.

Aitchison, J., 1982, The statistical analysis of compositional data: Journal of the Royal Statistical Society: Series B (Methodological), v. 44, p. 139-160.

Ayer, J., Amelin, Y., Corfu, F., Kamo, S., Ketchum, J., Kwok, K., and Trowell, N., 2002, Evolution of the southern Abitibi greenstone belt based on U–Pb geochronology: autochthonous volcanic construction followed by plutonism, regional deformation and sedimentation: Precambrian Research, v. 115, p. 63-95.

Baier, J., Audétat, A., and Keppler, H., 2008, The origin of the negative niobium tantalum anomaly in subduction zone magmas: Earth and Planetary Science Letters, v. 267, p. 290-300.

Barker, S.J., Wilson, C.J.N., Baker, J.A., Millet, M.-A., Rotella, M.D., I. C. Wright, and Wysoczanski, R.J., 2013, Geochemistry and petrogenesis of silicic magmas in the intra-oceanic Kermadec arc: Journal of Petrology, v. 54, p. 351-391.

Barrie, C.T., and Hannington, M.D., 1999, Classification of volcanic-associated massive sulfide deposits based on host-rock composition: Reviews in Economic Geology, v. 8, p. 1-11.

Barrie, C.T., Ludden, J.N., and Green, T.H., 1993, Geochemistry of volcanic rocks associated with Cu-Zn and Ni-Cu deposits in the Abitibi subprovince: Economic Geology, v. 88, p. 1341-1358.

Bartholomew, D. J., 2010, Principal Components Analysis, in Peterson et al., ed., International Encyclopedia of Education, 3rd ed: Elsevier Science, p 374-377.

Baxter, A.T., Hannington, M.D., Stewart, M.S., Emberley, J.M., Breker, K., Krätschell, A., Petersen, S., Brandl, P.A., Klischies, M., Mensing, R., and Anderson, M.O., 2020, Shallow seismicity and the classification of structures in the Lau back-arc basin: Geochemistry, Geophysics, Geosystems, v. 21, e2020GC008924, p 25.

Bédard, J.H., Harris, L.B., and Thurston, P.C., 2013, The hunting of the snArc: Precambrian Research, v. 229, p. 20-48.

Beier, C., Bach, W., Turner, S., Niedermeier, D., Woodhead, J., Erzinger, J., and Krumm, S., 2015, Origin of silicic magmas at spreading centres-an example from the South East rift, Manus basin: Journal of Petrology, v. 56, p. 255-272.

Bézos, A., Escrig, S., Langmuir, C.H., Michael, P.J., and Asimow, P.D., 2009, Origins of chemical diversity of back-arc basin basalts: A segment-scale study of the Eastern Lau spreading center: Journal of Geophysical Research, v. 114, B06212, p. 33.

Breiman, L., 2001, Random Forests: Machine Learning, v. 45, p. 5-32.

Briqueu, L., Bougault, H., and Joron, J.L., 1984, Quantification of Nb, Ta, Ti and V anomalies in magmas associated with subduction zones: petrogenetic implications: Earth and Planetary Science Letters, v. 68, p. 297-308.

Brophy, J.G., 2008, A study of rare earth element (REE)–SiO_2 variations in felsic liquids generated by basalt fractionation and amphibolite melting: a potential test for discriminating between the two different processes: Contributions to Mineralogy and Petrology, v. 156, p. 337-357.

Brophy, J.G., 2009, La–SiO_2 and Yb–SiO_2 systematics in mid-ocean ridge magmas: implications for the origin of oceanic plagiogranite: Contributions to Mineralogy and Petrology, v. 158, p. 99-111.

Chamberlain, K.J., Barclay, J., Preece, K., Brown, R.J., Davidson, J.P., and EIMF, 2016, Origin and evolution of silicic magmas at ocean islands: Perspectives from a zoned fall deposit on Ascension Island, South Atlantic: Journal of Volcanology and Geothermal Research, v. 327, p. 349-360.

Chauvel, C., Maury, R.C., Blais, S., Lewin, E., Guillou, H., Guille, G., Rossi, P., and Gutscher, M.-A., 2012, The size of plume heterogeneities constrained by Marquesas isotopic stripes: Geochemistry, Geophysics, Geosystems, v. 13, Q07005, p. 1-23.

Chawla, N. V., Bowyer, K. W., Hall, L. O., and Kegelmeyer, W. P., 2002, SMOTE: Synthetic minority over-sampling technique: Journal of Artificial Intelligence Research, v. 16, p. 321-357.

Chown, E.H., Daigneault, R., Mueller, W., and Mortensen, J.K., 1992, Tectonic evolution of the Northern Volcanic Zone, Abitibi belt, Quebec: Canadian Journal of Earth Sciences, v. 29, p. 2211-2225.

Danyushevsky, L.V., 2001, The effect of small amounts of H_2O on crystallisation of mid-ocean ridge and backarc basin magmas: Journal of Volcanology and Geothermal Research, v. 110, p. 265-280.

Deering, C.D., Bachmann, O., Dufek, J., and Gravley, D.M., 2011, Rift-related transition from andesite to rhyolite volcanism in the Taupo Volcanic Zone (New Zealand) controlled by crystal–melt dynamics in mush zones with variable mineral assemblages: Journal of Petrology, v. 52, p. 2243-2263.

Deering, C.D., Cole, J.W., and Vogel, T.A., 2008, A rhyolite compositional continuum governed by lower crustal source conditions in the Taupo Volcanic Zone, New Zealand: Journal of Petrology, v. 49, p. 2245-2276.

Dilek, Y., and Furnes, H., 2014, Ophiolites and their origins: Elements, v. 10, p. 93-100.

Dilek, Y., 2003, Ophiolite pulses, mantle plumes and orogeny: Geological Society, London, Special Publications, v. 218, p. 9-19.

Embley, R.W., and Rubin, K.H., 2018, Extensive young silicic volcanism produces large deep submarine lava flows in the NE Lau basin: Bulletin of Volcanology, v. 80, p. 1-23.

Escrig, S., Bézos, A., Langmuir, C.H., Michael, P.J., and Arculus, R., 2012, Characterizing the effect of mantle source, subduction input and melting in the Fonualei spreading center, Lau basin: Constraints on the origin of the boninitic signature of the back-arc lavas: Geochemistry, Geophysics, Geosystems, v. 13, Q10008, p. 29.

Falloon, T.J., and Danyushevsky, L.V., 2000, Melting of refractory mantle at 1.5, 2 and 2.5 GPa under anhydrous and H_2O-undersaturated conditions: Implications for the petrogenesis of high-Ca boninites and the influence of subduction components on mantle melting: Journal of Petrology, v. 41, p. 257-283.

Fernandez-Delgado, M., Cernadas, E., Barro, S., and Amorim, D., 2014, Do we need hundreds of classifiers to solve real world classification problems?: Journal of Machine Learning Research, v. 15, p. 3133-3181.

Flude, S., McGarvie, D.W., Burgess, R., and Tindle, A.G., 2010, Rhyolites at Kerlingarfjöll, Iceland: The evolution and lifespan of silicic central volcanoes: Bulletin of Volcanology, v. 72, p. 523-538.

Franklin, J.M., Gibson, H.L., Jonasson, I.R., and Galley, A.G., 2005, Volcanogenic massive sulfide deposits: Economic Geology, v. 100, p. 523-560.

Fretzdorff, S., Schwarz-Schampera, U., Gibson, H.L., Garbe-Schönberg, C.-D., Hauff, F., and Stoffers, P., 2006, Hydrothermal activity and magma genesis along a propagating back-arc basin: Valu Fa ridge (southern Lau basin): Journal of Geophysical Research, v. 111, B08205, p. 19.

Fretzdorff, S., Worthington, T.J., Haase, K.M., Hekinian, R., Franz, L., Keller, R.A., and Stoffers, P., 2004, Magmatism in the Bransfield basin: Rifting of the south Shetland arc?: Journal of Geophysical Research, v. 109, B12208, p. 17.

Freund, S., Beier, C., Krumm, S., and Haase, K.M., 2013, Oxygen isotope evidence for the formation of andesitic–dacitic magmas from the fast-spreading Pacific–Antarctic rise by assimilation–fractional crystallisation: Chemical Geology, v. 347, p. 271-283.

Furnes, H., Dilek, Y., and de Wit, M., 2015, Precambrian greenstone sequences represent different ophiolite types: Gondwana Research, v. 27, p. 649-685.

Gaboury, D., 2006, Geochemical approaches in the discrimination of synvolcanic intrusions as a guide for volcanogenic base metal exploration: an example from the Abitibi belt, Canada: Applied Earth Science, v. 115, p. 71-79.

Gaboury, D., and Pearson, V., 2008, Rhyolite geochemical signatures and association with volcanogenic massive sulfide deposits: Examples from the Abitibi belt, Canada: Economic Geology, v. 103, p. 1531–1562.

Grove, T.L., Elkins-Tanton, L.T., Parman, S.W., Chatterjee, N., Müntener, O., and Gaetani, G.A., 2003, Fractional crystallization and mantle-melting controls on calc-alkaline differentiation trends: Contributions to Mineralogy and Petrology, v. 145, p. 515-533.

Haase, K.M., Stroncik, N., Hekinian, R., and Stoffers, P., 2005, Nb-depleted andesites from the Pacific-Antarctic rise as analogs for early continental crust: Geological Society of America, v. 33, p. 921-924.

Haase, K.M., Fretzdorff, S., Mühe, R., Garbe-Schönberg, D., and Stoffers, P., 2009, A geochemical study of off-axis seamount lavas at the Valu Fa ridge: Constraints on magma genesis and slab contributions in the southern Tonga subduction zone: Lithos, v. 112, p. 137-148.

Haase, K.M., Stroncik, N., Garbe-Schönberg, D., and Stoffers, P., 2006, Formation of island arc dacite magmas by extreme crystal fractionation: An example from Brothers seamount, Kermadec island arc (SW Pacific): Journal of Volcanology and Geothermal Research, v. 152, p. 316-330.

Hamada, M., Okayama, Y., Kaneko, T., Yasuda, A., and Toshitsugu, F., 2014, Polybaric crystallization differentiation of H_2O-saturated island arc low-K tholeiite magmas: a case study of the Izu-Oshima volcano in the Izu arc: Earth Planet and Space, v. 66, 15, p. 10.

Hannington, M. D., Barrie, C. T. and Bleeker, W., 1999, The giant Kidd Creek volcanogenic massive sulfide deposit, western Abitibi subprovince, Canada: Preface and Introduction. In: The giant Kidd Creek volcanogenic massive sulfide deposit, western Abitibi subprovince, Canada. Economic Geology Monograph (10). The Economic Geology Publishing Company, Littleton, CO, pp. 1-30.

Hannington, M.D., De Ronde, C.E.J., and Petersen, S., 2005, Sea-floor tectonics and submarine hydrothermal systems: Economic Geology, v. 100, p. 111-141.

Haraguchi, S., Kimura, J.-I., Senda, R., Fujinaga, K., Nakamura, K., Takaya, Y., and Ishii, T., 2017, Origin of felsic volcanism in the Izu arc intra-arc rift: Contributions to Mineralogy and Petrology, v. 172, p. 1-21.

Harnois, L., and Stevenson, R.K., 2006, Major and trace elements geochemistry of basalts and trachyphonolites from Huahine island, Society Archipelago (French Polynesia): Bulletin de la Société Géologique de France, v. 177, p. 179-190.

Hart, T.R., Gibson, H.L., and Lesher, C.M., 2004, Trace element geochemistry and petrogenesis of felsic volcanic rocks associated with volcanogenic massive Cu-Zn-Pb sulfide deposits: Economic Geology, v. 99, p. 1003-1013.

Hofmann, A.W., 2014, Sampling mantle heterogeneity through oceanic basalts: Isotopes and trace elements, in Holland, H. D. and Turekian, K. K., ed., Treatise on Geochemistry, 2nd ed.: Elsevier, p. 67-101.

Hollis, S.P., Yeats, C.J.; Wyche, S., Barnes, S. J., Ivanic, T. J., Belford, S. M., Davidson, G. J., Roache, A. J., and Wingate, M. T. D., 2015, A review of volcanic-hosted massive sulfide (VHMS) mineralization in the Archaean Yilgarn craton, Western Australia: Tectonic, stratigraphic and geochemical associations: Precambrian Research, v. 260, p. 113-135.

Hunter, A.G., 1998, Intracrustal controls on the coexistence of tholeiitic and calc-alkaline magma series at Aso volcano, SW Japan: Journal of Petrology, v. 39, p. 1255-1284.

Husson, F., Josse, J., Le, S., Mazet, J., 2009, FactoMinerR: Multivariate Exploratory Data Analysis and Data Mining with R. (http://factominer.free.fr).

Huston, D.L., Pehrsson, S., Eglington, B.M., and Zaw, K., 2010, The geology and metallogeny of volcanic-hosted massive sulfide deposits: Variations through geologic time and with tectonic setting: Economic Geology, v. 105, p. 571-591.

Huston, D.L., Champion, D.C., and Doublier, M.P., 2019, Isotopic and geochemical indicators on volcanic-hosted massive sulfide prospectivity: a review [ext. abs.]: SGA Biennial Meeting, 15th, Glasgow, Scotland, Extended Abstracts, p. 1156-1159.

Jackson, S.L., Fyon, A., and Corfu, F., 1994, Review of Archean supracrustal assemblages of the southern Abitibi greenstone belt in Ontario, Canada: Products of microplate interaction within a large-scale plate-tectonic setting: Precambrian Research, v. 65, p. 183-205.

Jeffery, A.J., Gertisser, R., O'Driscoll, B., Pacheco, J.M., Whitley, S., Pimentel, A., and Self, S., 2016, Temporal evolution of a post-caldera, mildly peralkaline magmatic system: Furnas volcano, São Miguel, Azores: Contributions to Mineralogy and Petrology, v. 171, 42, p. 24.

Jenner, F.E., Arculus, R.J., Mavrogenes, J.A., Dyriw, N.J., Nebel, O., and Hauri, E.H., 2012, Chalcophile element systematics in volcanic glasses from the northwestern Lau Basin: Geochemistry, Geophysics, Geosystems, v. 13, Q06014, p. 24.

Jenner, F.E., St. O'Neill, H.C., Arculus, R.J., and Mavrogenes, J.A., 2010, The magnetite crisis in the evolution of arc-related magmas and the initial concentration of Au, Ag and Cu: Journal of Petrology, v. 51, p. 2445-2464.

Jicha, B.R., Singer, B.S., and Valentine, M.J., 2013, $^{40}Ar/^{39}Ar$ geochronology of subaerial Ascension Island and a re-evaluation of the temporal progression of basaltic to rhyolitic volcanism: Journal of Petrology, v. 54, p. 2581-2596.

Jónasson, K., 2007, Silicic volcanism in Iceland: Composition and distribution within the active volcanic zones: Journal of Geodynamics, v. 43, p. 101-117.

Karson, J.A., 2017, The Iceland plate boundary zone: propagating rifts, migrating transforms, and rift-parallel strike-slip faults: Geochemistry, Geophysics, Geosystems, v. 18, p. 4043-4054.

Kelemen, P.B., Hanghøj, K., and Greene, A.R., 2014, One view of the geochemistry of subduction-related magmatic arcs, with an emphasis on primitive andesite and lower crust, in Holland, H. D. and Turekian, K. K., ed., Treatise on Geochemistry, 2nd ed.: Elsevier, p. 749-806.

Keller, R.A., Fisk, M.R., Smellie, J.L., Strelin, J.A., and Lawver, L.A., 2002, Geochemistry of back arc basin volcanism in Bransfield Strait, Antarctica: Subducted contributions and along-axis variations: Journal of Geophysical Reasearch, v. 107, B8, p. 17.

Konter, J.G., and Jackson, M.G., 2012, Large volumes of rejuvenated volcanism in Samoa: Evidence supporting a tectonic influence on late-stage volcanism: Geochemistry, Geophysics, Geosystems, v. 13, Q0AM04, p. 23.

Lafrance, B., Mueller, W.U., Daigneault, R., and Dupras, N., 2000, Evolution of a submerged composite arc volcano: Volcanology and geochemistry of the Normetal volcanic complex, Abitibi greenstone belt, Quebec, Canada: Precambrian Research, v. 101, p. 277-311.

Lagabrielle, Y., Goslin, J., Martin, H., Thirot, J.-L., and Auzende, J.-M., 1997, Multiple active spreading centres in the hot north Fiji basin (Southwest Pacific): A possible model for Archean seafloor dynamics?: Earth and Planetary Science Letters, v. 149, p. 1-13.

Langmuir, C.H., Bézos, A., Escrig, S., and Parman, S.W., 2006, Chemical systematics and hydrous melting of the mantle in back-arc basins, in Christie, D.M., Fisher, C.R., Lee, S.-M., and Givens, S., ed., Back-arc Spreading Systems: Geological, Biological, Chemical, and Physical Interactions: Washington, D. C., American Geophysical Union, Geophyiscal Monograph 166, p. 87-146.

Le Maitre, R.W., 1989, A classification of igneous rocks and glossary of terms: Recommendations of the International Union of Geological Sciences, Subcommission on the Systematics of Igneous Rocks: Oxford, Blackwell Scientific Publications, 193 p.

Leat, P.T., Larter, R.D., and Millar, I.L., 2007, Silicic magmas of Protector Shoal, South Sandwich arc: indicators of generation of primitive continental crust in an island arc: Geological Magazine, v. 144, p. 179-190.

Lentz, D.R., 1998, Petrogenetic evolution of felsic volcanic sequences associated with Phanerozoic volcanic-hosted massive sulphide systems: the role of extensional geodynamics: Ore Geology Reviews, v. 12, p. 289-327.

Lesher, C.M., Goodwin, A.M., Campbell, I.H., and Gorton, M.P., 1986, Trace-element geochemistry of ore-associated and barren, felsic metavolcanic rocks in the Superior Province, Canada: Canadian Journal of Earth Sciences, v. 23, p. 222-237.

Lytle, M.L., Kelley, K.A., Hauri, E.H., Gill, J.B., Papia, D., and Arculus, R.J., 2012, Tracing mantle sources and Samoan influence in the northwestern Lau back-arc basin: Geochemistry, Geophysics, Geosystems, v. 13, Q10019, p. 23.

Mancini, A., Mattson, H. B., and Bachmann, O., 2015, Origin of the compositional diversity in the basalt-to-dacite series erupted along the Heidarspordur ridge, NE Iceland: Journal of Volcanology and Geothermal Research, v. 301, p. 116-127.

McKenzie, D., and Bickle, M.J., 1988, The volume and composition of melt generated by extension of the lithosphere: Journal of Petrology, v. 29, p. 625-679.

Mercier-Langevin, P., Dubé, B., Hannington, M.D., Davis, D.W., Lafrance, B., and Gosselin, G., 2007, The LaRonde Penna Au-rich volcanogenic massive sulfide deposit, Abitibi greenstone belt, Quebec: Part I. Geology and Geochronology: Economic Geology, v. 102, p. 585-609.

Monecke, T., Gibson, H.L., and Goutier, J., 2017, Volcanogenic massive sulfide deposits of the Noranda camp: Reviews in Economic Geology, v. 19, p. 169-223.

Monecke, T., Mercier-Langevin, P., Dubé, B., Frieman, B.M., 2017, Geology of the Abitibi Greenstone Belt, Canada Reviews in Economic Geology, v. 19, p. 7-49.

Mueller, W.U., Daigneault, R., Mortensen, J.K., and Chown, E.H., 1996. Archean terrane docking: upper crust collision tectonics, Abitibi greenstone belt, Quebec, Canada: Tectonophysics, v. 265, p. 127-150.

Palin, R.M., Santosh, M., Cao, W., Li, S.-S., Hernández-Uribe, D., and Parsons, A., 2020, Secular change and the onset of plate tectonics on Earth: Earth-Science Reviews, v. 207, 103172, p. 41.

Park, J.-W., Campbell, I.H., Kim, j., and Moon, J.-W., 2015, The role of late sulfide saturation in the formation of a Cu- and Au-rich magma: Insights from the platinum group element geochemistry of Niuatahi-Motutahi lavas, Tonga rear arc: Journal of Petrology, v. 56, p. 59-81.

Parson, L.M., and Wright, I.C., 1996, The Lau-Havre-Taupo back-arc basin: A southward-propagating, multi-stage evolution from rifting to spreading: Tectonophysics, v. 263, p. 1-22.

Pearce, J.A., 1996, A user`s guide to basalt discrimination diagrams, in Wyman, D.A., ed., Trace element geochemistry of volcanic rocks: Applications for massive sulphide exploration: Geological Association of Canada, Short Course Notes, v. 12, p. 79-113.

Pearce, J.A., Stern, R.J., Bloomer, S.H., and Fryer, P., 2005, Geochemical mapping of the Mariana arc-basin system: Implications for the nature and distribution of subduction components: Geochemistry, Geophysics, Geosystems, v. 6, Q07006, p. 27.

Percival, J. A., Skulski, T., Sanborn-Barrie, M., Stott, G. M., Leclair, A. D., Corkery, M. T., and Boily, M., 2012, Geology and tectonic evolution of the Superior Province, Canada, Tectonic styles in Canada: The Lithoprobe Perspective, Geological Association of Canada, Special Paper, 49, p. 321-378.

Perfit, M.R., and Fornari, D.J., 1983, Geochemical studies of abyssal lavas recovered by DSRV Alvin from Eastern Galapagos rift, Inca transform, and Ecuador rift 2. Phase Chemistry and Crystallization History: Journal of Geophysical Research, v. 88, p. 530-550.

Petersen, S., Herzig, P.M., Schwarz-Schampera, U., Hannington, M.D., and Jonasson, I.R., 2004, Hydrothermal precipitates associated with bimodal volcanism in the Central Bransfield Strait, Antarctica: Mineralium Deposita, v. 39, p. 358-379.

Piercey, S.J., 2011, The setting, style, and role of magmatism in the formation of volcanogenic massive sulfide deposits: Mineralium Deposita, v. 46, p. 449-471.

Piercey, S.J., Paradis, S., Murphy, D.C., Mortensen, J.K., 2001, Geochemistry and Paleotectonic Setting of Felsic Volcanic Rocks in the Finlayson Lake Volcanic-Hosted Massive Sulfide District, Yukon, Canada: Economic Geology, v. 96, p. 1877-1905.

Portnyagin, M., Hoernle, K., Storm, S., Mironov, N., van den Bogaard, C., and Botcharnikov, R., 2012, H_2O-rich melt inclusions in fayalitic olivine from Hekla volcano: Implications for phase relationships in silicic systems and driving forces of explosive volcanism on Iceland: Earth and Planetary Science Letters, 357-358, p. 337-346.

Prior, G.J., Gibson, H.L., Watkinson, D.H., Cook, R.E., and Hannington, M.D., 1999, Rare earth and high field strength element geochemistry of the Kidd Creek rhyolites, Abitibi greenstone belt, Canada: Evidence for Archean felsic volcanism and massive sulfide ore formation in an Iceland-style rift environment: Economic Geology, Monograph 10, p. 457-484.

R Core Team 2020, R: A language and environment for statistical computing: R Foundation for Statistical Computing, Vienna, Austria. (https://www.R-project.org).

Regelous, M., Niu, Y., Wendt, J.I., Batiza, R., Greig, A., and Collerson, K.D., 1999, Variations in the geochemistry of magmatism on the East Pacific rise at 10°30 N since 800 ka: Earth and Planetary Science Letters, v. 168, p. 45-63.

Rowland, J.V., Wilson, C.J., and Gravley, D.M., 2010, Spatial and temporal variations in magma-assisted rifting, Taupo Volcanic Zone, New Zealand: Journal of Volcanology and Geothermal Research, v. 190, p. 89-108.

Ross, P.S., Bédard, J.H., 2009, Magmatic affinity of modern and ancient subalkaline volcanic rocks determined from trace-element discriminant diagrams: Canadian Journal of Earth Sciences, v. 46, p. 823-839.

Ryan, W.B.F., Carbotte, S.M., Coplan, J. O., O'Hara, S., Melkonian, A., Arko, R., Weissel, R.A., Ferrini, V., Goodwillie, A., Nitsche, F., Bonczkowski, J., and Zemsky, R., 2009, Global multi-resolution topography synthesis. Geochemistry Geophysics Geosystems 10, Q03014, p. 9.

Rychert, A.C., Harmon, N., Constable, S., and Wang, S., 2020, The nature of the lithosphere-asthenosphere boundary, Journal of Geophysical Research: Solid Earth, v. 125, e2018JB016463, p. 39.

Schmidt, M.W., and Poli, S., 2014, Devolatilization during subduction, in Holland, H.D. and Turekian, K.K., ed., Treatise on Geochemistry, 2nd ed.: Elsevier, p. 669-701.

Shervais, J.W., 2001, Birth, death, and resurrection: The life cycle of suprasubduction zone ophiolites: Geochemistry Geophysics Geosystems, v. 2, 1010, p. 45.

Shinjo, R., and Kato, Y., 2000, Geochemical constraints on the origin of bimodal magmatism at the Okinawa Trough, an incipient back-arc basin: Lithos, v. 54, p. 117-137.

Shukuno, H., Tamura, Y., Tani, K., Chang, Q., Suzuki, T., and Fiske, R.S., 2006, Origin of silicic magmas and the compositional gap at Sumisu submarine caldera, Izu–Bonin arc, Japan: Journal of Volcanology and Geothermal Research, v. 156, p. 187-216.

Sigmarsson, O., and Steinthórsson, S., 2007, Origin of Icelandic basalts: A review of their petrology and geochemistry: Journal of Geodynamics, v. 43, p. 87-100.

Sinton, J.M., Ford, L.L., Chappell, B., and McCulloch, M.T., 2003, Magma genesis and mantle heterogeneity in the Manus back-arc basin, Papua New Guinea: Journal of Petrology, v. 44, p. 159-195.

Sleeper, J. D., and Martinez, F., 2016, Geology and kinematics of the Niuafo'ou microplate in the northern Lau basin: Journal of Geophysical Research: Solid Earth, v. 121, p. 4852-4875.

Sparks, D.W., Parmentier, E.M., and Morgan, J.P., 1993, Three-dimensional mantle convection beneath a segmented spreading center: Implications for along-axis variations in crustal thickness and gravity: Journal of Geophysical Research, v. 98, p. 977-995.

Stanley, C.R., Madeisky, H.E., 1996, Lithogeochemical exploration for metasomatic zones associated with hydrothermal mineral deposits using molar element ratio analysis: Lithogeochemical exploration for ore deposits using Pearce Element Ratio Analysis, v. 11. Geological Association of Canada, p. 193-212.

Stewart, M.S., Hannington, M.D., Emberley, J., Baxter, A.T., Krätschel, A., Petersen, S., Brandl, P.A., Anderson, M.O., Mercier-Langevin, P., Mensing, R., Breker, K., and Fassbender, M.L., 2022, A new geological map of the Lau basin reveals crustal growth processes in arc-backarc systems: Geosphere, v. 18, p. 910-943.

Sun, S., and McDonough, W.F., 1989, Chemical and isotopic systematics of oceanic basalts: implications for mantle composition and processes: in Saunders, A.D., ed., Magmatism in ocean basins, Geological Society, London, Special Publications, v. 42, p. 313-345.

Tamura, Y., Tani, K., Chang, Q., Shukuno, H., Kawabata, H., Ishizuka, O., and Fiske, R.S., 2007, Wet and dry basalt magma evolution at Torishima volcano, Izu–Bonin arc, Japan: The possible role of phengite in the downgoing slab: Journal of Petrology, v. 48, p. 1999-2031.

Tamura, Y., Tani, K., Ishizuka, O., Chang, Q., Shukuno, H., and Fiske, R.S., 2005, Are arc basalts dry, wet, or both? Evidence from the Sumisu caldera volcano, Izu–Bonin arc, Japan: Journal of Petrology, v. 46, p. 1769-1803.

Tamura, Y., Gill, J.B., Tollstrup, D., Kawabata, H., Shukuno, H., Chang, Q., Miyazaki, T., Takahashi, T., Hirahara, Y., Kodaira, S., Ishizuka, O., Suzuki, T., Kido, Y., Fiske, R.S., and Tatsumi, Y., 2009, Silicic magmas in the Izu–Bonin oceanic arc and implications for crustal evolution: Journal of Petrology, v. 50, p. 685-723.

Tani, K., Fiske, R.S., Tamura, Y., Kido, Y., Naka, J., Shukuno, H., and Takeuchi, R., 2008, Sumisu volcano, Izu-Bonin arc, Japan: site of a silicic caldera-forming eruption from a small open-ocean island: Bulletin of Volcanology, v. 70, p. 547-562.

Tatsumi, Y., and Suzuki, T., 2009, Tholeiitic vs calc-alkalic differentiation and evolution of arc crust: Constraints from melting experiments on a basalt from the Izu-Bonin-Mariana arc: Journal of Petrology, v. 50, p. 1575-1603.

Taylor, B., and Martinez, F., 2003, Back-arc basin basalt systematics: Earth and Planetary Science Letters, v. 210, p. 481-497.

Thordarson, T., and Larsen, G., 2007, Volcanism in Iceland in historical time: Volcano types, eruption styles and eruptive history: Journal of Geodynamics, v. 43, p. 118-152.

Thurston, P.C., 2015, Greenstone belts and granite−greenstone terranes: Constraints on the nature of the Archean world: Geoscience Canada, v. 42, p. 437-484.

Turner, S., Caulfield, J., Rushmer, T., Turner, M., Cronin, S., Smith, I., and Handley, H., 2012, Magma evolution in the primitive, intra-oceanic Tonga arc: Rapid petrogenesis of dacites at Fonualei volcano: Journal of Petrology, v. 53, p. 1231-1253.

van der Zander, I., Sinton, J.M., and Mahoney, J.J., 2010, Late shield-stage silicic magmatism at Wai'anae volcano: Evidence for hydrous crustal melting in Hawaiian volcanoes: Journal of Petrology, v. 51, p. 671-701.

Wade, J.A., Plank, T., Stern, R.J., Tollstrup, D.L., Gill, J.B., O'Leary, J.C., Eiler, J.M., Moore, R.B., Woodhead, J.D., Trusdell, F., Fischer, T.P., and Hilton, D.R., 2003, The may 2003 eruption of Anatahan volcano, Mariana Islands: Geochemical evolution of a silicic island-arc volcano: Journal of Volcanology and Geothermal Research, v. 146, p. 139-170.

Wanless, V.D., Perfit, M.R., Ridley, W.I., and Klein, E., 2010, Dacite petrogenesis on mid-ocean ridges: Evidence for oceanic crustal melting and assimilation: Journal of Petrology, v. 51, p. 2377-2410.

Willbold, M., Hegner, E., Stracke, A., Rocholl, A., 2009, Continental geochemical signatures in dacites from Iceland and implications for models of early Archean crust formation: Earth and Planetary Science Letters, v. 279, p. 44-52.

Winchester, J.A., and Floyd, P.A., 1977, Geochemical discrimination of different magma series and their differentiation products using immobile elements: Chemical Geology, v. 20, p. 325-343.

Wyman, D.A., 2013, A critical assessment of Neoarchean “plume only” geodynamics: Evidence from the Superior Province: Precambrian Research, v. 229, p. 3-19.

Yang, K., and Scott, S.D., 2003, Geochemical relationships of felsic magmas to ore metals in massive sulfide deposits of the Bathurst mining camp, Iberian pyrite belt, Hokuroku district, and the Abitibi belt: Economic Geology, p. 457-478.

Yeats, C.J., Hollis, S.P., Halfpenny, A., Corona, J.-C., LaFlamme, C., Southam, G., Fiorentini, M., Herrington, R.J., and Spratt, J., 2017, Actively forming Kuroko-type volcanic-hosted massive sulfide (VHMS) mineralization at Iheya North, Okinawa Trough, Japan: Ore Geology Reviews, v. 84, p. 20-41.

Zellmer, G., Rubin, K., Gronvold, K., and Jurado-Chichay, Z., 2008, On the recent bimodal magmatic processes and their rates in the Torfajökull–Veidivötn area, Iceland: Earth and Planetary Science Letters, v. 269, p. 388-398.

Zellmer, G.F., Hawkesworth, C.J., Sparks, R.S.J., Thomas, L.E., Harford, C.L., Brewer, T.S., and Loughlin, S.C., 2003, Geochemical evolution of the Soufriere Hills volcano, Monsterrat, Lesser Antilles Volcanic arc: Journal of Petrology, v. 44, p. 1249-1374.

Zhang, H., Yan, Q., Li, C., Zhu, Z., Zhao, R., and Shi, X., 2018, Geochemistry of diverse lava types from the Lau sasin (South West Pacific): Implications for complex back-arc mantle dynamics: Geological Journal, v. 56, p. 3643-3659.

Zierenberg, R.A., Schiffman, P., Barfod, G.H., Lesher, C.E., Marks, N.E., Lowenstern, J.B., Mortensen, A.K., Pope, E.C., Bird, D.K., Reed, M.H., Friðleifsson, G.Ó., and Elders, W.A., 2013, Composition and origin of rhyolite melt intersected by drilling in the Krafla geothermal field, Iceland: Contributions to Mineralogy and Petrology, v. 165, p. 327-347.

Figures

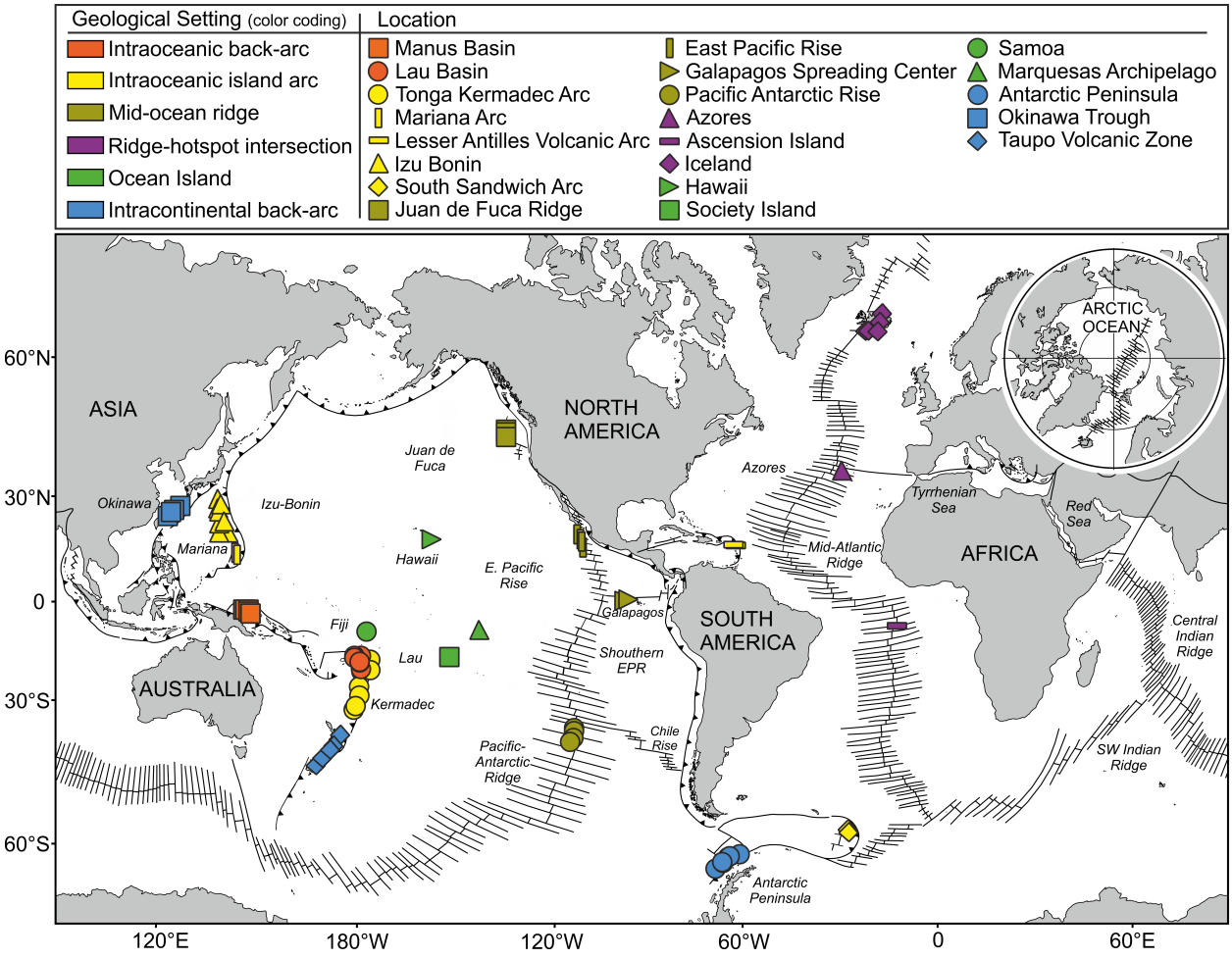


Figure 2.1: Global map of oceanic felsic volcanic rocks compiled for this study. Samples are included from intraoceanic back-arc basins (orange: Manus Basin, Lau Basin), intraoceanic island arcs (yellow: Tonga-Kermadec Arc, Mariana Arc, Lesser Antilles Volcanic Arc, Izu-Bonin Arc, South Sandwich Arc), mid-ocean ridges (olive: Juan de Fuca Ridge, East Pacific Rise, Galapagos Spreading Center, Pacific-Antarctic Rise), ridge-hotspot intersections (purple: Azores, Ascension Island, Iceland), ocean islands (green: Hawaii, Society Islands, Samoa, Marquesas Archipelago) and intracontinental arc-backarc basins (blue: Antarctic Peninsula, Okinawa Trough, Taupo Volcanic Zone). Details of the sample sources are provided in **Appendix A Table A1**.

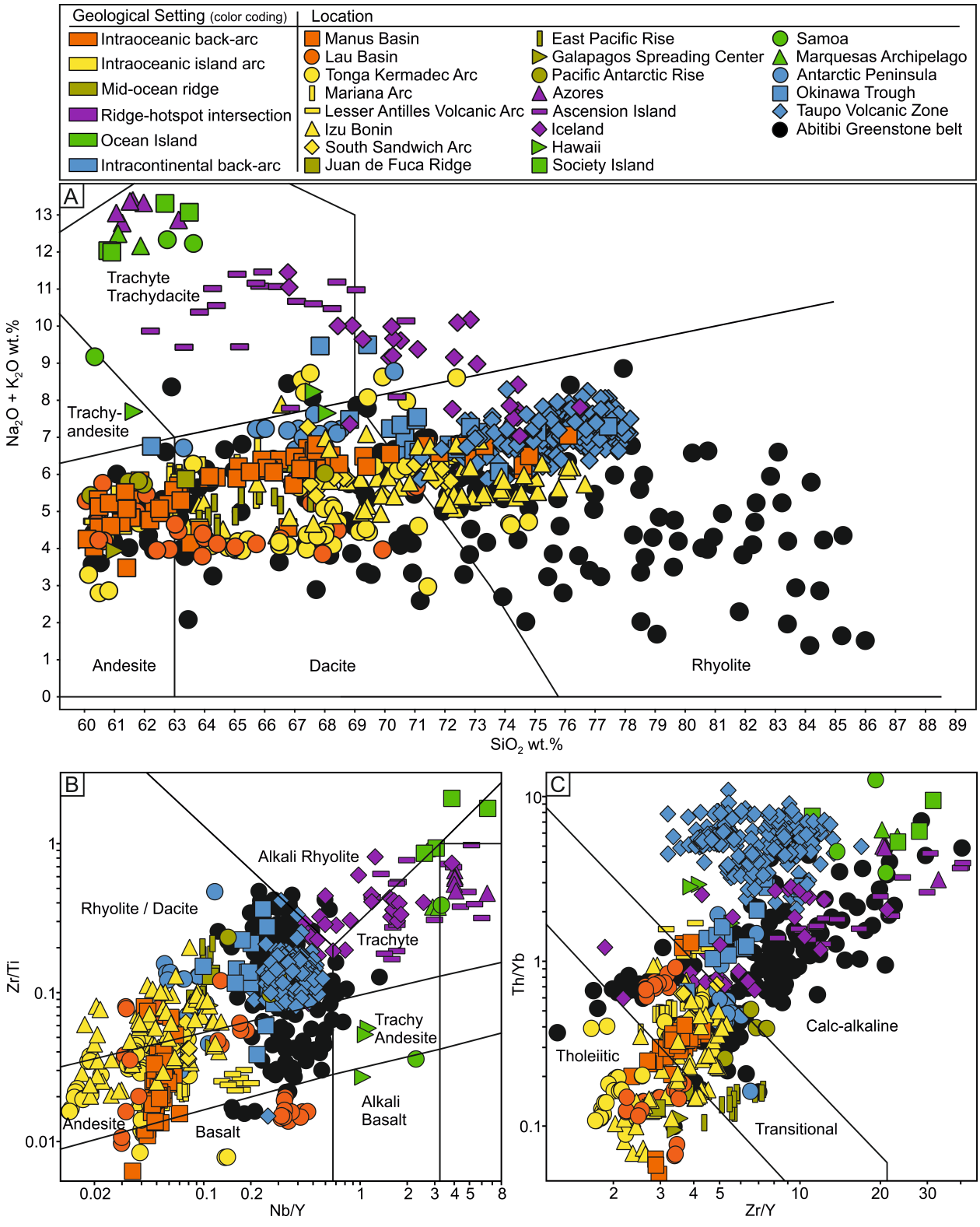
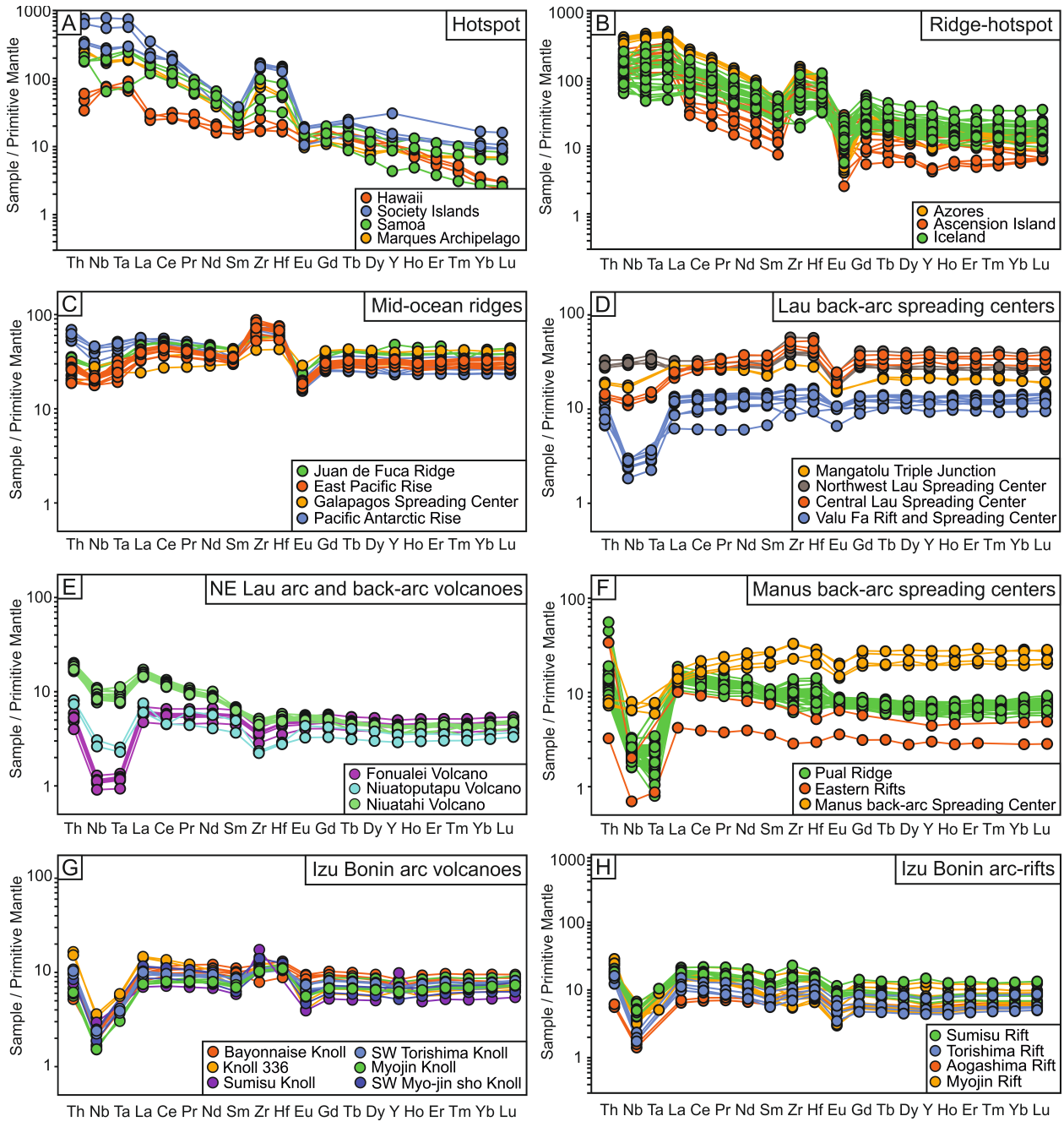

Geological Setting (color coding)
Intraoceanic back-arc
Intraoceanic island arc
Mid-ocean ridge
Ridge-hotspot intersection
Ocean Island
Intracontinental back-arc
Location
Manus Basin
Lau Basin
Tonga Kermadec Arc
Mariana Arc
Lesser Antilles Volcanic Arc
Izu Bonin
South Sandwich Arc
Juan de Fuca Ridge
East Pacific Rise
Galapagos Spreading Center
Pacific Antarctic Rise
Azores
Ascension Island
Iceland
Hawaii
Society Island
Samoa
Marquesas Archipelago
Antarctic Peninsula
Okinawa Trough
Taupo Volcanic Zone
Abitibi Greenstone belt
A
Trachyte
Trachydacite
Trachy-
andesite
Andesite
Dacite
Rhyolite
Na2O + K2O wt.%
SiO2 wt.%
B
Alkali Rhyolite
Rhyolite / Dacite
Trachyte
Trachy
Andesite
Alkali
Basalt
Andesite
Basalt
Zr/Ti
Nb/Y
C
Calc-alkaline
Tholeiitic
Transitional
Th/Yb
Zr/Y

Figure 2.2: A) Total alkali-silica plot (after Le Maitre, 1989) showing the distribution of modern oceanic felsic volcanic rocks and Archean felsic volcanic rocks from the Abitibi Greenstone Belt. Samples from ridge-hotspot intersections and ocean islands include mainly alkaline volcanic rocks. Mid-ocean ridge felsic volcanic rocks are tholeiitic with low SiO_2 concentrations. Samples from intraoceanic back-arc assemblages plot in a strong linear array from low SiO_2 to high SiO_2 with increasing $Na_2O + K_2O$ concentrations. Samples from intraoceanic island arc assemblages plot in a wide SiO_2 array with a narrower range of $Na_2O + K_2O$ concentrations. Samples from intracontinental arc-backarc assemblages have the highest SiO_2 concentrations with a similarly narrow range of $Na_2O + K_2O$ concentrations, although samples from the Okinawa Trough include both high and low $Na_2O + K_2O$ concentrations. The complete data are provided in **Appendix A Table A1** and **Appendix A Table A11**. The range of compositions of felsic volcanic rocks in the Abitibi Greenstone Belt is shown for comparison (see text for discussion). B) Volcanic rock discrimination plot of Pearce (1996) showing the distribution of modern oceanic felsic volcanic rocks and Archean felsic volcanic rocks from the Abitibi Greenstone Belt. Mid-ocean ridge felsic volcanic rocks from the East Pacific Rise, Pacific-Antarctic Rise and Juan de Fuca Ridge have low Nb/Y and high Zr/Ti and plot in the rhyolite/dacite field. Samples from different back-arc assemblages, such as the Lau Basin and Manus Basin plot mostly in the andesite field with a range of Zr/Ti and Nb/Y ratios extending into the rhyolite/dacite field. Samples from island-arc assemblages, such as Izu-Bonin, plot mostly in the rhyolite/dacite field. Felsic volcanic rocks from intracontinental arc-backarc assemblages, such as the Okinawa Trough and Western Antarctic Peninsula, have a very wide range of Zr/Ti and Nb/Y also spanning the rhyolite, dacite and andesite fields. Samples from the TVZ have a much narrower range of Zr/Ti and Nb/Y, entirely in the rhyolite field. The complete data are provided in **Appendix A Table A1** and **Appendix A Table A11**. C) Magmatic affinity plot of Ross and Bédard (2009) showing the distribution of modern oceanic felsic volcanic rocks and Archean felsic volcanic rocks from the Abitibi Greenstone Belt. Mid-ocean ridge felsic volcanic rocks from the East Pacific Rise, Pacific-Antarctic Rise and Juan de Fuca Ridge have low Zr/Y and low Th/Yb and plot in the tholeiitic and transitional fields. Samples from different back-arc assemblages, such as the Lau Basin and Manus Basin, and island-arc assemblages, such as Izu-Bonin, plot mostly in the transitional field with a range of Zr/Y and Th/Yb ratios extending to tholeiite. Felsic volcanic rocks from intracontinental arc-backarc assemblages, such as the Okinawa Trough and Western Antarctic Peninsula, have a very wide

range of Zr/Y and Th/Yb spanning the transitional and calc-alkaline field. Samples from the TVZ have a much narrower range of Zr/Y and Th/Yb. The complete data are provided in **Appendix A Table A1** and **Appendix A Table A11**. The range of compositions of felsic volcanic rocks in the Abitibi Greenstone Belt is shown for comparison (see text for discussion).


A
Hotspot
Hawaii
Society Islands
Samoa
Marques Archipelago
B
Ridge-hotspot
Azores
Ascension Island
Iceland
C
Mid-ocean ridges
Juan de Fuca Ridge
East Pacific Rise
Galapagos Spreading Center
Pacific Antarctic Rise
D
Lau back-arc spreading centers
Mangatolu Triple Junction
Northwest Lau Spreading Center
Central Lau Spreading Center
Valu Fa Rift and Spreading Center
E
NE Lau arc and back-arc volcanoes
Fonualei Volcano
Niuatoputapu Volcano
Niuatahi Volcano
F
Manus back-arc spreading centers
Pual Ridge
Eastern Rifts
Manus back-arc Spreading Center
G
Izu Bonin arc volcanoes
Bayonnaise Knoll
Knoll 336
Sumisu Knoll
SW Torishima Knoll
Myojin Knoll
SW Myo-jin sho Knoll
H
Izu Bonin arc-rifts
Sumisu Rift
Torishima Rift
Aogashima Rift
Myojin Rift
Sample / Primitive Mantle
1000
100
10
1
Th Nb Ta La Ce Pr Nd Sm Zr Hf Eu Gd Tb Dy Y Ho Er Tm Yb Lu

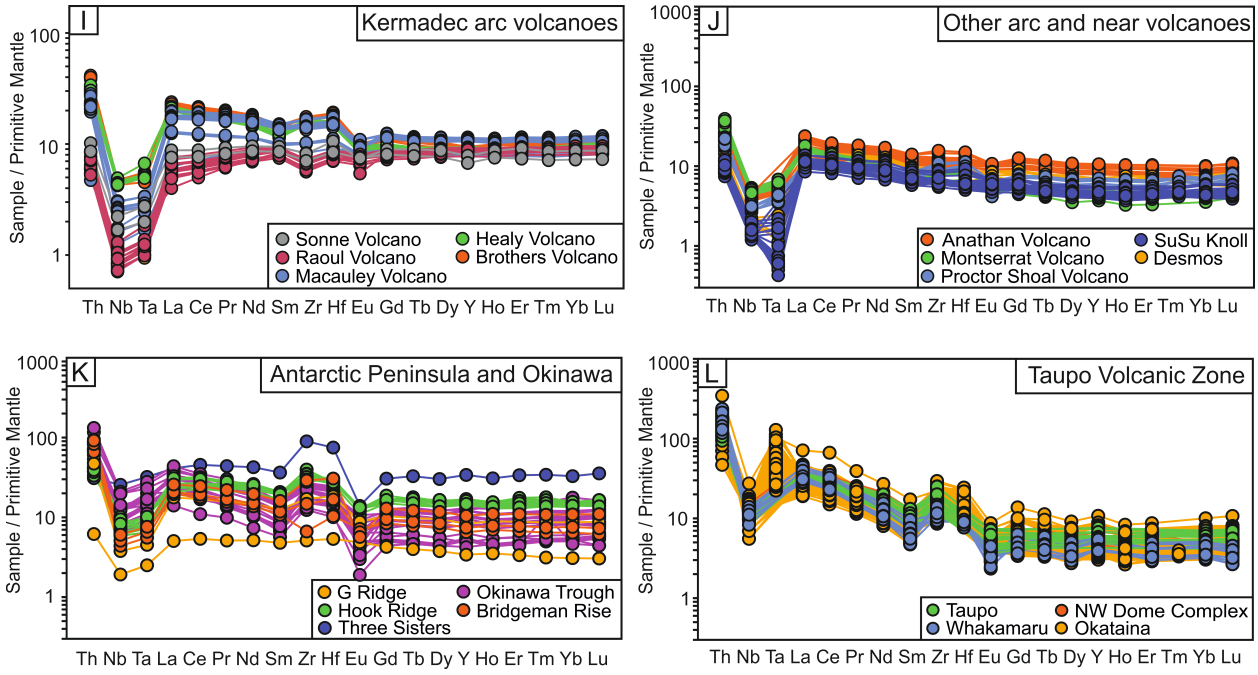


Figure 2.3: Primitive mantle-normalized trace element plots of modern oceanic felsic volcanic rocks. A) Plume (hotspot)-related samples have steeply dipping REE patterns, weak or no negative Eu anomalies and no negative Nb-Ta anomalies. B) Samples from ridge-hotspot intersections have steeply dipping REE patterns, negative Eu anomalies and no negative Nb-Ta anomalies. C) Mid-ocean ridge samples have flat REE patterns, enrichment in HREE, negative Eu anomalies and no negative Nb-Ta anomalies. D) Samples from Lau back-arc spreading centers, such as the Northwest and Central Lau back-arc spreading centers (NWLSC, CLSC) and the Mangatolu Triple Junction (MTJ), have flat REE patterns, elevated HREE, negative Eu anomalies and no negative Nb-Ta anomalies. Samples from the Valu Fa Rift, which is actively propagating into arc crust of the Tonga-Tofua Arc, have flat REE patterns, depleted HREE, weak negative Eu anomalies and strong negative Nb-Ta anomalies. E) Arc and back-arc volcanoes in the Northeast Lau Basin have flat and steeply dipping REE patterns, weak negative Eu anomalies, and strong to weak negative Nb-Ta anomalies, reflecting proximity to the arc. F) Samples from the arc rifts in the Eastern Manus Basin (Pual Ridge and Eastern Rifts) have slightly elevated REE concentrations depleted HREE, no Eu anomalies and strong negative Nb-Ta anomalies. Samples from the distant Manus back-arc spreading center (MSC) are enriched in HREE and have negative Eu anomalies and weak negative Nb-Ta anomalies. G) Arc volcanoes of the Izu-Bonin Arc (e.g., Myojin Knoll, Sumisu Knoll, Baiyonnaise Knoll) have slightly depleted total REE, depleted HREE, weak negative Eu

anomalies and strong negative Nb-Ta anomalies. H) Samples from arc rifts of the Izu-Bonin Arc (Sumisu Rift, Torishima Rift, Aogashima Rift, Myojin Rift) have mostly flat REE patterns, intermediate HREE concentrations, weak negative Eu anomalies, and intermediate negative Nb-Ta anomalies. I) Felsic rocks from volcanoes of the Kermadec Arc (Healy, Brothers, Macauley and Sonne Volcanoes) have mostly flat REE, intermediate negative Eu anomalies and strong negative Nb-Ta anomalies, although Raoul Volcano has slightly depleted REE. J) Near-arc volcanoes of the Manus Basin (SuSu Knoll, Desmos Knoll) and arc volcanoes of the Lesser Antilles Arc (Montserrat), Mariana Arc (Anatahan), and Proctor Shoal of the South Sandwich Arc have slightly enriched REE, depleted HREE, weak negative Eu anomalies and pronounced negative Nb-Ta anomalies. K) Felsic rocks from continental margin arc-backarc systems (Okinawa Trough and Western Antarctic Peninsula, including Hook Ridge, Bridgeman Rise, G-Ridge and the Three Sisters volcanoes) have mostly flat to slightly enriched REE, depleted HREE (except Three Sisters), weak negative Eu anomalies and negative Nb-Ta anomalies. One sample from the Three Sisters volcano has a flat REE pattern, strongly enriched HREE, strong negative Eu anomaly and no negative Nb-Ta anomaly. L) Felsic volcanic rocks from the Taupo Volcanic Zone (Taupo, Whakamaru, NW Dome Complex, Okataina) have steeply dipping REE patterns, negative Eu anomalies and pronounced negative Nb-Ta anomalies. Details of the sample sources are provided in **Appendix A Table A1**. Primitive mantle values are from Sun et al. (1989).

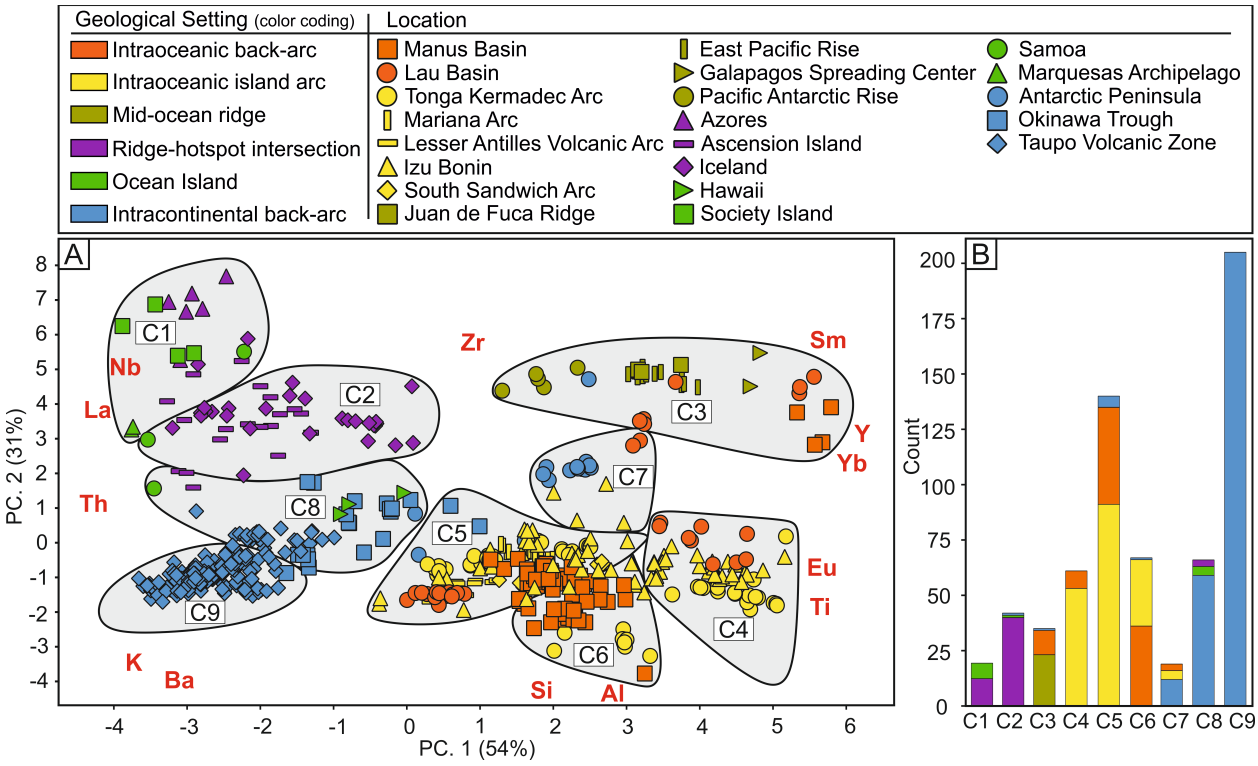


Figure 2.4: A) Principal components plot of the major and trace element geochemistry of modern oceanic felsic volcanic rocks. PC1 and PC2 account for 54% and 31%, respectively, of the total variance of the data set. The principal components analysis (PCA) was conducted using 13 elements (Si, Ti, Al, K, Y, Zr, Nb, Ba, La, Sm, Eu, Yb, Th) for all samples in the data set (see Appendix A Table A4). The loadings of each element on PC1 and PC2 are provided in Appendix A Table A5. The red element labels correspond to loadings for the entire data set; the symbols are the loadings for individual samples. The smallest number of clusters that show clear separation of the samples are indicated (C1-C9). The results of the cluster analysis are given in **Appendix A Tables A5** and **A6**, and details of the individual clusters are shown in **Appendix A Figure 2. A4**. The characteristics of each cluster and their relationship to specific lithotectonic assemblages are summarized in **Table 2.3** and described in the text. C1 = ocean islands (Society Islands, Marquesas Archipelago); C2 = ridge-hotspot intersections (Azores, Iceland, Ascension Island); C3 = mid-ocean ridges (Pacific-Antarctic Rise, East Pacific Rise, Galapagos Spreading Center, Juan de Fuca Ridge), intraoceanic back-arc spreading centers (Manus Spreading Center, Northwest Lau Spreading Center, Central Lau Spreading Centers) and one sample from a continental margin setting (Three Sisters Volcano in the Bransfield Strait of the Antarctic Peninsula); C4 =

intraoceanic arc volcanoes (Raoul Volcano on the Tonga-Kermadec Arc and Sumisu Knoll at the volcanic front of the Izu-Bonin Arc) and arc-related rifts (Valu Fa Rift and Spreading Center behind the Tofua Arc); C5 = intraoceanic arc volcanoes (Anatahan at the volcanic front of the Mariana Arc, Montserrat at the Lesser Antilles Arc, and Brothers and Healy volcanoes at the Kermadec Arc, as well as rear-arc volcanic complexes (Niuatahi rear-arc volcanic complex of the Tofua Arc, and G-Ridge and Bridgeman Rise from the Bransfield Strait); C6 = Nascent arc volcanoes (Fonualei and Niuatoputapu volcanoes near the Tofua Arc, Macauley volcano on the Kermadec Arc, Proctor shoal on the South Sandwich Arc, Bayonnaise Knoll behind the Izu-Bonin Arc, SuSu Knolls) and nascent back-arc rifts (Pual Ridge in the Manus Basin, Torishima Rift and Aogashima Rift behind the Izu volcanic arc and G-Ridge from the Bransfield Strait); C7 = Extending arc and continental margin rifts (Hook Ridge in Bransfield Strait, Sumisu and Myojin back-arc rifts behind the Izu-Bonin arc and Mangatolu Triple Junction in the northern Lau back-arc basin); C8 and C9 = intracontinental arc and back-arc related rifts (Okinawa Trough back-arc rift and the TVZ). B) Histogram of the sample distribution by target class sorted according to geological setting.

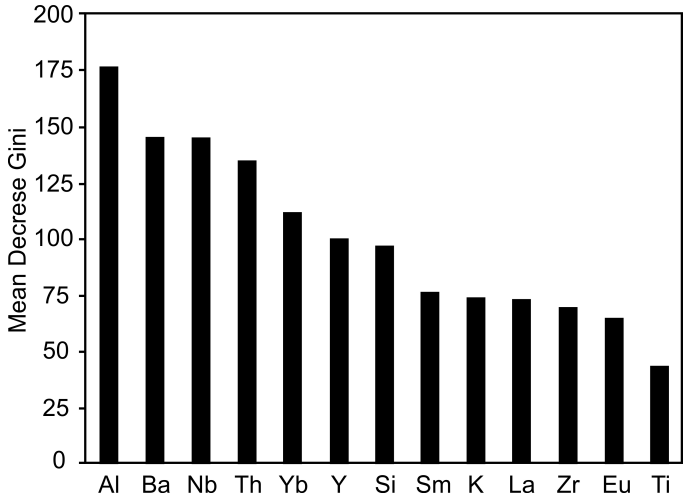


Figure 2.5: Plot of the "Mean Decrease Gini" value for individual elements in the classification of a sample into the target class or "cluster" (see text for discussion). The Mean Decrease Gini value corresponds to the probability of a correct classification of a sample and identifies Al, Ba, Nb, Th, Yb, and Y as the most important variables in determining the accuracy of the classification. Ti and Eu have low Mean Decrease Gini values and therefore less influence in the correct classification of a sample.

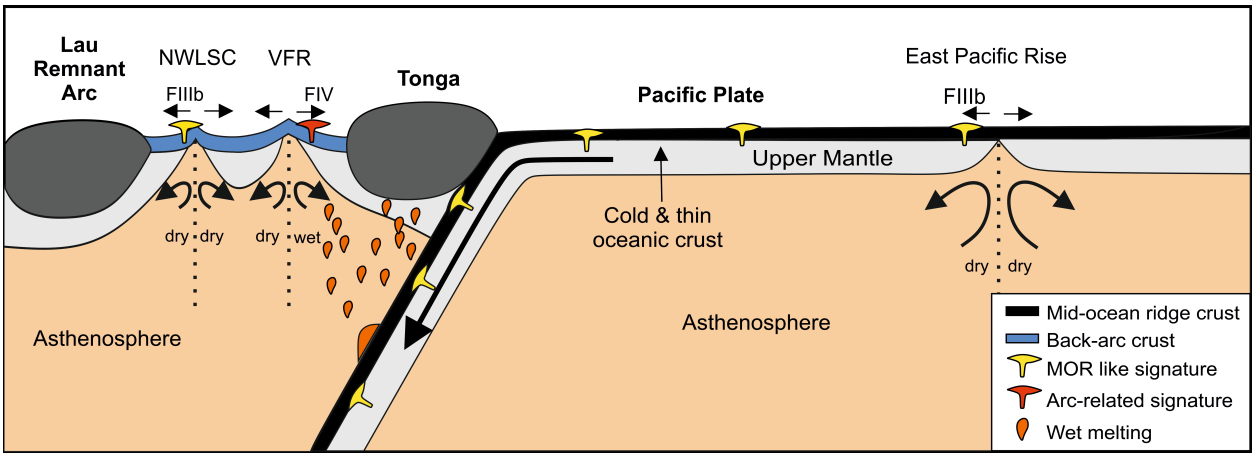


Figure 2.6: Schematic illustration of the geodynamic settings of dry versus wet melting in the example of the Lau Basin (**Figure 2.7**) with the inferred settings of FIV-type felsic volcanic rocks (red) and FIIIb-type felsic volcanic rocks (yellow) for reference (see text for discussion). Arc proximal felsic rocks, such as on the Valu Fa Rift and Spreading Center (VFR) are products of wet melting, resulting in FIV-like signatures, whereas more mature distal back-arc spreading centers, such as the Northwest Lau Spreading Center (NWLSC), are mainly associated with dry melting and produce FIIIb-like signatures. Note, in this scenario, FIIIb rhyolites that form at open ocean mid-ocean ridges such as the East pacific Rise are ultimately subducted and therefore have a low preservation potential.

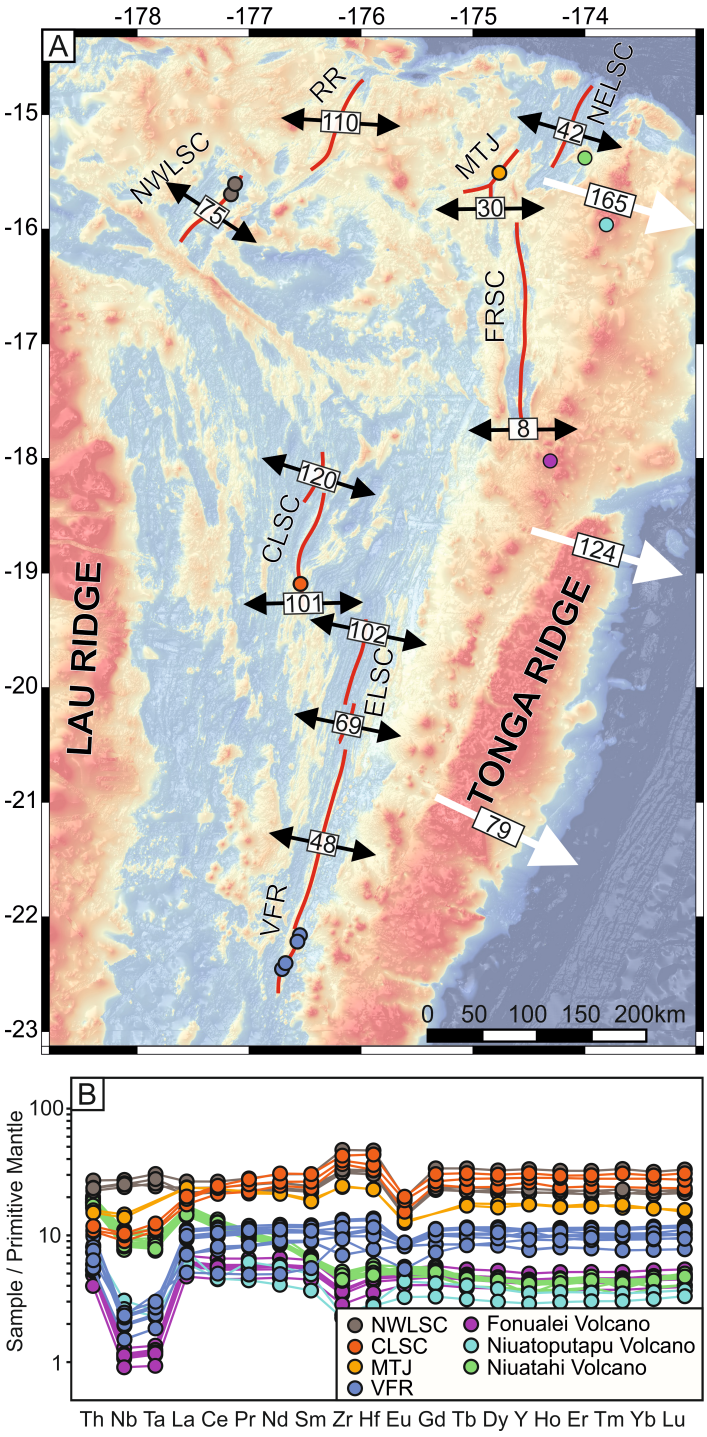


Figure 2.7: A) Locations of felsic volcanic rocks sampled in the northern Lau Basin, which contains at least eight major zones of active extension: CLSC = Central Lau Spreading Center; ELSC = Eastern Lau Spreading Center; VFR = Valu Fa Rift and Spreading Center; FRSC = Fonualei Rift and Spreading Center; MTJ = Mangatolu Triple Junction; NELSC = Northeast Lau

Spreading Center; NWLSC = Northwest Lau Spreading Center; RR = Rochambeau Rifts. Spreading rates in mm/yr are shown on the ridge axes (red lines), and convergence rates of the Indo-Australian and Pacific plates are shown by the white arrows. The sample locations are overlain on the regional bathymetry from (GMRT v3.5; Ryan et al. 2009). Symbols as in **Figure 2.3**. B) Primitive mantle-normalized trace element plot of Lau Basin felsic volcanic rocks shown together from **Figure 2.3**.

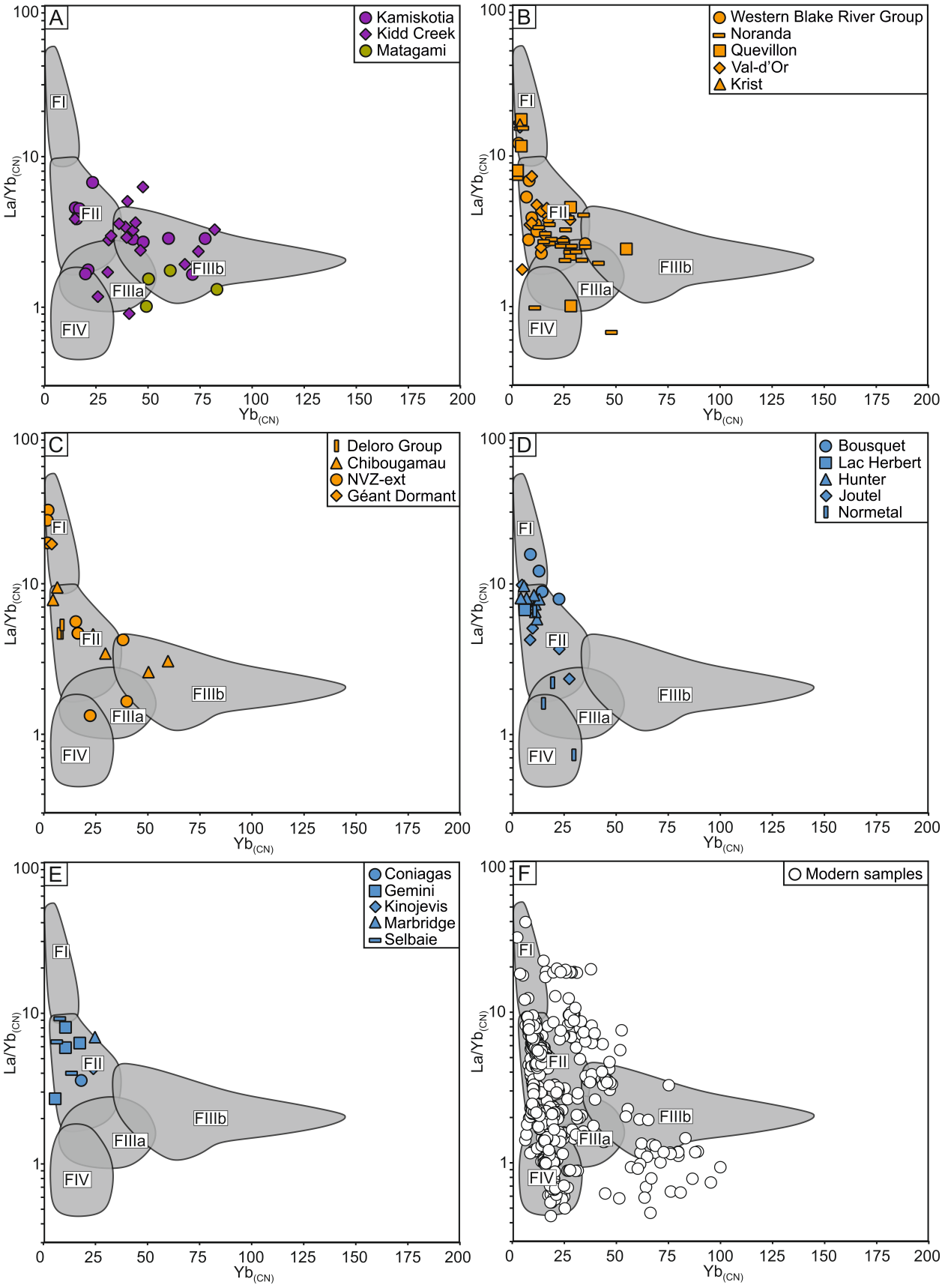

A
Kamiskotia
Kidd Creek
Matagami
B
Western Blake River Group
Noranda
Quevillon
Val-d'Or
Krist
C
Deloro Group
Chibougamau
NVZ-ext
Géant Dormant
D
Bousquet
Lac Herbert
Hunter
Joutel
Normetal
E
Coniagas
Gemini
Kinojevis
Marbridge
Selbaie
F
Modern samples
FI
FII
FIIIa
FIIIb
FIV
La/Yb(CN)
Yb(CN)
100
10
1
0
25
50
75
100
125
150
175
200

Figure 2.8: Chondrite-normalized La/Yb versus Yb plot of felsic volcanic rocks from the Abitibi Greenstone Belt (AGB) superimposed on the fields of the F-classification after Hart et al. (2004). Sample details are provided in Appendix A Table A11. A) Kamiskotia, Kidd Creek and Matagami samples, belonging mostly to target classes C2 and C3, plot close to or just outside the FIIIb field. B) Blake River Group, Noranda, Quevillon, Val-d'Or and Krist samples belonging to target class C5 plot mostly in the FII and FIII fields. C) Deloro Group, Chibougamau, NVZ-ext (Duvan, Vendome, Abcourt, Lamorandière) and Géant Dormant samples belonging to target class C5 plot mostly in the FII field. D) Bousquet, Lac Herbert, Hunter, Joutel and Normetal samples belonging mostly to target classes C8 and C9 plot close to or just outside the FI and FII fields. E) Coniagas, Gemini, Kinojevis, Marbridge and Selbaie samples belonging mostly to target classes C8 and C9 plot close to or just outside the FII field. F) The range of compositions of felsic volcanic rocks in modern oceans is shown for comparison (see text for discussion).

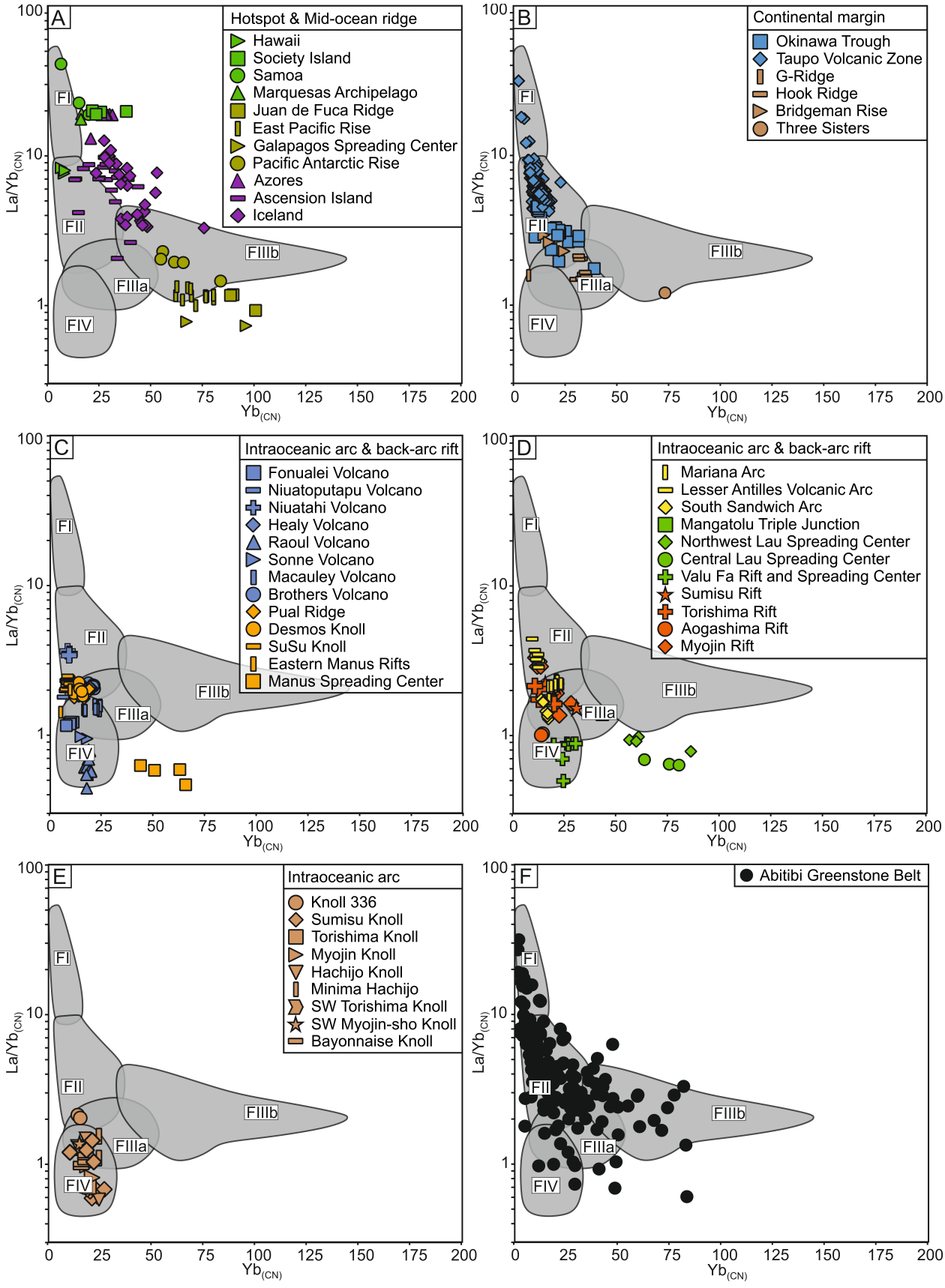

A
Hotspot & Mid-ocean ridge
Hawaii
Society Island
Samoa
Marquesas Archipelago
Juan de Fuca Ridge
East Pacific Rise
Galapagos Spreading Center
Pacific Antarctic Rise
Azores
Ascension Island
Iceland
B
Continental margin
Okinawa Trough
Taupo Volcanic Zone
G-Ridge
Hook Ridge
Bridgeman Rise
Three Sisters
C
Intraoceanic arc & back-arc rift
Fonualei Volcano
Niuatoputapu Volcano
Niuatahi Volcano
Healy Volcano
Raoul Volcano
Sonne Volcano
Macauley Volcano
Brothers Volcano
Pual Ridge
Desmos Knoll
SuSu Knoll
Eastern Manus Rifts
Manus Spreading Center
D
Intraoceanic arc & back-arc rift
Mariana Arc
Lesser Antilles Volcanic Arc
South Sandwich Arc
Mangatolu Triple Junction
Northwest Lau Spreading Center
Central Lau Spreading Center
Valu Fa Rift and Spreading Center
Sumisu Rift
Torishima Rift
Aogashima Rift
Myojin Rift
E
Intraoceanic arc
Knoll 336
Sumisu Knoll
Torishima Knoll
Myojin Knoll
Hachijo Knoll
Minima Hachijo
SW Torishima Knoll
SW Myojin-sho Knoll
Bayonnaise Knoll
F
Abitibi Greenstone Belt
FI
FII
FIIIa
FIIIb
FIV
La/Yb(CN)
Yb(CN)
100
10
1
0
25
50
75
100
125
150
175
200

Figure 2.9: Chondrite-normalized La/Yb versus Yb plot of modern oceanic felsic volcanic rocks superimposed on the fields of the F-classification of Archean felsic volcanic rocks (after Hart et al., 2004). A) Ocean island (green), mid-ocean ridge (olive) and ridge-hotspot intersection (purple) samples have a wide range of $La/Yb_{(CN)}$ and $Yb_{(CN)}$ values and plot close to or just outside the FI, FII, and FIIIb fields. B) Intracontinental arc-backarc (blue) samples have low $Yb_{(CN)}$ with FI, FII, FIIIa and FIV-like signatures. Three back-arc volcanoes of the rifted continental margin of the Antarctic Peninsula (brown) are also shown. The Three Sisters back-arc volcano of the Antarctica Peninsula has somewhat lower $La/Yb_{(CN)}$ and higher $Yb_{(CN)}$ and plots just outside FIIIb. C) Intraoceanic arc-backarc samples of the Tonga-Kermadec arc (dark blue) and Manus Basin (orange) have low $La/Yb_{(CN)}$ and low $Yb_{(CN)}$ with FII, FIIIa and FIV-like signatures. They include both near-arc volcanoes (mainly Tonga-Kermadec) and rifted arc crust (in the eastern Manus Basin). The samples from the Manus Spreading Center belong to a more distant back-arc spreading regime (see text for discussion). D) Samples from a range of intraoceanic island arcs (yellow), intraoceanic back-arc spreading centers from the Lau Basin (green), as well as samples from the near-arc rifts of the Izu-Bonin Arc (orange) have mostly in low $Yb_{(CN)}$ with FII, FIIIa and FIV-like signatures. Two of the back-arc spreading centers of the northern Lau Basin (Northwest Lau Spreading Center and the Central Lau Spreading Center) have somewhat lower $La/Yb_{(CN)}$ and higher $Yb_{(CN)}$ and plot just outside FIIIb. E) Arc and back-arc volcanoes ("knolls") of the Izu-Bonin Arc (brown) have uniformly low $La/Yb_{(CN)}$ and $Yb_{(CN)}$ with FIIIa and FIV-like signatures. F) The range of compositions of felsic volcanic rocks in the Abitibi Greenstone Belt is shown for comparison (see text for discussion). Details of the sample sources are provided in **Appendix A Table A1**.

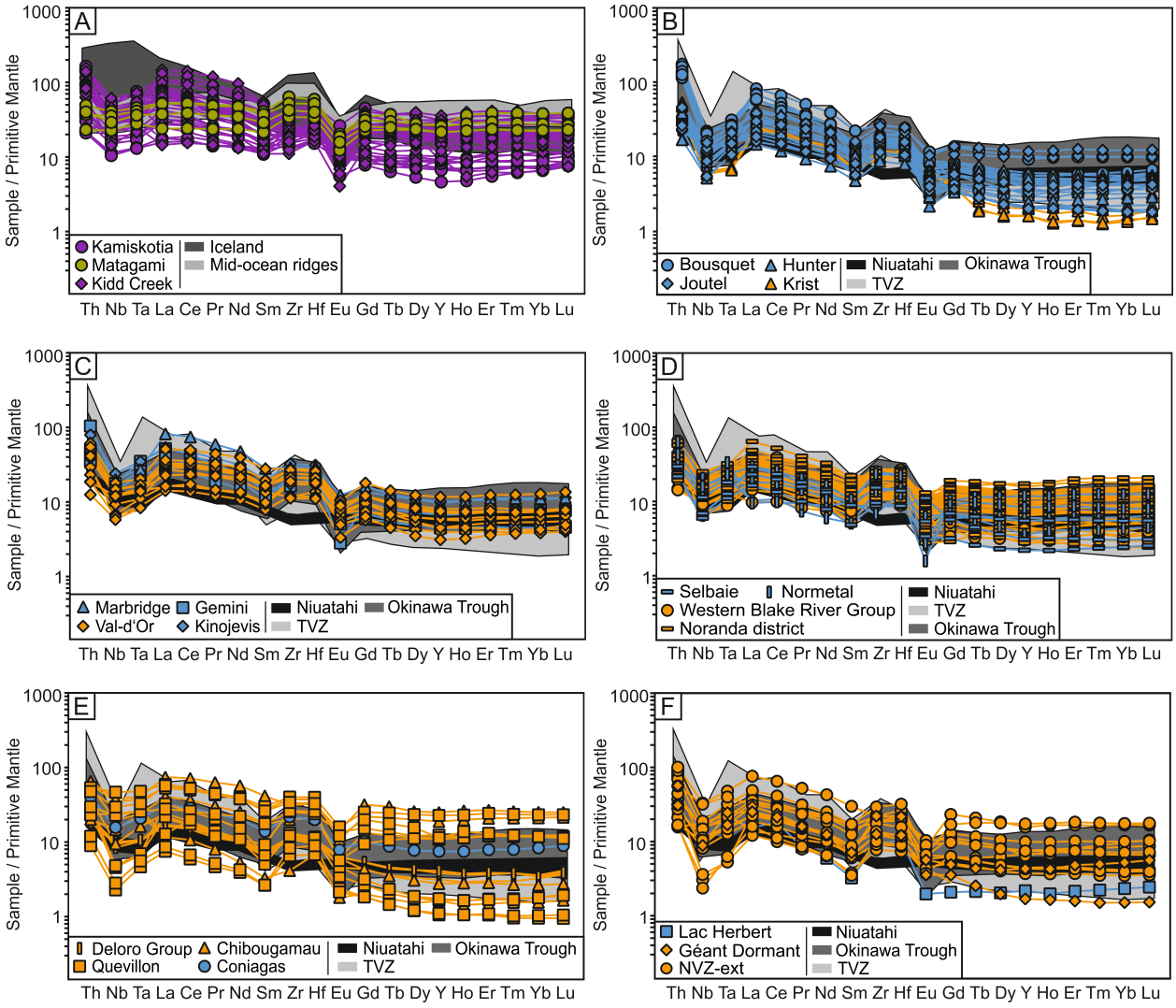


Figure 2.10: Primitive mantle-normalized trace element plots of felsic volcanic rocks of the Abitibi Greenstone Belt (AGB) compared to modern oceanic felsic volcanic rocks. Sample details are provided in **Appendix A Table A11**. A) Samples from Kamiskotia, and Kidd Creek have slightly elevated REE, enriched HREE, pronounced negative Eu anomalies and weak negative Nb-Ta anomalies, whereas samples from Matagami have flat REE patterns, enriched HREE, pronounced negative Eu anomalies and no Nb-Ta anomalies. Samples from Kamiskotia and Kidd Creek have strong similarities to felsic volcanic rocks from Iceland, whereas samples from Matagami are more similar to felsic volcanic rocks from mid-ocean ridges. B) Samples from Bousquet, Joutel, Hunter and the Krist Fragmental in the Timmins-Porcupine area have elevated REE patterns with moderate HREE enrichment, negative Eu anomalies and moderate to strong negative Nb-Ta anomalies. Samples from Bousquet have strong similarities to felsic volcanic rocks from the Taupo

Volcanic Zone and the Okinawa Trough. C) Samples from Marbridge, Val-d'Or, Gemini and Kinojevis have slightly enriched REE, moderate HREE, negative Eu anomalies and moderate negative Nb-Ta anomalies. D) Samples from the Blake River Group at Noranda, as well as samples from Normetal and Selbaie have slightly enriched REE, variable HREE, negative Eu anomalies and negative Nb-Ta anomalies. These samples also have similarities to felsic volcanic rocks from the Taupo Volcanic Zone and Okinawa Trough. E) Samples from the Deloro Assemblage, Quevillon, Chibougamau and Coniagas have slightly enriched REE, highly variable HREE, negative Eu anomalies, and variable negative Nb-Ta anomalies. F) Samples from NVZ-ext (Duvan, Vendome, Abcourt, Lamorandière), Géant Dormant and the Lac Herbert location are slightly enriched in REE and have highly variable HREE, negative Eu anomalies, and variable negative Nb-Ta anomalies. Primitive mantle values are from Sun et al. (1989).

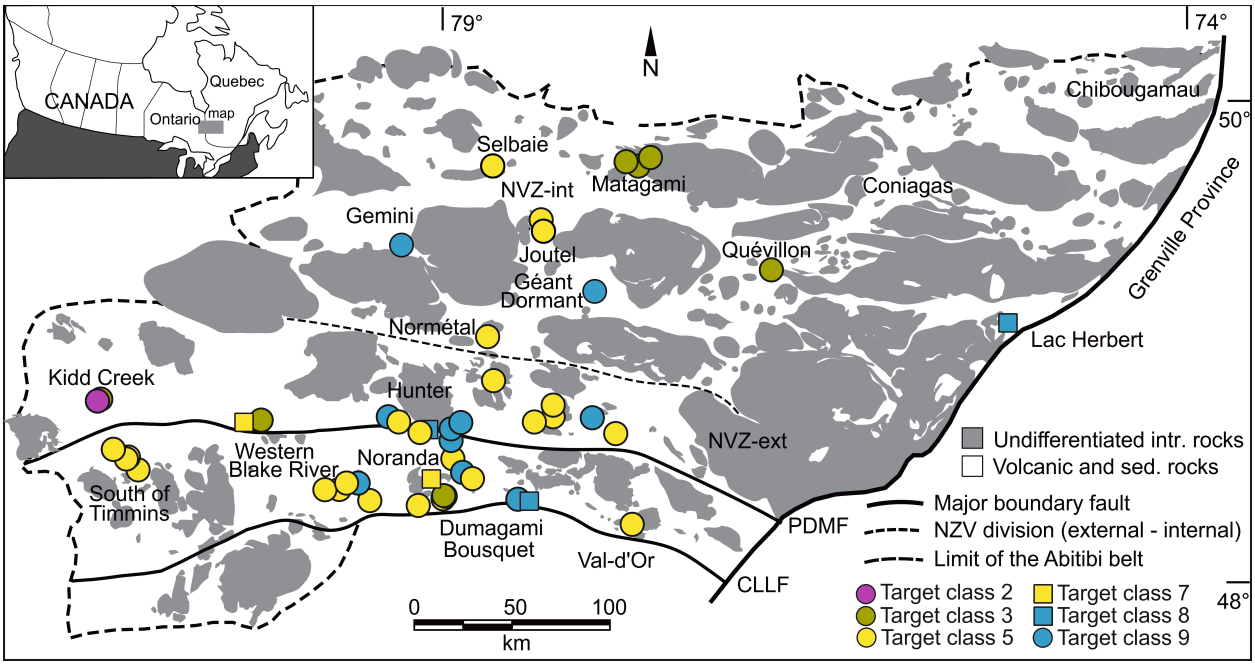


Figure 2.11: Results of the random forest classification of Abitibi felsic volcanic rocks according to target class C2 (purple), C3 (olive), C5 (yellow circle), C7 (yellow square), C8 (blue square) and C9 (blue circle). Sample details are provided in **Appendix A Table A11**. Samples from the Noranda Volcanic Complex and Blake River Group belong to several target classes (e.g., C2, C3, C5, and C8), whereas samples from Kidd Creek (C2) and Matagami (C3) fall into only one target class each (see text for discussion).

Tables

Table 2.1. Summary table of felsic rock compositions in modern oceanic settings illustrating geochemical differences in different lithotectonic assemblages.

Geodynamic setting	Lithotectonic assemblages	Example locations	Geochemical signature	Petrogenesis	References
Mid-ocean ridge	Extensional zones, overlapping spreading centers, propagating rift tips, ridge-transform intersections	East Pacific Rise, Juan de Fuca Ridge, Galapagos Spreading Center, Pacific Antarctic Rise	60.1-68.0 wt.% SiO_2; 0.60-1.9 wt.% TiO_2; 0.9-1.4 wt.% K_2O; 54.5-100.0 $Yb_{(CN)}$; 0.8-1.4 $La/Yb_{(CN)}$; 2.9-7.5 Zr/Y; 0.5-0.7 Eu anomaly	Fractional crystallization and assimilation of hydrated oceanic crust	Haase et al., 2005 Wanless et al., 2010 Freund et al., 2013
Intraoceanic arc and back-arc	Back-arc spreading centers	**Lau Basin** (Valu Fa Rift and Spreading Center, Central Lau Spreading Center, Mangatolu Triple Junction, Northwest Lau Spreading Center) **Manus Basin** (Manus Spreading Center)	60.1-74.6 wt.% SiO_2; 0.38-1.50 wt.% TiO_2; 0.32-2.08 wt.% K_2O; 8.64-79.69; $Yb_{(CN)}$; 0.51-2.39 $La/Yb_{(CN)}$; 2.23-3.84 Zr/Y; 0.61-1.00 Eu anomaly	Fractional crystallization or partial melting with low or no assimilation of oceanic crust	Fretzdorff et al., 2006 Lytle et al., 2012 Jenner et al., 2012 Beier et al., 2015
	Arc rifts	**Izu Bonin** (Sumisu Rift, Aogashima Rift, Myojin Rift, Torishima Rift) **Manus Basin** (Pual Rift, Susu Rift)	65.9-76.5 wt.% SiO_2; 0.17-0.61 wt.% TiO_2; 0.88-2.94 wt.% K_2O; 11.44-30.07 $Yb_{(CN)}$; 1.01-3.29 $La/Yb_{(CN)}$; 2.60-5.26 Zr/Y; 0.48-1.00 Eu anomaly	Partial melting of a basaltic to andesitic precursor and/or fractional crystallization with variable assimilation of oceanic crust	Tamura et al., 2009 Haraguchi et al., 2017
	Arc and back-arc volcanoes	**Izu Bonin** (Bayonnaise Knoll, Knoll 336, Myojin Knoll, Sumisu Knoll, Torishima Knoll, Hachijo Knoll, Minima Hachijo, SW Torishima Knoll) **Lau Basin** (Fonualei Volcano, Niuatahi Volcano, Niuatoputapu Volcano) **Kermadec Arc** (Raoul Volcano, Macauley Volcano, Healy Volcano, Brothers Volcano) **Manus Basin** (SuSu Knolls, Desmos Knoll) **Sandwich Arc** (Proctor Shoal) **Lesser Antilles Arc** (Montserrat Volcano) **Mariana Arc** (Anatahan Volcano)	60.1-76.6 wt.% SiO_2; 0.17-1.04 wt.% TiO_2; 0.10-2.49 wt.% K_2O; 7.04-30.54 $Yb_{(CN)}$; 0.44-3.55 $La/Yb_{(CN)}$; 1.65-6.48 Zr/Y; 0.61-1.00 Eu anomaly	Fractional crystallization of episodically replenished magma chambers with little or no assimilation of oceanic crust	Zellmer et al., 2003 Wade et al., 2005 Haase et al., 2006 Leat et al., 2007 Tamura et al., 2009 Turner et al., 2012 Barker et al., 2013 Beier et al., 2015 Park et al., 2015 Haraguchi et al., 2017 Embley et al., 2018

Ocean island volcanism and hot-spot association	Hotspot related	**Hawaii** (Waianae Volcano) Marquesas Archipelago (Hane) **Samoa** (Savaii, Tamaii) Society Islands (Pae Eo, Moua Tapu, Tiva)	61.0-68.1 wt.% SiO_2; 0.13-096 wt.% TiO_2; 2.83-6.01 wt.% K_2O; 6.27-37.73 $Yb_{(CN)}$; 0.95-21.82 $La/Yb_{(CN)}$; 3.04-31.54 Zr/Y; 0.68-0.99 Eu anomaly	Deep crustal melting with fractional crystallization and/or magma mixing and shallow differentiation; partial melting of oceanic crust	Harnois et al., 2006 Zander et al., 2010 Chauvel et al., 2012
	Hotspot and MOR related	**Azores** (Furnas Volcano) Ascension Fractures Zone (Ascension Island) **Iceland**	61.0-76.6 wt.% SiO_2; 0.08-0.61 wt.% TiO_2; 1.98-5.87 wt.% K_2O; 12.88-52.50 $Yb_{(CN)}$; 2.05-12.69 $La/Yb_{(CN)}$; 1.86-40.70 Zr/Y; 0.12-0.99 Eu anomaly		Jónasson 2007 Portnyagin et al., 2012 Jicha et al., 2013 Mancini et al., 2015 Chamberlain et al., 2016 Jeffery et al., 2016
Intra-continental backarc	Early-stage back-arc rift	**Ryukyu arc-trench system** (Okinawa Trough) Taupo Volcanic Zone	71.1-80.4 wt.% SiO_2; 0.06-0.45 wt.% TiO_2; 2.14-4.88 wt.% K_2O; 6.91-15.18 $Yb_{(CN)}$; 4.22-8.64 $La/Yb_{(CN)}$; 3.20-13.40 Zr/Y; 0.34-0.93 Eu anomaly	Fractional crystallization with variable assimilation of continental crust	Shinjo et al., 2002 Deering et al., 2011
	Extending marginal basin	Antarctic Peninsula (Bransfield Strait)	65.12-70.50 wt.% SiO_2; 0.35-1.05 wt.% TiO_2; 0.93-1.97 wt.% K_2O; 6.73-34.54 $Yb_{(CN)}$; 1.17-2.55 $La/Yb_{(CN)}$; 4.79-6.03 Zr/Y; 0.61-0.77 Eu anomaly		Keller et al., 2002 Fretzdorff et al., 2004 Petersen et al., 2004
Archean	Uncertain	**Abitibi greenstone belt** (Matagami, Noranda, Bousquet, ...)	60.24-85.95 wt.% SiO_2; 0.05-0.81 wt.% TiO_2; 0.02-4.43 wt.% K_2O; 1.27-50.04 $Yb_{(CN)}$; 0.04-12.19 $La/Yb_{(CN)}$; 1.40-17.57 Zr/Y; 0.15-1.07 Eu anomaly	Tholeiitic to calc-alkaline, high-degree partial melting, fractional crystallization and crustal contamination	Lesher et al., 1986 Barrie et al., 1993 Hart et al., 2004 Gaboury et al., 2008 Pearce 2008

Table 2.2. Summary Table of geochemical indicators of lithotectonic assemblages of felsic volcanic rocks (see text for discussion and references).

Indicator	Underlying behaviour	Result	Interpretation
LILE (K, Rb, Cs, Sr, Ba)	Incompatible behaviour; high fluid mobility	High LILE in enriched sources; high LILE in fractionated melts; high LILE in low degree partial melts; significant LILE enrichment in arc-related magmas	LILE enrichment controlled by dehydration of subducted slab; low LILE in MOR settings reflect lack of fluid enrichment from a slab
HFSE (Zr, Nb, Hf, REE)	Incompatible behaviour; low fluid mobility	High HFSE in enriched sources; high HFSE in fractionated melts; high HREE in low degree partial melts; significant HFSE depletion in arc-related magmas	HFSE depletion controlled by dehydration of subducted slab; HFSE enrichment in MOR controlled by enriched mantle sources
Nb-Ta anomaly	Incompatible behaviour; low fluid mobility	High Nb-Ta in enriched sources; high Nb-Ta in fractionated melts; high Nb-Ta in low degree partial melts; significant Nb-Ta depletion in arc-related magmas	Nb-Ta depletion due to selective enrichment by fluids derived from the slab
HREE	Incompatible behaviour; low fluid mobility	High HREE in fractionated melts; high HREE in low degree partial melts; high HREE in melts with wall rock assimilation; HREE depletion in arc magmas	Flat HREE patterns in arc settings at different concentrations reflect degree of partial melting; high HREE in MOR-settings reflect assimilation of hydrated crustal material
Eu anomaly	Plagioclase fractionation in dry melting; suppressed at high H_2O	Strong negative Eu anomaly in MOR melts; weak negative Eu anomaly in arc and back-arc magmas	Strong negative Eu anomaly reflects dry melting; weak negative Eu anomaly reflects wet melting
La/Sm	Slight difference in incompatible behaviour	High La/Sm in enriched sources (e.g., OIB); low La/Sm in depleted sources (e.g., MOR)	LREE enrichment originating from less depleted mantle in OIBs; MOR show different but mostly flat LREE patterns with variations due to mantle heterogeneity and degrees of depletion
La/Yb	Amphibole and garnet fractionation	High La/Yb in deep melting regimes at high pressure; low La/Yb in shallow melting regimes at low pressure	High pressure leads to amphibole and/or garnet fractionation resulting in high La/Yb
Zr/Y	Slight difference in incompatible behaviour	High Zr/Y in low-degree partial melts, commonly associated with higher alkalinity	Arc-related magmas have high Zr/Y reflecting calc-alkaline geochemical affinity due to high H_2O concentrations in arc-related environments, promoting deeper melting at lower degrees of partial melting
F-classification (Archean examples)	Different incompatible element behaviour of LREE and HREE; strong partitioning of HREE into garnet and amphibole	FI: alkaline to calc-alkaline affinity; low degree partial melts; HREE-depleted due to garnet fractionation	Melting at deep crustal levels (mostly unmineralized, with important exceptions)
		FII: calc-alkaline affinity; high-degree partial melts; slightly HREE depleted due to garnet fractionation	Melting at intermediate crustal levels (sometimes mineralized)
		FIIIa and FIIIb: tholeiitic affinity; low-pressure partial melts; HREE-enrichment controlled by differences in crustal composition	Melting at shallow crustal levels (commonly mineralized)
		FIV: tholeiitic affinity; low-pressure, moderate degree partial melts; HREE-enriched due to a lack of residual amphibole or garnet	Post-Archean intraoceanic island arc (sometimes mineralized)

Table 2.3. Summary of target classes in the hierarchical clustering of modern oceanic felsic volcanic rock compositions according to tectonic setting and principal components analysis (PCA).

Target class	Lithotectonic assemblages	Type examples*	Trace element characteristics	PCA loadings
C1	Dominantly ocean islands	Samoa, Society Islands	High La/Sm, high La/Yb, intermediate to strong negative Eu anomaly, no negative Nb-Ta anomaly	High Nb and La loadings and low HREE, Si and Al loadings
C2	Ridge-hotspot intersections and ocean islands	Ascension Island, Iceland	High La/Sm, high La/Yb, intermediate to strong negative Eu anomaly, no negative Nb-Ta anomaly, lower Nb, Th, Zr concentrations than C1	High Nb and La loadings and low Si and Al loadings, slightly higher HREE loadings than C1
C3	Mid-ocean ridges and mature back-arc spreading centers	Juan de Fuca Ridge, East Pacific Rise, Pacific Antarctic Rise, Galapagos Spreading Center, Manus Spreading Center, Northwest Lau Spreading Center, Central Lau Spreading Center	Flat REE pattern, HREE enrichment, slight negative Nb-Ta anomaly, intermediate negative Eu anomaly	High HREE and Zr loadings and, low Si and Al loadings
C4	Intraoceanic volcanic arc and arc-related rifts	Sumisu Knoll, (Valu Fa Rift and Spreading Center)	Flat REE pattern, less HREE enrichment than C7; strong negative Nb-Ta anomaly, weak negative Eu anomaly	High Ti, Eu and HREE loadings
C5	Intraoceanic backarc and arc-related rifts	Sumisu Rift, Niuatahi Volcano, Brothers Volcano, (Pual Ridge)	Flat to slightly LREE-enriched REE pattern, negative Nb-Ta anomaly, weak negative Eu anomaly	Intermediate Si and Al loadings
C6	Nascent back-arc rifts	Torishima Rift, Aogashima Rift	Similar to C5 but lower REE and Th concentrations, and stronger negative Nb-Ta anomaly	High Si and Al loadings
C7	Extending arc and continental margin crust	Bransfield Strait	Flat REE pattern, less HREE enrichment than C3, no to slight negative Nb-Ta anomaly, intermediate negative Eu anomaly	Intermediate HREE and Zr loadings, low Si and Al loadings
C8	Intracontinental back-arc spreading centers	Okinawa Trough	High La/Sm, high La/Yb, intermediate negative Eu anomaly, intermediate negative Nb-Ta anomaly	Intermediate Th, Ba, K loadings and low HREE loadings
C9	Intracontinental arc-related rift	Taupo Volcanic Zone	High La/Sm, high La/Yb, intermediate negative Eu anomaly, intermediate negative Nb-Ta anomaly, stronger HREE depletion than C8	High Th, Ba, K loadings and very low HREE loadings

*Note: The Pual Ridge is transitional, it is back-arc rifting in old arc crust. The Valu Fa Ridge is transitional, it is a back-arc spreading center propagating into arc crust. There is significant overlap between some clusters, with samples from different locations falling into multiple target classes, as shown in **Figure 2.4** (see text for discussion)

Chapter 3

Geochemical Signatures of Mafic Volcanic Rocks in Modern Oceanic Settings and Implications for Archean Mafic Magmatism

Article in review: Fassbender, M.L., Hannington, M., Baxter, A.T., Diekrup, D., Stewart, M., and Brandl, P.A, 2023, Geochemical Signatures of Mafic Volcanic Rocks in Modern Oceanic Settings and Implications for Archean Mafic Magmatism: Economic Geology, in review.

Abstract

Greenstone belts are dominated by mafic volcanic rocks with geochemical characteristics that indicate a range of possible geodynamic influences. Many analogies with modern tectonic settings have been suggested. Increasing exploration of the modern oceans and comprehensive sampling of volcanic rocks from the seafloor is now providing unique opportunities to characterize different melt sources and petrogenesis that can be more closely compared to greenstone belts. In this study, we have compiled high-quality geochemical analyses of more than 2850 unique samples of submarine mafic volcanic rocks (<60 wt.% SiO_2) from a wide range of settings, including mid-ocean ridges, ridge-hotspot intersections, intraoceanic arc and back-arc spreading centers, and ocean islands. The compiled data show significant geochemical variability spanning the full range of compositions of basalts found in greenstone belts. This diversity is interpreted to due to variable crustal thickness, dry melting versus wet melting conditions, mantle mixing and contamination. In particular, different melting conditions have been linked to mantle heterogeneity, complex mantle flow regimes, and short-lived tectonic domains, such as those associated with diffuse spreading, overlapping spreading centers, and triple junctions. These are well documented in the microplate mosaics of the Western Pacific.

Systematic differences in mafic volcanic rock compositions in modern oceanic settings are revealed by a combination of principal components analysis and unsupervised hierarchical clustering of the compiled data. Mafic volcanic rocks from most arc-backarc systems have strongly depleted mantle signatures and well-known subduction-related chemistry such as LILE enrichment in combination with strong negative Nb-Ta anomalies and low HREE. This contrasts with mafic volcanic rocks in Archean greenstone belts, which show no, or at least weaker, subduction-related chemistry, a less-depleted mantle, less wet melting, and variable crustal contamination. The differences are interpreted to be the result of the lower mantle temperatures, thinner crust and subduction-related processes of present-day settings. However, mafic rocks that are geochemically identical to those in Archean greenstone belts occur in many modern back-arc basins, including the Lau Basin, East Scotia Ridge, Bransfield Strait and Manus Basin that are characterized by fertile mantle sources, high heat flow and complex spreading regimes typical of small-scale microplate mosaics. These are increasingly recognized as favourable conditions for volcanogenic

massive sulfide (VMS) deposits, and therefore the geochemical signatures of the mafic volcanic rocks are potentially important for area selection in base and precious metal exploration.

3.1 Introduction

For over 40 years, geochemical signatures of volcanic rocks have been used to infer possible geodynamic settings of ancient greenstone belts and their contained mineral deposits (e.g., Lesher et al., 1986; Paradis et al., 1988; Kerrich and Wyman, 1997; Hart et al., 2004; Piercey, 2011). Comparisons with the modern oceans, however, have been limited by a lack of samples. This is changing with increased ocean exploration and the availability of high-precision analytical data on submarine volcanic rocks from diverse locations. In a companion paper, we compiled data on more than 2200 samples of felsic volcanic rocks from 70 different locations in the oceans and compared them to Archean rhyolites and dacites that host some of the world's most important volcanogenic massive sulfide (VMS) deposits. We found significant geochemical diversity in the modern samples, spanning the full range of compositions of felsic volcanic rocks found in greenstone belts (Fassbender et al., 2023). The present study takes a broader look at the geochemistry of mafic volcanic rocks (<60 wt.% SiO_2), which are found in nearly every niche of the modern oceans and are the dominant lithology of greenstone belts. We compiled high-quality geochemical analyses of more than 2800 unique samples of submarine mafic volcanic rocks from mid-ocean ridges, ridge-hotspot intersections, intraoceanic arc and back-arc spreading centers, and ocean islands **(Figure 1)** and compare these data to well-studied assemblages of the Abitibi Greenstone Belt (AGB) of Canada, the largest and best-preserved Neoarchean greenstone belt in the world. Precise analogs of ancient greenstone belts in modern settings seem unlikely due to the hotter mantle in the Archean, thicker oceanic crust, a potential lack of continental basement, and subduction regimes that were in their infancy (e.g., Bédard et al., 2013; Wyman, 2013; Palin et al., 2020). However, many of the fundamental petrogenetic indicators are very similar between modern and ancient systems. Major and trace element geochemistry have been widely used to infer conditions such as high heat flow associated with rifting, shallow depths of melting and increased fractionation that are favourable for the formation of VMS deposits (e.g., Galley et al., 1995; Gibson et al., 2007; Piercey, 2011). The most common lithotectonic discrimination diagrams for mafic volcanic rocks have been developed by inspection of relatively small data sets. Here, we use

a much larger compilation to identify the geochemical characteristics of mafic volcanic rocks in a full range of modern settings. The clusters identified in the data reflect highly variable melt sources and processes at different stages of basin evolution and reveal unexpected complexity in rapidly evolving microplate domains. We suggest these findings have implications for understanding similar magmatic processes in older terranes such as the AGB.

3.2 Petrogenesis of Modern Oceanic Mafic Volcanic Rocks

Mid-ocean ridges account for 75% of global mafic magmatism, with the balance in back-arc basins, volcanic arcs and ocean islands (Perfit and Davidson, 2000). Mafic melts in these different settings are produced by partial melting of the mantle due to: i) increased temperatures, as in hotspot-related regimes, ii) decreasing pressure, as in mid-ocean ridge spreading centers, iii) and by addition of volatiles in subduction zones. These major differences in melting process and different sources involved result in very different trace element geochemical signatures of the basalts (e.g., Arevalo and McDonough, 2010; Hofmann, 2014; Ueki et al., 2018). In the following, we review the systematics of mafic melt production in modern oceanic settings **(Figure 1)** and summarize the key geochemical characteristics **(Tables 1 and 2**). As shown in our previous paper (Fassbender et al., 2023), the petrogenesis of the mafic rocks have an important impact on felsic rock compositions, as fractionation of mafic melts, or melting of the associated basaltic crust, are the main sources of felsic magma.

3.2.1 Mid-ocean ridge basalts

Mid-ocean ridges are dominated by tholeiitic basalt (MORB) produced by decompression partial melting of the mantle (McKenzie and O`Nions, 1991). High degrees of partial melting result in low incompatible element concentrations, including Light Rare Earth Elements (LREE) and Large Ion Lithophile Elements (LILE), relative to the more compatible Heavy Rare Earth Elements (HREE) and High Field Strength Elements (HFSE) (Hofmann, 2014). Complexity is introduced by varying magmatic heat input and hydrothermal cooling, which change with spreading rate (Michael and Cornell, 1998; Haase et al., 2005). End-member examples include the fast spreading ridges, such as the East Pacific Rise at 20-21°S and the Pacific-Antarctic Rise at 37°S, which have stable axial melt lenses developed in a warm lithosphere and thickened oceanic crust, and slow

spreading ridges, such as the Mid-Atlantic Ridge at 45°N, where magma chambers are dispersed in a colder lithosphere and magmatism is episodic. These differences result in distinct geochemical signatures, especially at slow spreading ridges (White and Klein, 2014 and references therein) where greater tectonic extension can lead to strong hydrothermal cooling and fractionation. Isotopic systems such as $^{87}Sr/^{86}Sr$ and $^{143}Nd/^{144}Nd$ show that mantle heterogeneity is also important.

3.2.2 Ocean island basalts

Hotspot volcanism, such as at Hawaii and the Marquesas Archipelago, is characterized by deeply sourced alkaline melts produced by low degrees of partial melting of the mantle at high pressure and high temperature (Hofmann, 2014; Haase et al., 2019). This results in the enrichment of incompatible elements (LREE, LILE) relative to compatible elements (HREE, HFSE), producing the typical signatures of ocean island basalt (OIB). Additional complexity is introduced by mantle reservoirs with higher $^{87}Sr/^{86}Sr$ and lower $^{143}Nd/^{144}Nd$ than at mid-ocean ridges (Jackson et al., 2010; Price et al., 2014).

3.2.3 Intraoceanic arc and back-arc basalts

Arc volcanism in intraoceanic settings, such as the Tofua and Izu Bonin arcs, is mainly calc-alkaline. Melting in the sub-arc mantle is triggered by addition of volatiles from a dehydrating slab, which lowers the solidus temperature of the mantle (e.g., Hawkesworth et al., 1993; Langmuir et al., 2006). The volatiles are sourced from sediments, pore fluids, and hydrous minerals (from earlier alteration of the oceanic crust) and are released into the mantle wedge via pervasive or channeled flow during dehydration of the slab. The melts have high water contents, strong LILE enrichment, and high oxidation states. Certain trace elements, such as Ba, are mobile in the slab-derived fluids and become enriched in fluid-fluxed melts, while Nb and Yb are immobile, resulting in high Ba/Nb and Ba/Yb ratios (e.g., Pearce et al., 2005).

Back-arc rifts and spreading centers, such as in the Lau Basin and Manus Basin, produce both calc-alkaline and tholeiitic melts, depending on the volatile input from the slab (Langmuir et al., 2006). This mainly varies with proximity of the spreading center to the adjacent arc and trench, but also

with the age of the subducting lithosphere, the angle of subduction, the rate of slab rollback, the trajectory of the overriding plate, and different mantle flow regimes (Sdrolias and Müller, 2006; Castillo, 2012; Schmidt and Poli, 2014; Schellart, 2020). These, in turn, vary with the progress of basin opening, which begins with initial rifting and eventually leads to back-arc spreading (Taylor and Martinez, 2003; Pearce et al., 2005; Langmuir et al., 2006). With basin opening, melting regimes that may initially overlap become separated into zones of hydrous melting proximal to the arc and dry (MORB-like) melting of depleted mantle in the deeper back-arc basin. At the Valu Fa Ridge (VFR) in the Lau Basin and the Eastern Rifts (ER) of the Manus Basin, calc-alkaline melts are produced where the rifts are propagating into arc crust. At more distal spreading centers, such as the Northwest Lau Spreading Center (NWLSC) and the Manus Spreading Center (MSC) in the Manus Basin, the melts are tholeiitic.

3.2.4 Boninites

Boninitic melts have been found in a wide range of modern oceanic settings, including back-arc spreading centers and mantle plumes (Cooper et al., 2010; Resing et al., 2011; Golowin et al., 2017; Pearce and Reagan, 2019; Pearce and Arculus, 2020). They are produced by melting of previously depleted mantle material. In subduction zones, early rollback of the subducting slab triggers melting that leaves behind a depleted mantle (Arculus et al., 2019). Melting of this more refractory material is promoted by eventual addition of volatiles and increased heat. The resulting melts are widely interpreted to be indicative of subduction initiation (Arculus et al., 2019; Pearce and Arculus, 2020). However, similar melts are known from back-arc spreading centers and plume-related regimes (Pearce and Reagan, 2019). In the Fonualei Rift and Spreading Center (FRSC) of the northern Lau Basin, boninites are variably interpreted to be products of melting of sub-arc mantle that was depleted by earlier episodes of back-arc spreading or by melting of refractory material related to the Samoan plume (Falloon et al., 2007; Cooper et al., 2010; Resing et al., 2011; Escrig et al., 2012). In mantle-plume settings the melting is thought to be initiated by a pulse of hot material from the plume (Pearce and Arculus, 2020). The origin of these melts are of particular interest, as they have been widely recognized in greenstone belts (Kerrich et al., 1998).

3.3 Data Sources

Geochemical analyses of mafic lavas (<60 wt.% SiO_2) from 433 locations in the oceans were compiled from the literature **(Figure 1)**. From an original database of more than 3800 analyses, a subset of 2857 unique samples was selected for this study. The rejected samples included duplicate samples, repeat analyses of the same sample, samples analyzed by inappropriate methods, and samples with location errors or incomplete descriptions. Only samples with complete major and trace element data were retained; every sample in the final dataset was analyzed for at least Ti, Al, Ba, Th, Zr, Nb, La, Y, and Yb. No samples were included where the concentration of any element was equal to or below its detection limit or exceeded the upper limits of detection or where the limits of detection were not specified. To check for altered samples, we compared the data to fresh rock compositions of basalts and basaltic andesites, including immobile element ratios and REE profiles. In particular, we excluded samples with unusually high or low mobile element concentrations, such as Si, Na, K, and Eu. The final database is provided in **Appendix B Table A1**.

The mid-ocean ridge basalts in the database have low SiO_2 (48.7-52.1 wt.%), low K_2O (0.01-0.47 wt.%), intermediate TiO_2 (0.55-2.57 wt.%), and are depleted in LREE. Mafic volcanic rocks from ridge-hotspot intersections have variable SiO_2 concentrations (43.7-54.8 wt.%) but high K_2O (0.2-2.3 wt.%), high TiO_2 (1.6-3.9 wt.%), and LREE-enrichment. Ocean island basalts also have high K_2O (0.2-2.0 wt.%), high TiO_2 (2.4-4.5 wt.%), and LREE enrichment but low SiO_2 concentrations (42.4-51.2 wt.%). Samples from intraoceanic back-arc and island arc assemblages have high SiO_2 concentrations (44.9-58.9 wt.%), intermediate K_2O (0.01-1.1 wt.%), low TiO_2 (0.1-2.4 wt.%) and are only moderately LREE-enriched. Samples from intracontinental arc-backarc assemblages have high SiO_2 concentrations (45.9-58.6 wt.%), intermediate K_2O (0.2-1.9 wt.%), intermediate TiO_2 (0.6-2.8 wt.%) and moderate LREE enrichment. **Figure 2** (see **Appendix B Figure A1** for details) shows the range of mafic volcanic rock compositions in the database on a total alkali-silica plot (after Le Maitre, 1989) and an immobile element plot (after Winchester and Floyd 1977). The original Winchester and Floyd (1977) diagram is based on a limited number of samples, and so the full range of modern oceanic basalts considered here is not well classified by the depicted field boundaries. Pearce (1996) used a more comprehensive dataset; however, some of the modern

oceanic basalts are still not well classified (**Appendix B Figure A2**). Data for mafic volcanic rocks from the AGB are shown for comparison and discussed further below.

Figure 3 shows the range of magmatic affinities of modern oceanic rock (after Ross and Bédard, 2009). The mafic volcanic rocks from the Juan de Fuca Ridge, East Pacific Rise, Galapagos Spreading Center, Pacific Antarctic Rise, Mid-Atlantic Ridge and South Indian Ridge plot mainly in the tholeiitic field. Samples from ridge-hotspot intersections and ocean islands, such as Ascension Island, Iceland, Hawaii, and volcanoes of the Marquesas Archipelago, are mostly transitional to alkaline basalts, basanites and basaltic trachytes. Samples from intraoceanic back-arc assemblages, such as in the Manus Basin, the Lau Basin, Mariana Trough, East Scotia Ridge, and New Hebrides, are similar to MORB (i.e., dominantly tholeiitic basalts). Samples from island-arc assemblages, such as the Mariana, Izu-Bonin, Fiji, Tonga-Kermadec, and Lesser Antilles volcanic arcs, span the range from tholeiitic to calc-alkaline basalts and andesites. Mafic volcanic rocks from intracontinental arc-backarc settings, such as the Okinawa Trough and Western Antarctic Peninsula, are mostly calc-alkaline andesitic basalts. The corresponding tectonic affiliations are shown in the discrimination plot of Pearce (2014).

Extended trace elements plots of the mafic volcanic rocks in different settings are shown in **Figure 4**. They are grouped according to typical mid-ocean ridge-like signatures (**Figure 4A** and **B**), intraoceanic arc-backarc rift and spreading center signatures (**Figure 4C** and **D**) and arc-backarc signatures (**Figure 4E** and **F**). The mid-ocean ridge mafic volcanic rocks, represented by the East Pacific Rise and Mid-Atlantic Ridge, have mostly flat REE patterns and no negative Nb-Ta anomaly and plot in the N-MORB array of Pearce (2014). Samples from ridge-hotspot intersections and ocean islands have more steeply dipping REE patterns, no negative Nb-Ta anomaly and plot in the E-MORB array. Mafic volcanic rocks from intraoceanic back-arc assemblages, represented by the East Scotia Ridge have mostly flat REE patterns with strong negative Nb-Ta anomalies and low HREE concentrations and plot in the oceanic arc array. Samples from the terminations of back-arc spreading centers, represented by the Northeast Lau Spreading Center, Southern East Scotia Ridge, and the Northern Volcanic Tectonic Zone of the Mariana Trough, all have weak negative Nb-Ta anomalies and dipping REE patterns and plot between the E-MORB and continental arc arrays. Samples from back-arc rifts that are propagating

into arc crust, represented by the Fonualei Rift and Spreading Center, have even stronger negative Nb-Ta anomalies and low HREE concentrations. Mafic volcanic rocks from intracontinental arc-backarc settings, represented by the Okinawa Trough, have dipping REE patterns and intermediate negative Nb-Ta anomalies and overlap with the continental arc array.

3.4 Approach and Methods

Lithotectonic discrimination diagrams, such as those of Pearce (2014) and Ross and Bédard (2009), rely on a limited number of trace elements and trace element ratios that can be interpreted in non-unique ways. For example, the Zr/Y ratio is controlled by very slight differences in compatibility (Pearce and Norry, 1979), and the Nb/Yb ratio is strongly dependent on highly variable source depletion (Pearce, 2008). Th/Yb ratios reflect not only volatile input but also assimilation of subduction-related crust (Pearce, 2014). Increased Th may also be related to higher temperatures that are required to mobilize this element. These difficulties can be overcome by considering multiple trace element concentrations simultaneously, as we did in our study of oceanic rhyolites and dacites (Fassbender et al., 2023). We applied multivariate statistical techniques (PCA and agglomerative clustering) to identify and verify the geochemical differences between sample suites using multi-element data rather than individual element ratios. In this study we chose nine elements: Ti, Al, Ba, Th, Zr, Nb, La, Y, and Yb. All were recalculated to elemental concentrations in ppm and centered-log ratio (CLR) transformations were applied to overcome closure effects (Aitchison, 1982; see **Appendix B Table A2**). The PCA and clustering were performed with the R statistical software package (R Core Team 2020).

3.4.1 Principal components analysis

We used PCA to illustrate the minimum number of "components" that account for the largest variance in the data set (Bartholomew, 2010). Each principal component (PC) is affected by all the variables; the first and second components, PC1 and PC2, account for most of the variance in the data set (66% and 22% respectively; see **Appendix B Table A3**). The contribution of the different elements is described in terms of loadings of the element on each component. In **Figure 5**, the red labels represent the loadings of the elements for the entire data set (see **Appendix B Table A4**). The plotted points are individual sample scores in PC1-PC2 space, given in **Appendix B Table**

A5. Yb and Y have strong positive loadings on PC1, whereas Th and La have strong negative loadings, similar to the felsic volcanic rocks (Fassbender et al., 2022). Zr and Nb have strong positive loadings on PC2, whereas Ba and Al have strong negative loadings. The PCA shows very consistent behaviour among the mobile elements (e.g., Ba and La) and less mobile elements (Th and Al).

3.4.2 Agglomerative hierarchical clustering

To identify geochemically distinct groups of samples in the data set we used unsupervised agglomerative hierarchical clustering of the CLR-transformed data (**Appendix B Table A6**). This type of cluster analysis can identify subtle differences in geochemical signatures between sample types, particularly for volcanic rocks that show small but systematic variations between lithotectonic settings. In Fassbender et al. (2023), we performed cluster analysis on the PCA results for the felsic volcanic rocks, rather than the raw geochemical data. Here, we performed clustering on the CLR-transformed trace elements of the mafic volcanics, which yielded much better separation of individual clusters. The analysis was performed in R using the hierarchical clustering function "hclust". Agglomerative hierarchical clustering uses a set of queries to classify samples in a way that maximizes the differences between the groups. In this type of analysis, no pre-assigned groups or clusters are identified (i.e., the analysis is unsupervised). The analysis starts by assuming that every individual sample forms its own cluster, and then the statistical differences (or "distances") from all other samples are calculated. The two samples with the closest distance to each other form the next level of clusters. The distances are calculated using Ward's criterion, which determines the center of each cluster and then the sum of the squared distances of individuals from the center. Each sample was assigned to one cluster (Appendix Table A6). The smallest number of clusters representing all of the samples was determined using an iterative approach discussed below. The workflow is presented in **Appendix B Figure A3** and can be replicated with the code and instructions provided in the Appendix. Seven different clusters (C1-C7) were selected to train our classifier and are outlined in **Figures 5** and **6**.

3.4.3 Training a classifier

The results of the unsupervised clustering can be used to train a classifier. We did this by performing a supervised classification on the newly defined clusters identified above. We then conducted a blind test to determine if the classification scheme can accurately predict geodynamic influences in the mafic volcanic rock geochemistry. Supervised classification is a machine-learning task used for large data sets that sorts samples into known classes based on a "training" data set. The training is an iterative process by which a machine-learning classifier, such as random forest (RF), learns what elements achieve the best classification outcome and then builds a model that can be used as a classification scheme. Random forest has proven to be particularly useful for supervised classification based on multivariate data sets (Breiman, 2001; Fernandez-Delgado et al., 2014). The steps involve initial processing of the data to create the training set, training of the classifier, and then evaluation of its prediction success. The input is a selection of parameters (i.e., the analyzed elements) and the predetermined clusters (i.e., target classes). The starting database is randomly split into the training data set, used to build and validate the RF classifier, and the blind test data used to evaluate the prediction rate.

RF functions using multiple decision trees with true or false outcomes (e.g., "are SiO_2 concentrations <60 wt. % ?"; if yes, the sample is a mafic rock; if not, the sample is a felsic rock). The decision points are referred to as "nodes", and the cut-offs are determined by the classifier's ability to separate the training data. For example, the correct cut-off for SiO_2 is identified by testing several SiO_2 concentrations until the best separation of the clusters is achieved. "Pure" separation is achieved if the cut-off value of 60 wt.% SiO_2 correctly identifies all basalts. At every node, the "impurity" of the separation can be measured in terms of the probability of a parameter falsely classifying a sample. This is commonly determined using the "Gini index":

$$Gini(t) = \sum_{c=1}^{j} g_c(1 - g_c)$$

$$g_c = \frac{n_c}{n}$$

where “t” is the node in the decision tree (e.g., Ti), “c” is the target class, “j” refers to the possible classes, “g_c” is the relative frequency of classification, “n_c” is the number of samples belonging to target class “c”, and “n” is the total number of samples evaluated at this node. Nodes, or parameters (e.g., Ti), with a low Gini index have a high probability of correctly classifying a sample and therefore greater importance in making the decision.

Machine-learning classifiers may work very well with the training data but perform poorly in blind tests. Random forest overcomes this problem by using a large number of uncorrelated decision trees operating as a “committee” that casts votes for each decision. Many decision trees (100 to 1000) are created by randomly selecting elements from a training data set as the nodes. The least number of decision trees (usually 500 or more) is selected for the final random forest model. Typically, after this many decision trees, the performance of the classifier does not improve, and the smallest number is chosen to lower computational cost and minimize any potential artifacts in the data analysis. Each decision tree is then “trained” with randomly chosen samples equal to the total number of samples in the training data base, a method commonly known as “bootstrapping”. During this process samples can be picked multiple times, and a pool of samples that were not picked, and therefore not involved in training (so-called “out of bag” samples), is left behind. This is typically about 1/3 of all samples. These “out of bag” samples are used to validate the classification scheme (see below). To classify an unknown sample, each of the randomized decision trees casts a single “vote” for a single target class or cluster from the training set. The votes cast by all of the decision trees for each cluster are given in percentages (summing to 100%), and RF uses the majority vote to finally classify a sample (Breiman, 2001). A disadvantage of the RF classifier is that it will force a decision regarding the classification of a sample even if the sample does not match any of the target classes. Forced decisions commonly return a randomly distributed set of votes.

We selected 80% of our database at random (see **Appendix B Table A7**) to train and validate our RF classifier; the remaining 20% was used for the blind test (see **Appendix B Table A8**), which is a standard approach (Gholamy et al., 2018). We used the target classes identified by the unsupervised hierarchical clustering to train the classifier. Different numbers of samples assigned to the target classes in the training data set can create a class imbalance and lead to poor

performance of the classifier. To overcome this, we equalized the number of samples in each target class in the training set using the synthetic minority oversampling technique (SMOTE: Chawla et al., 2002). SMOTE randomly "removes" samples from classes with too many samples, and "creates" new samples for classes that have too few by slightly altering the geochemical composition of individual samples until each class contains the same number of samples. In our study, this resulted in a modified training set with 2288 samples (**Appendix B Table A9**).

To validate the model, we used the subset of samples remaining from the bootstrapping procedure (i.e., "out of bag" samples). 97.2% of the "out of bag" samples from all target classes were correctly classified (**Appendix B Table A10**). The probability of misclassification by a particular node, averaged over the entire RF classification scheme, is referred to as the Mean Decrease Gini. This parameter identified Nb, Th, Y, Yb, and Al as the most important variables in determining whether a sample is classified correctly (**Figure 7**). Nodes corresponding to La and Zr have low Mean Decrease Gini values and therefore less influence in the correct classification of a sample. We then conducted a blind test on the 20% of the original samples in the database that were not used in the training set (see **Appendix B Table A8**; none were created by SMOTE) to determine how well the classifier performs on new data. The test samples were correctly classified in almost every case, identifying 96% or 547 of 569 samples (**Appendix B Table A11**). To exclude any potential control of Ba mobility on the random forest classification we created a second classifier excluding Ba yielding almost identical results and correct classification of 93% or 530 of 569 samples (see **Appendix B Text** and **Appendix B Table A12**).

3.5 Results

We identified 7 target classes of mafic volcanic rocks from the modern oceans, corresponding to distinct geodynamic settings and different melting conditions. Based on these target classes, we constructed a RF classifier that accurately identifies rocks from those settings. Here, we discuss the tectonic and petrogenetic significance of the target classes, and then assess the application of the RF classifier to ancient volcanic rocks.

In the PCA, we interpreted the loadings on PC1 to represent different mantle sources, from depleted mid-ocean ridges to enriched ocean island settings, whereas the loadings on PC2 mainly reflect different melting regimes from dry melting at mid-ocean ridges and distal back-arc basin spreading centers to wet melting in near-arc environments. Mafic volcanic rocks from mid-ocean ridges and mature back-arc spreading centers have positive loadings on PC1 and PC2 (**Appendix B Table A5**) and belong to target class C1 (**Table 3** and **Appendix B Table A6**). These rocks have low Nb and La, typical of mid-ocean ridge magmas and an incompatible element-depleted mantle source. Mafic rocks from less-depleted mid-ocean ridges and back-arc spreading centers have intermediate positive loadings on PC1 and positive loadings on PC2 and belong to target class C2. Mafic rocks from enriched mid-ocean ridges and back-arc spreading centers have slightly negative loadings on PC1 and positive loadings on PC2 and belong to target class C3, with low to intermediate Nb and La. Mafic rocks from ocean island-like settings have negative loadings on PC1 and positive loadings on PC2 and belong to target class C4, with mantle sources that are highly enriched in incompatible elements (i.e., high Nb and La). Mafic rocks from immature back-arc rifts have small positive loadings on PC1 and negative loadings on PC2 and belong to target class C5, influenced by at least some fluid-fluxed melt components and having intermediate Al and Ba. Mafic rocks from arc volcanoes and arc-related rifts have intermediate loadings on PC1 and negative loadings on PC2 and belong to target class C6, reflecting mostly fluid-fluxed melts. These rocks have high Al and Ba, typical of island arcs. Finally, mafic volcanic rocks from nascent back-arc rifts, especially in continental margin settings, have small loadings on PC1 and negative loadings on PC2 and belong to target class C7, including both fluid-fluxed melt components and enriched mantle or crustal sources. These rocks have high Ba, Nb, Th and La, at least partly due to crustal contamination.

The cluster analysis illustrates the significant geodynamic control on the trace element signatures (**Figures 5**, **6**, and **8**): C1, C2 and C3 are mid-ocean ridge-like assemblages; C4 corresponds to ocean island-like assemblages; and C5-C7 correspond to arc and back-arc assemblages (**Table 3**). The type localities for clusters C1-C3 are the Juan de Fuca Ridge, East Pacific Rise, Galapagos Spreading Center, Pacific Antarctic Rise, Mid-Atlantic Ridge, South Indian Ridge as well as mature back-arc spreading centers such as the Central Lau Spreading Center (Lau Basin) and the Manus Spreading Center (Manus Basin). Samples in C1 (e.g., East Pacific Rise and Central Lau

Spreading Center) have very low La/Sm, La/Yb, Th/Yb, Nb/Yb, and Ba/Nb, and no negative Nb-Ta anomaly. Samples in C2 (e.g., Mid-Atlantic Ridge and Central Scotia back-arc spreading center) have low La/Sm, La/Yb, Th/Yb and Nb/Yb and very low Ba/Nb, with no negative Nb-Ta anomaly. Samples in C3 (e.g., Galapagos Spreading Center and Northwest Lau Spreading Center) have intermediate La/Sm, La/Yb, Th/Yb and Nb/Yb, very low Ba/Nb, and no negative Nb-Ta anomaly. The type localities for cluster C4 are the Samoa hotspot, Hawaii and the Marquesas Archipelago (ocean island settings), Ascension Island (a ridge-hotspot intersection), and other settings with ocean island-like signatures, such as the Mid-Atlantic Ridge north of Iceland. Samples in C4 have high La/Sm, La/Yb, Th/Yb and Nb/Yb, low Ba/Nb and no negative Nb-Ta anomaly. Samples in C5 include mafic volcanic rocks from the Myojin Rift (Izu-Bonin) and Ngatoroirangi Rift (Havre Trough), which have intermediate La/Sm, La/Yb and Th/Yb, low Nb/Yb, intermediate Ba/Nb, and moderate negative Nb-Ta anomalies. Samples from the Fonualei Rift and Spreading Center (Lau Basin) and the Tofua volcanic in C6 have intermediate La/Sm, high Th/Yb, low Nb/Yb, high Ba/Nb and strong negative Nb-Ta anomalies. Finally, samples from the nascent back-arc rift of the Northeast Lau Spreading Center (Lau Basin) and continental margin arc settings, such as the Bransfield Strait fall in C7 and have high La/Sm and Th/Yb, intermediate Nb/Yb and Ba/Nb, and moderate negative Nb-Ta anomalies. The results of training the RF classifier using these different clusters is discussed below.

3.6 Discussion

Highly variable melt sources and conditions, ranging from the thickness of the crust, to the composition of the sub-arc mantle wedge and mantle mixing (e.g., corner flow and incursion through slab tears and windows: Taylor and Martinez, 2003; Haase et al., 2009; Cooper et al., 2010; Price et al., 2017) all contribute to the overall complexity observed in modern oceanic basalts. It can be difficult to unravel all of the possible influences from just a few trace-element ratios. By using 9 elements simultaneously, even samples with a weak influence from subduction fluids (target class C5) can be distinguished from samples with a stronger influence (target class C6). We can also distinguish between truly arc-related assemblages (e.g., target class C5 and C6) from mafic volcanic suites that are only affected by crustal contamination, such as the Icelandic

basalts in target class C3 (Caracciolo et al., 2022: **Figure 4A**). Such distinctions often require difficult isotopic studies to unravel.

Although no prior knowledge of the geodynamic settings of the samples influenced the clustering, the classification outcome presented here corresponds closely to established geochemical characteristics associated with different melt sources. The most important are: the absence of negative Nb-Ta anomalies in target classes C1-C4, indicating no subduction-derived fluids; increasing La/Sm and Nb/Yb ratios from target class C1 to C4, indicating the transition from depleted mantle sources to enriched sources; negative Nb-Ta anomalies and LILE enrichments with low Th in target classes C5 and C6, related to subduction zone processes; and weak negative Nb-Ta anomalies and LILE enrichments but high Th in target class C7, with enriched-mantle components and crustal contamination. The increase in La/Sm and Nb/Yb ratios from C1 to C3 reflects undepleted mantle in C2 and more enriched mantle in C3, but they all lack high Ba/Nb and LILE (Pearce, 2008, Hofmann, 2014, White and Klein, 2014). Although the high La/Sm and Nb/Yb ratios are related mainly to enriched mantle sources (e.g., Haase et al., 2019), they may also be produced by different degrees of partial melting and variations in the depth of melting (Engel et al., 1965; Wanless and Shaw, 2012).

Mafic volcanic rocks in mid-ocean ridge-like settings and mature back-arc spreading centers, captured in target classes C1-C3, are products of decompression melting due to adiabatic rise of mantle material into mid-ocean ridge spreading centers (McKenzie and O`Nions, 1991, Hofmann, 2014). Although they all have depleted mantle sources with very low La/Sm, Nb/Yb and no negative Nb-Ta anomaly, the geochemical signatures are influenced by a range of melting conditions. Increased depth of melting can leave garnet in the melt residue, which results in depletion of Yb (Hofmann, 2014). The transition from C1-C3 to C4 reflects deep, low-degree partial melting of anhydrous depleted mantle, characteristic of hotspots and ocean island settings, that results in high La/Sm, high Nb/Yb and no negative Nb-Ta anomaly (van der Zander et al., 2010; Chauvel et al., 2012; Jicha et al., 2013; Haase et al., 2020). Melting that is influenced to different degrees by fluids from a dehydrating slab is captured in target classes C5, C6 and C7. In this case, the mafic volcanic rocks are products of mixing between hydrous melts derived from devolatilization of the downgoing slab and a water-poor mid-ocean ridge-like melt with negative

Nb-Ta anomalies and LILE enrichment compared to MOR basalts (Taylor and Martinez, 2003; Langmuir et al., 2006). Less fluid from the dehydrating slab at back-arc spreading centers distant from the volcanic arc, results in weak negative Nb-Ta anomalies, intermediate Ba/Nb, and low Th/Yb (Fretzdorff et al., 2006, Bezos et al., 2009), which is captured in target class C5. The large volatile fluxes above a dehydrating slab that result in strong negative Nb-Ta anomalies, high Ba/Nb and intermediate Th/Yb, characteristic of arc volcanoes and arc-related rifts (Keller et al., 2008, Escrig et al., 2012), are captured in target class C6. Arc rifting and initial back-arc spreading may be related to processes entirely within the upper plate (e.g., Tontini et al., 2019) or to complex mantle flow regimes related to the subducting slab (Heuret and Lallemand, 2005; Schellart, 2008). Finally, in nascent back-arc rifts and continental margin rifts, crustal assimilation produces the high Th/Yb and La/Sm (Fretzdorff et al., 2004, Haase et al., 2020) captured in target class C7.

3.6.1 A case study of the Lau basin

The Lau Basin is the type example of an intraoceanic back-arc basin and a key location to explore the geochemical variations in mafic volcanic rocks in response to subduction, microplate interactions, and mantle heterogeneity (Taylor et al., 1996; Keller et al., 2008; Yan et al., 2012; Sleeper and Martinez, 2016). It shows remarkable variations in arc- and non-arc petrogenesis that may be encountered in a single back-arc basin at scales of tens to just a few hundred kilometers. The V-shaped basin is ~450 km wide and ~1000 km in length (**Figure 9**). It is flanked by the active Tofua Arc in the east, the Lau Ridge remnant arc in the west and the Vitiaz lineament or fracture zone in the north (Hawkins, 1995). The opening of the basin, which began approximately 6 m.y. ago and has been propagating southward (Hawkins, 1995; Taylor et al., 1996), is accommodated by the Eastern Lau Spreading Center (ELSC) in the south, Valu Fa Ridge (VFR) and Central Lau Spreading Center (CLSC) in the middle, and the Fonualei Rift and Spreading Center (FRSC), Mangatolu Triple Junction (MTJ), Northeast Lau Spreading Center (NELSC), and the Northwest Lau Spreading Center (NWLSC) in the north. The southern part is tectonically simple, but the north is a complex mosaic of microplates that are variably influenced by the subduction of the Pacific Plate and large-scale transcurrent faulting (Stewart et al., 2022). In addition to the structural complexity, a number of researchers have suggested that the mantle below the back-arc region is characterized by complex flow regimes including contributions from the nearby Samoan mantle

plume (Pearce et al., 2007; Escrig et al., 2009, 2012; Price et al., 2014; Yan et al., 2020; Haase et al., 2022). Isotopic studies of Hf, Nd, Sr, and Pb indicate significant mantle mixing and crustal assimilation in the northeastern Lau Basin (Regelous et al., 2008; Tian et al., 2011; Price et al., 2014; Nebel and Arculus, 2015).

Mafic volcanic rocks from spreading centers closest to the Tofua arc (VFR and FRSC) have trace-element signatures that reflect the subduction, including strong negative Nb-Ta anomalies, low HREE, high LILE and high Ba/Nb ratios (**Figures 9** and **10**). Rocks from the Valu Fa Ridge show the greatest influence of volatiles from the dehydrating slab (Haase et al., 2009), indicated by the high Ba/Nb and Ba/Yb (**Figure 10**). With increasing distance from the slab, the amount of fluid that enters the melting regime decreases resulting in decreasing Ba/Nb, Ba/Yb, Th/Yb, and Th/Yb (**Figure 10**). Similarly, mafic rocks from the FRSC show decreasing influence of the arc (e.g., decreasing Ba/Nb) from south to north (**Figure 10**), while Th/Yb increases due to enriched mantle sources and potential assimilation of pre-existing arc crust. In contrast, the dominant source for melts along the CLSC and NWLSC is the Indian Ocean mantle, with only a minor subduction component (Tian et al., 2008). The MTJ, FRSC, ELSC and NELSC show a range of contributions from the slab, the modified mantle wedge, as well as Indian MORB (Yan et al., 2012; Zhang et al., 2018). Sampling of has revealed complex melt sources in a very small area, with mixing of depleted mantle, enriched mantle, and boninitic sources (Haase et al., 2022). The enriched mantle component, indicated by the high Nb/Yb in **Figure 10**, has been attributed to Samoan plume material crossing into the northern Lau Basin (Price et al., 2014), although this is debated (e.g., Falloon et al., 2008; Lupton et al., 2015; Nebel et al., 2018; Haase et al., 2022). Another possibility is that the enriched melts are related to the subduction of the Louisville Seamount Chain; another is assimilation of crustal material noted above (Beier et al., 2017; Price et al., 2017; Schönhofen, 2021). A contribution from the Samoan plume is also considered to be the source of the high Nb/Yb at the NWLSC and Rochambeau Rifts (RR) (Zhang et al., 2018). High He isotope ratios, which are a diagnostic feature of the Samoan plume, are well known in mafic melts in the NWLSC and RR (Lupton et al., 2009; Lupton et al., 2015). However, volcanic rocks from the FRSC and NELSC lack the He isotope anomaly. Boninitic melts from FRSC and NELSC, indicated by elevated SiO_2, low TiO_2 and low REE concentrations, reflect enhanced melting caused by a high

volatile flux from the subduction zone (Falloon et al., 2007; Regelous et al., 2008; Resing et al., 2011, Escrig et al., 2012).

Mafic volcanic rocks with these highly variable geochemical signatures have been dredged in almost every back-arc basin investigated in this study, including the western Manus Spreading Center, the Mariana back-arc spreading center, the East Scotia Ridge, and the Bransfield Strait (**Figure 4**). The locations of the anomalous samples are almost always at the terminations of the spreading centers, which are typically associated with complex mantle flow (Pearce and Stern, 2006). These locations are commonly affected by localized upwelling of mantle, mantle flow around the edges of the slab, and mantle mixing (**Figure 11**: Fretzdorff et al., 2002, 2004; Sinton et al., 2003; Pearce et al., 2005; Pearce and Stern, 2006; Beier et al., 2010; Haase et al., 2020). Strong toroidal flow has been proposed in the northern Lau Basin (Schellart and Moresi, 2013) and elsewhere (northern East Scotia Ridge: Fretzdorff et al., 2002). This has been the subject of analog and numerical modeling (Chen et al., 2016; Magni, 2019) that suggest flow through a slab tear at the northern termination of the Tonga Ridge is introducing fertile mantle into the back-arc region.

The different mantle domains that are suggested by the hierarchical clustering model and most reasonably interpreted in terms of the complex microplate architecture of the basin (**Figure 12**: Baxter et al., 2020; Schmid et al., 2020; Stewart et al., 2022). Enriched mantle material at the NWLSC and RR is reflected in the predominance of samples in target classes C2 and C3. Mafic volcanic rocks of the FRSC are mainly in target class C6, with a shift to target class C7 among the samples from the NELSC where there is less fluid-fluxed melting, enriched mantle sources and possible assimilation of crustal material. Low-degree partial melting of fertile mantle is also observed at several locations, producing OIB-like mafic volcanic rocks of target class C4.

3.6.2 Comparison with Archean mafic volcanic rocks

The volcanic and sedimentary rocks of the AGB are widely interpreted to be part of an intraoceanic arc-backarc system with similarities to modern oceanic microplate mosaics (Jackson et al., 1994; Percival et al., 2012; Wyman, 2013). However, other authors have suggested significant differences between Archean and post-Archean magmatism and tectonics, with some Archean terranes possibly having no modern analog (e.g., Bédard et al., 2013). Submarine volcanism in the AGB produced seven temporally distinct assemblages between 2795 and 2695 Ma, traditionally divided into the Northern and Southern Volcanic Zones (**Figure 13A**). We used the RF classifier developed in this paper to test whether Archean mafic volcanic rocks of the AGB can be classified along the same geochemical lines as modern samples and thereby possibly interpreted in terms of processes like those observed in the modern oceans. The comparison complements our earlier study of modern felsic volcanic rocks, which showed significant geochemical diversity similar to Archean rhyolites from the AGB (Fassbender et al., 2023).

We used data from Mole et al. (2021) and several datasets of the Ontario Geological Survey (MRD 378, 292, 362, 377, 393, 355, 085), the Geological Survey of Canada (Open File 6623) and the SIGEOM (Système d'information géominière of Québec). The samples include tholeiitic to calc-alkaline volcanic rocks from the Selbaie area, Geant-Dormant, and Joutel in the Northern Volcanic Zone (NVZ), dominantly tholeiitic rocks from the Matagami area, and tholeiitic to calc-alkaline volcanic rocks from from the Hunter Mine Group, Val-d'Or, Noranda, Bousquet, the western Blake River Group, and the Timmins-Porcupine area, including Kidd Creek and Kamiscotia, in the Southern Volcanic Zone (SVZ) (**Figure 13A**). These locations host some of the world's most important volcanogenic massive sulfide deposits (e.g., Franklin et al., 2005). 5746 samples were selected for the final database, following the same QA/QC applied to the modern volcanic rocks (see **Appendix B Text** and **Table A13**). Because the RF classifier uses elements that are mostly immobile (Ti, Al, Y, Zr, Nb, Ba, La, Yb, Th), effects of alteration are minimized, although the larger range of K_2O and Na_2O in the AGB samples (e.g., **Figure 2**) suggests that some altered samples are present.

The mafic volcanic rocks from the AGB are distinguished from modern ocean floor basalts by more variable K_2O and Na_2O, lower TiO_2 and flat to steeply dipping REE patterns. The larger range of Zr/TiO_2 could be related to higher temperatures, more contamination in the AGB, or a sampling bias. Extraction of melts from the Archean mantle required melting at very high temperatures under mostly dry melting conditions (Prior et al., 1999; Piercey, 2011; Thurston, 2015). However, examples of negative Nb-Ta anomalies and LILE enrichment, which are the dominant features of melting hydrated crust in modern submarine arcs, are found in every assemblage of the AGB (Ayer et al., 2002). Samples of mafic volcanic rocks from the Val-d'Or formation, for example, have strong negative Nb-Ta anomalies, low REE concentrations and LILE enrichment (**Figure 14**), interpreted to indicate an arc-like regime (Scott et al., 2002). Samples from Noranda have overall weaker negative Nb-Ta anomalies with slightly dipping REE patterns that have been interpreted as originating in a back-arc regime (e.g., Yang and Scott, 2003). Samples from north east of Matagami lack negative Nb-Ta anomalies and LILE enrichment, and they have significantly higher REE concentrations that have been attributed melt generation at an oceanic spreading center (Hart et al., 2004). The weak negative Nb-Ta anomalies and higher Th concentrations in Abitibi mafic volcanic rocks are commonly cited as important differences compared to basalts from modern oceanic subduction zones (Bédard et al., 2013). Arc-like geochemical signatures could have been created in a number of different ways, including assimilation of hydrated basalt (e.g., amphibolite containing altered crustal components) and/or ilmenite fractionation (e.g., Haase et al., 2005; Pearce, 2008; Mole et al., 2021). The example of Icelandic basalts perhaps bests illustrates this. They have high Th/Yb and plot close to the continental arc field in the lithotectonic discrimination diagram of Pearce (2014) (**Figure 4B**), although they lack the Ba enrichment that is typical for arc-like rocks. Mafic volcanic rocks nearly identical to those from the Eastern Blake River Group, also occur at the terminations of modern back-arc spreading centers (e.g., in the NELSC, the southern East Scotia Ridge, the western Bransfield Strait, and the southern and northern Mariana Trough: **Figures 4** and **14**). Similar rocks are clearly identified in the AGB by the RF classifier developed from modern oceanic basalts.

In the AGB data set, Nb, Ba, Yb, Y and Th had the greatest influence on the classification of the rocks by RF. Of the 5746 samples in the database, 1065 were not classified (i.e., no class received more than 50% of the votes). This indicates either fundamental differences from modern oceanic mafic volcanic rocks or geochemical variation due to alteration and metamorphism. The remaining 4681 samples were assigned to a target class comparable to that of modern oceanic basalts. Rocks belonging to C2, C3, C5, C6, and C7 were confidently identified in the AGB data set (**Appendix B Table A14**). They can be broadly divided into two groups, which in the modern classification would correspond to dry melting (C2 and C3) and wet melting conditions (C5, C6, and C7: **Figure 13B**). The latter could be interpreted as dehydration of hydrated basalts in a downgoing slab or, in other models, hydrated basaltic crust that sank into the mantle during delamination. None of the samples were fully classified (100% of the votes) into C1 (i.e., depleted mid-ocean ridges) or C4 (i.e., ocean island settings). Samples from Kidd Creek were classified as belonging to target class C2 and C3, indicating similarities to ridge-hotspot intersections, such as Iceland, as previously suggested by Prior et al. (1999). The samples from the Blake River Group (and Noranda specifically) show greater geochemical variability. Samples from the western part of the Blake River Group are mostly classified in C2 (i.e., undepleted mid-ocean ridge volcanic suites), whereas samples from the Eastern Blake River Group and Noranda are mostly classified in C7. The latter are most similar to mafic volcanic rocks from nascent back-arc rifts as in the NELSC and the eastern Manus Basin, as previously suggested by Yang and Scott (2003). A high proportion of mafic volcanic rocks in the Bousquet and Val d'Or districts were classified in target classes C5, C6 and C7 (i.e., intraoceanic back-arc and arc-related rifts). This is in agreement with previous studies characterizing the Val-d'Or formation as arc-like crust (Scott et al., 2002).

Conclusions

We compared the major and trace element geochemistry of modern submarine mafic volcanic rocks from different geodynamic settings using PCA, agglomerative hierarchical clustering, and random forest. Automated hierarchical clustering reveals significant geochemical diversity related to mantle heterogeneity, highly variable melting regimes, and contributions of fluids from the subducting slab. Back-arc basalt and mid-ocean ridge-like mafic volcanic rocks, such as at the NWLSC and the Pacific Antarctic Rise, as well as ridge-hotspot intersections such as in Iceland, all share enriched mantle signatures typical of spreading centers far from any subduction. However, significant variation in the trace element geochemistry is found in complex microplate mosaics at very small scales (e.g., distances of less than 100 km along the FRSC and the NELSC). The greatest diversity occurs at the terminations or propagating tips of back-arc spreading centers, such as the NELSC, the northern and southern East Scotia Ridge and the northern and southern Mariana Trough, owing to complex mantle flow regimes.

Comparisons with mafic volcanic rocks of the AGB indicate magmas generated above the hot Archean mantle were most similar geochemically to those of modern back-arc spreading centers with weak arc-signatures and enriched mantle sources, similar to the NWLSC of the Lau Basin and, in the open ocean, similar to the Pacific Antarctic Rise and Iceland. The mafic volcanic rocks from these settings bear a strong similarity to volcanic rocks from north east of Matagami and Kidd Creek. Significant variations in mafic rock compositions in the AGB, including in the Eastern Blake River Group at Noranda and at Val d'Or, occur at about the same scale as in the northern Lau Basin. We interpret these variations to reflect mantle heterogeneity and mantle flow regimes influenced by microplate formation. The ability to recognize modern analogs of different mantle sources and melt regimes in greenstone belts raises the possibility of improved area selection for mineral exploration, focussing on the enhanced magmatic productivity of back-arc spreading centers with enriched mantle sources, at the terminal or propagating tips of arc-related rifts, and at ridge-hotspot intersections where mantle upwelling likely provided the heat for melting.

Acknowledgments

We thank two anonymous referees for the helpful comments that improved the manuscript. This research was funded by the Canada First Research Excellence Fund (CFREF, Metal Earth at Laurentian University) and the Marine Mineral Resources Group at the GEOMAR Helmholtz Centre for Ocean Research Kiel. The Natural Sciences and Engineering Research Council of Canada (NSERC), the Helmholtz Association, and the German Ministry of Science and Education (BMBF, grant 03G0267) are acknowledged for the support of this work through research grants to the authors. The project was also supported by the NSERC Collaborative Research and Training Experience program (iMAGE-CREATE) on Marine Geodynamics and Georesources.

References

Aitchison, J., 1982, The statistical analysis of compositional data: Journal of the Royal Statistical Society: Series B (Methodological), v. 44, p. 139-160.

Arculus, R.J., Gurnis, O., Ishizuka, O., Reagan, M.K., Pearce, J.A., and Sutherland, R., 2019, How to Create New Subduction Zones: A Global Perspective: Oceanography, v. 32, p. 160-174.

Arevalo, R. and McDonough, W. F., 2010, Chemical variations and regional diversity observed in MORB: Chemical Geology, v. 271, p. 70-85.

Ayer, J., Amelin, Y., Corfu, F., Kamo, S., Ketchum, J., Kwok, K., and Trowell, N., 2002, Evolution of the southern Abitibi greenstone belt based on U-Pb geochronology: autochthonous volcanic construction followed by plutonism, regional deformation and sedimentation: Precambrian Research, v. 115, p. 63-95.

Bartholomew, D. J., 2010, Principal Components Analysis, in Peterson et al., ed., International Encyclopedia of Education, 3rd ed: Elsevier Science, p 374-377.

Baxter, A.T., Hannington, M.D., Stewart, M.S., Emberley, J.M., Breker, K., Krätschell, A., Petersen, S., Brandl, P.A., Klischies, M., Mensing, R., and Anderson, M.O., 2020, Shallow seismicity and the classification of structures in the Lau back-arc basin: Geochemistry, Geophysics, Geosystems, v. 21, e2020GC008924, p 25.

Bédard, J.H., Harris, L.B., and Thurston, P.C., 2013, The hunting of the snArc: Precambrian Research, v. 229, p. 20-48.

Beier, C., Turner, S.P., Sinton, J.M., and Gill, J.B., 2010, Influence of subducted components on back-arc melting dynamics in the Manus Basin: Geochemistry, Geophysics, Geosystems, v. 11, article Q0AC03, p. 21.

Beier, C., Bach, W., Turner, S., Niedermeier, D., Woodhead, J., Erzinger, J., and Krumm, S., 2015, Origin of silicic magmas at spreading centres – an example from the South East Rift, Manus Basin: Journal of Petrology, v. 56, p. 255-272.

Beier, C., Turner, S.P., Haase, K.M., Pearce, A.J., Münker, C., and Regelous, M., 2017, Trace element and isotope geochemistry of the northern and central Tongan Islands with an emphasis on the genesis of high Nb/Ta signatures at the northern volcanoes of Tafahi and Niuatoputapu: Journal of Petrology, v. 58, p. 1073-1106.

Bézos, A., Escrig, S., Langmuir, C.H., Michael, P.J., and Asimow, P.D., 2009, Origins of chemical diversity of back-arc basin basalts: A segment-scale study of the Eastern Lau spreading center: Journal of Geophysical Research, v. 114, article B06212, p. 33.

Breiman, L., 2001, Random Forests: Machine Learning, v. 45, p. 5-32.

Caracciolo, A., Halldórsson, S.A., Bali, E., Marshall, E.W., Jeon, H., Whitehouse, M.J., Barnes, J.D., Guofinnsson, G.H., Kahl, M., and Hartley, M.E., Oxygen isotope evidence for progressively assimilating trans-crustal magma plumbing systems in Iceland: Geology, v. 50, p. 796-800.

Castillo, P.R., 2012, Adakite petrogenesis: Lithos, v. 134-135, p. 304-316.

Chauvel, C., Maury, R.C., Blais, S., Lewin, E., Guillou, H., Guille, G., Rossi, P., and Gutscher, M.-A., 2012, The size of plume heterogeneities constrained by Marquesas isotopic stripes: Geochemistry, Geophysics, Geosystems, v. 13, Q07005, p. 23.

Chawla, N. V., Bowyer, K. W., Hall, L. O., and Kegelmeyer, W. P., 2002, SMOTE: Synthetic minority over-sampling technique: Journal of Artificial Intelligence Research, v. 16, p. 321-357.

Chen, Z., Schellart, W.P., Strak, V., and Duarte, J.C., 2016, Does subduction-induced mantle flow drive backarc extension?: Earth and Planetary Science Letters, v. 441, p. 200-210.

Cooper, L.B., Plank, T., Arculus, R.J., Hauri, E.H., Hall, P.S., and Parman, S.W., 2010, High-Ca boninites from the active Tonga Arc: Journal of Geophysical Research, v. 115, p. 1-23.

Dubé, B., and Mercier-Langevin, P., 2020, Gold Deposits of the Archean Abitibi Greenstone Belt, Canada, in Sillitoe, R.H., Goldfarb, R.J., Robert, F., and Simmons, S.F., ed., Geology of the World's Major Gold Deposits and Provinces: Special Publications of the Society of Economic Geologists, p. 669-708.

Engel, A.E.J., Engel, C.G., and Havens, R.G., 1965, Chemical characteristics of oceanic basalts and the upper mantle: Geological Society of America Bulletin, v.76, p. 719-734.

Escrig, S., Bézos, A., Goldstein, S.L., Langmuir, C.H., and Michael, P.J., 2009, Mantle source variations beneath the Eastern Lau Spreading Center and the nature of subduction components in the Lau basin-Tonga arc system: Geochemistry, Geophysics, Geosystems, v.10, Q04014, p. 33.

Escrig, S., Bézos, A., Langmuir, C.H., Michael, P.J., and Arculus, R., 2012, Characterizing the effect of mantle source, subduction input and melting in the Fonualei spreading center, Lau

basin: Constraints on the origin of the boninitic signature of the back-arc lavas: Geochemistry, Geophysics, Geosystems, v. 13, Q10008, p. 29.

Falloon, T.J., Danyushevsky, L.V., Crawford, T.J., Maas, R., Woodhead, J.D., Eggins, S.M., Bloomer, S.H., Wright, D.J., Zlobin, S.K., and Stacey A.R., 2007, Multiple mantle plume components involved in the petrogenesis of subduction-related lavas from the northern termination of the Tonga Arc and northern Lau Basin: Evidence from the geochemistry of arc and backarc submarine volcanics: Geochemistry, Geophysics, Geosystems, v. 8, Q09003, p. 45.

Falloon, T.J., Danyushevsky, L.V., Crawford, A.J., Meffre, S., Woodhead, J.D., and Bloomer, S.H., 2008, Boninites and adakites from the northern termination of the Tonga trench: Implications for adakite petrogenesis: Journal of Petrology, v. 49, p. 697-715.

Fassbender, M.L., Hannington, M., Stewart, M., Brandl, P.A., Baxter, A.T., and Diekrup, D., 2023, Geochemical signatures of felsic volcanic rocks in modern oceanic settings and implications for archean greenstone belts: Economic Geology, v, 118, p. 319-345.

Franklin, J.M., Gibson, H.L., Jonasson, I.R., and Galley, A.G., 2005, Volcanogenic massive sulfide deposits: Economic Geology, v. 100, p. 523-560.

Fretzdorff, S., Livermore, R.A., Devey, C.W., Leat, P.T., and Stoffers, P., 2002, Petrogenesis of the back-arc East Scotia Ridge, South Atlantic Ocean: Journal of Petrology, v. 43, p. 1435-1467.

Fretzdorff, S., Worthington, T.J., Haase, K.M., Hekinian, R., Franz, L., Keller, R.A., and Stoffers, P., 2004, Magmatism in the Bransfield basin: Rifting of the south Shetland arc?: Journal of Geophysical Research, v. 109, B12208, p. 17.

Fretzdorff, S., Schwarz-Schampera, U., Gibson, H.L., Garbe-Schönberg, C.-D., Hauff, F., and Stoffers, P., 2006, Hydrothermal activity and magma genesis along a propagating back-arc basin: Valu Fa ridge (southern Lau basin): Journal of Geophysical Research, v. 111, article B08205.

Gale, A., Dalton, C.A., Langmuir, C.H., Su, Y., and Schilling, J.-G., 2013, The mean composition of ocean ridge basalts: Geochemistry, Geophysics, Geosystems, v. 14, p. 489-518.

Galley, A.G., Watkinson, D.H., Jonasson, I.R., and Riverin, G., 1995, The subsea-floor formation of volcanic-hosted massive sulfide: Evidence from the Ansil Deposit, Rouyn-Noranda, Canada: Economic Geology, v. 90, p. 2006-2017.

Gholamy, A., Kreinovich, V., and Kosheleva, O., 2018, Why 70/30 or 80/20 relation between training and testing sets: A pedagogical explanation: Departmental Technical Reports (CS), 1209 (https://scholarworks.utep.edu/cs_techrep/1209).

Gibson, H.L., Allen, R.L., Riverin, G., and Lane, T.E., 2007, The VMS Model: Advances and application to exploration targeting: Proceedings of Exploration, v. 7, p. 713-730.

Golowin, R., Portnyagin, M., Hoernle, K., Hauff, F., Gurenko, A., Garbe-Schönberg, D., Werner, R., and Turner, S., 2017, Boninite-like intraplate magmas from Manihiki Plateau require ultra-depleted and enriched source components: Nature Communications, v. 8, 14322, p. 10.

Haase, K.M., Stroncik, N., Hekinian, R., and Stoffers, P., 2005, Nb-depleted andesites from the Pacific-Antarctic Rise as analogs for early continental crust: Geological Society of America, v. 33, p. 921-924.

Haase, K.M., Fretzdorff, S., Mühe, R., Garbe-Schönberg, D., and Stoffers, P., 2009, A geochemical study of off-axis seamount lavas at the Valu Fa Ridge: Constraints on magma genesis and slab contributions in the southern Tonga subduction zone: Lithos, v. 112, p. 137-148.

Haase, K.M., Beier, C., and Kemner, F., 2019, A comparison of the magmatic evolution of Pacific intraplate volcanoes: Constraints on melting in mantle plumes: Frontiers in Earth Science, v. 6, p. 13.

Haase, K.M., Gress, M.U., Lima, S.M., Regelous, M., Beier, C., Romer, R.L., and Bellon, H., 2020, Evolution of magmatism in the New Hebrides island arc and in initial back-arc rifting, SW Pacific: Geochemistry, Geophysics, Geosystems, v. 21, e2020GC008946, p. 21.

Haase, K.M., Schönhofen, M.V., Storch, B., Beier, C., Regelous, M., Rubin, K., and Brandl, P.A., 2022, Effects of the hydrous domain in the mantle wedge on magma formation and mixing at the Northeast Lau Spreading Center, SW Pacific: Geochemistry, Geophysics, Geosystems, v. 23, e2021GC010066, p. 22.

Haraguchi, S., Kimura, J.-I., Senda, R., Fujinaga, K., Nakamura, K., Takaya, Y., and Ishii, T., 2017, Origin of felsic volcanism in the Izu arc intra-arc rift: Contributions to Mineral Petrology, v. 172, p. 1-25.

Hart, T.R., Gibson, H.L., and Lesher, C.M., 2004, Trace element geochemistry and petrogenesis of felsic volcanic rocks associated with volcanogenic massive Cu-Zn-Pb sulfide deposits: Economic Geology, v. 99, p. 1003-1013.

Hawkesworth, C., Gallagher, K., Hergt, J.M., and McDermott, F., 1993, Mantle and slab contributions in arc magmas: Annual Review of Earth and Planetary Sciences, v. 21, p. 175-204.

Hawkins, J. W., 1995, The Geology of the Lau Basin, in Taylor, B., ed., Backarc Basins: Tectonics and Magmatism. Springer US, p, 63-138.

Heuret, A., and Lallemand, S., 2005, Plate motions, slab dynamics and back-arc deformation: Physics of the Earth and Planetary Interiors, v. 149, p. 31-51.

Hofmann, A.W., 2014, Sampling mantle heterogeneity through oceanic basalts: Isotopes and trace elements, in Holland, H. D. and Turekian, K. K., ed., Treatise on Geochemistry, 2nd ed.: Elsevier, p. 67-101.

Jackson, M.G., Hart, S.R., Konter, J.G., Koppers, A.A.P., Staudigel, H., Kurz, M.D., Blusztajn, J., and Sinton, J.M., 2010, Samoan hot spot track on a "hot spot highway": Implications for mantle plumes and a deep Samoan mantle source: Geochemistry, Geophysics, Geosystems, v. 11, Q12009, p. 24.

Jackson, S.L., Fyon, A., and Corfu, F., 1994, Review of Archean supracrustal assemblages of the southern Abitibi greenstone belt in Ontario, Canada: Products of microplate interaction within a large-scale plate-tectonic setting: Precambrian Research, v. 65, p. 183-205.

Jenner, F.E., Arculus, R.J., Mavrogenes, J.A., Dyriw, N.J., Nebel, O., and Hauri, E.H., 2012, Chalcophile element systematics in volcanic glasses from the northwestern Lau Basin: Geochemistry, Geophysics, Geosystems, v. 13, Q06014, p. 25.

Jicha, B.R., Singer, B.S., and Valentine, M.J., 2013, $^{40}Ar/^{39}Ar$ geochronology of subaerial Ascension Island and a re-evaluation of the temporal progression of basaltic to rhyolitic volcanism: Journal of Petrology, v. 54, p. 2581-2596.

Keller, N.S., Arculus, R.J., Hermann, J., and Richards, S., 2008, Submarine back-arc lava with arc signature: Fonualei Spreading Center, northeast Lau Basin, Tonga: Journal of Geophysical Research: Solid Earth v. 113, B08S07, p. 28.

Keller, R.A., Fisk, M.R., Smellie, J.L., Strelin, J.A., and Lawver, L.A., 2002, Geochemistry of backarc basin volcanism in Bransfield Strait, Antarctica: Subducted contributions and along-axis variations: Journal of Geophysical Research, v. 107, article B8, 2171.

Kerrich R., and Wyman, D.A., 1997, Review of developments in trace-element fingerprinting of geodynamic settings and their implications for mineral exploration: Australian Journal of Earth Sciences v. 44, p. 465-487.

Kerrich, R., Wyamn, D., Fan, J., and Bleeker, W., 1998, Boninite series: low Ti-tholeiite associations from the 2.7 Ga Abitibi greenstone belt: Earth and Planetary Science Letters, v. 164, p. 303-316.

Langmuir, C.H., Bézos, A., Escrig, S., and Parman, S.W., 2006, Chemical systematics and hydrous melting of the mantle in back-arc basins, in Christie, D.M., Fisher, C.R., Lee, S.-M., and Givens, S., ed., Back-arc Spreading Systems: Geological, Biological, Chemical, and Physical Interactions: Washington, D. C., American Geophysical Union, Geophysical Monograph 166, p. 87-146.

Le Maitre, R.W., 1989, A classification of igneous rocks and glossary of terms: Recommendations of the International Union of Geological Sciences, Subcommission on the Systematics of Igneous Rocks: Oxford, Blackwell Scientific Publications, 193 p.

Lesher, C.M., Goodwin, A.M., Campbell, I.H., and Gorton, M.P., 1986, Trace-element geochemistry of ore-associated and barren, felsic metavolcanic rocks in the Superior Province, Canada: Canadian Journal of Earth Sciences, v. 23, p. 222-237.

Lupton, J., Rubin, K.H., Arculus, R., Lilley, M., Butterfield, D., Resing, J., Baker, E., and Embley, R., 2015, Helium isotope, C/^{3}He, and Ba-Nb-Ti signatures in the northern Lau Basin: Distinguishing arc, back-arc, and hotspot affinities: Geochemistry, Geophysics, Geosystems, v. 16, p. 1133-1155.

Lupton, J.E., Arculus, R.J., Greene, R.R., Evans, L.J., and Goddard, C.I., 2009, Helium isotope variations in seafloor basalts from the Northwest Lau Backarc Basin: Mapping the influence of the Samoan hotspot: Geophysical Research Letters, v. 36, L17313.

Lytle, M.L., Kelley, K.A., Hauri, E.H., Gill, J.B., Papia, D., and Arculus, R.J., 2012, Tracing mantle sources and Samoan influence in the northwestern Lau back-arc basin: Geochemistry, Geophysics, Geosystems, v. 13, article Q10019.

Magni, V., 2019, The effects of back-arc spreading on arc magmatism: Earth and Planetary Science Letters, v. 519, p. 141-151.

McKenzie, D., and O`Nions, R.K., 1991, Partial melt distribution from inversion of rare earth element concentrations: Journal of Petrology, v. 32, p. 1021-1091.

Michael, P.J., and Cornell, W.C., 1998, Influence of spreading rate and magma supply on crystallization and assimilation beneath mid-ocean ridges: Evidence from chlorine and major element chemistry of mid-ocean ridge basalts: Journal of Geophysical Research, v. 103, p. 18325-18356.

Mole, D.R., Frieman, B.M., Thurston, P.C., Marsh, J.H., Jorgensen, T.R.C., Stern, R.A., Martin, L.A.J., Lu, Y.J., and Gibson, H.L., 2022, Crustal architecture of the south-east Superior Craton and controls on mineral systems: Ore Geology Reviews, v. 148, 105017, p. 34.

Mole, D.R., Thurston, P. C., Marsh, J.H., Stern, R.A., Ayer, J.A., Martin, L.A.J., and Lu, Y.J., 2021, The formation of Neoarchean continental crust in the south-east Superior Craton by two distinct geodynamic processes: Precambrian Research, v. 356, 106104, p. 23.

Monecke, T., Mercier-Langevin, P., Dubé, B., and Frieman, B.M., 2017, Geology of the Abitibi Greenstone Belt, Canada: Reviews in Economic Geology, v. 19, p. 7-49.

Monecke, T., Gibson, H.L., and Goutier, J., 2017, Volcanogenic massive sulfide deposits of the Noranda camp: Reviews in Economic Geology, v. 19, p. 169-223.

Nebel, O., Sossi, P.A., Foden, J., Bénard, A., Brandl, P.A., and Stammeier, J.A., 2018, Iron isotope variability in ocean floor lavas and mantle sources in the Lau back-arc basin: Geochimica et Cosmochimica Acta, v. 241, p. 150-163.

Nebel, O., and Arculus, R.J., 2015, Selective ingress of a Samoan plume component into the northern Lau backarc basin. Nature Communications v. 6, 6554, p. 7.

Palin, R.M., Santosh, M., Cao, W., Li, S.-S., Hernández-Uribe, D., and Parsons, A., 2020, Secular change and the onset of plate tectonics on Earth: Earth-Science Reviews, v. 207, 103172, p. 41.

Paradis, S., Ludden, J., and Gelinas, L., 1988, Evidence of contrasting compositional spectra in comagmatic intrusive and extrusive rocks of the late Archean Blake River Group, Abitibi, Quebec: Canadian Journal of Earth Sciences, v. 25, p. 134-144.

Park, J.-W., Campbell, I.H., Kim, j., and Moon, J.-W., 2015, The role of late sulfide saturation in the formation of a Cu- and Au-rich magma: Insights from the platinum group element geochemistry of Niuatahi-Motutahi lavas, Tonga rear arc: Journal of Petrology, v. 56, p. 59-81.

Pearce, J.A., and Norry, M.J., 1979, Petrogenetic implications of Ti, Zr, Y, and Nb variations in volcanic rocks: Contributions to Mineralogy and Petrology, v. 69, p. 33-47.

Pearce, J.A., 1996, A user`s guide to basalt discrimination diagrams, in Wyman, D.A., ed., Trace element geochemistry of volcanic rocks: Applications for massive sulphide exploration: Geological Association of Canada, Short Course Notes, v. 12, p. 79-113.

Pearce, J.A., Stern, R.J., Bloomer, S.H., and Fryer, P., 2005, Geochemical mapping of the Mariana arc-basin system: Implications for the nature and distribution of subduction components: Geochemistry, Geophysics, Geosystems, v. 6, Q07006, p. 27.

Pearce, J.A., Kempton, P.D., and Gill, J.B., 2007, Hf–Nd evidence for the origin and distribution of mantle domains in the SW Pacific: Earth and Planetary Science Letters, v. 260, p. 98-114.

Pearce, J.A., 2008, Geochemical fingerprinting of oceanic basalts with applications to ophiolite classification and the search for Archean oceanic crust: Lithos, v. 100, p. 14-48.

Pearce, J.A., 2014, Immobile element fingerprinting of ophiolites: Elements v. 10, p. 101-108.

Pearce, J.A., and Arculus, R.J., 2020, Boninites. In, Alderton, D., and Scott, A.E., ed., Encyclopedia of Geology, 2nd ed.: American press, p. 113-129.

Pearce, J.A., and Reagan, M.K., 2019, Identification, classification, and interpretation of boninites from Anthropocene to Eoarchean using Si-Mg-Ti systematics: Geosphere v. 15, p. 1008-1037.

Pearce, J.A., and Stern, R.J., 2006, Origin of back-arc basin magmas: Trace element and isotope perspectives, in Christie, D.M., Fisher, C R., Lee, S.-M. and Givens, S., ed., Back-Arc Spreading Systems: Geological, Biological, Chemical, and Physical Interactions: American Geophysical Union, p. 63-86.

Percival, J. A., Skulski, T., Sanborn-Barrie, M., Stott, G. M., Leclair, A. D., Corkery, M. T., and Boily, M., 2012, Geology and tectonic evolution of the Superior Province, Canada, Tectonic styles in Canada: The Lithoprobe Perspective, Geological Association of Canada, Special Paper, 49, p. 321-378.

Perfit, M.R., and Davidson, J.P., 2000, Plate tectonics and volcanism, in Sigurdsson, H., Houghton, B.F., McNutt, S.R., Rymer, H., Stix, J., and Ballard, R.D., eds., Encyclopedia of volcanoes: San Diego, CA, Academic Press, p. 89–113.

Piercey, S.J., 2011, The setting, style, and role of magmatism in the formation of volcanogenic massive sulfide deposits: Mineralium Deposita, v. 46, p. 449-471.

Price, A.A., Jackson, M.G., Blichert-Toft, J., Hall, P.S., Sinton, J.M., Kurz, M.D., and Blusztajn, J., 2014, Evidence for a broadly distributed Samoan-plume signature in the northern Lau and North Fiji Basins: Geochemistry, Geophysics, Geosystems, v. 15, p. 986-1008.

Price, A.A., Jackson, M.G., Blichert-Toft, J., Blusztajn, J., Conatser, C.S., Konter, J.G., Koppers, A.A.P., and Kurz, M.D., 2016, Geochemical evidence in the northeast Lau Basin for

subduction of the Cook-Austral volcanic chain in the Tonga Trench: Geochemistry, Geophysics, Geosystems, v. 17, p. 1694-1724.

Price, A.A., Jackson, M.G., Blichert-Toft, J., Kurz, M.D., Gill, J., Blusztajn, J., Jenner, F., Brens, R., and Arculus, R., 2017, Geodynamic implications for zonal and meridional isotopic patterns across the northern Lau and North Fiji Basins: Geochemistry, Geophysics, Geosystems, v. 18, p. 1013-1042.

Prior, G.J., Gibson, H.L., Watkinson, D.H., Cook, R.E., and Hannington, M.D., 1999, Rare earth and high field strength element geochemistry of the Kidd Creek rhyolites, Abitibi greenstone belt, Canada: Evidence for Archean felsic volcanism and massive sulfide ore formation in an Iceland-style rift environment: Economic Geology, Monograph 10, p. 457-484.

R Core Team 2020, R: A language and environment for statistical computing: R Foundation for Statistical Computing, Vienna, Austria. (https://www.R-project.org).

Regelous, M., Turner, S., Falloon, T.J., Taylor, P., Gamble, J., and Green, T., 2008, Mantle dynamics and mantle melting beneath Niuafo'ou Island and the northern Lau back-arc basin. Contributions to Mineralogy and Petrology, v. 156, p. 103-118.

Resing, J.A., Rubin, K.H., Embley, R.W., Lupton, J.E., Baker, E.T., Dziak, R.P., Baumberger, T., Lilley, M.D., Huber, J.A., Shank, T.M., Butterfield, D.A., Clague, D.A., Keller, N.S., Merle, S.G., Buck, N.J., Michael, P.J., Soule, A., Caress, D.W., Walker, S.L., Davis, R., Cowen, J.P., Reysenback, A.-L., and Thomas, H., 2011, Active submarine eruption of boninite in the northeastern Lau Basin: Nature Geoscience, v. 4, p. 799-806.

Ross, P.S., and Bédard, J.H., 2009, Magmatic affinity of modern and ancient subalkaline volcanic rocks determined from trace-element discriminant diagrams: Canadian Journal of Earth Sciences, v. 46, p. 823-839.

Ryan, W.B.F., Carbotte, S.M., Coplan, J. O., O'Hara, S., Melkonian, A., Arko, R., Weissel, R.A., Ferrini, V., Goodwillie, A., Nitsche, F., Bonczkowski, J., and Zemsky, R., 2009, Global multi-resolution topography synthesis. Geochemistry Geophysics Geosystems 10, Q03014, p. 9.

Schellart, W.P., 2008, Subduction zone trench migration: Slab driven or overriding-plate-driven?: Physics of the Earth and Planetary Interiors, v. 170, p. 73-88.

Schelart, W.P., and Moresi, L., 2013, A new driving mechanism for backarc extension and backarc shortening through slab sinking induced toroidal and poloidal mantle flow: Results from dynamic subduction models with an overriding plate: Journal of Geophysical Research, v. 118, p. 3221-3248.

Schellart, W.P., 2020, Control of subduction tone age and size on flat slab subduction. Frontiers in Earth Science v. 8, p. 18.

Schmid, F., Kopp, H., Schnabel, M., Dannowski, A., Heyde, I., Riedel, M., Hannington, M.D., Engels, M., Beniest, A., Klaucke, I., Augustin, N., Brandl, P.A., Devey, C., 2020, Crustal structure and evolution of the Niuafo'ou Microplate in the northeastern Lau Basin, Southwestern Pacific: Journal of Geophysical Research, Solid Earth, v. 125, doi: 10.1029/2019JB019184, 21 p.

Schmidt, M.W., and Poli, S., 2014, Devolatilization during subduction, in Holland, H.D. and Turekian, K.K., ed., Treatise on Geochemistry, 2nd ed.: Elsevier, p. 669-701.

Schönhofen, M.V., 2021, Melting and source variability in the Tonga-Kermadec Lau arc-backarc system: Doctoral thesis.

Scott, C.R., Mueller, W.U., and Pilote, P., 2002, Physical volcanology, stratigraphy, and lithogeochemistry of an Archean volcanic arc: evolution from plume-related volcanism to arc rifting of SE Abitibi Greenstone Belt, Val d'Or, Canada: Precambrian Research, v. 115, p. 223-260.

Sdrolias, M., and Müller, R., D., 2006, Controls on back-arc basin formation. Geochemistry, Geophysics, Geosystems v. 7, Q04016, p. 40.

Sinton, J.M., Ford, L.L., Chappell, B., and McCulloch, M.T., 2003, Magma genesis and mantle heterogeneity in the Manus back-arc basin, Papua New Guinea: Journal of Petrology, v. 44, p. 159-195.

Sleeper, J.D., and Martinez, F., 2014, Controls on segmentation and morphology along the back-arc Eastern Lau Spreading Center and Valu Fa Ridge: Journal of Geophysical Research: Solid Earth, v. 119, p. 1678-1700.

Sleeper, J.D., and Martinez, F., 2016, Geology and kinematics of the Niuafo'ou microplate in the northern Lau Basin: Journal of Geophysical Research, v. 121, p. 4852-4875.

Smith, G.P., Wiens, D.A., Fischer, K.M., Dorman, L.M., Webb, S.C., and Hildebrand, J.A., 2001, A complex pattern of mantle flow in the Lau backarc: Science, v. 292, p. 713-716.

Sobolev, A.V., and Danyushevsky, L.V., 1994, Petrology and geochemistry of boninites from north termination of the Tonga trench: Constraints on the generation conditions of primary high-Ca boninite magmas: Journal of Petrology, v. 35, p. 1183-1211.

Stewart, M.S., Hannington, M.D., Emberley, J., Baxter, A.T., Krätschel, A., Petersen, S., Brandl, P.A., Anderson, M.O., Mercier-Langevin, P., Mensing, R., Breker, K., and Fassbender,

M.L., 2022, A new geological map of the Lau basin reveals crustal growth processes in arc-backarc systems: Geosphere, v. 18, p. 910-943.

Sun, S., and McDonough, W.F., 1989, Chemical and isotopic systematics of oceanic basalts: implications for mantle composition and processes: Geological Society, London, Special Publications, v. 42, p. 313-345.

Taylor, B., Zellmer, K., Martinez, F., and Goodliffe, A., 1996, Sea-floor spreading in the Lau back-arc basin: Earth and Planetary Science Letters, v. 144, p. 35-40.

Taylor, B., and Martinez, F., 2003, Back-arc basin basalt systematics: Earth and Planetary Science Letters, v. 210, p. 481-497.

Thurston, P.C., Ayer, J.A., Goutier, J., and Hamilton, M.A., 2008, Depositional gaps in Abitibi greenstone belt stratigraphy: A key to exploration for syngenetic mineralization: Economic Geology, v. 103, p. 1097-1134.

Thurston, P.C., 2015, Greenstone belts and granite−greenstone terranes: Constraints on the nature of the Archean world: Geoscience Canada, v. 42, p. 437-484.

Tian, L., Castillo, P.R., Hilton, D.R., Hawkins, J.W., Hanan, B.B., and Pietruszka, A.J., 2011, Major and trace element and Sr-Nd isotope signatures of the northern Lau Basin lavas: Implications for the composition and dynamics of the back-arc basin mantle: Journal of Geophysical Research: Solid Earth v. 116, B11201, p. 18.

Tian, L., Castillo, P.R., Hawkins, J.W., Hilton, D.R., Hanan, B.B., and Pietruszka, A.J., 2008, Major and trace element and Sr-Nd isotope signatures of lavas from the Central Lau Basin: Implications for the nature and influence of subduction components in the back-arc mantle: Journal of Volcanology and Geothermal Research, v. 178, p. 657-670.

Todd, E., Gill, J.B., Wysoczanski, R.J., Hergt, J., Wright, I.C., Leybourne, M.I., and Mortimer, N., 2011, Hf isotopic evidence for small-scale heterogeneity in the mode of mantle wedge enrichment: Southern Havre Trough and south Fiji basin back arcs: Geochemistry, Geophysics, Geosystems, v. 12, article Q09011.

Tontini, F.C., Bassett, D., de Ronde, C.E.J., Timm, C., and Wysoczanski, R., 2019, Early evolution of a young back-arc basin in the Havre Trough: Nature Geoscience, v. 12, p. 856-862.

Ueki, K., Hino, Hideitsu, H., and Kuwatani, T., 2018, Geochemical discrimination and characteristics of magmatic tectonic settings: A machine-learning-based approach: Geochemistry, Geophysics, Geosystems, v. 19, p. 1327-1347.

Wanless, V.D., and Shaw, A.M., 2012, Lower crustal crystallization and melt evolution at mid-ocean ridges: Nature Geoscience, v. 5, p. 651-655.

White, W.M., and Klein, E.M., 2014, Composition of the Oceanic Crust, in Holland, H.D. and Turekian, K.K., ed., Treatise on Geochemistry, 2nd ed.: Elsevier, p. 457-496.

Winchester, J.A., and Floyd, P.A., 1977, Geochemical discrimination of different magma series and their differentiation products using immobile elements: Chemical Geology, v. 20, p. 325-343.

Wyman, D.A., 2013, A critical assessment of Neoarchean "plume only" geodynamics: Evidence from the Superior Province: Precambrian Research, v. 229, p. 3-19.

Yan, Q., Castillo, P.R., and Shi, X., 2012, Geochemistry of basaltic lavas from the southern Lau Basin: input of compositionally variable subduction components: International Geology Review, v. 54, p. 1456-1474.

Yan, Q., Straub, S., Castillo, P., Zhang, H., Tian, L., and Xuefa, Shi., 2020, Hafnium isotope constraints on the nature of the mantle beneath the Southern Lau basin (SW Pacific): Scientific reports, v. 10, 17476, p. 11.

Yang, K., and Scott, S.D., 2003, Geochemical relationships of felsic magmas to ore metals in massive sulfide deposits of the Bathurst mining camp, Iberian pyrite belt, Hokuroku district, and the Abitibi belt: Economic Geology, p. 457-478.

van der Zander, I., Sinton, J.M., and Mahoney, J.J., 2010, Late shield-stage silicic magmatism at Wai'anae volcano: Evidence for hydrous crustal melting in Hawaiian volcanoes: Journal of Petrology, v. 51, p. 671-701.

Zellmer, G.F., Hawkesworth, C.J., Sparks, R.S.J., Thomas, L.E., Harford, C.L., Brewer, T.S., and Loughlin, S.C., 2003, Geochemical evolution of the Soufrière Hills volcano, Montserrat, Lesser Antilles volcanic arc: Journal of Petrology, v. 44, p. 1349-1374.

Zellmer, G.F., Rubin, K.H., Grönvold, K., and Jurado-Chichay, Z., 2008, On the recent bimodal magmatic processes and their rates in the Torfajökull-Veidivötn area, Iceland: Earth and Planetary Science Letters, v. 269, p. 388-398.

Zhang, H., Yan, Q., Li, C., Zhu, Z., Zhao, R., and Shi, X., 2018, Geochemistry of diverse lava types from the Lau sasin (South West Pacific): Implications for complex back-arc mantle dynamics: Geological Journal, v. 56, p. 3643-3659.

Figures

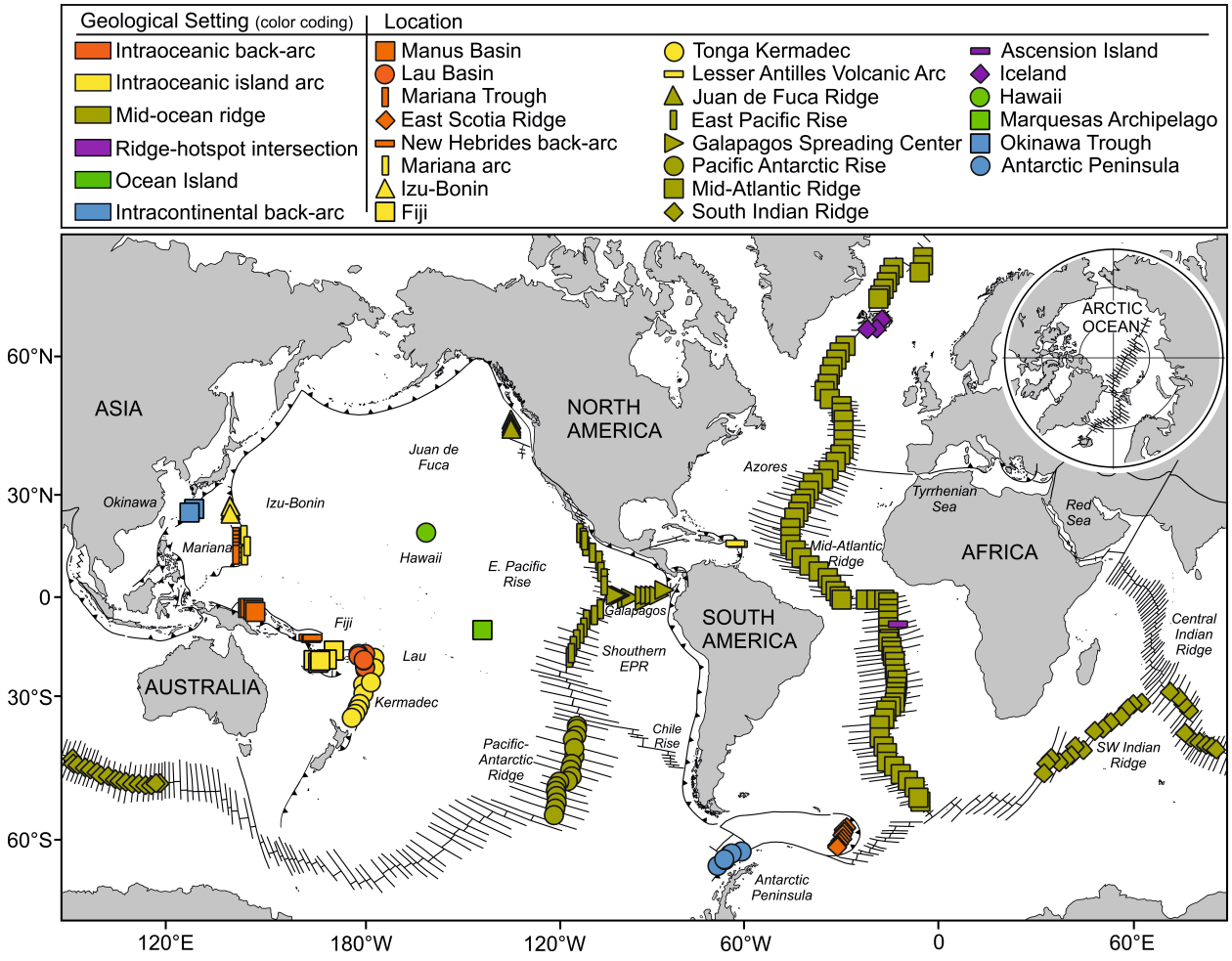


Figure 3.1: Global map of mafic volcanic rock samples from the oceans compiled for this study. Six different tectonic settings are represented including intraoceanic back-arc basins (orange: Manus Basin, Lau Basin, Mariana Trough, East Scotia Ridge, New Hebrides arc-backarc), intraoceanic island arcs (yellow: Mariana arc, Izu-Bonin, Fiji, Tonga Kermadec Arc, Lesser Antilles Volcanic Arc), mid-ocean ridges (olive: Juan de Fuca Ridge, East Pacific Rise, Galapagos Spreading Center, Pacific Antarctic Rise, Mid-Atlantic Ridge, South Indian Ridge), ridge-hotspot intersections (purple: Ascension Island, Iceland), ocean islands (green: Hawaii, Marquesas Archipelago) and intracontinental arc-backarc basins (blue: Antarctic Peninsula, Okinawa Trough). Details of the samples are provided in **Appendix Table A1.**

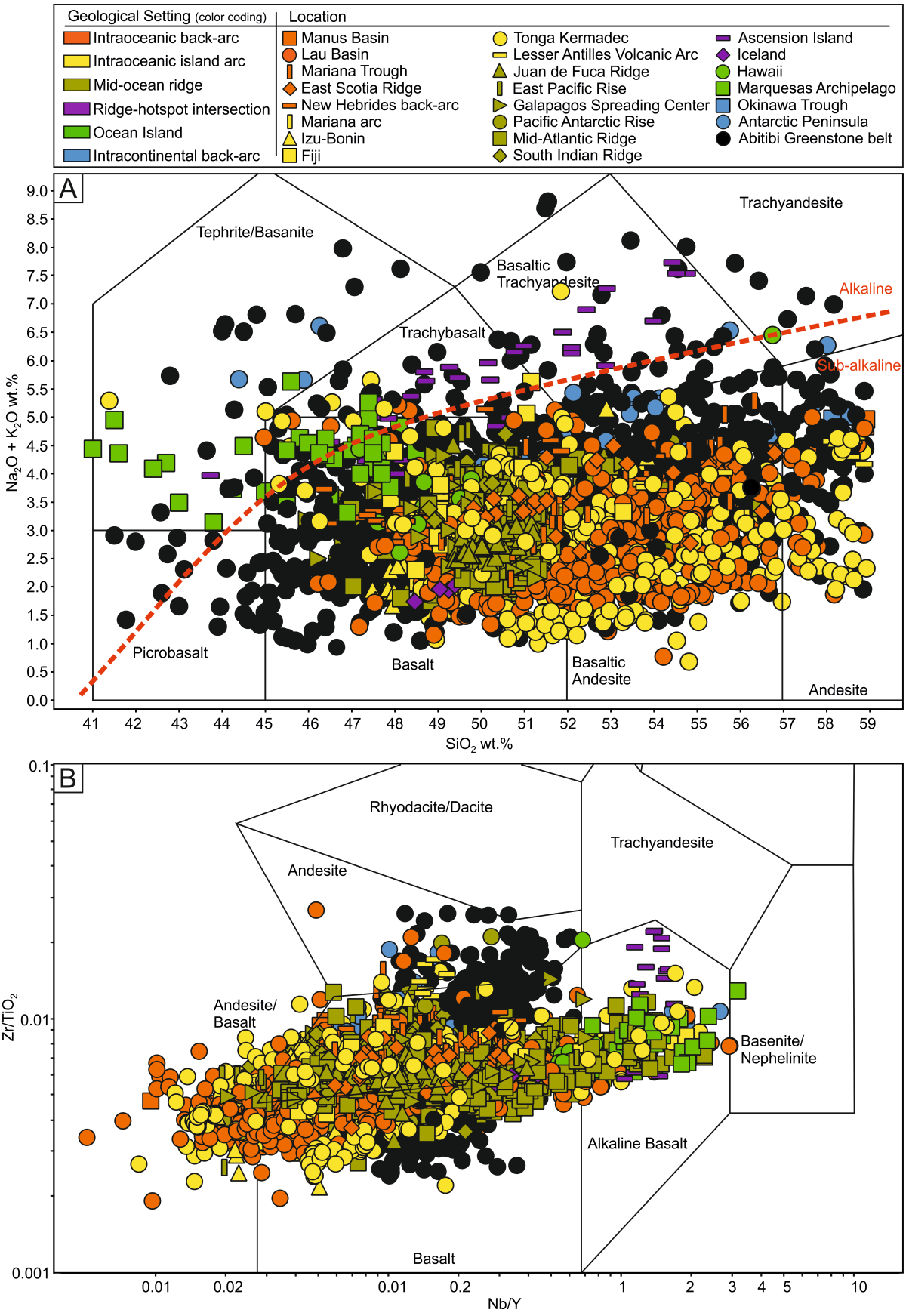
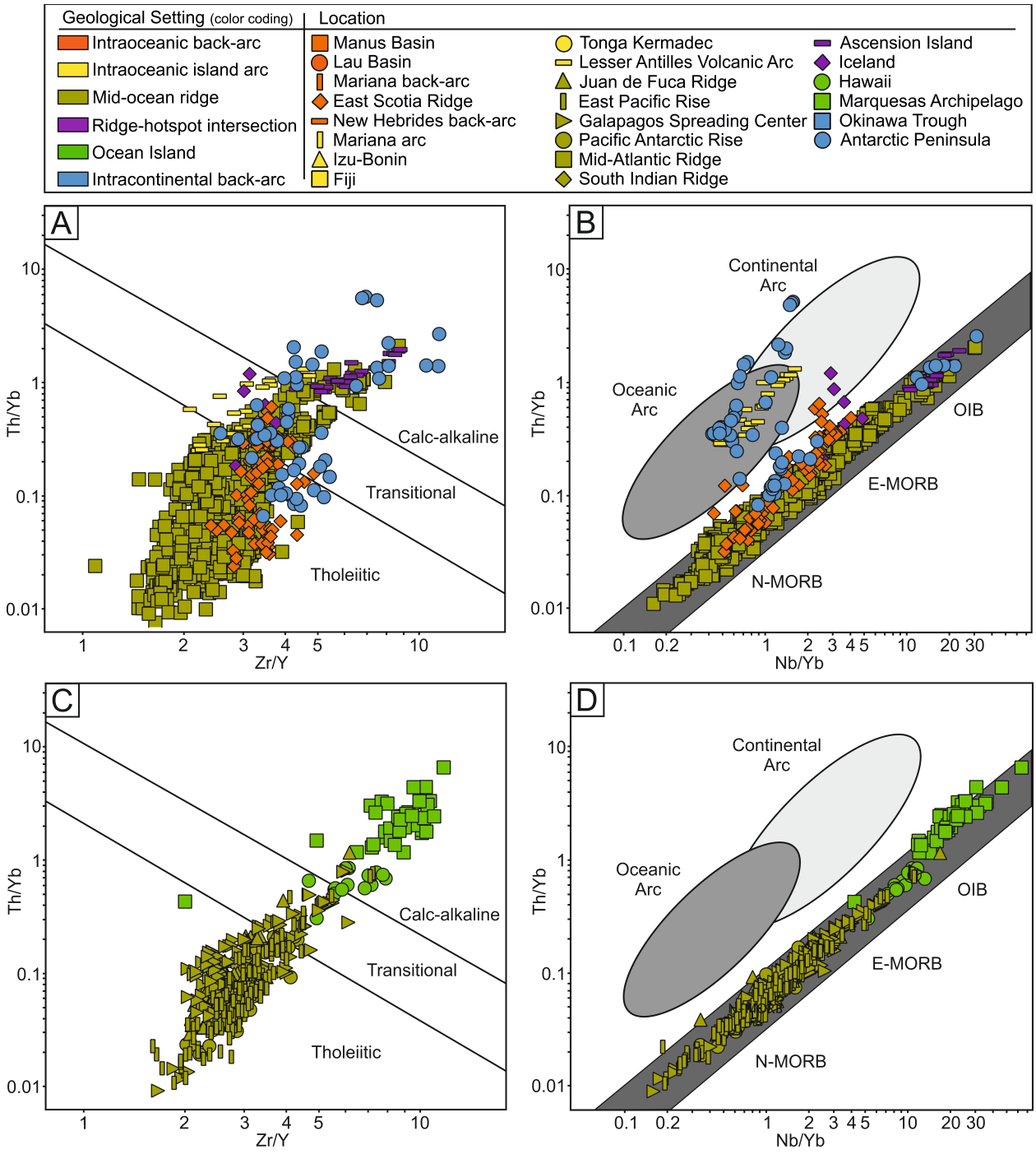

Geological Setting (color coding)
Intraoceanic back-arc
Intraoceanic island arc
Mid-ocean ridge
Ridge-hotspot intersection
Ocean Island
Intracontinental back-arc
Location
Manus Basin
Lau Basin
Mariana Trough
East Scotia Ridge
New Hebrides back-arc
Mariana arc
Izu-Bonin
Fiji
Tonga Kermadec
Lesser Antilles Volcanic Arc
Juan de Fuca Ridge
East Pacific Rise
Galapagos Spreading Center
Pacific Antarctic Rise
Mid-Atlantic Ridge
South Indian Ridge
Ascension Island
Iceland
Hawaii
Marquesas Archipelago
Okinawa Trough
Antarctic Peninsula
Abitibi Greenstone belt
A
Tephrite/Basanite
Trachyandesite
Basaltic Trachyandesite
Trachybasalt
Alkaline
Sub-alkaline
Picrobasalt
Basalt
Basaltic Andesite
Andesite
Na2O + K2O wt.%
SiO2 wt.%
B
Rhyodacite/Dacite
Andesite
Trachyandesite
Andesite/ Basalt
Basenite/ Nephelinite
Alkaline Basalt
Basalt
Zr/TiO2
Nb/Y

Figure 3.2: Total alkali-silica plot (after Le Maitre, 1989) showing the distribution of modern oceanic mafic volcanic rocks (see **Appendix Figure A1** for details). Samples from ridge-hotspot intersections and ocean islands have a dominantly alkaline affinity. Mid-ocean ridge basalts are subalkaline with low SiO_2 concentrations. Samples from intraoceanic back-arc assemblages plot in a strong linear array from low SiO_2 to high SiO_2 with increasing $Na_2O + K_2O$ concentrations. Samples from intraoceanic island arc assemblages have a wider range of SiO_2 concentrations with a narrower range of $Na_2O + K_2O$. Samples from intracontinental arc-backarc assemblages have the highest SiO_2 concentrations and a wide range of $Na_2O + K_2O$. The range of compositions of mafic volcanic rocks in the Abitibi Greenstone Belt is shown for comparison (black symbols beneath the other data points: see text for discussion and **Appendix Figure A1** for details). B) Discrimination plot of Winchester and Floyd (1977) showing the distribution of modern oceanic mafic volcanic rocks (see **Appendix Figure A1** for details). Mid-ocean ridge mafic volcanic rocks from the East Pacific Rise, Pacific-Antarctic Rise and Juan de Fuca Ridge have low Nb/Y and high Zr/TiO_2 and plot in the basalt/andesite field. Samples from different back-arc assemblages, such as the Lau Basin and Manus Basin, and island-arc assemblages, such as Izu Bonin, plot mostly in the basalt field with a range of Zr/TiO_2 and Nb/Y ratios extending into the andesite/basalt field. Mafic volcanic rocks from intracontinental arc-backarc assemblages, such as the Okinawa Trough and Western Antarctic Peninsula, have a very wide range of Zr/TiO_2 and Nb/Y spanning the entire field of basalt and andesite (beneath the mid-ocean ridge samples: see **Appendix Figure A1** for details). Note that the boundaries in Winchester and Floyd (1977) are based on a limited number of oceanic arc samples and therefore are not fully representative of the samples in this study. As a result, many of the new samples are misclassified.


Geological Setting (color coding)
Intraoceanic back-arc
Intraoceanic island arc
Mid-ocean ridge
Ridge-hotspot intersection
Ocean Island
Intracontinental back-arc
Location
Manus Basin
Lau Basin
Mariana back-arc
East Scotia Ridge
New Hebrides back-arc
Mariana arc
Izu-Bonin
Fiji
Tonga Kermadec
Lesser Antilles Volcanic Arc
Juan de Fuca Ridge
East Pacific Rise
Galapagos Spreading Center
Pacific Antarctic Rise
Mid-Atlantic Ridge
South Indian Ridge
Ascension Island
Iceland
Hawaii
Marquesas Archipelago
Okinawa Trough
Antarctic Peninsula
A
Th/Yb
Zr/Y
Calc-alkaline
Transitional
Tholeiitic
B
Th/Yb
Nb/Yb
Continental Arc
Oceanic Arc
OIB
E-MORB
N-MORB
C
Th/Yb
Zr/Y
Calc-alkaline
Transitional
Tholeiitic
D
Th/Yb
Nb/Yb
Continental Arc
Oceanic Arc
OIB
E-MORB
N-MORB

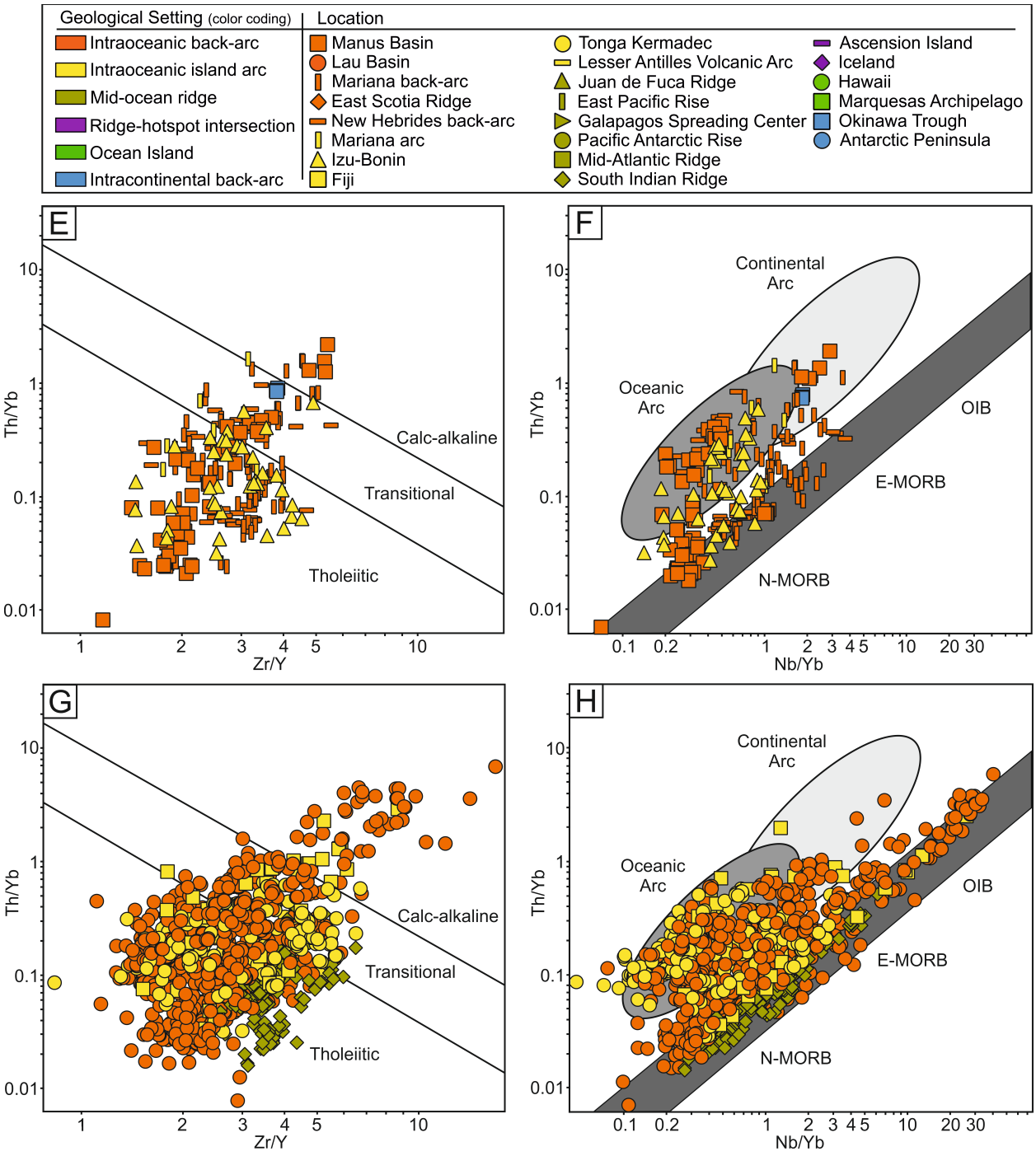


Figure 3.3: Examples of geochemical and tectonic affinity diagrams for mafic volcanic rocks showing the classifications of modern oceanic basalts. A) Geochemical affinity diagram of Ross and Bédard (2009) showing trace element data for mafic volcanic rocks from the Mid-Atlantic Ridge, Iceland, Ascension Island, Lesser Antilles Volcanic Arc, East Scotia Ridge and Antarctic Peninsula. The samples range from dominantly tholeiitic to calc-alkaline; the tholeiitic array

includes samples from the Mid-Atlantic Ridge and East Scotia Ridge, and the calc-alkaline array includes samples from Ascension Island and Antarctic Peninsula. The transitional array includes samples from Iceland, East Scotia Ridge, the Antarctic Peninsula and the Lesser Antilles Arc. B) Lithotectonic discrimination plot of Pearce (2014) showing trace element data for the same mafic volcanic rocks in A). The N-MORB and OIB array includes mainly samples from the Mid-Atlantic Ridge and East Scotia Ridge. Samples from Ascension Island plot in the OIB array. The oceanic arc and continental arc fields include samples from the Lesser Antilles and Antarctic Peninsula. However, there is overlap with the E-MORB to OIB array. C) Trace element data for mafic volcanic rocks from the Juan de Fuca Ridge, East Pacific Rise, Galapagos Spreading Center, Pacific Antarctic Rise, Marquesas Archipelago, and Hawaii on the geochemical affinity diagram of Ross and Bédard (2009). Samples from the Juan de Fuca, East Pacific Rise, Galapagos Spreading Center, and Pacific Antarctic Rise are almost all tholeiitic. Samples from the Marquesas Archipelago and Hawaii plot mostly in the calc-alkaline array. D) Trace element data for mafic volcanic rocks in C) on the lithotectonic discrimination plot of Pearce (2014). Samples from the Juan de Fuca Ridge, East Pacific Rise, Galapagos Spreading Center and Pacific Antarctic Rise plot in the N-MORB to E-MORB array. Samples from the Marquesas Archipelago and Hawaii plot in the OIB array. E) Trace element data for mafic volcanic rocks from the Manus Basin, Mariana arc-backarc, New Hebrides arc-backarc, Izu-Bonin, and Okinawa Trough on the geochemical affinity diagram of Ross and Bédard (2009). Samples from the Manus Basin and the Mariana arc-backarc are tholeiitic to calc-alkaline. Samples from the New Hebrides arc-backarc and the Izu-Bonin are tholeiitic to transitional. Samples from the Okinawa Trough plot mostly in the transitional array. F) Trace element data for mafic volcanic rocks in E) on the lithotectonic discrimination plot of Pearce (2014). Samples from the Manus Basin, New Hebrides arc-backarc and Izu-Bonin plot in the N-MORB array. Samples from the Mariana arc-backarc plot in the E-MORB and oceanic arc arrays. Samples from the Manus Basin, New Hebrides arc-backarc and the Izu Bonin mainly plot in the oceanic arc field. A few samples from the Manus Basin, Mariana arc-backarc, and New Hebrides arc-backarc plot in the continental arc field. Samples from the Okinawa Trough plot only in the continental arc field. G) Trace element data for mafic volcanic rocks from Fiji, Tonga-Kermadec, and the South Indian Ridge on the geochemical affinity diagram of Ross and Bédard (2009). Samples from Fiji and the Tonga-Kermadec plot in the tholeiitic to calc-alkaline array. Samples from South Indian Ridge are mostly tholeiitic. H) Trace element data for mafic volcanic

rocks from G) on the lithotectonic discrimination plot of Pearce et al. (2014). Samples from Fiji and the Tonga-Kermadec plot in the N-MORB to OIB array and oceanic and continental arc fields. Samples from the South Indian Ridge plot in the N-MORB to E-MORB array.

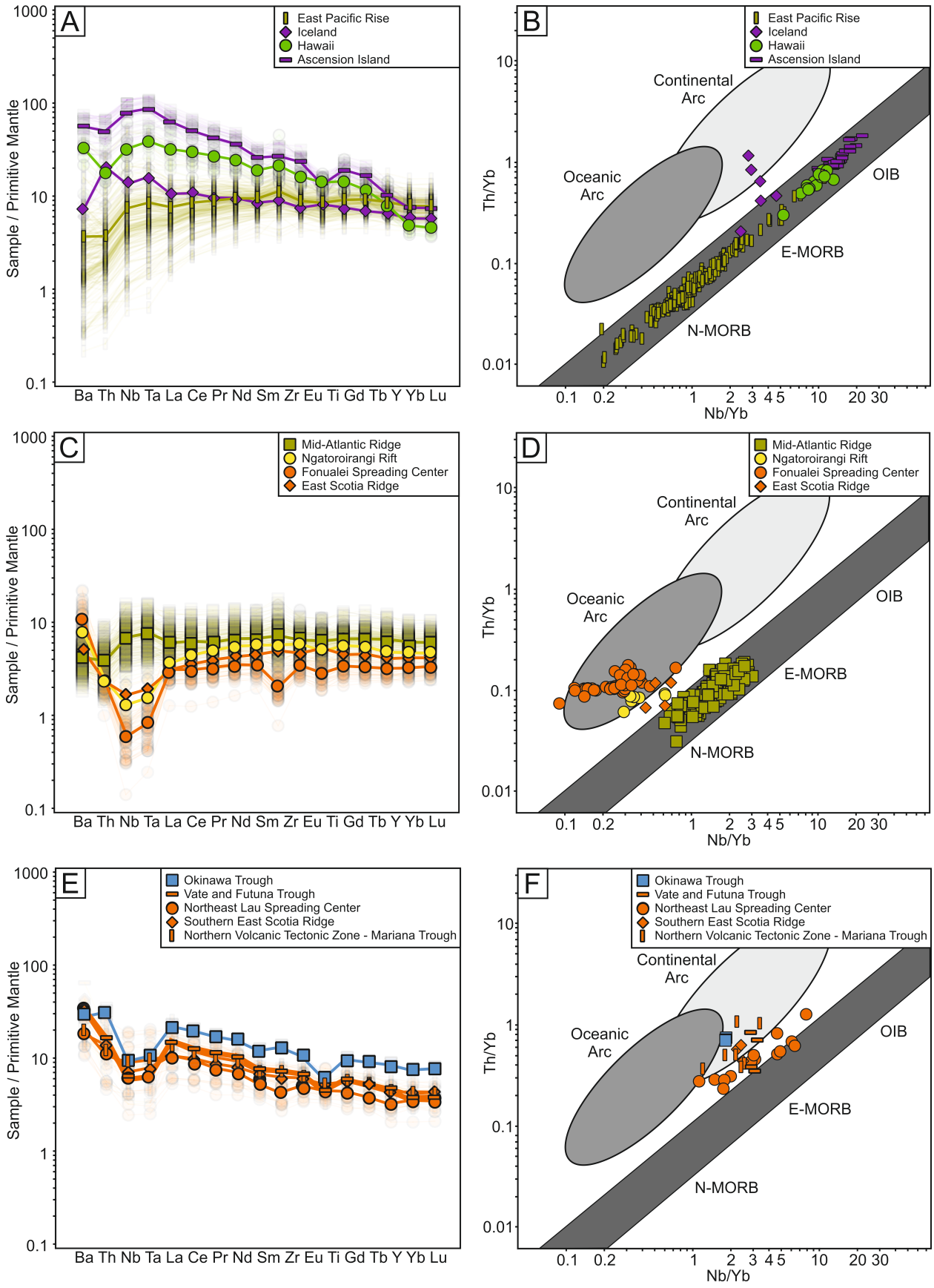

A
East Pacific Rise
Iceland
Hawaii
Ascension Island
Sample / Primitive Mantle
1000
100
10
1
0.1
Ba Th Nb Ta La Ce Pr Nd Sm Zr Eu Ti Gd Tb Y Yb Lu
B
East Pacific Rise
Iceland
Hawaii
Ascension Island
Continental Arc
Oceanic Arc
OIB
E-MORB
N-MORB
Th/Yb
10
1
0.1
0.01
0.1 0.2 1 2 3 4 5 10 20 30
Nb/Yb
C
Mid-Atlantic Ridge
Ngatoroirangi Rift
Fonualei Spreading Center
East Scotia Ridge
Sample / Primitive Mantle
1000
100
10
1
0.1
Ba Th Nb Ta La Ce Pr Nd Sm Zr Eu Ti Gd Tb Y Yb Lu
D
Mid-Atlantic Ridge
Ngatoroirangi Rift
Fonualei Spreading Center
East Scotia Ridge
Continental Arc
Oceanic Arc
OIB
E-MORB
N-MORB
Th/Yb
10
1
0.1
0.01
0.1 0.2 1 2 3 4 5 10 20 30
Nb/Yb
E
Okinawa Trough
Vate and Futuna Trough
Northeast Lau Spreading Center
Southern East Scotia Ridge
Northern Volcanic Tectonic Zone - Mariana Trough
Sample / Primitive Mantle
1000
100
10
1
0.1
Ba Th Nb Ta La Ce Pr Nd Sm Zr Eu Ti Gd Tb Y Yb Lu
F
Okinawa Trough
Vate and Futuna Trough
Northeast Lau Spreading Center
Southern East Scotia Ridge
Northern Volcanic Tectonic Zone - Mariana Trough
Continental Arc
Oceanic Arc
OIB
E-MORB
N-MORB
Th/Yb
10
1
0.1
0.01
0.1 0.2 1 2 3 4 5 10 20 30
Nb/Yb

Figure 3.4: A) Primitive mantle-normalized (Sun and McDonough, 1989) trace element plot comparing a subset of mafic volcanic rocks from mid-ocean ridges, ridge-hotspot intersections and ocean islands (individual samples are transparent; averages are non-transparent). Samples from the East Pacific Rise have no negative Nb-Ta anomaly and a rising REE pattern, whereas samples from Iceland, Hawaii and Ascension Island have elevated REE and dipping REE patterns. B) Lithotectonic discrimination plot of Pearce (2014) of the samples in A) showing a strong linear array from N-MORB to OIB. Samples from the East Pacific Rise plot mostly in the N-MORB array, whereas samples from Iceland, Hawaii and Ascension Island plot mostly in the array from E-MORB to OIB. C) Primitive mantle-normalized trace element plot comparing a subset of mafic volcanic rocks from the Mid-Atlantic Ridge and representative back-arc rifts and back-arc spreading centers. Samples from the Mid-Atlantic Ridge have a positive Nb-Ta anomaly and flat REE pattern, whereas samples from the back-arc rifts and spreading center (Ngatoroirangi Rift, Fonualei Rift and Spreading Center and East Scotia Ridge) have negative Nb-Ta anomalies and flat REE patterns. D) Lithotectonic discrimination plot of the samples in C) showing differences in the samples from arcs with strong fluid-fluxed components (Fonualei Spreading Center) and those with weaker fluid-fluxed components (East Scotia Ridge, Ngatoroirangi Rift). Samples from the Ngatoroirangi Rift, Fonualei Rift and Spreading Center, and the East Scotia Ridge plot mostly within the oceanic arc field. Samples from the Mid-Atlantic Ridge plot in a strong linear array within the N-MORB field. E) Primitive mantle-normalized trace element plot comparing a subset of mafic volcanic rocks from and intracontinental back-arc rift (Okinawa Trough), the Vate and Futuna Troughs, and propagating rifts in nascent back-arc crust (Northeastern Lau Spreading Center, Southern East Scotia Ridge, Northern Volcanic Tectonic Zone – Mariana Trough). All samples have weak negative Nb-Ta anomalies and shallowly dipping REE patterns. F) Lithotectonic discrimination plot of the samples in E) showing composition intermediate between the continental arc and the MORB fields.

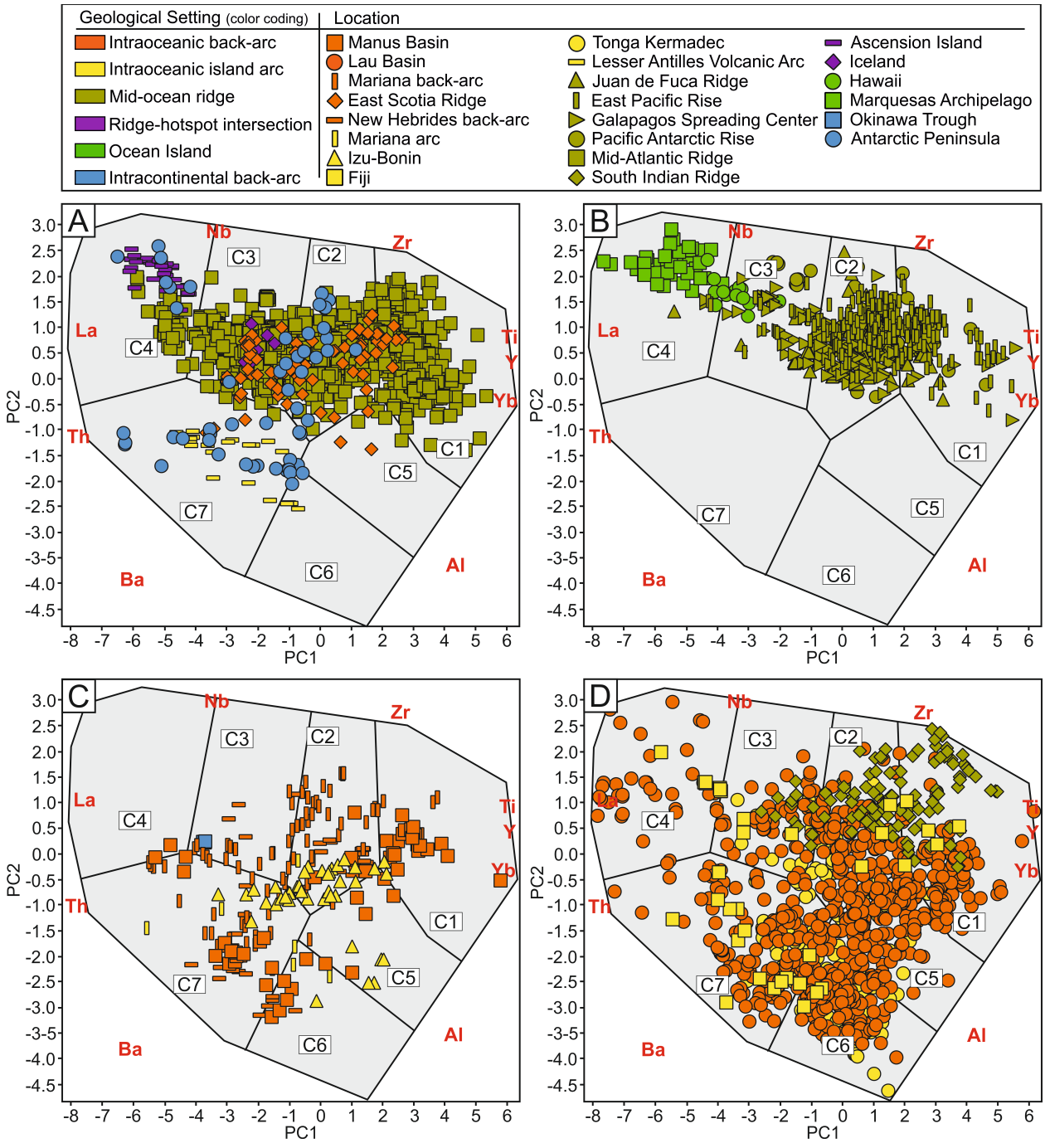


Figure 3.5: Principal components plots of the major and trace element geochemistry of modern oceanic mafic volcanic rocks. The principal components analysis (PCA) was conducted using 9 elements (Ti, Al, Y, Zr, Nb, Ba, La, Yb, Th) for all samples in the data set. PC1 and PC2 account for 66% and 28%, respectively, of the total variance of the data set. The red element labels correspond to loadings for the entire data set (see Appendix Table A4); the symbols are individual

sample scores given in Appendix Table A5 For illustration purposes, the different clusters of samples identified in this study are outlined and labelled (C1-C7: Appendix Table A6). See Figure 6 for the explanation of the polygons. The characteristics of each cluster and their relationship to specific lithotectonic assemblages are summarized in Table 3 and discussed in the text. A) PCA plot of samples from the Mid-Atlantic Ridge, Iceland, Ascension Island, Lesser Antilles Volcanic Arc, East Scotia Ridge and Antarctic Peninsula. Samples from the Mid-Atlantic Ridge have a wide range of loadings on PC1 and positive loadings on PC2 spanning C1 to C4. Samples from the ridge-hotspot intersection at Iceland have intermediate loadings on PC1 and PC2 and fall mainly in C3. Samples from the ridge-hotspot intersection at Ascension Island have large negative loadings on PC1 and strong positive loadings on PC2 and fall in C4. Samples from the intraoceanic island arc of the Lesser Antilles have intermediate loadings on PC1 and negative loadings on PC2 and fall mainly in C7. Samples from the intraoceanic back-arc of the East Scotia Ridge have intermediate loadings on PC1 and PC2, spanning C2 and C3. Samples from the intracontinental arc-backarc of the Antarctic Peninsula have intermediate to negative loadings on PC1 and intermediate to positive and negative loadings on PC2 and include samples in C2, C4, and C7. B) Mid-ocean ridge mafic volcanic rocks from the Pacific Antarctic Rise, Juan de Fuca Ridge, and the Galapagos Spreading Center have intermediate loadings on PC1 and positive loadings on PC2, spanning C1 to C3. Samples from the East Pacific Rise have a range of mostly positive loadings on PC1 and PC2 and fall in C1 and C2. Samples from the Marquesas Archipelago have strong negative loadings on PC1 and positive loadings on PC2 and fall in C4. Samples from Hawaii have large negative loadings on PC1 and strong positive loadings on PC2 and fall mainly in C3. C) Samples from the Manus Basin have a wide range of loadings on PC1 and PC2 and include samples in C1, C6, and C7. Samples from the Mariana Trough and New Hebrides have intermediate loadings on PC1 and intermediate to negative loadings on PC2 and include samples in C2, C3, and C7. Samples from the Izu-Bonin Arc have a narrow range of intermediate loadings on PC1 and PC2 and fall between C2 and C7. Three samples from the Okinawa Trough have negative loadings on PC1 and intermediate loadings on PC2 and fall between C3 and C7. D) Samples from intraoceanic island arc assemblages from Fiji and Tonga-Kermadec have a wide range of loadings on PC1 and PC2 and do not belong to a particular cluster. Mid-ocean ridge mafic volcanic rocks from the South Indian Ridge have positive loadings on PC1 and PC2, similar to the other mid-ocean ridge assemblages.

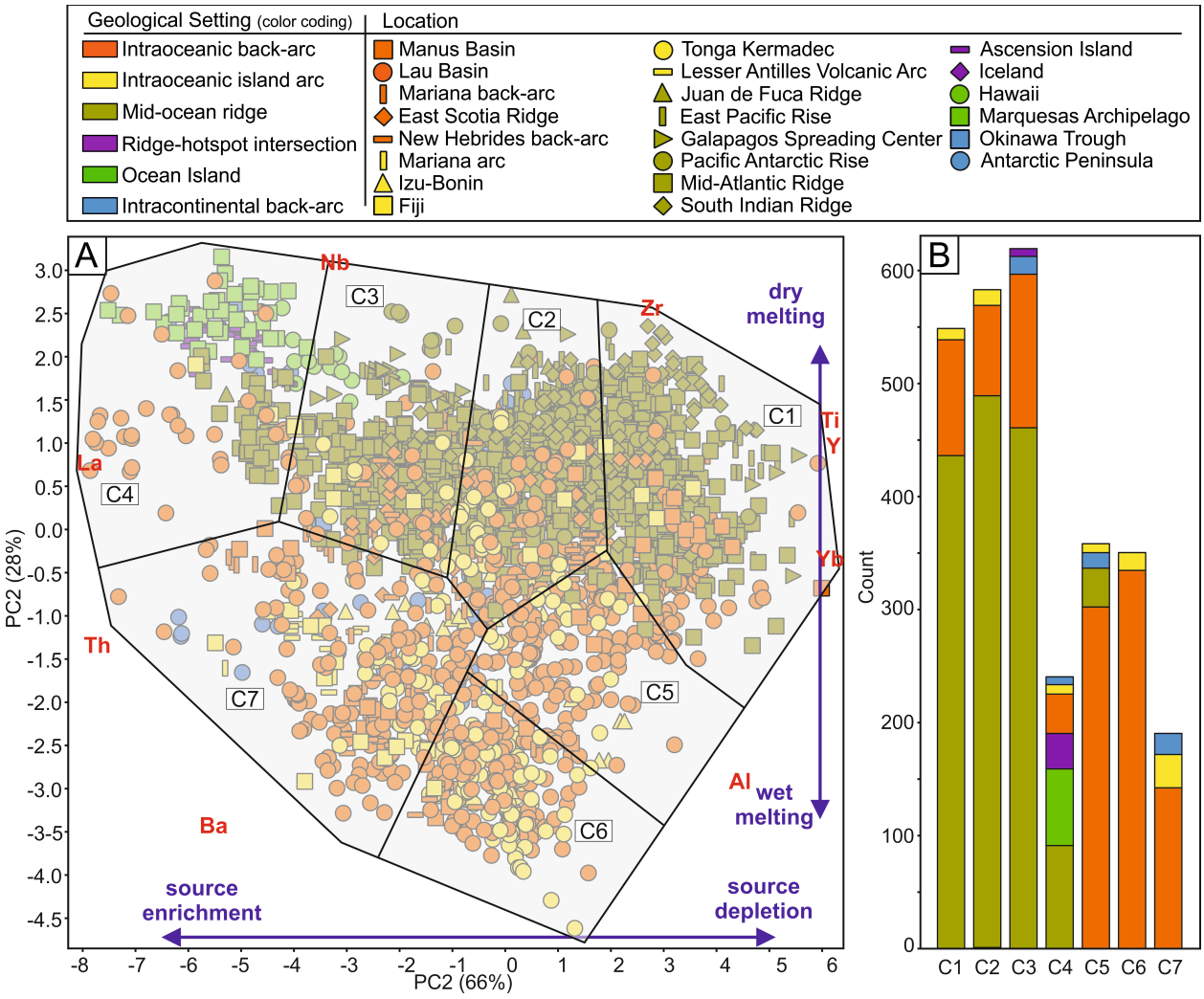


Figure 3.6: A) Summary of hierarchical clustering classification overlain on PC1-PC2. Different clusters of samples from the hierarchical cluster analysis are outlined by the labelled polygons (C1-C7). The assigned target classes are listed in Table A6. The lines dividing the clusters were drawn outward from the center of the plot, first between samples in C1 and C2, and then sequentially to C7. The outer boundary encloses the samples with the highest and lowest scores in PC1 and PC2. B) Numbers of samples in each target class of the hierarchical clustering colored according to the different geodynamic settings in A. See the text for discussion of the inferred melting conditions and sources.

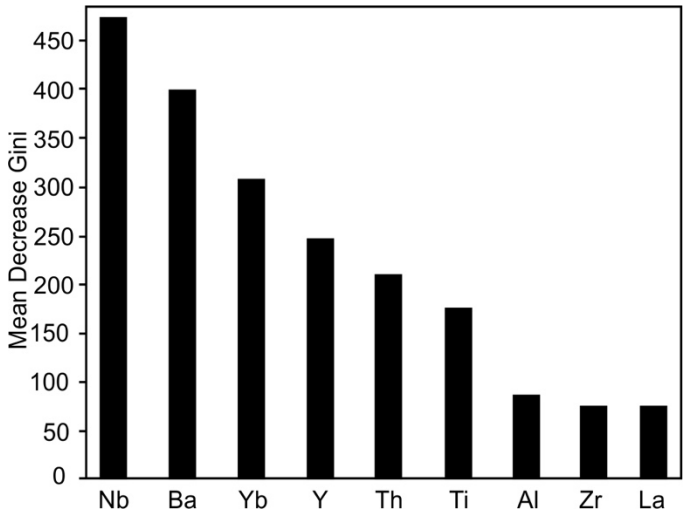


Figure 3.7: Plot of the "Mean Decrease Gini" value for individual elements for the classification of a sample into a target class or "cluster" (see text for discussion). The Mean Decrease Gini value corresponds to the probability of a correct classification of a sample and identifies Nb, Ba, Yb, Y, Th and Ti as the most important variables in determining the accuracy of the classification. Al, Zr and La have low Mean Decrease Gini values and therefore less influence in the correct classification of a sample.

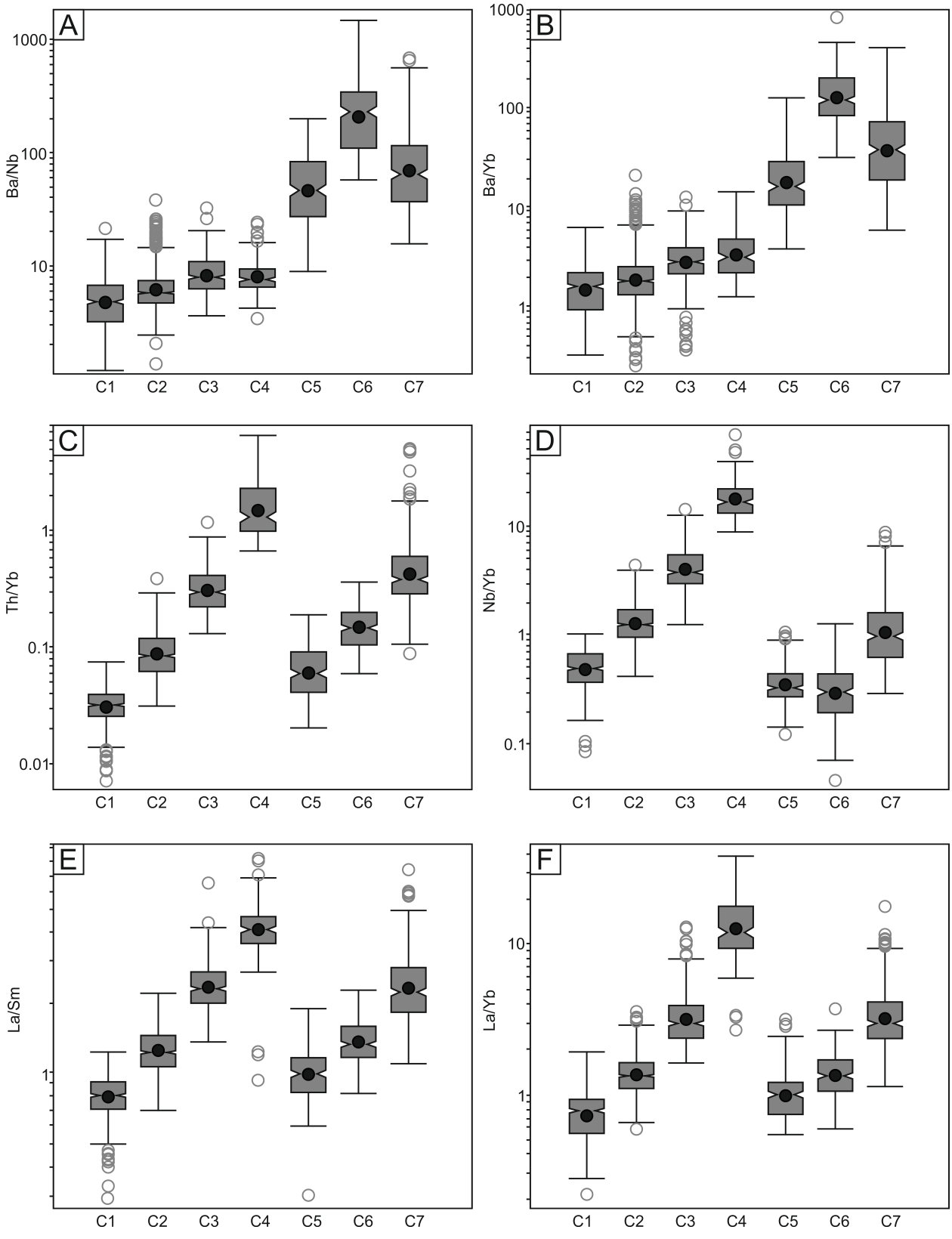

A
Ba/Nb
1000
100
10
C1
C2
C3
C4
C5
C6
C7
B
Ba/Yb
1000
100
10
1
C
Th/Yb
1
0.1
0.01
D
Nb/Yb
10
1
0.1
E
La/Sm
1
F
La/Yb
10
1

Figure 3.8: Selected trace element ratios for samples assigned to each target cluster (C1-C7). The black circle represents the mean and the notch the median of the data. The upper and lower boundaries of the boxes are the upper and lower 50th percentiles. The whiskers are the 25th and 75th percentiles. A) Ba/Nb ratios showing the distinct differences between clusters C1-C4 (samples with low Ba/Nb) and C5-C7 (samples with high Ba/Nb). The high Ba/Nb values of C5-C7 are interpreted to indicate volatile input from dehydration of the subducted slab. B) Ba/Yb ratios showing the same differences between C1-C4 and C5-C7. C) Th/Yb ratios showing increasing values from C1 to C4 and C5 to C7. High Th/Yb ratios are interpreted to indicate volatile input at high temperatures and assimilation of crustal material. D) Nb/Yb ratios showing increasing values from C1 to C4 and C5 to C7. High Nb/Yb is interpreted to indicate enriched mantle sources and low degrees of melting. E) La/Sm ratios showing increasing values from C1 to C4 and C5 to C7, similar to Nb/Yb. F) La/Yb ratios showing increasing values from C1 to C4 and C5 to C7. See Table 2 for details.

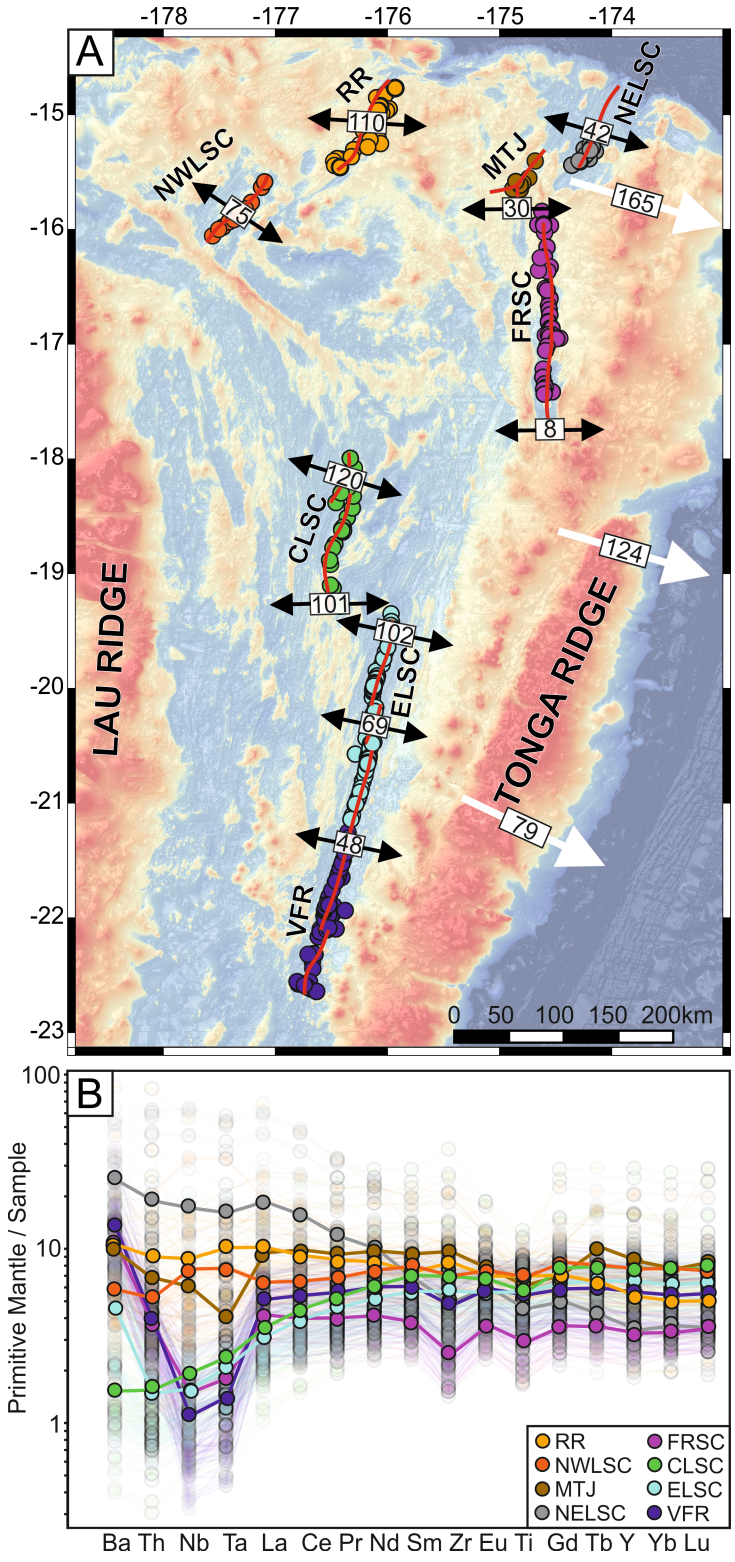

A
-178
-177
-176
-175
-174
-15
-16
-17
-18
-19
-20
-21
-22
-23
RR
110
NWLSC
75
MTJ
30
NELSC
42
165
FRSC
8
120
CLSC
101
102
ELSC
69
48
VFR
124
79
LAU RIDGE
TONGA RIDGE
0 50 100 150 200km
B
100
10
1
Primitive Mantle / Sample
RR
NWLSC
MTJ
NELSC
FRSC
CLSC
ELSC
VFR
Ba Th Nb Ta La Ce Pr Nd Sm Zr Eu Ti Gd Tb Y Yb Lu

Figure 3.9: A) Regional bathymetric map of the Lau back-arc basin (Ryan et al., 2009) showing spreading ridges, spreading rates and rates of retreat of the active arc (in mm/yr; modified from Sleeper and Martinez, 2016). The basin includes at least eight major zones of active extension: ELSC = Eastern Lau Spreading Center; VFR = Valu Fa Ridge; CLSC = Central Lau Spreading Center; FRSC = Fonualei Rift and Spreading Center; MTJ = Mangatolu Triple Junction; NELSC = Northeast Lau Spreading Center; NWLSC = Northwest Lau Spreading Center; RR = Rochambeau Rifts. B) Primitive mantle-normalized (Sun and McDonough, 1989) trace element plots of Lau Basin mafic volcanic rocks considered in this study. Samples from the RR, NWLSC, and MTJ have no negative Nb-Ta anomaly, flat REE patterns and high HREE concentrations indicating dry melting. Samples from the NELSC have a very weak negative Nb-Ta anomaly, steeply dipping REE patterns and low HREE concentrations indicating limited wet melting. Samples from the FRSC have a strong negative Nb-Ta anomaly, flat REE patterns and low HREE concentrations (i.e., wet melting). Samples from the CLSC have no negative Nb-Ta anomaly, increasing REE pattern and high HREE concentrations (dry melting). Samples from the ELSC have an intermediate negative Nb-Ta anomaly, flat REE pattern and high HREE concentrations (limited wet melting). Samples from the VFR have a strong negative Nb-Ta anomaly, flat REE pattern and high HREE concentrations (wet melting).

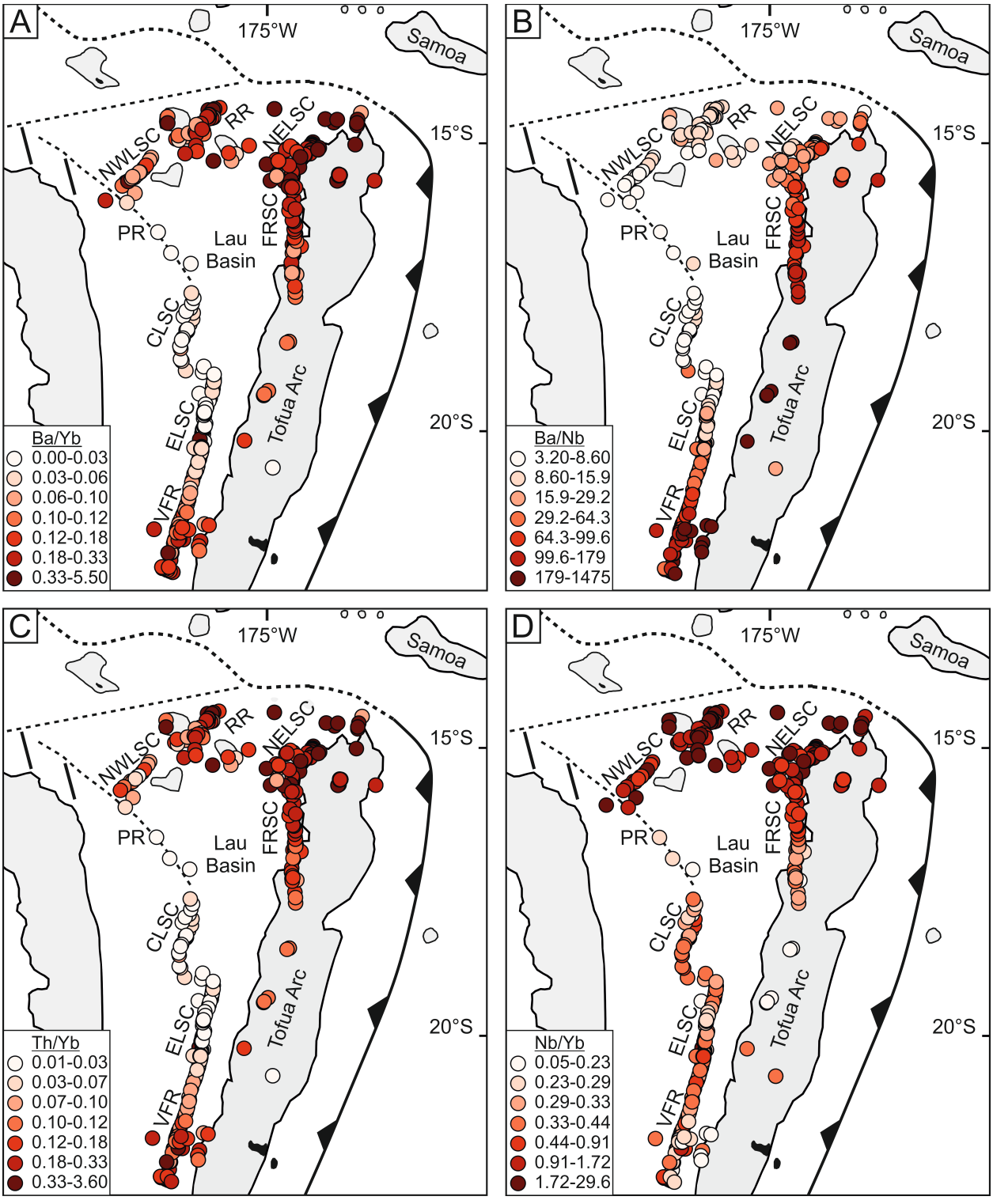

A
175°W
Samoa
15°S
20°S
NWLSC
RR
NELSC
FRSC
PR
Lau
Basin
CLSC
ELSC
VFR
Tofua Arc
Ba/Yb
0.00-0.03
0.03-0.06
0.06-0.10
0.10-0.12
0.12-0.18
0.18-0.33
0.33-5.50
B
175°W
Samoa
15°S
20°S
NWLSC
RR
NELSC
FRSC
PR
Lau
Basin
CLSC
ELSC
VFR
Tofua Arc
Ba/Nb
3.20-8.60
8.60-15.9
15.9-29.2
29.2-64.3
64.3-99.6
99.6-179
179-1475
C
175°W
Samoa
15°S
20°S
NWLSC
RR
NELSC
FRSC
PR
Lau
Basin
CLSC
ELSC
VFR
Tofua Arc
Th/Yb
0.01-0.03
0.03-0.07
0.07-0.10
0.10-0.12
0.12-0.18
0.18-0.33
0.33-3.60
D
175°W
Samoa
15°S
20°S
NWLSC
RR
NELSC
FRSC
PR
Lau
Basin
CLSC
ELSC
VFR
Tofua Arc
Nb/Yb
0.05-0.23
0.23-0.29
0.29-0.33
0.33-0.44
0.44-0.91
0.91-1.72
1.72-29.6

Figure 3.10: Spatial distribution of selected trace element ratios in mafic volcanic rocks of the northern Lau Basin illustrating enrichment and depletion patterns in Ba, Nb, Yb, and Th. Samples from the VFR, ELSC and CLSC show decreasing Ba/Yb (A), Ba/Nb (B), and Th/Yb (C) with increasing distance from the arc indicating less input of fluids from the dehydrating subducting slab. Nb/Yb ratios (D) show significant variations between the northern and southern Lau Basin. Samples from the FRSC to NELSC show decreasing Ba/Nb with distance from the arc but increasing Ba/Yb, Th/Yb, and Nb/Yb. The increasing Ba/Yb, Th/Yb, and Nb/Yb indicate an enriched mantle source. Samples from NWLSC and RR show low Ba/Nb but high Ba/Yb, Th/Yb, and Nb/Yb values indicating no input from arc-related fluids and a notably enriched mantle source.

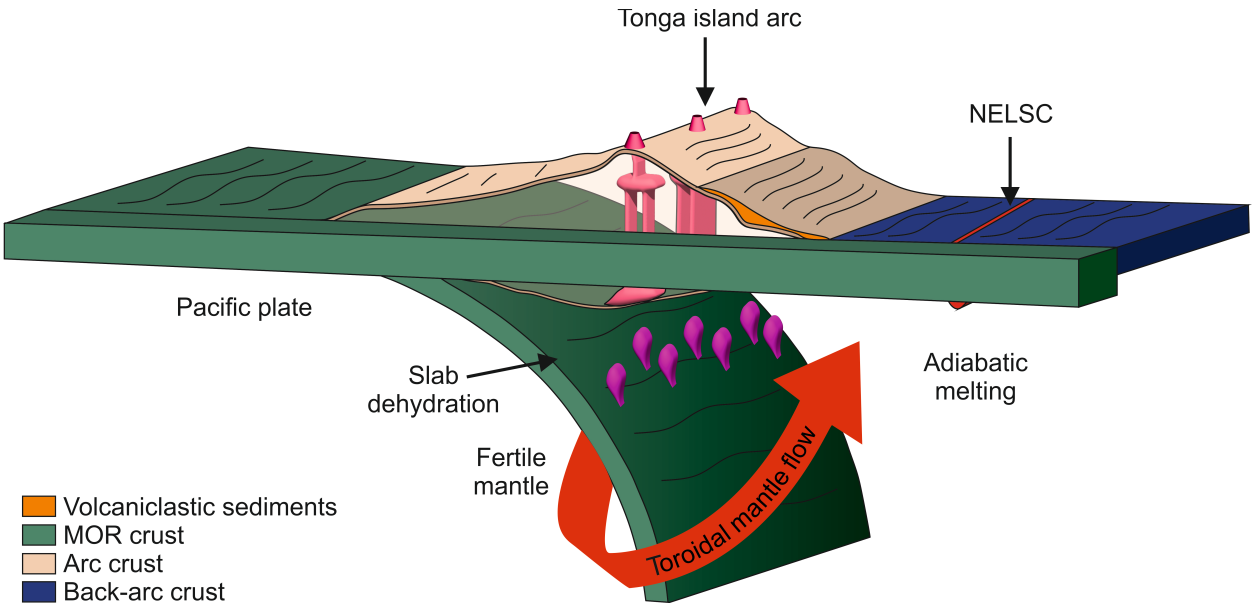


Figure 3.11: Schematic illustration of general mantle flow at microplate edges and terminating back-arc spreading centers as in the NE Lau Basin. Different mantle flow regimes may be dominated by: i) hydrated mantle, due to dehydration of the subducting slab; ii) asthenospheric dry mantle, due to mantle upwelling; and iii) fertile mantle introduced into the back-arc region via flow around the subducting slab. These three mantle components are all present near the slab tear at the northeast corner of the Tonga Plate. Models suggest the fertile asthenospheric mantle is brought into the backarc by toroidal flow around the slab (e.g., Magni, 2019) and is not related to direct influx from the Samoan hotspot (Haase et al., 2022).

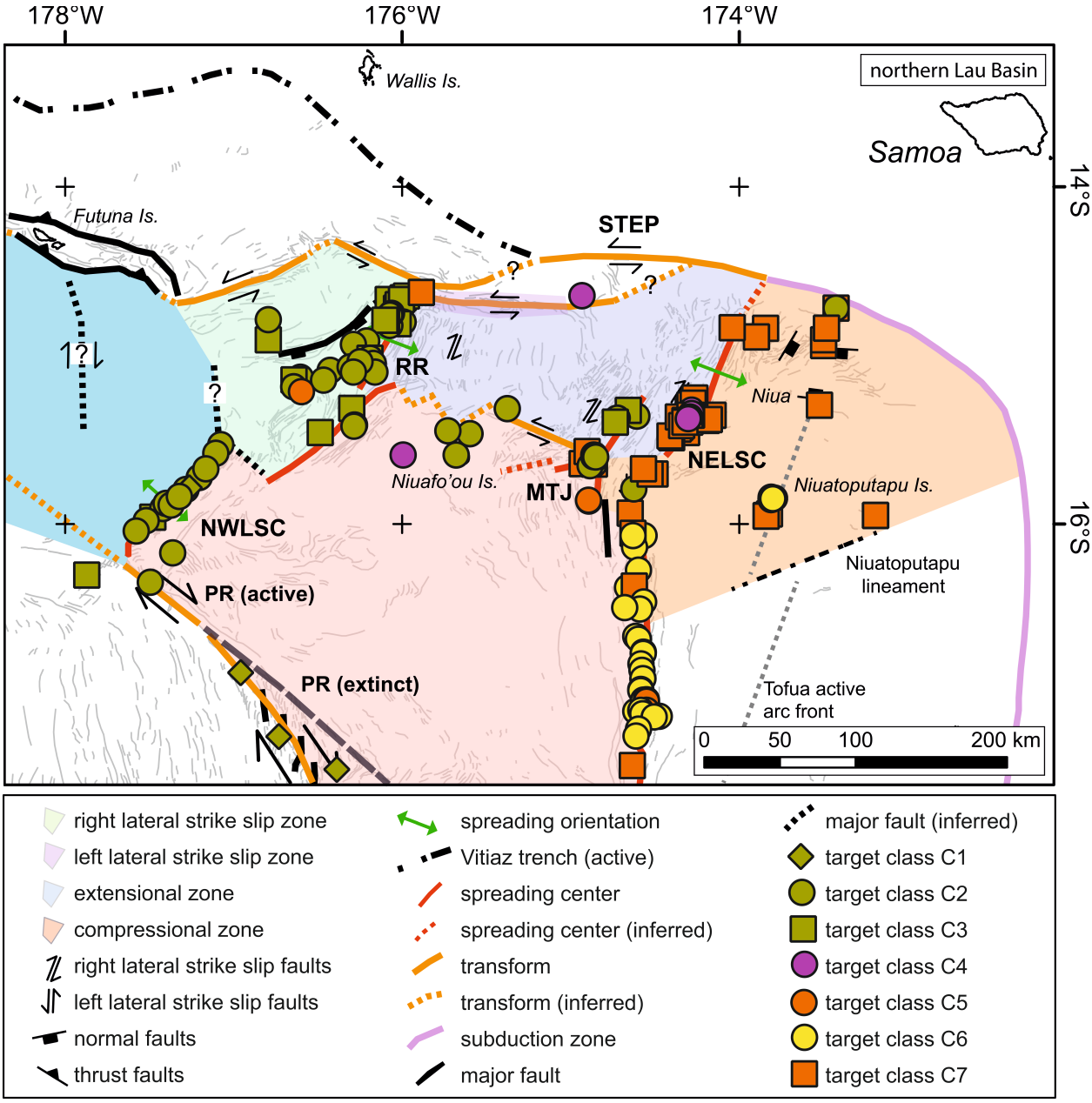


Figure 3.12: Map showing the locations of basalt belonging to different target classes in the northern Lau Basin. The different microplates of the basin are shown (from Baxter et al., 2020, and Stewart et al., 2022). Samples from the extinct Peggy Ridge (PR) belong to target class C1 (i.e., depleted MORB-like samples). Samples from the Northwest Lau Spreading Center (NWLSC) and the Rochambeau Rifts (RR) belong to target classes C2 and C3 (i.e., MORB and E-MORB-like samples). Samples from the Fonualei Rift and Spreading Center (FRSC) belong to target class C6 (i.e., arc-related rifts). Samples from the Mangatolu Triple Junction (MTJ) belong to target

classes C2, C3 (i.e., MORB and E-MORB-like samples) and C7 (i.e., nascent back-arc rift). Samples from the Northeastern Lau Spreading Center (NELSC) belong to target classes C4 (i.e., ocean island affinity) and C7 (i.e., nascent back-arc rift). See text for discussion.

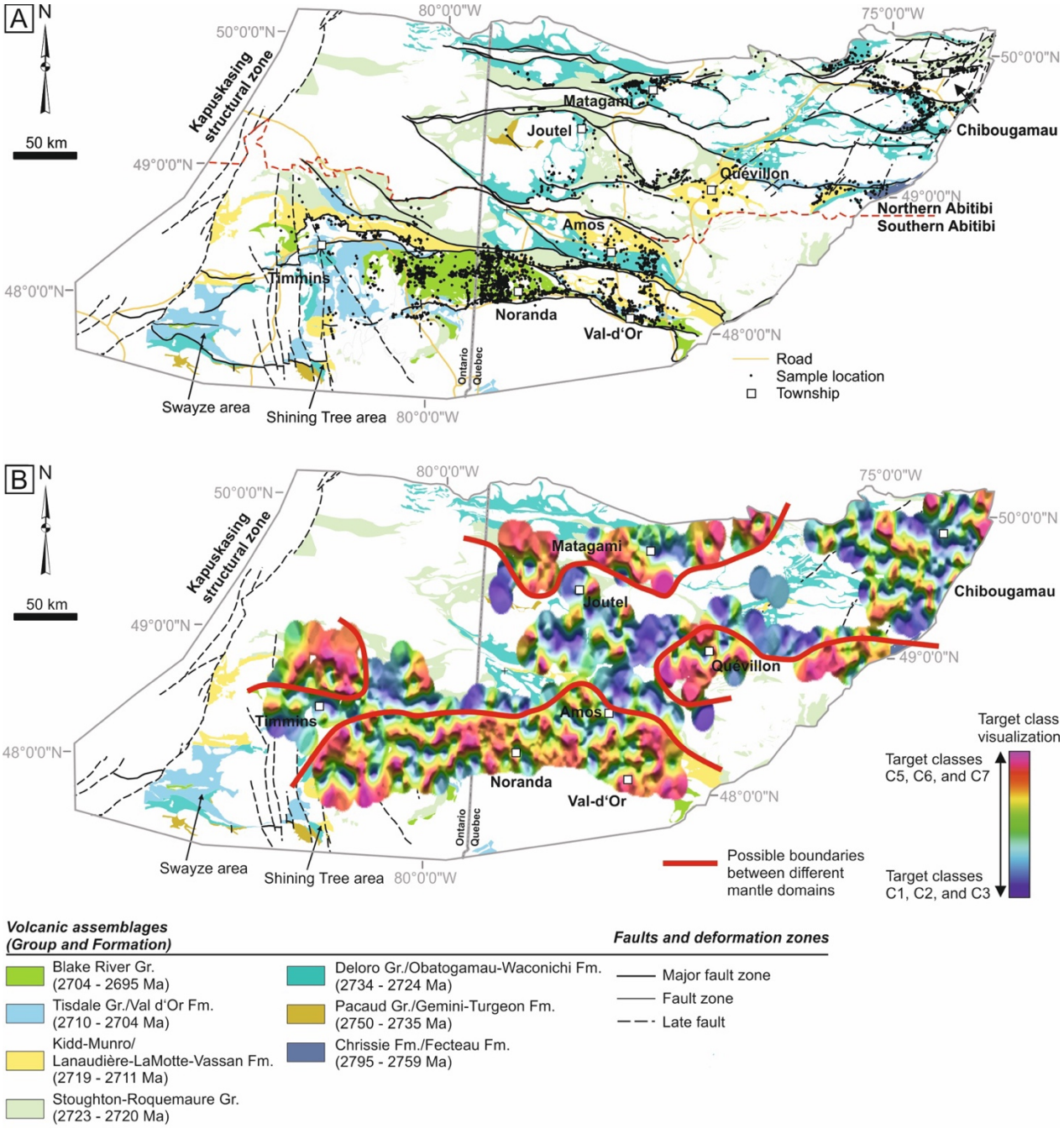


Figure 3.13: A) Geological assemblage map of the Abitibi Greenstone Belt showing the locations of mafic volcanic rock samples compiled for this study (modified from Thurston et al., 2008, Monecke et al., 2017, and Dubé and Mercier-Langevin, 2020). B) Contoured probabilities of different target classes of mafic volcanic rocks derived from the random forest classifier for modern settings developed in this study. The distribution of the different target classes indicate potential boundaries between different mantle domains (outlined in red) corresponding generally

to the north and south rift zones of the Abitibi previously identified by Mole et al. (2022) and interpreted to represent boundaries between distinct mantle domains. In the Southern Volcanic Zone, samples from the Noranda Volcanic Complex (Blake River Assemblage) mostly belong to target class C7, consistent with a combination of arc-like magmas influenced by wet melting and probable crustal contamination. Samples from the Kidd Munro Assemblage belong to target class C2, with strong similarities to ridge-hotspot intersections. In the Northern Volcanic Zone, the mafic volcanic rocks of the Deloro Assemblage also show similarities to mid-ocean ridge like tectonic settings. The colour scheme is an outcome of inverse distance weighted (IDW) interpolation of the assigned target classes of the samples shown in A). We limited the search radius for IDW interpolation to 10 km to avoid the large plutonic bodies. Sample details are provided in **Appendix B Table A13**.

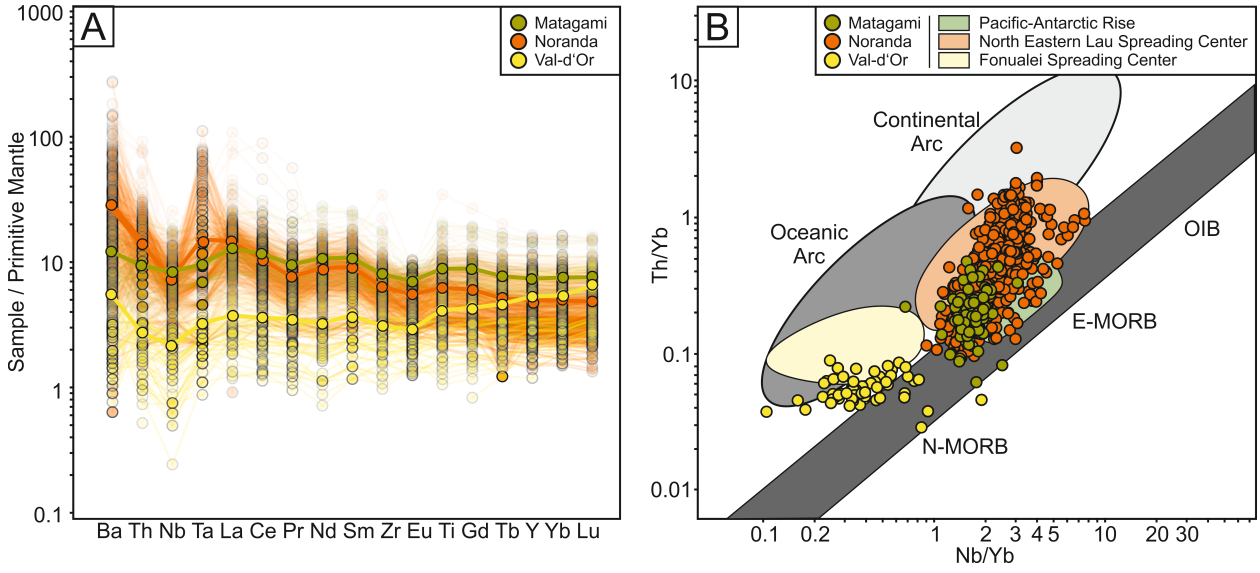


Figure 3.14: A) Primitive mantle-normalized trace element plot of representative mafic volcanic rocks from NE Matagami, Noranda, and Val-d'Or (individual samples are transparent; averages are non-transparent). Samples from NE Matagami have no negative Nb-Ta anomaly and flat REE patterns, similar to NWLSC and RR. Samples from Noranda have weak negative Nb-Ta anomalies and dipping REE patterns, suggesting limited wet melting. Samples from Val-d'Or have strong negative Nb-Ta anomalies and flat REE patterns characteristic of wet melting. B) Plot of mafic volcanic rocks from NE Matagami, Noranda, and Val-d'Or on the tectonic discrimination diagram of Pearce (2014). Samples from NE Matagami plot mostly in the E-MORB array, whereas samples from Noranda plot within or slightly below the continental arc field. Samples from Val-d'Or plot between the oceanic arc field and N-MORB array. Fields for modern oceanic mafic volcanic rocks from the Fonualei Rift and Spreading Center and Northeast Lau Spreading Center of the Lau Basin, as well as the Pacific-Antarctic Rise (see Figure 3), are shown for comparison.

Tables

Table 3.1. Summary characteristics of mafic volcanic rock compositions in modern oceanic settings.

Geodynamic setting	Lithotectonic assemblages	Example locations	Geochemical signatures	Petrogenesis	References
Mid-ocean ridge	Extensional zones, overlapping spreading centers, propagating rift tips, ridge-transform intersections	East Pacific Rise, Juan de Fuca Ridge, Galapagos Spreading Center, Pacific Antarctic Rise	48.4-51.5 wt.% SiO_2; 0.87-3.27 wt.% TiO_2; 0.01-0.41 Th/Yb; 1.76-11.35 Ba/Nb; 0.24-5.58 Nb/Yb; 0.57-2.54 La/Sm	Decompression melting by adiabatic rise of mantle material	Freund et al., 2013 Gale et al., 2013
Intraoceanic arc and back-arc	Back-arc spreading centers	**Lau Basin** (Valu Fa Rift and Spreading Center, Central Lau Spreading Center, Northwest Lau Spreading Center, Northeast Lau Spreading Center) **Manus Basin** (Manus Spreading Center) **East Scotia Ridge** (East Scotia back-arc spreading center) **Mariana Arc** (Mariana Trough back-arc spreading center)	48.5-58.4 wt.% SiO_2; 0.41-2.40 wt.% TiO_2; 0.02-2.33 Th/Yb; 3.88-191.0 Ba/Nb; 0.20-22.9 Nb/Yb; 0.47-5.0 La/Sm	Combination of wet and dry melting varying with distance from the dehydrating slab	Fretzdorff et al., 2002 Pearce et al., 2005 Fretzdorff et al., 2006 Langmuir et al., 2006 Beier et al., 2010 Escrig et al., 2012 Jenner et al., 2012 Lytle et al., 2012 Haase et al., 2022
	Arc rifts	**Izu-Bonin** (Aogashima Rift, Myjoin Rift, Torishima Rift, Sumisu Rift) **Manus Basin** (Pual Rift, Susu Rift)	47.5-58.9 wt.% SiO_2; 0.34-1.60 wt.% TiO_2; 0.32-0.57 Th/Yb; 15.3-362.4 Ba/Nb; 0.16-0.96 Nb/Yb; 0.90-2.84 La/Sm	Wet melting induced by fluids released from dehydrating subducting slab	Beier et al., 2010 Beier et al., 2015 Haraguchi et al., 2017
	Arc and back-arc volcanoes	**Lau Basin** (Niuatahi Volcano, Niuatoputapu Volcano) **Kermadec Arc** (Raoul, Healy, Monowai, Rumble) **Lesser Antilles Arc** (Montserrat)	48.1-58.9 wt.% SiO_2; 0.34-1.42 wt.% TiO_2; 0.11-1.29 Th/Yb; 36.7-302.4 Ba/Nb; 0.11-1.89 Nb/Yb; 0.85-3.71 La/Sm	Wet and dry melting	Haase et al., 2002 Zellmer et al., 2003 Todd et al., 2011 Park et al., 2015 Beier et al., 2017
Ocean island volcanism and hot-spot association	Hotspot related	**Hawaii** (Waianae Volcano) **Marquesas Archipelago** (Hane, Hanatetena, Hikitau)	42.7-51.2 wt.% SiO_2; 2.48-4.46 wt.% TiO_2; 0.30-6.57 Th/Yb; 4.52-11.67 Ba/Nb; 4.38-47.74 Nb/Yb; 2.03-6.88 La/Sm	Deep crustal melting and low degree partial melting	Zander et al., 2010 Chauvel et al., 2012
	Hotspot and MOR related	**Ascension Fracture Zone** (Ascension Island) **Iceland**	43.7-54.78 wt.% SiO_2; 1.57-3.87 wt.% TiO_2; 0.66-1.87 Th/Yb; 5.16-8.45 Ba/Nb; 10.23-23.11 Nb/Yb; 3.20-4.72 La/Sm	Low degree partial melting of enriched mantle material	Jicha et al., 2013 Zellmer et al., 2008
Intra-continental back-arc	Early-stage back-arc rift	**Ryukyu arc-backarc system** (Okinawa Trough)	45.9-58.6 wt.% SiO_2;0.58-2.75 wt.% TiO_2; 0.08-5.06 Th/Yb; 4.30-190.1 Ba/Nb; 0.42-2.31 Nb/Yb; 1.17-6.40 La/Sm	Combination of wet and dry melting varying with distance from the dehydrating slab, with variable assimilation of crustal material	Shinjo et al., 2000
	Extending marginal basin	**Antarctic Peninsula** (Bransfield Strait)			Keller et al., 2002 Fretzdorff et al., 2004

Table 3.2. Interpreted significance of trace element indicators of mafic volcanic rocks from different modern oceanic settings (see text for details and references).

Elements/Ratios	Underlying behaviour	Result	Interpretation
LILE (K, Rb, Cs, Sr, Ba)	Incompatible behaviour; high fluid mobility	High LILE in enriched sources (e.g., OIB), in fractionated melts, and in low degree partial melts; significant LILE enrichment in arc-related magmas	LILE enrichment controlled by dehydration of subducted slab; low LILE in MOR settings reflecting lack of fluid-mobilized elements and depleted mantle
HFSE (Zr, Nb, Hf, REE)	Incompatible behaviour; low fluid mobility	High HFSE in enriched sources and in fractionated melts; high HREE in low degree partial melts; significant HFSE depletion in arc-related magmas	HFSE controlled by residual enrichment compared to fluid-mobile elements and by enriched mantle sources
Nb-Ta anomaly	Incompatible behaviour; low fluid mobility	High Nb-Ta in enriched sources in fractionated melts, and in low degree partial melts; significant Nb-Ta depletion in arc-related magmas	Nb-Ta depletion due to selective enrichment of nearby elements in the multielement diagram by fluids from a dehydrating slab
Th/Yb	Th mobilized in melts only at high subduction temperatures compared to Yb; crustal assimilation of Th-enriched subduction- related crust	High Th/Yb in continental arc crust, proximal to subduction zones, and in areas of crustal assimilation settings; low Th/Yb in oceanic arcs and as a result of dry melting	High volatile input and high Th/Yb controlled by dehydration and melting of a subducted slab at high temperature; contamination by subduction related crust
Ba/Nb	Ba mobilized in melts and fluids over wide range of subduction temperatures compared to Nb	High Ba/Nb proximal to subduction zones; low Ba/Nb distal to subduction zones	High volatile input controlled by dehydration of a subducted slab
Th/Nb	Th mobilized in melts only at high subduction temperatures	High Th/Nb proximal to subduction zones; low Th/Nb distal to subduction zones	High volatile input controlled by dehydration of a subducted slab at high temperature
La/Sm	Slight difference in incompatible behaviour	High La/Sm in enriched sources (e.g., OIB); low La/Sm in depleted sources (e.g., MOR)	LREE enrichment originating from less depleted mantle (e.g., OIB); variable enrichment and mostly flat LREE patterns due to mantle heterogeneity and degrees of depletion
Nb/Yb	Slight difference in incompatible behaviour	High Nb/Yb in enriched sources (e.g., OIB); low Nb/Yb in depleted sources (e.g., MOR)	Enriched mantle sources and low degrees of melting

Table 3.3. Summary attributes of the target classes of oceanic mafic volcanic rocks according to tectonic setting.

Cluster	Lithotectonic assemblages	Type examples*	Trace element characteristics	PCA loadings
C1	Depleted mid-ocean ridges and mature back-arc spreading centers	East Pacific Rise; Central Lau Spreading Center	Very low La/Sm, very low La/Yb, very low Ba/Nb, very low Th/Yb, very low Nb/Yb; no negative Nb-Ta anomaly	Very high Yb and Y loadings on PC1 and low Th and La loadings on PC2
C2	Undepleted mid-ocean ridges and mature back-arc spreading centers	Mid-Atlantic Ridge; Central Scotia back-arc spreading center	Low La/Sm, low La/Yb, very low Ba/Nb, low Th/Yb, low Nb/Yb; no negative Nb-Ta anomaly	High Yb and Y loadings on PC1 and low Th and La loadings on PC2
C3	Enriched mid-ocean ridges and mature back-arc spreading centers	Galapagos Spreading Center; Northwestern Lau Spreading Center, Rochambeau Rift	Intermediate La/Sm, intermediate La/Yb, very low Ba/Nb, intermediate Th/Yb, intermediate Nb/Yb; no negative Nb-Ta anomaly	Intermediate Yb, Y Th and La loadings on PC1 and PC2
C4	Ocean island related settings	Ascension Island, Hawaii	High La/Sm, high La/Yb, low Ba/Nb, high Th/Yb, high Nb/Yb; no negative Nb-Ta anomaly	High Nb and Zr loadings on PC2 and low Al and Yb loadings on PC1
C5	Back-arc and arc-related rifts	Myojin Rift (Izu-Bonin), Ngatoroirangi Rift (Havre Trough)	Intermediate La/Sm, intermediate La/Yb, intermediate Ba/Nb, intermediate Th/Yb, low Nb/Yb; moderate negative Nb-Ta anomaly	Very high Al loadings on PC1 and low La and Nb loadings on PC2
C6	Arc volcanoes and arc-related rifts	Fonualei Rift and Spreading Center (Lau Basin), Tofua volcano (Tofua arc)	Intermediate La/Sm, high Ba/Nb, high Th/Yb, low Nb/Yb, strong negative Nb-Ta anomaly	High Al and Ba loadings on PC1 and low Zr and Nb loadings on PC2
C7	Nascent back-arc rift and continental margin crust	Bransfield Strait	High La/Sm, intermediate Ba/Nb, high Th/Yb, intermediate Nb/Yb, moderate negative Nb-Ta anomaly	High Ba, Th and La loadings on PC1 and low Yb and Ti loadings on PC2

Chapter 4

Highly Episodic Growth of the Niuafo'ou Microplate, NE Lau Basin, from Ar-Ar Dating: Implications for Crustal Growth in Greenstone Belts

Article in prep.: Fassbender, M.L., Hannington, M., Baxter, A.T., Diekrup, D., Stewart, M.S., and Brandl, P.A., Highly Episodic Growth of the Niuafo'ou Microplate, NE Lau Basin, from Ar-Ar Dating: Implications for Crustal Growth in Greenstone Belts.

Abstract

The northern Lau Basin formed as a complex microplate mosaic following the collision of the Ontong Java Plateau with the Indo-Australian margin. The opening of the basin was accommodated by crustal growth of numerous microplates bordered by discrete spreading centers. However, interpretation of their growth history has been complicated by a lack of clearly defined magnetic chrons. This study attempts to resolve part of the growth history of the largest microplate, Niuafo'ou, by establishing absolute ages of the crust across its southern margin using Ar-Ar dating.

The Niuafo'ou microplate is bound by the Mangatolu Triple Junction, the Fonualei Rift, the Central Lau Spreading Center (CLSC), the Lau Extensional Transform Zone, the Peggy Ridge and the Northwestern Lau Spreading Center. However, its northern and southern boundaries are less clear, showing no seismic activity typical for plate boundaries. New Ar-Ar ages of volcanic rocks from the southern margin of the microplate provide evidence of complex ridge jumps, rift propagation into older crust, and diffuse extension since 5.5 Ma, with rocks as young as 13.4 ka and as old as 11 Ma forming part of the microplate. The ages of 7 samples within an area of just a few 100 km^2 span the entire age range of the opening of the basin with significant geochemical variability from mid-ocean ridge-like lavas to arc-like lavas. The oldest rocks record the earliest stages of back-arc basin opening and the presence of relict arc crust from an early phase of asymmetric rifting now stranded in the middle of the plate. The youngest rocks immediately southwest of the Fonualei Rift are thought to be related to the emergence of a new plate boundary. Key observations are the range of ages compared to the width of the basin (and inferred spreading rates), the clear progression in ages increasing from east to west, and the unexpected proximity of crust that dates from the earliest opening of the basin to the actively spreading CLSC. The old crust found at this location could not have been derived from the nearby spreading center but must have come from earlier asymmetric spreading closer to the arc. The observed age differences are also strongly correlated to the whole-rock geochemistry.

The new Ar-Ar ages challenge the view of back-arc basin opening as a linear progression from rifting to eventual spreading with uniform crustal accretion and growth. The result can be a complex structural evolution and interaction of mantle sources that are not uniquely tied to a single spreading center. Similar data from greenstone belts, the ages of which are well constrained by U-Pb zircon dating, also span several millions of years within a few 10s of kilometers and likely reflect similarly complex crustal growth history.

4.1 Introduction

The opening of back-arc basins is among the most complex processes at convergent margins (Taylor and Martinez, 2003; Langmuir et al., 2006; Yan et al., 2013, 2020). Studies have shown volcanic rocks exhibit strong spatial and temporal variations in geochemistry that reflect the progress of basin opening (Taylor and Martinez, 2003; Langmuir et al., 2006; Ueki et al., 2018; Zhang et al., 2018; Yan et al., 2020; Fassbender et al., 2023). A common interpretation in modern arc and back-arc environments (and greenstone belts) is that early arc-related calc-alkaline magmas evolve to more transitional and tholeiitic compositions with the opening of the basin (Taylor et al., 2003; Langmuir et al., 2006). Many authors have recognized that the transition from arc rifting to back-arc basin formation is rarely a uniform geodynamic process, with many complex deviations caused by rift propagation, overlapping spreading centers, and transcurrent faulting (Anderson et al., 2021; Sleeper et al., 2021; Stewart et al., 2022). However, interpretation of the growth history can be difficult because of a lack of clearly defined magnetic chrons in many basins.

The Lau back-arc basin is an ideal location to study the relationship between arc rifting, basin opening, the growth of back-arc crust and highly variable melt compositions. Previous studies have focused on individual spreading centers in the Lau Basin, highlighting the rapid opening of the basin since 6 Ma and the diversity of geochemical signatures of the volcanic rocks along the spreading centers depending on the distance from the arc (Fretzdorff et al., 2006; Keller et al., 2008; Bézos et al., 2009; Escrig et al., 2009, 2012; Haase et al., 2009; Tian et al., 2011; Meffre et al., 2012; Zhang et al., 2018; Yan et al., 2020). Most studies assume a basic principle of seafloor spreading: that the age of the crust increases linearly with distance from the spreading ridge. However, few attempts have been made to precisely date the volcanic rocks and establish their

link to specific spreading centers (Yan et al., 2012). In this study, we show that the origin of back-arc crust is not always clearly linked to proximal sources of melt, and interpretation of crustal age or composition in terms of distance from the spreading ridge can be complicated by a pattern of distributed rather than localized extension (e.g., Martinez et al. 2018; Sleeper et al., 2021).

The Niuafo'ou microplate is the largest intact region of back-arc crust in the northern Lau Basin. It is bordered by at least 7 spreading centers with different spreading rates (**Figure 4.1**; Zellmer and Taylor, 2001; Sleeper et al., 2016; Sleeper and Martinez, 2016). Its crustal structure in the west shares many similarities with typical mid-ocean ridge crust, while eastern portions share similarities with arc rifting and back-arc spreading (Sleeper and Martinez, 2016). There is also significant geochemical diversity reflecting a range of crustal thickness, dry versus wet melting, and complex mantle flow (Fassbender et al., submitted). However, the growth history of the plate remains poorly understood. The southern plate boundary is indistinct and shows no obvious morphologic or seismic evidence of deformation. Although the location of the plate boundary was suggested by Zellmer and Taylor (2001), there is still some uncertainty regarding the exact location and the lack of closure between the established plate boundaries (Sleeper and Martinez, 2016). Because the mapped structures do not meet, the nascent plate boundary has been interpreted as an area of non-rigid deformation, with the precise location of a triple junction still unclear (Baxter et al., 2020; Stewart et al., 2022). Previous authors attributed much of the geochemical variability to input of volatiles and melt with proximity to the active arc. Accordingly, samples closest to the subduction zone record input from the dehydrating subducting slab, while samples further away are more mid-ocean ridge-like basalts resulting from decompression melting (e.g., Keller et al., 2008; Bézos et al., 2009; Escrig, et al., 2009, 2012; Yan et al., 2012; Zhang et al., 2018). However, all previous studies have focused only on the youngest volcanic products along the active spreading centers. To better understand the relationship of the geochemical signatures to the history of crustal growth, it is essential to know the absolute ages of samples away from the active spreading centers.

Previous models of the opening of the northern Lau Basin mostly relied on magnetic reversals (Zellmer et al., 2001; Zellmer and Taylor, 2001; Sleeper and Martinez, 2016). However, the pattern of the magnetic anomalies particularly east of the Central Lau Basin is unclear (Sleeper and Martinez, 2016). In this study, we report Ar-Ar dates of 7 samples of lavas collected between the

Fonualei Rift and the Central Lau Spreading Center in the region of missing strain originally identified by Conder and Wiens (2011) in the south of the Niuafo'ou microplate. The results show significant differences between the crystallization ages of a range of lavas and the interpreted spreading ages or ages based on magnetic chrons, confirming a much more complicated spreading regime than previously suggested for the region.

4.2 Emergence of the Niuafo'ou Microplate

The Lau Basin is the type locality for intra-oceanic back-arc basin formation, first recognized by Karig (1970). The V-shaped basin is up to 450 km wide in the north and measures 1000 km in length (Taylor et al., 1996; Smith et al., 2001; Keller et al., 2008; Sleeper and Martinez, 2014). It is bordered by the active Tofua Arc in the east, the remnant Lau Ridge in the west, and the Vitiaz lineament in the north. The opening of the basin was triggered by the collision of the Ontong Java and Melanesian Borderland plateaus with the Australian plate in the Miocene (Ruellan et al., 2003; Ruellan and Lagabrielle, 2005). Progressive splitting of the older arc crust and asymmetric opening toward the west is reflected in the shape of the basin. Active seafloor spreading started between 6 and 5.5 Ma in the north and has since propagated 700 km south (Parson and Hawkins, 1994; Ruellan et al., 2003). The now inactive Lau Ridge (former Vitiaz arc) in the west of the basin originally separated from the Tonga Ridge at the forearc, resulting in almost all of the original Eocene arc becoming part of the Lau Ridge (Taylor et al., 1996). Active volcanism continued in the remnant arc even as the early back-arc basin opened (Hawkins, 1995). Arc magmatism in the west eventually stepped across the basin and reinitiated closer to its present position along the Tofua arc (Martinez and Taylor, 2006). Active rifting of the Tofua arc has resumed at several locations, including the Valu Fa Ridge (VFR) in the south, the Fonualei Rift (FRSC), and the Northeast Lau Spreading Center (NELSC) in the north (**Figure 4.1**).

Zellmer and Taylor (2001) first proposed a three-plate kinematic model for the region consisting of the Australian plate to the west, the Niuafo’ou microplate between the FRSC and the Central Lau Spreading Center (CLSC), and the Tonga plate to the east. Magnetic chrons and GPS measurements show that opening between the northern Tonga Ridge and the Lau Ridge is occurring at 91 and 159 mm/yr in the south and >160 mm/yr in the north (Bevis et al., 1995).

However, different models disagree on the distribution of strain (Pelletier et al., 2001; Zellmer and Taylor, 2001; Conder and Wiens, 2011; Sleeper and Martinez, 2016). Today, the opening is partitioned among several spreading systems (**Figure 4.1**; Stewart et al., 2022). They include, in the south, the Eastern Lau Spreading Center (ELSC) and its southern extension along the Valu Fa Ridge (VFR), the Central Lau Spreading Center (CLSC) and the Lau Extensional Transform Zone (LETZ), a short relay zone between the ELSC and CLSC, the Northeast Lau Spreading Center (NELSC), the Mangatolu Triple Junction (MTJ) and the Fonualei Rift and Spreading Center (FRSC). This geometry was first described from GLORIA side-scan sonar surveys (Parson et al., 1990) and has since been refined by analysis of regional magnetics, gravity, and SeaMARC II side-scan sonar data (Zellmer and Taylor, 2001; Martinez and Taylor, 2006; Sleeper and Martinez, 2014, 2016; Sleeper et al., 2016). North of the Niuafo'ou microplate, a complex pattern of small, poorly defined microplates has been recognized that formed in response to left-lateral shear (Conder and Wiens, 2011; Baxter et al., 2020), suggesting that the northern margin of the basin is highly unstable and actively breaking up (Baxter et al., 2020). Both the ELSC and CLSC are propagating south at an estimated rate of 120 mm/yr (Parson et al., 1990). Spreading at the northern end of the ELSC is interpreted to be 102 mm/yr and more than 120 mm/yr at the CLSC (Sleeper and Martinez, 2006). Based on spreading fabric and magnetic anomalies, the ELSC initially formed near 17°S and has propagated south. Its northern segment has since been taken over by the CLSC near 18°S, which is now the main spreading center as far north as 19.5°S (Sleeper and Martinez, 2014). The overlap between the ELSC and CLSC is marked by numerous sub-basins interpreted to be failed rift segments (Parson et al., 1990; Sleeper and Martinez, 2016).

Zellmer and Taylor (2001) originally placed the Euler pole for opening of the northern Lau Basin in the far south and proposed a "diffuse" boundary between the Niuafo'ou and Tonga Plates requiring high deformation rates (>40 mm/yr). However, shallow seismicity shows that the main extensional faulting is occurring only at the northern and southern terminations of the spreading segments (Conder and Wiens, 2011; Baxter et al., 2020). Little evidence could be found for the southern boundary of the Niuafo'ou microplate. To account for the missing strain, it was proposed that the Euler pole is located much closer to the northern termination of the ELSC. Sleeper et al. (2016) revised the position further, moving it to the southern termination of the FRSC. Although moving the Euler pole helped to satisfy the three-plate kinematic solution, it did not address the

lack of seismicity or clearly identify an active plate boundary in the south of Niuafo'ou. Maximum spreading at the FRSC was originally estimated at 94 mm/yr in the north (Zellmer and Taylor, 2001); however, Sleeper and Martinez (2016) predicted much slower opening rates (~8 mm/yr) at the southern tip of the FRSC, which is in better agreement with the seafloor magnetization patterns and ridge morphology. The volcanic rocks of the FRSC are dominated by fluid-fluxed melt components from the dehydrating subducting slab, which decrease in importance to the north with increasing distance of the FRSC from the arc (Keller et al., 2008). A new volcanic center is also emerging in advance of the southward propagating rift tip of the FRSC. Although there is no clear connection between the FRSC and northernmost termination of the ELSC, volcanic ridges in this area are aligned subparallel to the FRSC. The large nodal basins between the ELSC and CLSC have a similar orientation.

Stewart et al. (2022) reviewed the geochronological framework established from magnetic chrons and assigned ages to different assemblages (**Figure 4.2**). Although the ages of the magnetic anomalies are not well known, Zellmer and Taylor (2001) postulated a paleo-spreading axis near the arc during magnetic anomaly 2 (Gaus magnetic polarity chron: 3.58–2.58 Ma), with the spreading axis moving away from the arc as the basin opened. The crustal ages (**Figure 4.3**) in the area correspond generally to: i) the Gauss magnetic chron (3.58–2.58 Ma) in the west of the basin; ii) the Matuyama magnetic chron (2.58–0.78 Ma) in the East Lau Assemblage; iii) the Brunhes magnetic chron (<0.78 Ma) in the Central Lau Assemblage. Rifting of the arc crust at the FRSC is thought to have initiated during magnetic anomaly 2A (3.05–2.58 Ma: Sleeper and Martinez, 2016) and is actively propagating into the arc today. However, ship-based data show strong variation in the magnetic fabric in this area, and in detail it is difficult to interpret in terms of magnetic chrons (Barckhausen et al., 2019; Hannington et al., 2019). To better constrain the progression of ages across the southern boundary of the Niuafo'ou microplate, we dated samples from 7 locations spanning the diffuse zone of extension between the southern tip of the FRSC and the northern termination of the ELSC (**Figure 4.4**).

4.3 Samples

Fresh mafic volcanic rock samples from seven dredges in the area (Hannington et al., 2019) were chosen for study based on the presence of fresh glass, fine-grained matrix and unaltered plagioclase phenocrysts. In each case the dredges were conducted on the upper flanks of volcanic structures free of sediment.

Sample SO267-DR48 (**Figure 4.5**) was collected from a small conical volcano located 40 km southwest of the southern tip of the Fonualei Rift. The sampled material is composed of massive and moderately vesicular mafic volcanic rock. The cones formed on older arc crust in this area are thought to be the most recent volcanic features of the FRSC rifting (Hannington et al., 2019). Magnetic chrons are difficult to interpret and mainly reflect the arc basement (Zellmer and Taylor, 2001), whereas the freshness of the glass from the sampled cone suggest that the lavas are much younger.

Sample SO267-DR49 (**Figure 4.6**) was dredged from a series of small fissure volcanoes about 50 km south of the FRSC (and south of SO267-DR48). Fresh volcanic material similar to DR48 was recovered. This location is considered to be part of a young magmatic center emerging in advance of the southward-propagating FRSC (Hannington et al., 2019). As for DR48, the freshness of the glass suggests that the lavas are much younger than the interpreted magnetic chron in the area.

SO267-DR60 (**Figure 4.7**) was sampled close to the location of DR49 and also consists of fresh, massive, and moderately vesicular mafic volcanic rock. As for DR48 and DR49, the freshness of the glasses suggest that the lavas are young.

SO267-DR58 (**Figure 4.8**) was collected from the southern of three north-south striking volcanic ridges, 25 km west of the Tofua arc, in a heavily sedimented area at the transition from the arc to the back-arc basin. The recovered samples consist of blocky, massive, moderately vesicular mafic volcanic rock as well as hydrothermally altered volcaniclastic material. The ridges are located in the rear-arc crust parallel to the FRSC and the actively ELSC and CLSC (Hannington et al., 2019). This area is interpreted to be a transition zone between the northernmost ELSC and southernmost FRSC, possibly incorporating some of the missing strain in this area (e.g., Conder and Weins,

2011; Baxter et al., 2020). The assigned magnetic anomaly is a subchron (Olduvai) of the Matuyama reversals with an age of 1.78 – 2.00 Ma (Sleeper and Martinez, 2016). It is unclear if the volcanic rocks at this location are part of the crust derived from the ELSC or CLSC or if they are dike-like intrusions into the rear-arc crust between the FRSC and ELSC.

SO267-DR65 (**Figure 4.9**) was collected from the inside wall of a nodal basin in back-arc crust about 160 km southwest of the FRSC. The recovered samples are composed of slightly vesicular mafic volcanic rock and strongly altered rock with a gabbroic texture. This location was selected to sample the back-arc crust in the narrow basins interpreted to be failed rifts in the overlap between the ELSC and CLSC (Sleeper and Martinez, 2016). The magnetic chrons assigned to this area correspond to the Matuyama anomalies with ages of 2.58 – 0.78 Ma (Zellmer and Taylor, 2001).

SO267-DR69 (**Figure 4.10**) was collected from a large volcanic edifice in the south-central part of the Niuafo'ou microplate. The sampled material consists of mafic to intermediate, moderately vesicular and partly olivine-, and feldspar-phyric lava with variable degrees of alteration. The origins of the volcanic edifices in this part of the plate are uncertain but could be intraplate volcanoes, parts of abandoned spreading centers, or relict crustal fragments from the early opening of the basin. The magnetic chrons assigned to this area correspond to the Gaus anomalies with ages of 3.58–2.58 Ma (Zellmer and Taylor, 2001).

SO267-DR77 (**Figure 4.11**) was collected from the wall of another nodal basin about 150 km southwest of the FRSC. The sampled material consists of massive, non-vesicular to moderately vesicular, mafic volcanic rock. As for DR 65, this narrow basin is interpreted to be a failed rift in the abandoned overlap between the ELSC and CLSC (Sleeper and Martinez, 2016). The magnetic chrons assigned to this area also correspond to the Matuyama anomalies with ages of 2.58–0.78 Ma (Zellmer and Taylor, 2001).

The samples selected for dating range from aphyric to medium-grained with small phenocrysts of plagioclase, clinopyroxene, olivine +/- orthopyroxene, and Fe-Ti oxides. The majority of the lavas have a groundmass that is composed of fine-grained crystalline material with only minor devitrified interstitial glass. However, the plagioclase phenocrysts were generally not large enough for clear separation; only one sample contained plagioclase phenocrysts of sufficient quality for

age determination. Details of the petrography of the samples are provided below. Geochemical data for all samples are summarized in **Table 4.1**. The samples can be divided into 3 distinct groups based on their geochemical signatures: those with strong arc signatures (DR48, DR49 and DR60), those with weak arc signatures (DR58 and DR77), and those with no arc signatures (DR65 and DR69), according to the classifications of Fassbender et al. (submitted). The samples with strong arc signatures have large negative Nb-Ta anomalies, LILE enrichment, low HFSE concentrations, high Th/Yb and high Ba/Nb ratios. Samples with weak arc signatures have small negative Nb-Ta anomalies, weak LILE enrichment, low HFSE concentrations, intermediate Th/Yb and intermediate Ba/Nb ratios. Samples with no arc signatures lack the negative Nb-Ta anomalies, have low LILE enrichment, intermediate HFSE concentrations, low Th/Yb and low Ba/Nb ratios (**Figure 4.12**).

4.4 Methodology

Ar-Ar dating is an effective method for determining crystallization ages of young mafic volcanic rocks. Sample preparation was carried out at the GEOMAR Helmholtz Centre for Ocean Research in Kiel, Germany and at the University of Ottawa, Canada. Whole-rock blocks were dried for 24 h at 50 °C, crushed in a steel jaw crusher, sieved into 5 size fractions (< 0.25 mm, 0.25 - 0.5 mm, 0.5 - 1 mm, 1 - 2 mm, > 2 mm), repeatedly washed in deionized water in an ultrasonic bath to remove seawater salts, fine dust and adhering fragments and afterwards dried in an oven at 50 °C for 24 h again. First, in an attempt to produce datable plagioclase separated, the 0.25 - 0.5 mm fractions were handpicked using a binocular microscope. The plagioclase separates were further investigated for inclusions and other potential sources of contamination using the scanning electron microscope at the University of Ottawa. Many of the plagioclase samples showed signs of alteration, leading to significant loss of plagioclase during the HF bath (see below). As a result, there was only enough material left for a reliable age determination on one sample. Instead, we used the <0.25 mm size fraction for the recovery of groundmass material, which is a useful approach when plagioclase crystals are of insufficient quality (Koppers et al., 2000, 2003). A larger portion of the sample was recovered than in the plagioclase separates providing a better age determination in each case.

Analyses of the samples were performed at the Oregon State University (OSU) Argon Geochronology Laboratory, USA. The groundmass samples were rinsed with distilled water several times until the water remained clear, and then the sample was dried in an oven at ~ 80 °C for several hours. Magnetic and heavy-liquid separation were performed to remove any oxides or other undesirable mineral phases from the groundmass material. This was followed by mild acid cleaning (1 N acetic acid to remove carbonates, 1 N HNO_3) to remove minor alteration, ultrasonic washing in DI water, and drying again. Plagioclase phenocrysts were further cleaned with a short 5-minute wash in 5 % HF. However, most of the plagioclase was dissolved.

The leached samples were irradiated for 6 h in the TRIGA nuclear reactor at OSU, together with the FCT sanidine flux monitor. The individual J-values (i.e., a measure of the fraction of radiogenic argon) for each sample were calculated by parabolic extrapolation of the measured flux gradient against irradiation height, which typically gives 0.1 - 0.2 % uncertainties (1σ). The Ar-Ar incremental heating age was determined with two multicollector ARGUS-VI mass spectrometers. After loading the irradiated samples into Cu-planchettes in an ultra-high vacuum sample chamber, they were incrementally heated by scanning a defocussed 25 W CO_2 laser beam in pre-set patterns across the sample, in order to release the Ar evenly. Each pass involved incremental heating of groundmass material or plagioclase phenocrysts. Samples were held in the extraction line for a total time of 3 - 6 min. Blank intensities were measured every 3 steps of incremental heating for groundmass and every 2 steps for plagioclase phenocrysts. The ArArCALC v2.7.0 software available from the https://earth ref.org/ArArCALC/ website was used by the lab to calculate the ages and their errors (Koppers, 2002). The complete analytical metadata are given in Appendix C.

4.5 Results and interpretation

All seven groundmass samples and one plagioclase sample returned usable ages. The results are shown in **Table 4.2** and **Figure 4.13**. Good analytical reproducibility was achieved for all samples, and internal reproducibility is indicated by agreement between concordant plateaus, inverse isochrons, and total fusion ages at the 2-sigma confidence level (**Table 4.2** and Appendix C; Koppers et al., 2000). Loss of mass during the HF bath of the plagioclase separates indicates alteration of the plagioclase phenocrysts in samples DR60 and DR69. The samples DR48, DR49,

DR58, and DR65 had enough plagioclase after the HF bath but mostly atmospheric argon was measured in these samples.

The data are presented as plateau ages and inverse isochron ages. Plateau ages reflect constant argon ages across a range of temperatures and are considered to be representative of the eruption age. In cases where the sample has undergone argon loss or alteration, we use the inverse isochron ages. In this method, the $^{39}Ar/^{40}Ar$ ratio from individual heating steps is plotted against $^{36}Ar/^{40}Ar$ from the same steps (see Appendix C), and the best fit through the data points yields the $^{40}Ar/^{39}Ar$ value. The $^{40}Ar/^{39}Ar$ values at the x-intercept is purely radiogenic from which the age is determined.

SO267 DR48-1B: The sample selected for dating contains ~ 30% round to elongate vesicles ranging in size from 0.1 to 1.5 mm (**Figure 4.5**). The sample has a slightly porphyritic texture, with a groundmass composed of fine pyroxene, plagioclase needles, and some brownish glass as well a few olivine crystals. Plagioclase phenocrysts measure up to 1.5 mm and have no chemical zonation. Low-temperature heating steps of the groundmass of this sample yield $^{40}Ar/^{39}Ar$ proportions that result in young ages and high K/Ca values measured during the step heating process (**Figure 4.13A** and **B**). This suggests that altered phases in the groundmass–located interstitially and at grain boundaries of the fine-grained plagioclase/pyroxene have undergone degassing. The plateau age of 146.2 ± 82.1 ka has a large error but agrees with the inverse isochron age of 147.0 ± 61.5 ka, indicating that this is the eruption age. Heating of the plagioclase phenocrysts yielded only atmospheric argon.

SO267 DR49-1: The sample selected for dating contains ~20 % round to elongate vesicles ranging from 0.1 to 1.0 mm in length (**Figure 4.6**). The sample has a well crystallized hyalopilitic texture with only few phenocrysts that measure up to 0.5 mm. The groundmass consists of fine pyroxene, plagioclase needles, some brownish glass and few olivine crystals. The step-heating profile of the groundmass sample shows a well-developed plateau from low to high temperatures. K/Ca ratios only slightly decrease indicating that alteration phases in the groundmass are minor components (**Figure 4.13C** and **D**). The plateau age of 13.4 ± 21.9 ka has a large error but generally agrees

with the inverse isochron age of 13.4 ± 21.9 ka, which is interpreted to be the eruption age. Heating of the plagioclase phenocrysts yielded only atmospheric argon.

SO267 DR58-4: The sample selected for dating contains ~50 % spherical to elongate vesicles that range from 0.1 to 1.5 mm in length (**Figure 4.7**). The sample has a slightly porphyritic texture. The groundmass consists mostly of fine plagioclase needles. Pyroxenes and brownish glass are minor components. Plagioclase phenocrysts measure up to 1.5 mm and have no chemical zonation. Low-temperature steps in the step heating of the groundmass sample yield $^{40}Ar/^{39}Ar$ proportions that result in young ages and the high K/Ca indicates degassing of altered phases that are located interstitially or at the grain boundaries of fine-grained plagioclase/clinopyroxene in the groundmass (**Figure 4.13E** and **F**). The plateau age of 1.64 ± 0.07 Ma agrees with the inverse isochron age of 1.64 ± 0.14 Ma, which is interpreted to be the eruption age. Heating of the plagioclase phenocrysts yielded only atmospheric argon.

SO267 DR60-1B: The sample selected for dating contains ~20 % spherical to elongate vesicles that range from 0.1 to 1.0 mm in length (**Figure 4.8**). The sample has a slightly porphyritic texture, and the groundmass consists mostly of fine plagioclase needles and a few magnetite crystals. Pyroxenes and brownish glass are minor components. Plagioclase phenocrysts measure up to 0.8 mm and have no chemical zonation. The low-temperature steps of heating the groundmass yield $^{40}Ar/^{39}Ar$ proportions that result in young ages and high K/Ca indicating degassing of altered phases (**Figure 4.13G** and **H**). The plateau age of 20.5 ± 35.1 ka has a large error but mostly agrees with the inverse isochron age of 55.8 ± 23.7 ka, indicating the eruption age. All plagioclase phenocrysts in this sample were completely dissolved during the HF-leaching.

SO267 DR65-1G: The sample selected for dating contains < 5 % vesicles (**Figure 4.9**). The sample has a slightly porphyritic texture, with plagioclase phenocrysts up to 2 mm, and the groundmass consists mostly of fine plagioclase needles, pyroxene and a few magnetite crystals. Brownish glass is a minor component. Low temperature steps of heating the groundmass yield $^{40}Ar/^{39}Ar$ proportions that result in young ages and high K/Ca (**Figure 4.13I** and **J**) indicating degassing of altered phases. The plateau is not well developed, but the K/Ca remains low throughout this part of the heating spectrum suggesting that the ages may not have been significantly affected. The

minor plateau gives an age of 5.05 ± 1.00 Ma, which agrees with the inverse isochron age of 4.47 ± 1.60 Ma, indicating the eruption age. Heating of the plagioclase phenocrysts yielded only atmospheric argon.

SO267 DR69-2A: The sample selected for dating contains < 5 % vesicles (**Figure 4.10**). The sample has a slightly glomerophyric texture and few phenocrysts. The plagioclase phenocrysts measure up to 1.5 mm but are a minor component. The groundmass consists mostly of fine plagioclase needles, pyroxene, and a few magnetite crystals. Brownish glass is a minor component. Step heating of the groundmass of this sample gave a well-developed plateau from low to high temperatures, and K/Ca ratios decrease only slightly indicating that alteration phases in the groundmass are minor components (**Figure 4.13K** and **L**). The plateau age of 11.81 ± 1.83 Ma agrees with the inverse isochron age of 11.78 ± 3.60 Ma. All plagioclase phenocrysts in this sample were completely dissolved during the HF-leaching.

SO267 DR77-4A: The sample selected for dating contains no vesicles (**Figure 4.11**). The sample is slightly coarse grained and has a doleritic texture; it is fully crystallized and consists mostly of plagioclase, pyroxene and olivine. The crystal size varies between 0.2 to 1.5 mm. This was the only sample where alteration of coarse-grained plagioclase did not prevent a meaningful analysis. The low-temperature steps of the heating of plagioclase phenocrysts yield $^{40}Ar/^{39}Ar$ proportions that result in young ages and high K/Ca, indicating degassing of altered phases, most likely on the surfaces of the plagioclase crystals or degassing of fluid inclusions (**Figure 4.13M** and **N**). The plateau age has a significant error of 3.13 ± 4.06 Ma but agrees well with the inverse isochron age of 3.82 ± 1.35 Ma, which is interpreted to be the crystallization age of the plagioclase. This sample did not have any fine-grained groundmass.

4.6 Discussion

The Ar-Ar age data of the southern Niuafo'ou microplate highlight the complexity of crustal growth in the northern Lau Basin. Opening of the basin ~6 m.y. ago started with a characteristic V shape and asymmetric widening of the basin toward the west. However, sampling during Leg 135 of the Ocean Drilling Program (ODP) gave a range of ages spanning several millions of years that did not increase linearly with distance from the inferred spreading center (Hawkins, 1995).

Instead, seafloor morphology and the thickness and composition of sediment in numerous sub-basins indicated a more complex history. Results from ODP Leg 135 confirmed that volcaniclastic sediments in the local basins were derived first from the west and then from the east as the Lau Ridge separated from the Tonga Platform (Clift and Dixon, 1994).

Within the last 2-3 m.y., basin opening has been further complicated by the emergence of multiple spreading centers and new microplates. Individual spreading centers in the south have higher spreading rates but the larger number of microplates in the north accommodate overall greater opening (Stewart et al., 2022). This opening likely adjusted episodically to overlapping spreading between the ELSC and CLSC and to ridge jumps (e.g., to the current location of the FRSC). The deep "nodal" basins in the transfer zone between the ELSC and CLSC are thought to be relics of the east-west extension, now dominated by shear stresses along within-plate strike-slip faults (Baxter et al., 2020). Early suggestions of an emerging plate boundary in the south of the Niuafo'ou microplate (e.g., Conder and Wiens, 2011) are supported by the evidence of diffuse deformation at the southern tip of the FRSC (Baxter et al., 2020).

The ages of the samples studied here shed light on the possible evolution of the southern Niuafo'ou microplate. The analyzed samples can be divided into: i) young arc-proximal samples with strong arc-related geochemical signatures (<0.15 Ma: DR48, DR49 and DR60); ii) a sample from the arc-to-backarc transition with weaker arc-related signatures (1.6 Ma: DR58); iii) samples of distal back-arc crust with no arc-related signature (3.8-5.1 Ma: DR65 and DR77); and iv) a sample of an older crustal relic stranded on the microplate (11.8 Ma: DR69) (**Figures 4.12, 4.13**).

The old back-arc crust from the nodal basins at the northern termination of the ELSC (3.8-5.1 Ma at DR65 and DR77) is much older than any crust that might have originated from the adjacent CLSC. At this distance from the spreading ridge the age of the crust at DR77 and DR65 would have been only 1.3 Ma and 0.8 Ma, respectively, if it had originated at the CLSC, assuming a half-spreading rate of 6 cm/y. Therefore, DR77 and DR65 must have originated from an earlier episode of back-arc spreading, probably along the ELSC before it was overtaken by the CLSC. The emergence of the CLSC as the dominant spreading center in the basin occurred after the formation of the back-arc crust sampled at DR65 and DR77. Until now, this complexity has prevented any

correlation with the magnetic chrons and is more reasonably interpreted in terms of a series of spreading events prior to the CLSC becoming the dominant spreading center. Rather, the crust in this part of the basin is a mixture of older deformed and rotated crustal components from now extinct spreading centers belonging to the northern segments of the ELSC (Taylor et al. 1996; Zellmer and Taylor, 2001). The mixture of tectonized and newly formed crust results in the diffuse magnetic pattern (Taylor et al., 1996; Zellmer et al., 2001; Sleeper and Martinez, 2016) and corresponds closely to the inferred location of missing strain of the Central Lau "nanoplate" originally postulated in this area by Conder and Wiens (2011).

A remnant of even older back-arc crust (11.8 Ma at DR69) is stranded in the back-arc north of the nodal basins (**Figure 4.4**). The sample collected here pre-dates the Lau Basin opening (**Figure 4.14A**). A well-developed plateau age and good reproducibility indicate that the result is reliable and, if an eruption age, then the sample may represent an early phase of tholeiitic magmatism, prior to the rapid opening of the basin. The sample has a glomerophyric texture (i.e., phenocrysts are clustered into larger aggregates) possibly indicating a long-lived magma chamber and several magma pulses.

Farther east, in the arc-to-backarc transition, the dike-like intrusions subparallel to the active spreading are somewhat younger (1.64 Ma at DR58). This series of elongated, dike-like bodies probably represent failed attempts at rifting as the locus of younger extension migrated east toward its present location at the FRSC (Stewart et al., 2022).

The youngest samples were collected southwest of the Fonualei Rift and Spreading Center (FRSC) where the rift is actively propagating into arc crust. Despite the large errors, we can confirm for example in the case of 21±50 ka that the maximum age of the sample is <70,000 years, which agrees with the fresh appearance of the lavas and is consistent with a new volcanic center emerging in advance of the FRSC. A high density of normal faults and seismicity indicate a potential weak spot in the crust, which may develop into a future triple junction (Baxter et al., 2020; Brandl et al., 2020; Schmid et al., 2020).

As noted above, the geochemistry of the samples closely reflects the proximity to the arc and the progression of crustal ages. The young arc-proximal volcanics (<0.15 Ma: DR48, DR49 and DR60 Ma) have strong arc-related geochemical signatures influenced by fluid-fluxed components (**Figure 4.12C, D).** The mafic intrusive rocks located at the arc-to-backarc transition (1.6 Ma: DR58) have a weak arc-related signature. The older samples (3.8-5.1 Ma: DR65 and DR77) from the nodal basins north of the ELSC have mid-ocean ridge-like geochemical signatures, reflecting dry melting, most likely from the first seafloor spreading in the basin. Sample DR69, which is too old to have been from the same melt regime is most similar to early tholeiites typically associated with young and/or hotter subduction (Reagan et al., 2010). Melts of this type may have dominated the area in the early development of the Lau Basin.

We suggest that deformation in the south of the Niuafo'ou microplate was continuous during the opening of the basin, beginning with the now sediment-filled failed rifts at the northern termination of the ELSC (DR65 and 77), followed by intrusion into the crust close to the arc-to-backarc transition (DR58), and eventually new rifting close to the arc front at the southern termination of the FRSC (DR48, 49, 60). As there is no new crust in the basin that is older than ~6 Ma, the much older sample in the north of the study area (DR69) must be a relic of early arc crust now stranded on the Niuafo'ou microplate. The geochemical signatures of the samples are interpreted to reflect essentially decompression melting at an early spreading center in the back-arc and increasing contributions from fluid-fluxed melting as later extension jumped to the east. In highly asymmetric growth, as in the Niuafo'ou microplate, one part of the plate may be more dense and dominated dry melting, typical of MORB-like spreading centers, and another part of the plate may be more buoyant and more influenced by fluid-fluxed melting (Taylor and Martinez, 2003; Langmuir et al., 2007; Haase et al., 2009). Importantly, lavas of very different age and composition are found only a few 10s of kilometers apart.

4.6.1 Possible implications for crustal growth in greenstone belts

It has long been considered that crustal growth in ancient greenstone belts may have similarities to modern microplate mosaics and complex crustal growth such as the Niuafo'ou microplate (e.g., Jackson et al., 1994). The youngest samples in the Lau Basin have been collected from volcanic centers located on much older units of the Tofua arc with significant depositional gaps, and ridge jumps and rift propagation have juxtaposed rocks of very different ages over short distances. This is similar to age relationships in some greenstone belts, such as the Abitibi Greenstone Belt (AGB) of the Superior Province of Canada (e.g., Ayer et al., 2002; Thurston et al., 2008).

Submarine volcanism in the AGB produced seven temporally distinct assemblages between 2795 and 2695 Ma (Monecke et al., 2017). They contain a number of mafic and felsic synvolcanic intrusive complexes, such as at NE Matagami and Noranda, and mafic-ultramafic successions, such as in the Blake River assemblage that are interpreted by some authors to be part of an intraoceanic arc-backarc system with similarities to modern oceanic settings (Percival et al., 2012; Wyman, 2013). The individual volcanic episodes have durations of 3 to 10 m.y. suggesting relatively slow growth compared to the opening of the Lau Basin despite the presumed high heat flow in the Archean (Hawkesworth et al., 2020). As in the Lau Basin, this growth was likely driven by many spreading centers and oceanic rifts ranging from mafic-ultramafic dominated (komatiite and tholeiitic basalts) to calc-alkaline mafic and felsic dominated (Ayer et al., 2002; Thurston et al., 2008; Gaboury et al., 2008). Five dominantly tholeiitic and komatiitic assemblages and two dominantly calc-alkaline assemblages were formed (Ayer et al., 2002; Thurston et al., 2008). The Blake River Assemblage, which formed from 2704 to 2695 Ma, was dominated by tholeiitic mafic volcanism in its earliest stages of growth that included the Hébécourt Formation and the Horne succession (≥ 2702 Ma). This was followed by largely bimodal volcanism in the central Blake River Group, that was contemporaneous with the emplacement of the Flavrian Pluton (<2702-2700 Ma). Mafic-dominated bimodal volcanic rocks with tholeiitic to transitional affinities of the Noranda mine sequence were erupted between 2698 and 2697 Ma, and the transitional to calc-alkaline Bousquet Formation in the east formed between 2697 and 2696 Ma. Both the youngest and oldest volcanic events are located along strike within 15 km of each other. The 9 m.y. of

volcanic activity produced an assemblage of about 160 km in length, similar in size to the Central Lau "nanoplate" (Péloquin et al., 2008; McNicoll et al., 2014; Monecke, et al., 2017).

The coeval development of tholeiitic and calc-alkaline assemblages at this scale is very similar to the architecture of the modern Lau Basin. Previous workers have argued that modern plate dynamics cannot be an analog of Archean greenstone belts precisely because the modern systems have been perceived to be dominated by large-scale, relatively uncomplicated back-arc basin opening (e.g., Bédard et al., 2013). We have shown that crustal growth at the microplate (and "nanoplate") scale may be a dominant feature of back-arc basin development, matched by variations in mantle input and fluid-fluxed melting, that could explain some features of the southern AGB.

Conclusion

The opening of the northern Lau Basin was accommodated by growth of numerous microplates bordered by discrete spreading centers. However, interpretation of the growth history has been complicated by a lack of clearly defined magnetic chrons. In an attempt to resolve part of the growth history we determined absolute ages of the crust using Ar-Ar dating across the southern margin of the largest microplate (Niuafo'ou). The new Ar-Ar ages challenge the view of back-arc basin opening as a linear progression from rifting to eventual spreading with uniform crustal accretion and growth and instead provide evidence of ridge jumps, rift propagation into older crust, and diffuse extension throughout the opening of the Basin, with rocks as young as 13.4 ka and as old as 11 Ma forming part of the microplate. The oldest rocks record the earliest stages of back-arc basin opening, and the youngest rocks are related to arc rifting and the emergence of a new plate boundary. The ages illustrate the complexity of crustal growth from east to west, and the unexpected proximity of old crust from the earliest opening of the basin to the active spreading centers in the middle of the basin. The observed age differences are strongly correlated to the whole rock geochemistry, and significant geochemical variability, from mid-ocean ridge-like lavas to arc-like lavas, is found within an area of just a few 100 km^2 spanning the entire age range of the opening of the basin. The result can be a complex structural evolution and interaction of mantle sources that are not uniquely tied to progressive basin opening or a single spreading center. Early

asymmetric rifting and back-arc spreading is recorded by 5 Ma and 3.8 Ma crust juxtaposed against the much younger CLSC. Migrating zones of extension are recorded by 1.64 Ma intrusions in the arc-to-backarc transition, and active volcanism southwest of the Fonualei Rift and Spreading Center may indicate a future plate boundary and triple junction with the Tofua arc.

Age data and volcanic rock geochemistry from greenstone belts, such as the AGB, show similar geochemical diversity and age ranges and likely reflect similarly complex crustal growth history. Rapidly evolving microplate mosaics such as the northern Lau Basin may be important modern analogs of complex crustal growth in greenstone belts, including structural evolution and different processes of melt generation in spatially and temporally restricted domains. The sizes of those domains are debated, but their origins could be similar to the microplate mosaic of the Lau Basin where individual plates are forming at scales of less than 100 km. Knowledge of these processes in modern tectonic settings may help to identify microplate mosaics in ancient greenstone belts that were gateways for melts and fluids in some particularly well-endowed terranes.

Acknowledgements

This research was funded by the Canada First Research Excellence Fund (CFREF, Metal Earth at Laurentian University) and the Marine Mineral Resources Group at the GEOMAR Helmholtz Centre for Ocean Research Kiel. The Natural Sciences and Engineering Research Council of Canada (NSERC), the Helmholtz Association, and the German Ministry of Science and Education (BMBF, grant 03G0267) are acknowledged for the support of this work through research grants to the authors. The project was also supported by the NSERC Collaborative Research and Training Experience program (iMAGE-CREATE) on Marine Geodynamics and Georesources. We are grateful to the captain and crew of RV Sonne for their support during expedition SO267. Special thanks to all the scientists (including P. Mercier-Langevin, and S. Petersen). Particularity, we would like to express our thanks and memory to Reinhard Werner.

References

Anderson, M.O., Norris-Julseth, C., Rubin, K.H., Haase, K., Hannington, M.D., Baxter, A.T., and Stewart, M.S., 2021, Geologic and structural evolution of the NE Lau Basin, Tonga: Morphotectonic analysis and classification of structures using shallow seismicity: Frontiers in Earth Science, v. 9, article 665185.

Ayer, J., Amelin, Y., Corfu, F., Kamo, S., Ketchum, J., Kwok, K., and Trowell, N., 2002, Evolution of the southern Abitibi greenstone belt based on U-Pb geochronology: autochthonous volcanic construction followed by plutonism, regional deformation and sedimentation: Precambrian Research, v. 115, p. 63-95.

Barckhausen, U., Heyde, I., Kopp, H., and Hannington, M.D., 2019, Seafloor spreading and crustal extension of the Central and Northern Lau Basin: Some insights from new magnetic data: Abstract T33F-0424 presented at 2019 Fall Meeting, American Geophysical Union, San Francisco, California, 9-13 December.

Baxter, A.T., Hannington, M.D., Stewart, M.S., Emberley, J.M., Breker, K., Krätschell, A., Petersen, S., Brandl, P.A., Klischies, M., Mensing, R., and Anderson, M.O., 2020, Shallow seismicity and the classification of structures in the Lau back-arc basin: Geochemistry, Geophysics, Geosystems, v. 21, article e2020GC008924.

Bevis, M., Taylor, F.W., Schutz, B.E., Recy, J., Isacks, B.L., Helu, S., Singh, R., Kendrick, E., Stowell, J., Taylor, B., and Calmantli, S., 1995, Geodetic observations of very rapid convergence and back-arc extension at the Tonga arc: Nature, v. 374, p. 249-251.

Bédard, J.H., Harris, L.B., and Thurston, P.C., 2013, The hunting of the snArc: Precambrian Research, v. 229, p. 20-48.

Bézos, A., Escrig, S., Langmuir, C.H., Michael, P.J., and Asimow, P.D., 2009, Origins of chemical diversity of back-arc basin basalts: A segment-scale study of the Eastern Lau Spreading Center: Journal of Geophysical Research, v. 114, article B06212.

Brandl, P.A., Schmid, F., Augustin, N., Grevemeyer, I., Arculus, R.J., Devey, C.W., Petersen, S., Steward, M., Kopp, H., and Hannington, M.D., 2020, The 6-8 Aug 2019 eruption of 'Volcano F' in the Tofua Arc, Tonga: Journal of Volcanology and Geothermal Research, v. 390, article 106695.

Clift, P.D., and Dixon, J.E., 1994, Variations in arc volcanism and sedimentation related to rifting of the Lau Basin (southwest Pacific), in Hawkins, J.W., Parson, L.M., Allan, J.F., et al., Proceedings of the Ocean Drilling Program, Scientific Results, v. 135: College Station, Texas, Ocean Drilling Program, p. 23-49.

Conder, J.A., and Wiends, D.A., 2011, Shallow seismicity and tectonics of the central and northern Lau Basin: Earth and Planetary Science Letters, v. 304, p. 538-546.

Escrig, S., Bézos, A., Langmuir, C.H., Michael, P.J., and Arculus, R., 2012, Characterizing the effect of mantle source, subduction input and melting in the Fonualei Spreading Center, Lau Basin: Constraints on the origin of the boninitic signature of the back-arc lavas: Geochemistry, Geophysics, Geosystems, v. 13, article Q10008.

Escrig, S., Bézos, A., Goldstein, S.L., Langmuir, C.H., and Michael, P.J., 2009, Mantle source variations beneath the Eastern Lau Spreading Center and the nature of subduction components in the Lau basin-Tonga arc system: Geochemistry, Geophysics, Geosystems, v. 10, article Q04014.

Fassbender, M.L., Hannington, M., Stewart, M., Brandl, P.A., Baxter, A.T., and Diekrup, D., 2023, Geochemical signatures of felsic volcanic rocks in modern oceanic settings and implications for Archean greenstone belts: Economic Geology, v. 118, p. 319-345.

Fassbender, M.L., Hannington, M., Baxter, A.T., Diekrup, D., Stewart, M., and Brandl, P.A, submitted, Geochemical signatures of mafic volcanic rocks in modern oceanic settings and implications for Archean mafic magmatism: Economic Geology, in review.

Freund, S., Beier, C., Krumm, S., and Haase, K.M., 2013, Oxygen isotope evidence for the formation of andesitic-dacitiv magmas from the fast-spreading Pacific-Antarctic Rise by assimilation-fractional crystallization: Chemical Geology, v. 347, p. 271-283.

Fretzdorff, S., Schwarz-Schampera, U., Gibson, H.L., Garbe-Schönberg, C.-D., Hauff, F., and Stoffers, P., 2006, Hydrothermal activity and magma genesis along a propagating back-arc basin: Valu Fa Ridge (southern Lau Basin): Journal of Geophysical Research, v. 111, article B08205.

Gaboury, D., and Pearson, V., 2008, Rhyolite geochemical signatures and association with volcanogenic massive sulfide deposits: Examples from the Abitibi belt, Canada: Economic Geology, v. 103, p. 1531-1562.

Galley, A.G., Watkinson, D.H., Jonasson, I.R., and Riverin, G., 1995, The subsea-floor formation of volcanogenic-hosted massive sulfide: Evidence from the Ansil Deposit, Rouyn-Noranda, Canada: Economic Geology, v. 90, p. 2006-2017.

Haase, K.M., Fretzdorff, S., Mühe, R., Garbe-Schönberg, D., and Stoffers, P., 2009, A geochemical study of off-axis seamount lavas at the Valu Fa Ridge: Constraints on magma genesis and slab contributions in the southern Tonga subduction zone: Lithos, v. 112, p. 137-148.

Hannington, M.D., Kopp, H., and Schnabel, M., 2019, RV Sonne Fahrtbericht / cruise report SO267: Archimedes I: Arc Rifting, Metallogeny and Microplate Evolution – An Integrated Geodynamic, Magmatic and Hydrothermal Study of the Fonualei Rift System, NE Lau Basin, Suva (Fiji)-Suva (Fijji), 11.12.2018-26.01.2019: Kiel, Germany, GEOMAR Helmholtz-Zentrum für Ozeanforschung, GEOMAR Report N. Ser.049, p. 275.

Hawkesworth, C.J., Cawood, A.P., and Dhuime, B., 2020, The evolution of the continental crust and the onset of plate tectonics: Frontiers in Earth Sciences, v. 8, article 326.

Hawkins, J.W., 1995, The geology of the Lau basin, in Taylor, B., ed., Backarc Basins: Tectonics and magmatism: Boston, MA, Springer US, p. 63-138.

Jackson, S.L., Fyon, A., and Corfu, F., 1994, Review of Archean supracrustal assemblages of the southern Abitibi greenstone belt in Ontario, Canada: Products of microplate interaction within a large-scale plate-tectonic setting: Precambrian Research, v. 65, p. 183-205.

Karig, D.E., 1970, Ridges and basins of the Tonga-Kermadec island arc system: Journal of Geophysical Research, v. 75, p. 239-254.

Keller, N.S., Arculus, R.J., Hermann, J., and Richards, S., 2008, Submarine back-arc lava with arc signature: Fonualei Spreading Center, northeast Lau Basin, Tonga: Journal of Geophysical Research: Solid Earth, v. 113, article B08S07.

Koppers, A.A.P., 2002, ArArCALC-software for $^{40}Ar/^{39}Ar$ age calculations: Computers and Geosciences, v. 28, p. 605-619.

Koppers, A.A.P., Staudigel, H., and Wijbrans, J.R., 2000, Dating crystalline groundmass separates of altered Cretaceous seamount basalts by the Ar-40/Ar-39 incremental heating technique: Chemical Geology, v. 166, p. 139-158.

Koppers, A.A.P., Staudigel, H., and Duncan, R.A., 2003, High-resolution 40Ar/39Ar dating of the oldest oceanic basement basalts in the western Pacific basin: Geochemistry, Geophysics, Geosystems, v. 4, article 8914.

Langmuir, C.H., Bézos, A., Escrig, S., and Parman, S.W., 2006, Chemical systematics and hydrous melting of the mantle in back-arc basins: American Geophysical Union, Geophysical Monograph 166, p. 87-146.

Le Maitre, R.W., 1989, A classification of igneous rocks and glossary of terms: Recommendations of the International Union of Geological Sciences: Subcommission on the Systematics of Igneous Rocks: Oxford, Blackwell Scientific Publications, 193 p.

Martinez, F., Stern, R.J., Kelley, K.A., Ohara, Y., Sleeper, J.D., Ribeiro, J.M., and Brounce, M., 2018, Diffuse extension of the southern Mariana margin: Journal of Geophysical Research: Solid Earth, v. 123, p. 892-916.

McNicoll, V., Goutier, J., Dubé, B., Mercier-Langevin, P., Ross, P.-S., Dion, C., Monecke, T., Legault, M., Percival, J., and Gibson, H., 2014, U-Pb Geochronology of the Blake River Group, Abitibi greenstone belt, Quebec, and implications for base metal exploration: Economic Geology, v. 109, p. 27-59.

Meffre, S., Falloon, T.J., Crawford, T.J., Hoernle, K., Hauff, F., Duncan, R.A., Bloomer, S.H., and Wright, D.J., 2012, Basalts erupted along the Tongan fore arc during subduction initiation: Evidence from geochronology of dredged rocks from the Tonga fore arc and trench: Geochemistry, Geophysics, Geosystems, v. 13, article Q12003.

Monecke, T., Mercier-Langevin, P., Dubé B., and Frieman, B.M., 2017, Geology of the Abitibi greenstone belt, Canada: Reviews in Economic Geology, v. 19, p. 7-49.

Paradis, S., Ludden, J., and Gélinas, L., 1988, Evidence for contrasting compositional spectra in comagmatic intrusive and extrusive rocks of the late Archean Blake River Group, Abitibi, Quebec: Canadian Journal of Earth Sciences, v. 25, p. 134-144.

Parson, L.M., and Hawkins, J.W., 1994, Two-stage propagation and the geological history of the Lau backarc basin, in Hawkins, J.W., Parson, L.M., Allan, J.F., et al., Proceedings of the Ocean Drilling Program, Scientific Results, v. 135: College Station, Texas, Ocean Drilling Program, p. 819-828.

Parson, L.M., Pearce, J.A., Murton, B.J., Hodkinson, R.A., Bloomer, S., Ernewein, M., Huggett, Q.J., Miller, S., Johnson, L., Rodda, P., and Helu, S., 1990, Role of ridge jumps and ridge propagation in the tectonic evolution of the Lau back-arc basin, southwest Pacific: Geology, v. 18, p. 470-473.

Pearce, J.A., 2014, Immobile element fingerprinting in ophiolites: Elements, v. 10, p. 101-108.

Péloquin, A.S., Piercey, S.J., and Hamilton, M.A., 2008, The Ben Nevis volcanic complex, Ontario, Canada: Part of the late volcanic phase of the Blake River Group, Abitibi subprovince, Economic Geology, v. 103, p. 1219-1241.

Pelletier, B., Lagabrielle, Y., Benoit, M., Cabioch, G., Calmant, S., and Gare, E., 2001, Newly identified segments of the Pacific-Australia plate boundary along the North Fiji transform zone: Earth and Planetary Science Letters, v. 193, p. 347-358.

Percival, J.A., Skulski, T., Sanborn-Barrie, M., Stott, G.M., Leclair, A.D., Corkery, M.T., and Boily, M., 2012, Geology and tectonic evolution of the Superior province, Canada: Geological Association of Canada, Special Paper 49, p. 321-378.

Price, A.A., Jackson, M.G., Blichert-Toft, J., Hall, P.S., Sinton, J.M., Kurz, M.D., and Blusztajn, J., 2014, Evidence for a broadly distributed Samoan-plume signature in the northern Lau and North Fiji Basins: Geochemistry, Geophysics, Geosystems, v. 15, p. 986-1008.

Price, A.A., Jackson, M.G., Blichert-Toft, J., Blusztajn, J., Conatser, C.S., Konter, J.G., Koppers, A.A.P., and Kurz, M.D., 2016, Geochemical evidence in the northeast Lau Basin for subduction of the Cook-Austral volcanic chain in the Tonga trench: Geochemistry, Geophysics, Geosystems, v. 17, p. 1694-1724.

Reagan, M.K., Ishizuka, O., Stern, R.J., Kelley, K.A., Ohara, Y., Blichert-Toft, J., Bloomer, S.H., Cash, J., Fryer, P., Hanan, B.B., Hickey-Vargas, R., Ishii, T., Kimura, J.-I., Peate, D.W., Rowe, M.C., and Woods, M., 2010, Fore-arc basalts and subduction initiation in the Izu-Bonin-Mariana system: Geochemistry, Geophysics, Geosystems, v., 11, article Q03X12.

Ruellan, E., and Lagabrielle, Y., 2005, Subductions et ouvertures océaniques dans le Sud-Ouest Pacifique: Géomorphologie: Relief, Processus, Environnement, v. 11, p. 121-142.

Ruellan, E., Delteil, J., Wright, I., and Matsumoto, T., 2003, From rifting to active spreading in the Lau Basin–Havre Trough backarc system (SW Pacific): Locking/unlocking induced by seamount chain subduction: Geochemistry Geophysics Geosystems, v. 4, article 8909.

Ryan, W.B.F., Carbotte, S.M., Coplan, J.O., O'Hara, S., Melkonian, A., Arko, R., Weissel, R.A., Ferrini, V., Goodwillie, A., Nitsche, F., Bonczkowski, J., and Zemsky, R., 2009, Global multi-resolution topography synthesis: Geochemistry, Geophysics, Geosystems, v. 10, article Q03014.

Schmid, F., Kopp, H., Schnabel, M., Danowski, A., Heyde, I., Riedel, M., Hannington, M.D., Engels, M., Beniest, A., Klaucke, I., Augustin, N., Brandl., P.A., and Devey, C., 2020, Crustal structure of the Niuafo'ou microplate and Fonualei Rift and Spreading Center in the northeastern Lau Basin, southwestern Pacific: Journal of Geophysical Research: Solid Earth, v. 125, article e2019JB019184.

Sleeper, J.D., and Martinez, F., 2014, Controls on segmentation and morphology along the back-arc Eastern Lau Spreading Center and Valu Fa Ridge: Journal of Geophysical Research: Solid Earth, v. 119, p. 1678-1700.

Sleeper, J.D., and Martinez, F., 2016, Geology and kinematics of the Niuafo'ou microplate in the northern Lau Basin: Journal of Geophysical Research: Solid Earth, v. 121, 4852-4875.

Sleeper, J.D., Martinez, F., and Arculus, R., 2016, The Fonualei Rift and Spreading Center: Effects of ultraslow spreading and arc proximity on back-arc crustal accretion: Journal of Geophysical Research: Solid Earth, v. 121, p. 4814-4835.

Sleeper, J.D., Martinez, F., Fryer, P., Stern, R.J., Kelley, K.A., and Ohara, Y., 2021, Diffuse spreading, a newly recognized mode of crustal accretion in the southern Mariana Trough backarc basin: Geosphere, v. 17, p. 1382-1404.

Smith, G.P., Wiens, D.A., Fischer, K.M., Dorman, L.M., Webb, S.C., and Hildebrand, J.A., 2001, A complex pattern of mantle flow in the Lau backarc: Science, v. 292, p. 713-716.

Stewart, M.S., Hannington, M.D., Emberley, J., Baxter, A.T., Krätschel, A., Petersen, S., Brandl, P.A., Anderson, M.O., Mercier-Langevin, P., Mensing, R., Breker, K., and Fassbender, M.L., 2022, A new geological map of the Lau basin reveals crustal growth processes in arc-backarc systems: Geosphere, v. 18, p. 910-943.

Taylor, B., and Martinez, F., 2003, Back-arc basin basalt systematics: Earth and Planetary Science Letters, v. 210, p. 481-497.

Taylor, B., Zellmer, K., Martinez, F., and Goodliffe, A., 1996, Sea-floor spreading in the Lau back-arc basin: Earth and Planetary Science Letters, v. 144, p. 35-40.

Thurston, P.C., Ayer, J.A., Goutier, J., and Hamilton, M.A., 2008, Depositional gaps in Abitibi greenstone belt stratigraphy: A key to exploration for syngenetic mineralization: Economic Geology, v. 103, p. 1097-1134.

Tian, L., Castillo, P.R., Hilton, D.R., Hawkins, J.W., Hanan, B.B., and Pietruszka, A.J., 2011, Major and trace element and Sr-Nd isotope signatures of the northern Lau Basin lavas: Implications for the composition and dynamics of the back-arc basin mantle: Journal of Geophysical Research: Solid Earth, v. 116, p. 657-670.

Ueki, K., Hino, H., and Kuwatani, T., 2018, Geochemical discrimination and characteristics of magmatic tectonic settings: A machine-learning-based approach: Geochemistry, Geophysics, Geosystems, v. 19, p. 1327-1347.

Wyman, D.A., 2013, A critical assessment of Neoarchean “plume only” geodynamics: Evidence from the Superior Province: Precambrian Research, v. 229, p. 3-19.

Yan, Q., Castillo, P.R., and Shi, X., 2012, Geochemistry of basaltic lavas from the southern Lau Basin: input of compositionally variable subduction components: International Geology Review, v. 54, p. 1456-1474.

Yan, Q., Shi, X., Li, N., Gao, J., and Su, T., 2013, Preliminary K-Ar geochronology of lavas from southern Lau Basin: Acta Oceanologica Sinica, v. 32, p. 18-23.

Yan, Q., Straub, S., Castillo, P., Zhang, H., Tian, L., and Shi, X., 2020, Hafnium isotope constraints on the nature of the mantle beneath the Southern Lau basin (SW Pacific): Scientific reports, v. 10, article 17476.

v.d. Zander, I., Sinton, J.M., and Mahoney, J.J., 2010, Late shield-stage silicic magmatism at Waianae volcano: Evidence for Hydrous Crustal Melting in Hawaiian Volcanoes: Journal of Petrology, v. 51, p. 671-701.

Zellmer, K.E., and Taylor, B., 2001, A three-plate kinematic model for Lau Basin opening: Geochemistry, Geophysics, Geosystems, v. 2, article 2000GC000106.

Zhang, H., Yan, Q., Li, C., Zhu, Z., Zhao, R., and Shi, X., 2018, Geochemistry of diverse lava types from the Lau Basin (South West Pacific): Implications for complex back-arc mantle dynamics: Geological Journal, v. 56, p. 1-17.

Figures

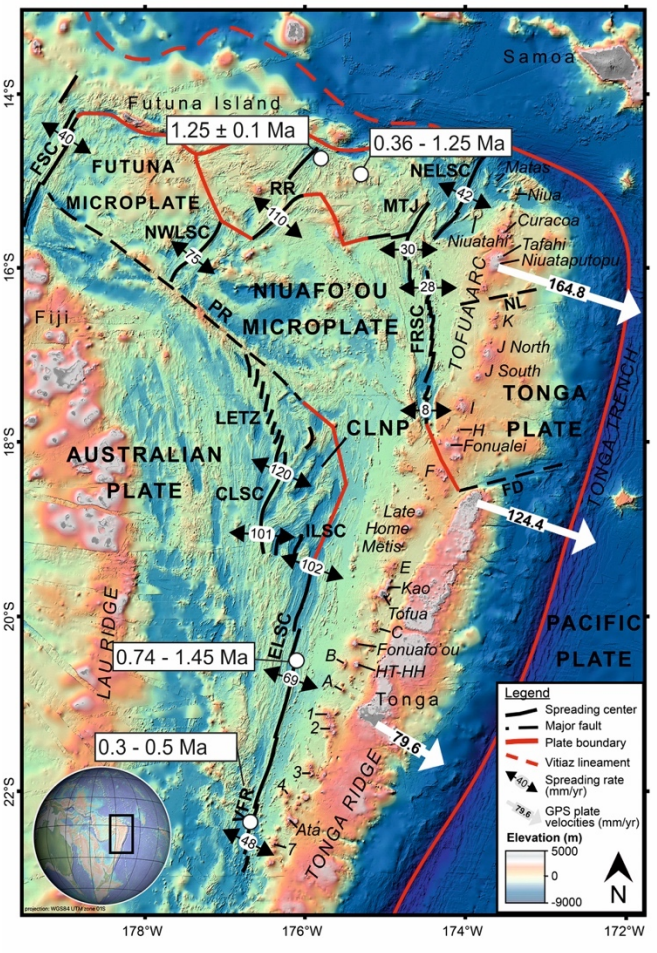


Figure 4.1: Regional bathymetric map of the Lau back-arc basin (from Stewart et al., 2022) showing spreading ridges, spreading rates, rates of retreat of the active arc (in mm/yr), and radiometric ages from Price et al. (2016) and Yan et al. (2013). The basin comprises at least eight major zones of active extension: CLSC = Central Lau Spreading Center; ELSC = Eastern Lau Spreading Center; FRSC = Fonualei Rift and Spreading Center; MTJ = Mangatolu Triple Junction; NELSC = Northeast Lau Spreading Center; NWLSC = Northwest Lau Spreading Center; VFR = Valu Fa Ridge; RR = Rochambeau Rifts. This study focuses on the emergence of the Niaufo'ou microplate and specifically evidence for the origin of the Central Lau Nanoplate (CLNP) between the CLSC, ELSC and FRSC.

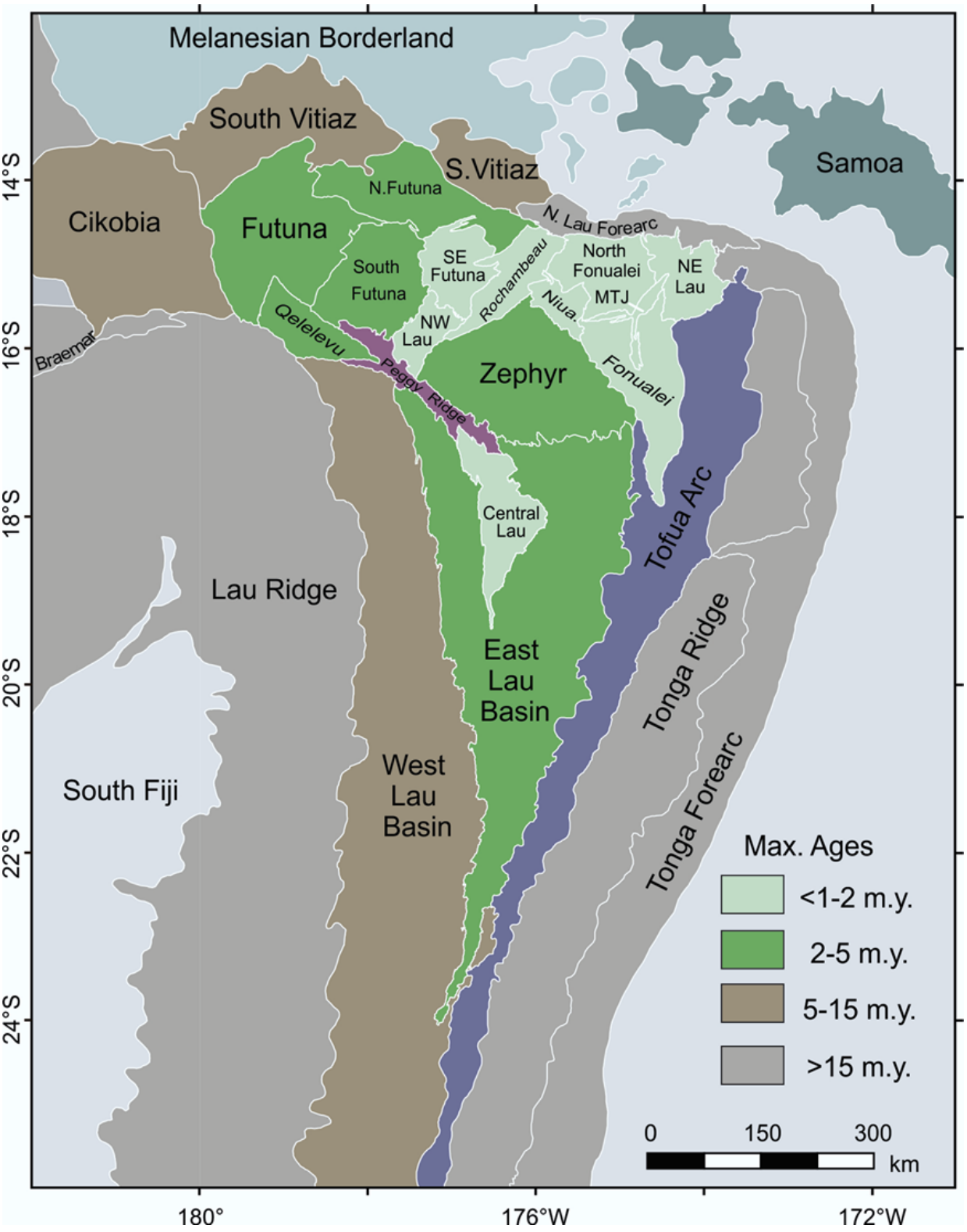

Melanesian Borderland
South Vitiaz
S.Vitiaz
Samoa
N.Futuna
Cikobia
Futuna
N. Lau Forearc
South Futuna
SE Futuna
Rochambeau
North Fonualei
NE Lau
MTJ
Niua
Qelelevu
NW Lau
Braemar
Peggy Ridge
Zephyr
Fonualei
Central Lau
Tofua Arc
Lau Ridge
East Lau Basin
Tonga Ridge
West Lau Basin
South Fiji
Tonga Forearc
Max. Ages
<1-2 m.y.
2-5 m.y.
5-15 m.y.
>15 m.y.
0
150
300
km
14°S
16°S
18°S
20°S
22°S
24°S
180°
176°W
172°W

Figure 4.2: Assemblage map of the Lau Basin (from Stewart et al., 2022). Each assemblage consists of one or more geological formations grouped in terms of their origin, lithology, inferred age, and tectonic and structural regime. Colors assigned to the assemblages are for illustration purposes only (MTJ refers to Mangatolu Triple Junction; Niua. refers to Niuafo'ou).

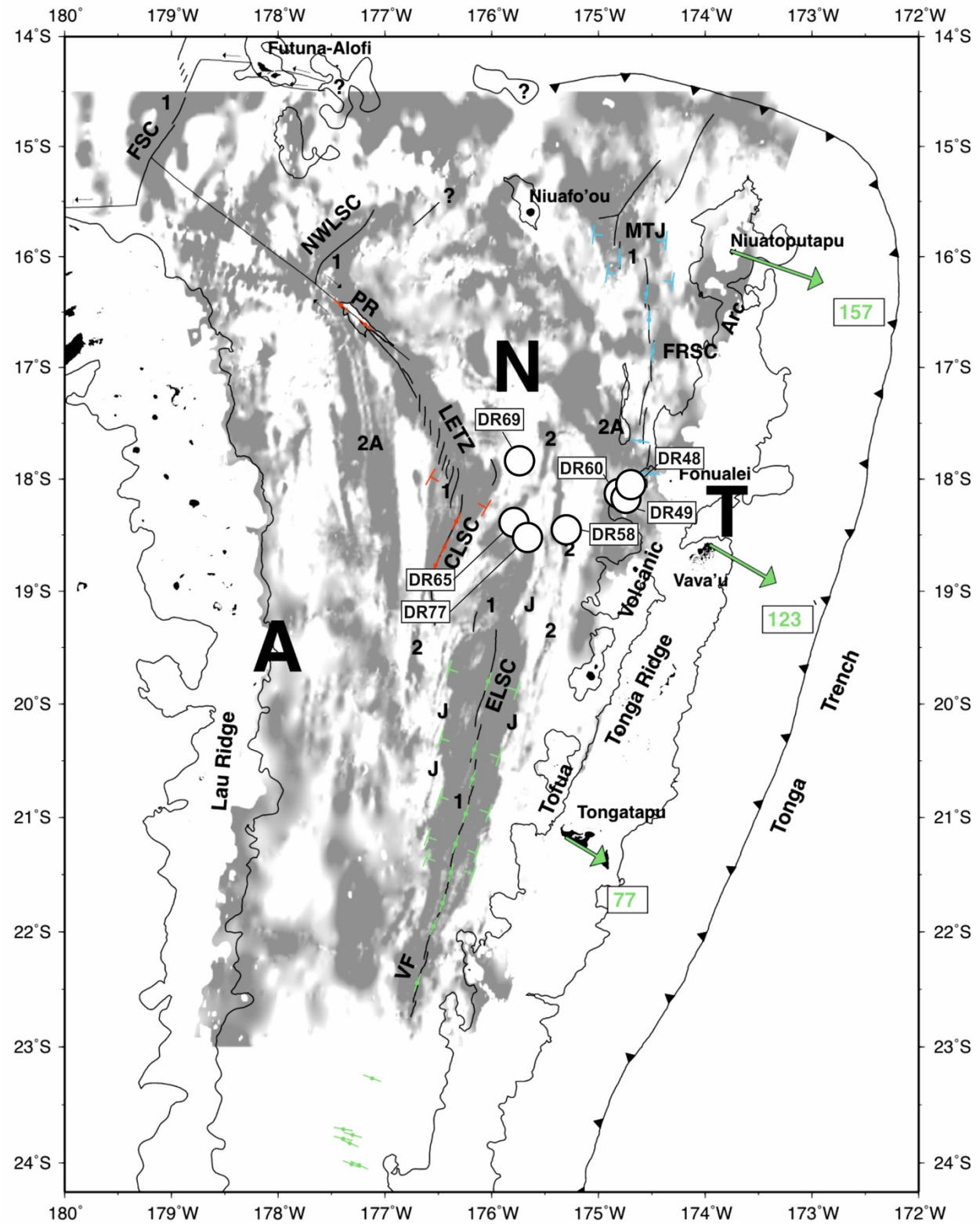

Futuna-Alofi
FSC
NWLSC
PR
Niuafo'ou
MTJ
Niuatoputapu
157
Arc
FRSC
N
LETZ
DR69
2A
DR48
DR60
Fonualei
DR49
T
DR58
CLSC
DR65
DR77
Volcanic
Vava'u
123
A
ELSC
Tonga Ridge
Trench
Lau Ridge
Tofua
Tongatapu
Tonga
77
VF
180°
179°W
178°W
177°W
176°W
175°W
174°W
173°W
172°W
14°S
15°S
16°S
17°S
18°S
19°S
20°S
21°S
22°S
23°S
24°S

Figure 4.3: Magnetic anomaly map of the Lau Basin from the two-dimensional (2-D) magnetic inversions (from Zellmer and Taylor, 2001) showing the sample locations of this study. The anomalies are labelled with magnetic polarity chrons indicated (Sleeper and Martinez, 2016): 1 = Brunhes normal chron (0 – 0.78 Ma), J = Jaramillo normal subchron (0.9 – 1.06 Ma; within Matuyama reversed chron), 2 = Olduvai normal subchron (1.78 – 2.00 Ma; within Matuyama reversed chron), 2A = Gaus chron (2.59 – 3.59 Ma). The ”T” markers indicate the Brunhes/Matuyama (0.78 – 2.59 Ma) boundary.

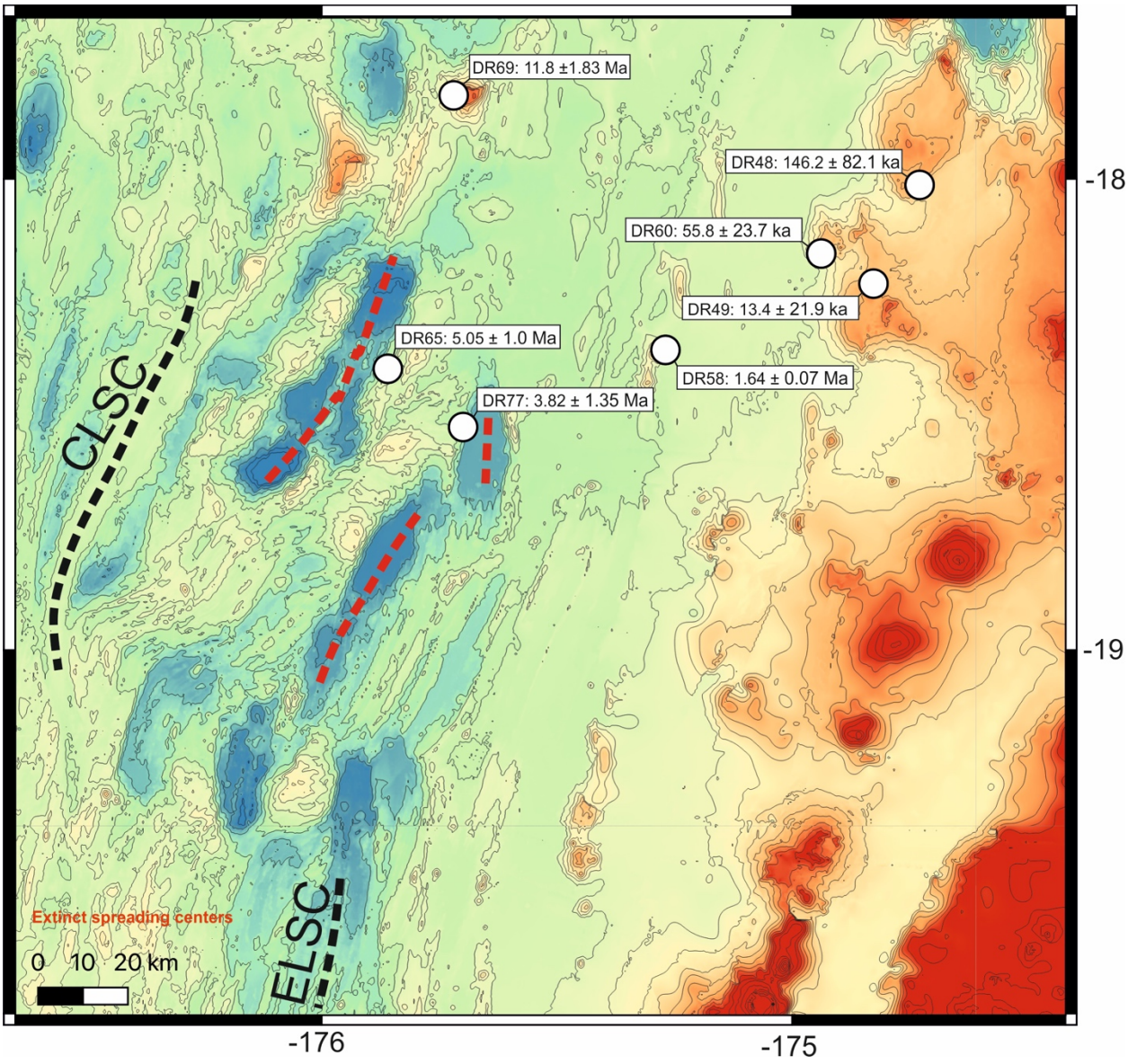


Figure 4.4: Bathymetric map of the southern FRSC, northern ELSC, CLSC and the proposal Central Lau "nanoplate" (CLNP of Conder and Wiens, 2011) in the south of the Niuafo'ou Microplate showing the location and results of Ar-Ar radiometric ages.

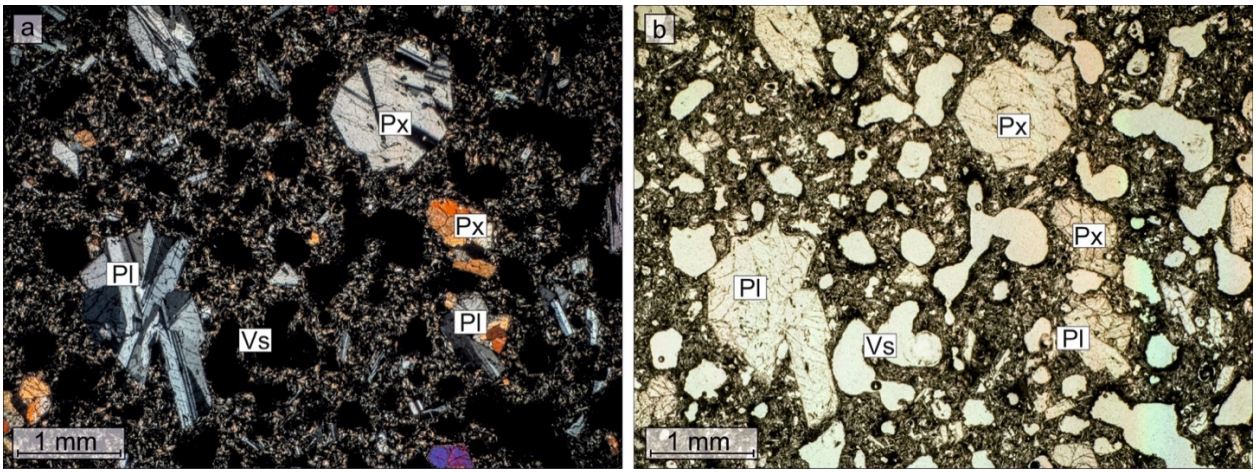


Figure 4.5: Representative photomicrographs of SO267 DR48-1B. A) Photomicrograph under cross polarized light showing a fine-grained matrix and few plagioclase and pyroxene phenocrysts. B) **Figure 4.5A** under plane polarized light. Pl = plagioclase, Px = pyroxene, Vs = vesicles.

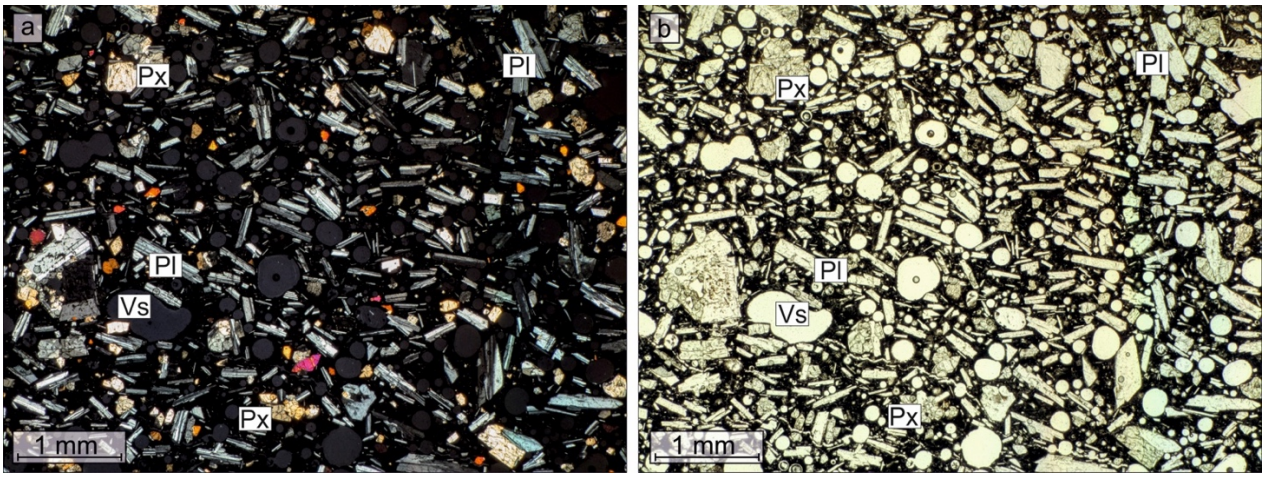


Figure 4.6: Representative photomicrographs of SO267 DR49-1. A) Photomicrograph under cross polarized light showing a fine-grained plagioclase dominated matrix and few plagioclase and pyroxene phenocrysts. B) **Figure 4.6A** under plane polarized light. Pl = plagioclase, Px = pyroxene, Vs = vesicles.

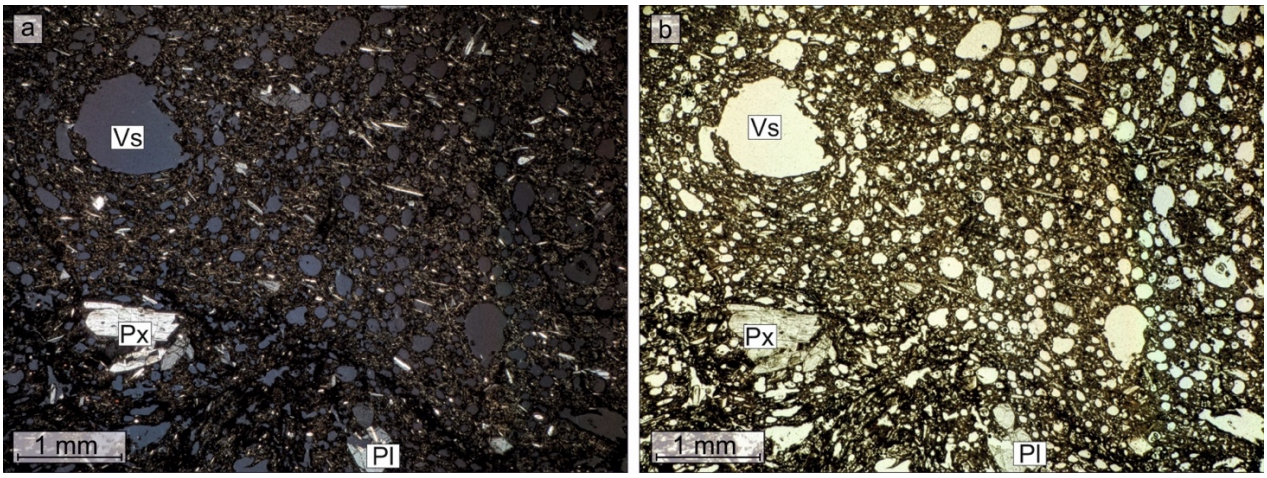


Figure 4.7: Representative photomicrographs of SO267 DR49-1. A) Photomicrograph under cross polarized light showing a very fine-grained plagioclase dominated matrix and few plagioclase and pyroxene phenocrysts. B) **Figure 4.7A** under plane polarized light. Pl = plagioclase, Px = pyroxene, Vs = vesicles.

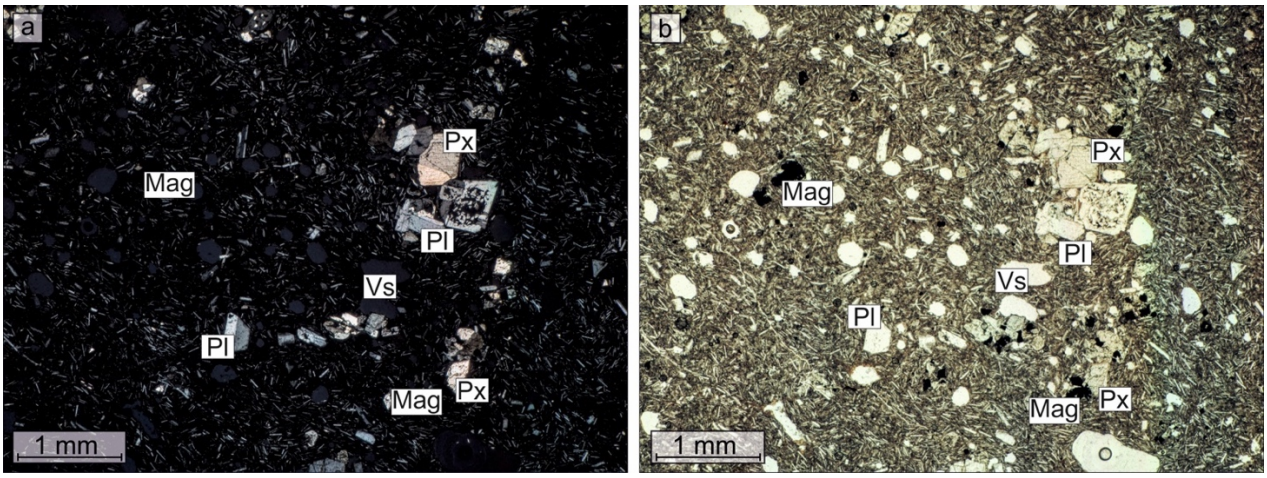


Figure 4.8: Representative photomicrographs of SO267 DR60-1B. A) Photomicrograph under cross polarized light showing a very fine-grained plagioclase dominated matrix and few plagioclase, pyroxene and magnetite phenocrysts. B) **Figure 4.8A** under plane polarized light. Pl = plagioclase, Px = pyroxene, Vs = vesicles, Mag = magnetite.

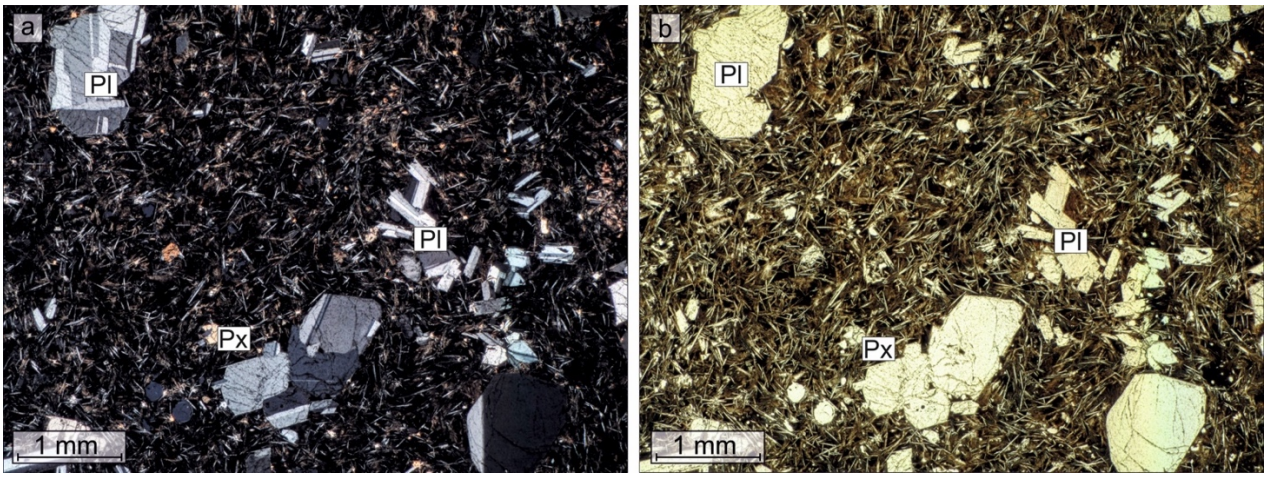


Figure 4.9: Representative photomicrographs of SO267 DR65-1G. A) Photomicrograph under cross polarized light showing a very fine-grained plagioclase dominated matrix and few plagioclase, and pyroxene and magnetite phenocrysts. B) **Figure 4.9A** under plane polarized light. Pl = plagioclase, Px = pyroxene, Mag = magnetite.

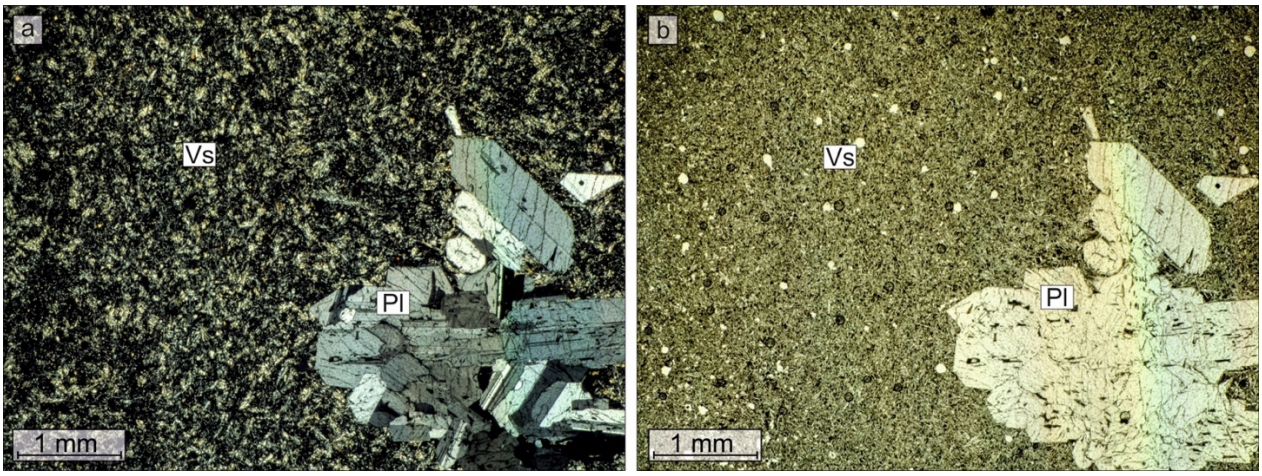


Figure 4.10: Representative photomicrographs of SO267 DR69-2A. A) Photomicrograph under cross polarized light showing a very fine-grained plagioclase dominated matrix and few plagioclase phenocrysts including glomerophenocrysts. B) **Figure 4.10A** under plane polarized light. Pl = plagioclase, Vs = vesicles.

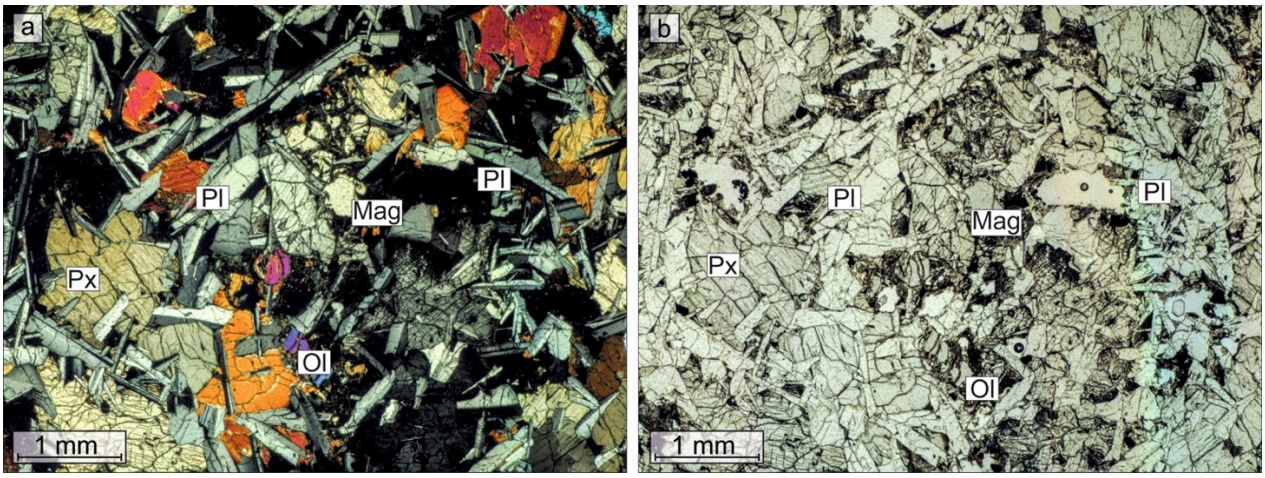


Figure 4.11: Representative photomicrographs of SO267 DR77-4A. A) Photomicrograph under cross polarized light showing a dioritic texture with well crystallized plagioclase and pyroxene and few olivine and magnetite crystals. B) **Figure 4.11A** under plane polarized light. Pl = plagioclase, Px = pyroxene, Ol = olivine, Mag = magnetite.

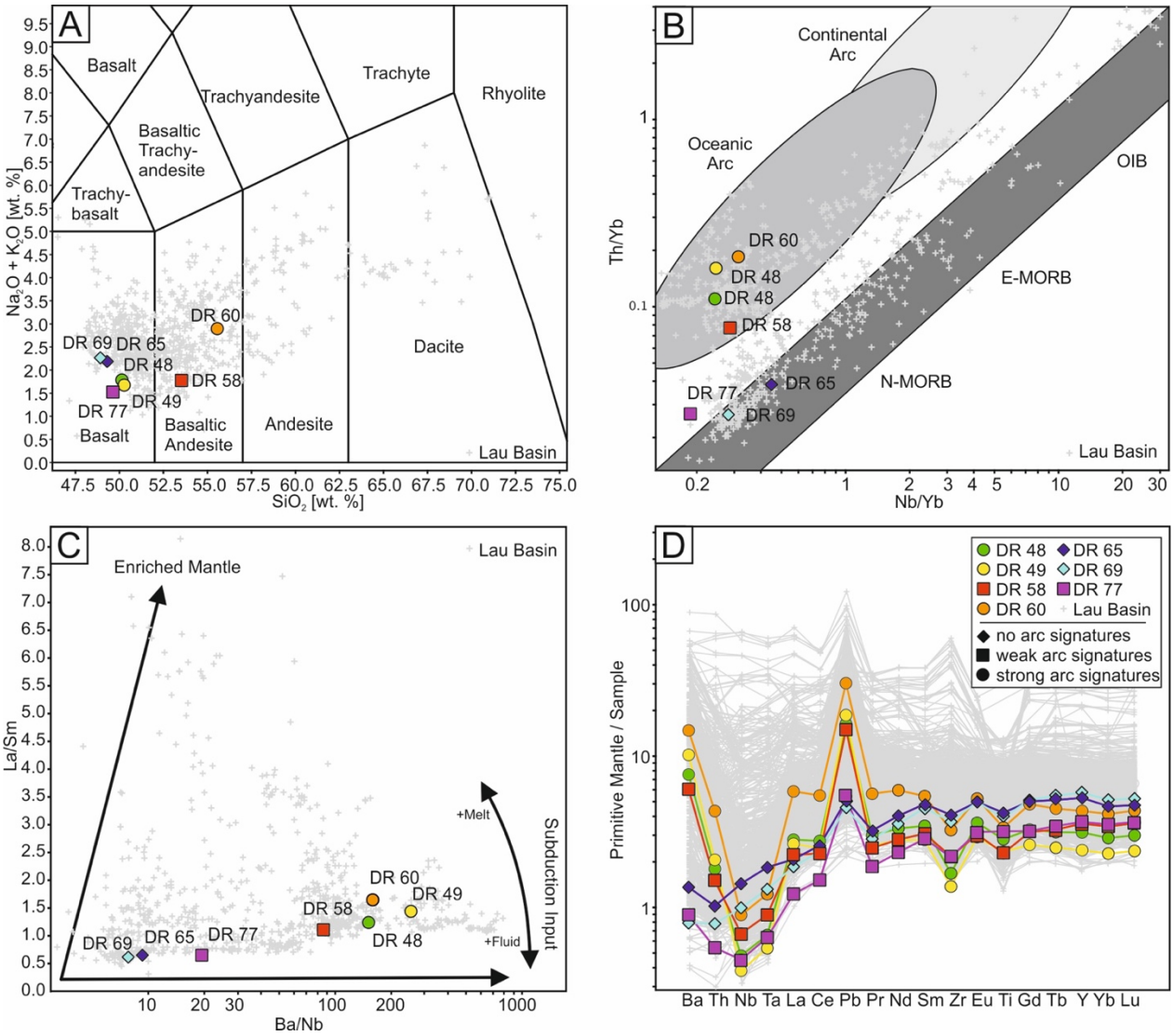
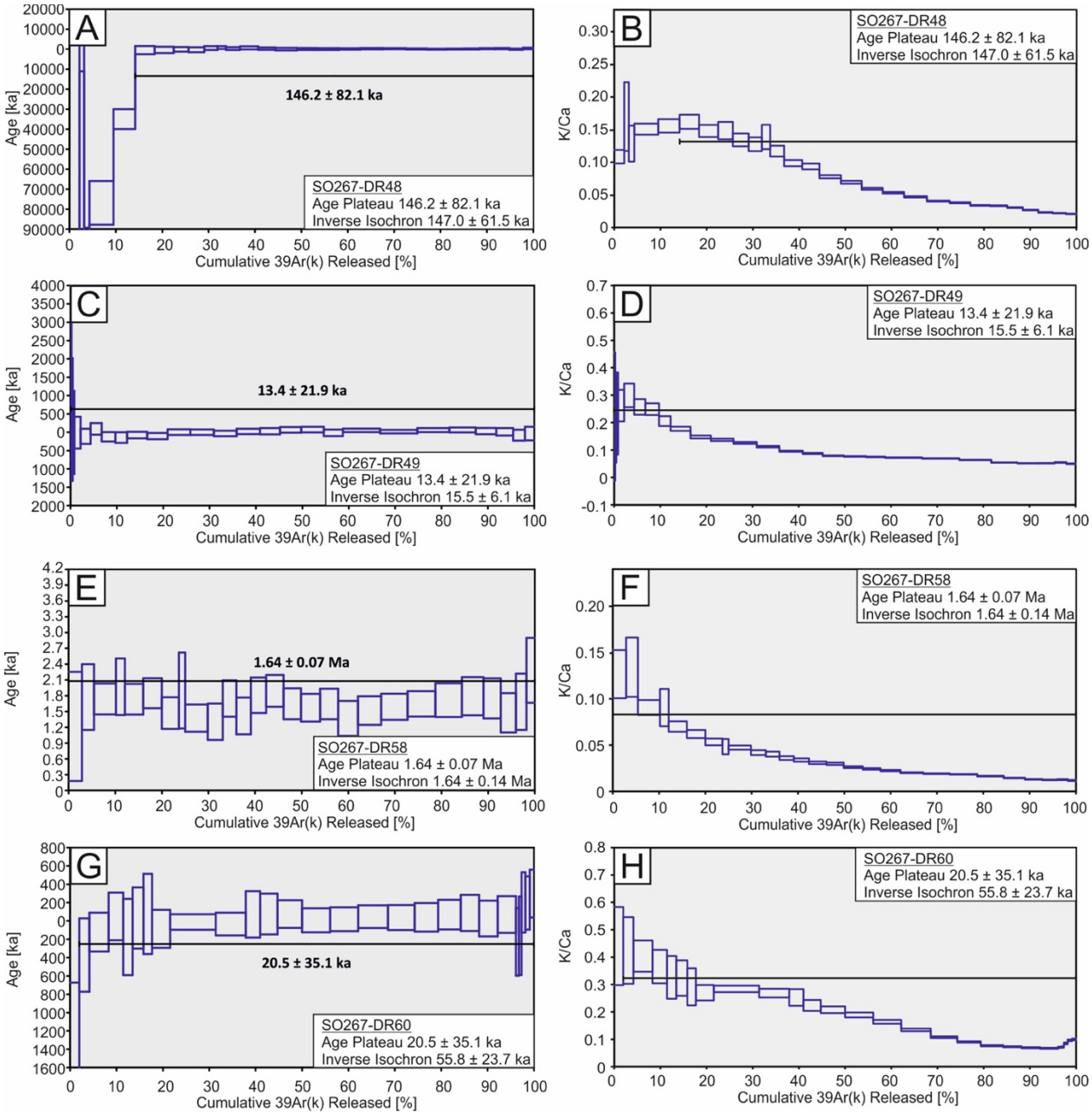


Figure 4.12: A) Total alkali-silica plot (after Le Maitre, 1989) showing the distribution Lau Basin volcanic rocks in the background from databases compiled by Fassbender et al. submitted and the dated samples from this study (labelled). Symbols correspond to intensity of fluid fluxed melting (diamonds: no arc-related geochemical signatures; squares: weak arc-related geochemical signatures; circles: strong arc-related geochemical signatures). A) All Ar-Ar samples have low SiO_2 and Na_2O + K_2O concentrations plotting in the basalt and basaltic andesite fields. B) Lithotectonic discrimination plot of Pearce et al. (2014), showing the distribution Lau Basin volcanic rocks in the background from databases compiled by Fassbender et al. (2023) and the dated samples from this study (labelled). C) Ba/Nb versus La/Sm plot illustrating influence of subduction input and enriched mantle components. The dated samples in this study plot in a linear

array from low La/Sm, low Ba/Nb to low La/Sm, and high Ba/Nb. Samples DR65 and DR69 have low Ba/Nb, sample DR77 has intermediate Ba/Nb and samples DR48, DR49, DR58, and DR60 have high Ba/Nb. D) Primitive mantle-normalized trace element plot showing the distribution Lau Basin volcanic rocks (including felsic volcanic rocks with higher concentrations of incompatible trace elements) in the background from databases compiled by Fassbender et al. (2023) and the dated samples from this study (labelled). Samples DR49 and DR58 have strong negative Nb-Ta anomalies, flat REE patterns and low HREE. Sample DR60 has a strong negative Nb-Ta anomaly, flat REE pattern and high HREE. Sample DR77 has a weak negative Nb-Ta anomaly, increasing REE pattern and intermediate HREE. Samples DR65 and DR69 have no negative Nb-Ta anomalies, increasing REE patterns and high HREE.


A
Age [ka]
146.2 ± 82.1 ka
SO267-DR48
Age Plateau 146.2 ± 82.1 ka
Inverse Isochron 147.0 ± 61.5 ka
Cumulative 39Ar(k) Released [%]
B
K/Ca
SO267-DR48
Age Plateau 146.2 ± 82.1 ka
Inverse Isochron 147.0 ± 61.5 ka
Cumulative 39Ar(k) Released [%]
C
Age [ka]
13.4 ± 21.9 ka
SO267-DR49
Age Plateau 13.4 ± 21.9 ka
Inverse Isochron 15.5 ± 6.1 ka
Cumulative 39Ar(k) Released [%]
D
K/Ca
SO267-DR49
Age Plateau 13.4 ± 21.9 ka
Inverse Isochron 15.5 ± 6.1 ka
Cumulative 39Ar(k) Released [%]
E
Age [ka]
1.64 ± 0.07 Ma
SO267-DR58
Age Plateau 1.64 ± 0.07 Ma
Inverse Isochron 1.64 ± 0.14 Ma
Cumulative 39Ar(k) Released [%]
F
K/Ca
SO267-DR58
Age Plateau 1.64 ± 0.07 Ma
Inverse Isochron 1.64 ± 0.14 Ma
Cumulative 39Ar(k) Released [%]
G
Age [ka]
20.5 ± 35.1 ka
SO267-DR60
Age Plateau 20.5 ± 35.1 ka
Inverse Isochron 55.8 ± 23.7 ka
Cumulative 39Ar(k) Released [%]
H
K/Ca
SO267-DR60
Age Plateau 20.5 ± 35.1 ka
Inverse Isochron 55.8 ± 23.7 ka
Cumulative 39Ar(k) Released [%]

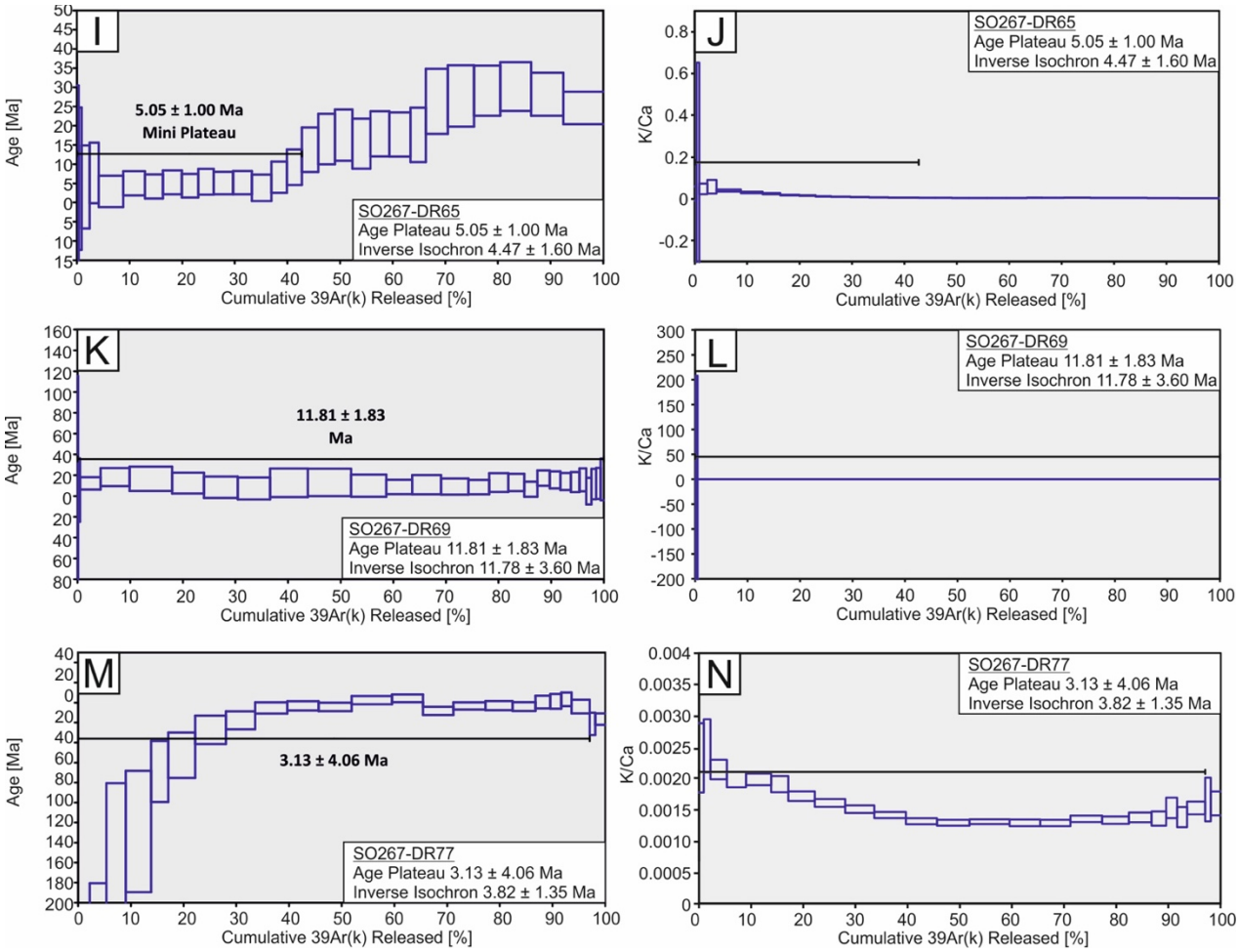
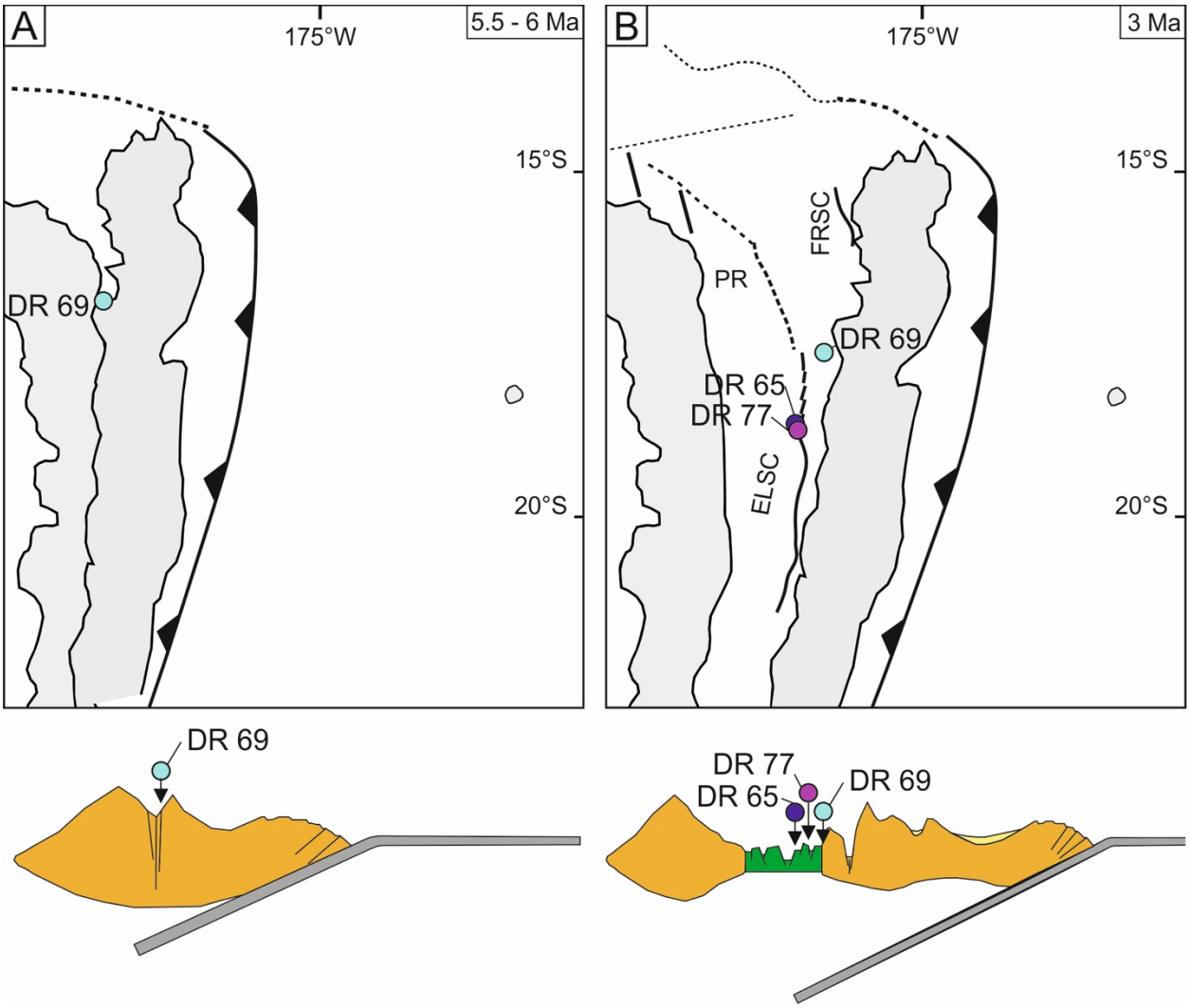


Figure 4.13: Results of high-resolution incremental heating Ar-Ar analyses for the SO267 basaltic volcanic rocks showing cumulative Ar-release and variable K/Ca ratios during the step heating process. The reported Ar-Ar ages are weighted age estimates and inverse isochron ages (Appendix C). A) Sample DR48-1B released $^{40}Ar/^{39}Ar$ proportions resulting in young ages in the low temperatures steps and gave a plateau age of 146.2 ± 82. B) High K/Ca at low-temperature steps indicating altered phases likely contributed to early degassing. C) Sample DR49-1 has consistent Ar-Ar ages from low to high temperature steps and a plateau age of 13.4 ± 21.9 ka. D) K/Ca decreases only slightly indicating no alteration phases in the groundmass. E) Sample DR58-4 released $^{40}Ar/^{39}Ar$ proportions resulting in young ages in the low temperatures steps and gave a plateau age of 1.64 ± 0.07. F) High K/Ca at low temperature steps indicating altered phases likely contributed to early degassing. G) Sample DR60-1 released $^{40}Ar/^{39}Ar$ proportions resulting in young ages in the low temperatures steps and gave a plateau age of 20.5 ± 35.1 ka. H) High K/Ca

at low temperature steps indicating altered phases likely contributed to early degassing. I) Sample DR65-1G released $^{40}Ar/^{39}Ar$ proportions resulting in young ages in the low temperatures steps and gave a plateau age of 5.05 ± 1.00 Ma. J) High K/Ca at low temperature steps indicating altered phases likely contributed to early degassing. K) Sample DR69-2A has consistent Ar-Ar ages from low to high temperature steps and a plateau age of 11.81 ± 1.83 Ma. L) K/Ca ratios decrease only slightly at low temperature steps indicating minor altered phases. M) Sample DR77-4A released $^{40}Ar/^{39}Ar$ proportions resulting in young ages in the low temperatures steps and gave a plateau age of 3.82 ± 1.35 Ma. N) K/Ca slightly decrease at low temperatures steps and slightly increase at high temperature steps indicating degassing of inclusions.


A
175°W
5.5 - 6 Ma
15°S
20°S
DR 69
B
175°W
3 Ma
15°S
20°S
FRSC
PR
DR 69
DR 65
DR 77
ELSC
DR 69
DR 77
DR 65
DR 69

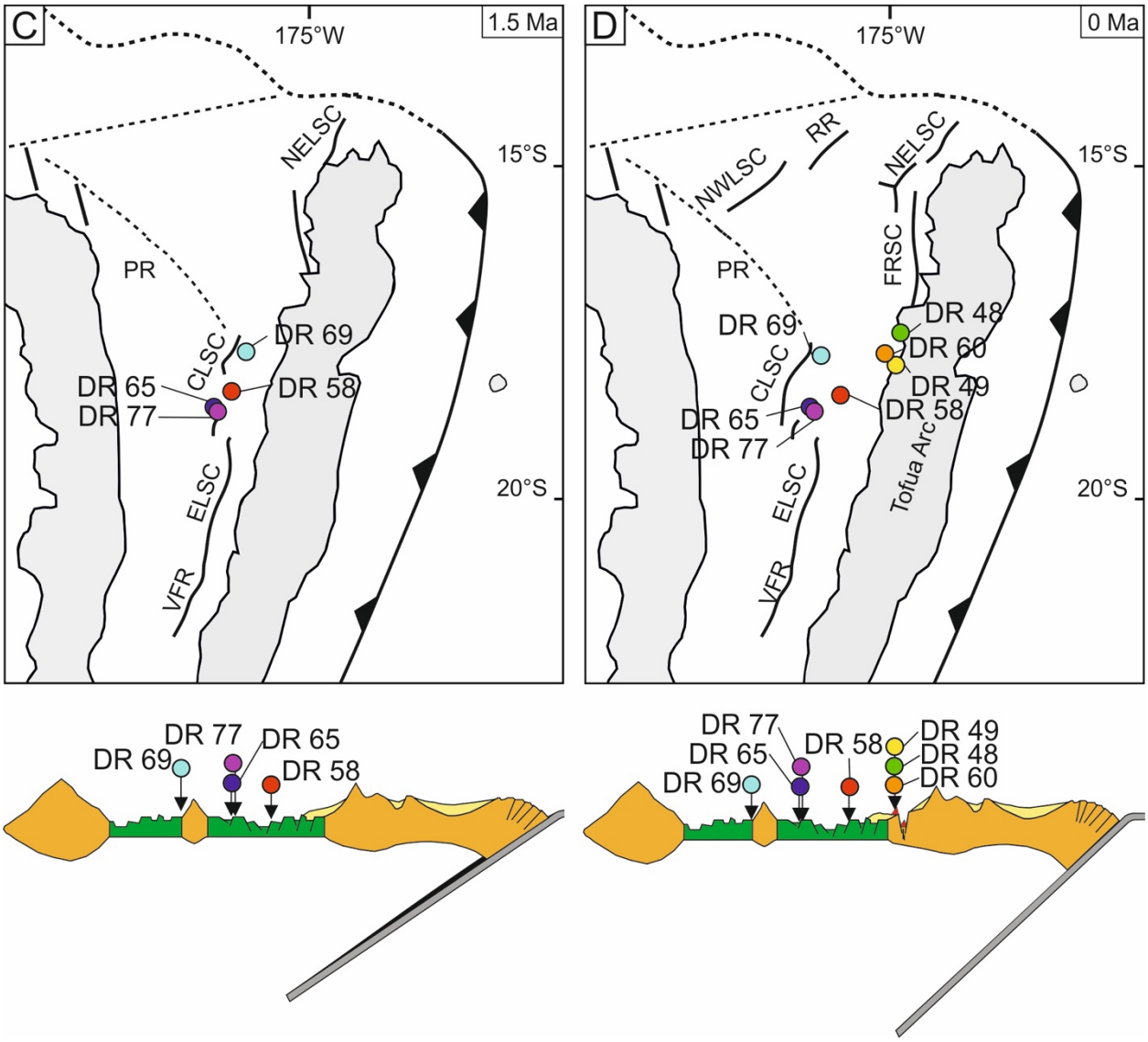


Figure 4.14: Schematic illustration of the Lau Basin opening and the sequence of eruption of lavas sampled for this study. A) 5.5 – 6 Ma: At this age opening of the Lau Basin is in its infancy and no back-arc basin has been developed. DR69 sampled lava erupted behind the arc during an early phase of arc-tholeiitic magmatism, prior to rapid opening. B) ca. 3 Ma: Beginning of asymmetric opening of the back-arc basin along the ELSC and prior to the formation of the CLSC. DR 65 and DR 77 sampled crust in the nodal basins at the northern termination of the ELSC. C) ca. 1.5 Ma: The beginning of back-arc spreading at the CLSC which eventually overtake the ELSC. DR 58 sampled a dike-like ridge intruded into older back-arc crust as extension migrated back toward the arc. The FRSC is in its infancy. D) Current plate configuration. DR48, DR49, and DR60 sampled the most recent volcanic field emerging in advance of the propagating tip of the FRSC.

Tables

Table 4.1. Whole rock geochemistry of the Ar-Ar samples. The samples have been prepared and analyzed at the GEOMAR Helmholtz Centre, Kiel and ICPMS-Lab at the institute of Geosciences, at the University of Kiel, Germany. Major elements have been produced by X-ray fluorescence spectroscopy (XRF) and trace-elements by solution Inductively Couple Plasma – Mass Spectrometry (ICP-MS).

Sample	Method	SO267 DR48-1B	SO267 DR49-1	SO267 DR58-4	SO267 DR60-1B	SO267 DR65-1G	SO267 DR69-2A	SO267 DR77-4A
	Longitude	-174.73	-174.83	-175.27	-174.94	-175.86	-175.72	-175.7
	Latitude	-18.01	-18.22	-18.36	-18.16	-18.4	-17.82	-18.52
SiO_2 wt.%	XRF	50.16	50.29	53.54	55.57	49.33	48.94	49.65
TiO_2 wt.%	XRF	0.63	0.52	0.51	0.75	0.94	0.87	0.71
Al_2O_3 wt.%	XRF	15.93	17.15	15.13	15.8	16.87	16.51	14.2
Fe_2O_3 wt.%	XRF	11.27	10.82	10.12	11.04	9.41	9.04	9.64
MnO wt.%	XRF	0.19	0.18	0.17	0.19	0.16	0.15	0.16
MgO wt.%	XRF	7	6.45	6.56	3.56	8.02	8.25	8.63
CaO wt.%	XRF	12.43	12.35	11.08	8.58	12.81	13.29	14.1
Na_2O wt.%	XRF	1.38	1.11	1.54	2.02	2.09	2.1	1.41
K_2O wt.%	XRF	0.37	0.53	0.2	0.84	0.06	0.13	0.08
P_2O_5 wt.%	XRF	0.13	0.1	0.06	0.2	0.08	0.05	0.04
SO_3 wt.%	XRF	0	0	0	0.03	0.17	0.12	-0.01
LOI wt.%	XRF	-0.26	-0.28	0.14	0.42	-0.27	-0.1	0.34
Sum		99.31	99.32	99.15	99.1	99.79	99.47	99.11
Sr ppm	ICP-MS	236.44	283.37	126.89	313.96	85.08	85.26	84.71
Y ppm	ICP-MS	14.64	11.20	16.73	20.24	24.67	26.66	17.17
Zr ppm	ICP-MS	19.44	15.93	25.05	37.36	46.95	42.47	24.81
Nb ppm	ICP-MS	0.35	0.28	0.49	0.66	1.05	0.73	0.33
Ba ppm	ICP-MS	53.91	72.54	43.17	104.85	9.83	5.73	6.49
La ppm	ICP-MS	1.98	1.86	1.58	4.10	1.47	1.31	0.87
Ce ppm	ICP-MS	5.02	4.49	4.14	9.97	4.69	4.30	2.78
Pr ppm	ICP-MS	0.84	0.72	0.70	1.59	0.91	0.80	0.53
Nd ppm	ICP-MS	4.63	3.86	3.91	8.23	5.59	4.95	3.22
Sm ppm	ICP-MS	1.57	1.27	1.40	2.47	2.19	2.06	1.30
Eu ppm	ICP-MS	0.62	0.50	0.52	0.90	0.85	0.85	0.54
Gd ppm	ICP-MS	2.00	1.59	1.92	2.93	3.06	3.14	1.96
Tb ppm	ICP-MS	0.34	0.27	0.36	0.49	0.56	0.60	0.38
Dy ppm	ICP-MS	2.34	1.83	2.54	3.25	3.89	4.23	2.72
Ho ppm	ICP-MS	0.50	0.39	0.56	0.68	0.83	0.91	0.60
Er ppm	ICP-MS	1.43	1.11	1.63	1.99	2.36	2.59	1.73
Tm ppm	ICP-MS	0.21	0.16	0.25	0.30	0.35	0.39	0.26
Yb ppm	ICP-MS	1.46	1.15	1.73	2.09	2.35	2.6	1.79
Lu ppm	ICP-MS	0.22	0.18	0.27	0.33	0.35	0.39	0.27
Hf ppm	ICP-MS	0.60	0.5	0.79	1.10	1.42	1.28	0.79
Ta ppm	ICP-MS	0.02	0.02	0.03	0.05	0.07	0.05	0.02
Th ppm	ICP-MS	0.15	0.18	0.13	0.37	0.09	0.06	0.04

Table 4.2. Summary of Ar-Ar ages from the southern Niuafo'ou microplate (this study).

Sample	Latitude	Longitude	Depth (m)	Material	Age	Plateau		MSWD	Normal Isochron		MSWD	Inverse Isochron		MSWD
						Age	± 2σ (i)		Age	± 2σ (i)		Age	± 2σ (i)	
SO267 DR48-1B	-18.01	-174.73	1037	Groundmass	Plateau	146.2	± 82.1 ka	0.66	145.1	± 108.1 ka	0.73	147	± 61.5 ka	0.73
SO267 DR49-1	-18.22	-174.83	1342	Groundmass	Plateau	13.4	± 21.9 ka	1.65	11.3	± 27.1 ka	1.87	15.5	± 6.1 ka	1.79
SO267 DR58-4	-18.36	-175.27	2057	Groundmass	Plateau	1.64	± 0.07 Ma	1.2	1.63	± 0.15 Ma	1.44	1.64	± 0.14 Ma	1.45
SO267 DR60-1	-18.16	-174.94	1680	Groundmass	Inverse Isochron	20.5	± 35.1 ka	0.85	52.6	± 46.1 ka	0.64	55.8	± 23.7 ka	0.67
SO267 DR65-1G	-18.4	-175.86	2545	Groundmass	Minor Plateau	5.05	± 1.00 Ma	0.46	4.47	± 1.97 Ma	0.84	4.47	± 1.60 Ma	0.84
SO267 DR69-2A	-17.82	-175.72	1003	Groundmass	Plateau	11.81	± 1.83 Ma	0.54	11.74	± 4.78 Ma	0.75	11.78	± 3.60 Ma	0.75
SO267-DR77-4A	-18.52	-175.7	2646	Plagioclase	Inverse Isochron	64.8	± 0.9 ka	9.94	3.74	± 2.19 Ma	2.1	3.82	± 1.35 Ma	2.1

*Note: Minor plateau indicates that a lower percentage of the released Ar is representative for this age. Every plateau must include at least 50% of the released Ar. All metadata are provided in Appendix C.

Chapter 5

Summary and Conclusions

5.1 Chapter highlights

This study examined the geochemical diversity of submarine mafic and felsic volcanic rocks in modern oceanic crust and compared them to volcanic rocks from ancient settings. We compiled and investigated large global databases of volcanic rocks from mid-ocean ridges, ridge-hotspot intersections, oceanic islands, intraoceanic arc and back-arc and intracontinental arc-related regimes, and we presented a new data driven approach to their classification. In each of these settings we investigated geochemical signatures that are related to specific melting conditions, mantle contributions, and lithotectonic setting with implications for characterizing episodes of crustal growth. The main points of each chapter are summarized below.

Chapter 2: Geochemical Signatures of Felsic Volcanic Rocks in Modern Oceanic Settings and Implications for Archean Greenstone Belts

- This chapter explores the geochemical compositions of felsic volcanic rocks in modern submarine environments, highlighting similarities with dacites and rhyolites from the Abitibi Greenstone Belt.
- We identified 9 target classes of modern submarine felsic volcanic rocks from different lithotectonic settings.
- Using random forest, we identified similar geochemical signatures in the Abitibi Greenstone Belt.
- Mid-ocean ridge like felsic volcanic rocks occur in both modern and ancient data sets and are common in back-arc basins, such as the Lau Basin.
- The compositions of modern felsic volcanic rocks include the entire spectrum of compositions of Archean dacites and rhyolites.
- FIIIb-like geochemical signatures exist in modern ocean settings but they occur at locations that likely won't be preserved in the geological record, such as mid-ocean ridges.

Chapter 3: Geochemical Signatures of Mafic Volcanic Rocks in Modern Oceanic Settings and Implications for Archean Mafic Magmatism

- This chapter explores the geochemical compositions of mafic volcanic rocks in modern submarine environments, highlighting similarities with basalts from the Abitibi Greenstone Belt.
- We identified 7 target classes of modern submarine mafic volcanic rocks from different lithotectonic settings.
- Rocks with different geochemical signatures may be closely juxtaposed in microplate regimes with multiple rifting and spreading center regimes.
- Melts with weak arc-related geochemical signatures, similar to those in Archean greenstone belts, occur at termination points of back-arc rifts and spreading centers due to complex mantle flow at these locations and are found in almost every back-arc basin.
- Different mantle flow regimes, such as those encountered in the Lau Basin, may produce geochemical signatures similar to many of the assemblages of the AGB at the same scale.

Chapter 4: Highly Episodic Growth of the Niuafo'ou Microplate, NE Lau Basin, from Ar-Ar Dating: Implications for Crustal Growth in Greenstone Belts

- This chapter explores the age-relationships of mafic volcanic rocks in a portion of the Niuafo'ou microplate of the Lau Basin, highlighting the complexity of crustal growth during basin opening.
- Seven new radiometric ages are provided for mafic volcanic rocks of the Niuafo'ou microplate.
- The ages span the entire history of opening of the Lau Basin within a space of 100 km, similar to the range of ages of volcanic rocks in the Blake River Group of the AGB.
- The new Ar-Ar ages challenge the view of back-arc basin opening as a linear progression from rifting to eventual spreading and instead suggest ridge jumps, rift propagation, and diffuse extension throughout the basin development.

5.2 Comparison between modern oceans and the AGB

We used a combination of principal components analysis, agglomerative hierarchical clustering and random forest to investigate groups of geochemical signals from the modern oceanic settings and compare them with samples from the Archean Abitibi Greenstone Belt. This revealed exceptional geochemical diversity in both felsic and mafic volcanic rocks in modern arc and back-arc environments. This diversity reflects melting caused by fluid fluxed components from the dehydrating subducting slap, melting of dry-asthenospheric mantle, and complex mantle flow regimes, especially at propagating rift tips and termination points of spreading centers.

Mid-ocean ridge-like dacites form by fractional crystallization and assimilation of hydrated oceanic crust resulting in systematic geochemical signatures similar to Archean FIIIb rhyolites such as felsic volcanic rocks from NE Matagami. Similarly, back-arc basalt and mid-ocean ridge-like mafic volcanic rocks, such as at the NWLSC and the Pacific Antarctic Rise, as well as basalts from ridge-hotspot intersections such as in Iceland, all share enriched mantle signatures typical of spreading centers far from any subduction and associated high geothermal gradients. **Table 5.1** lists similarities and differences of major Lau assemblages and Archean assemblages. Comparisons with volcanic rocks of the AGB indicate magmas generated above the hot Archean mantle were most similar geochemically to those of modern back-arc spreading centers with weak arc-signatures and enriched mantle sources. In contrast, rocks from ocean island-like settings such as Hawaii or Marquesas Archipelago show almost no similarity to volcanic rocks from the AGB.

We have identified mid-ocean ridge-like dacites, similar to Archean FIIIb felsic volcanic rocks, in complex microplate mosaics of the northern Lau and Manus Basins that are related to anomalous heat flow, rising asthenopheric mantle and rift propagation especially at overlapping spreading centers. These rocks have flat REE patterns, significant HREE enrichment, and strong negative Eu anomalies similar to FIIIb felsic volcanic rocks that have been uniquely linked to major volcanic centers of the AGB such as Matagami. Major differences in the abundance of Archean and post-Archean felsic volcanic rocks of different types may be at least partly explained by their preservation potential. Modern mid-ocean ridges and mature back-arc spreading centers have low preservation potential, owing to their eventual subduction at basin margins. In contrast, the inferred

complex microplate mosaics of Archean greenstone belts might have been important settings for preservation of this type of crust, promoted by the thickness of the crust and high heat flow in the Archean. While they are not exact tectonic analogs, the geochemical evolution of felsic volcanic rocks in Archean greenstone belts may share many of the same influences observed in modern microplate breakouts, such as in the northern Lau Basin. Many samples from the northeastern Lau basin are nearly identical to mafic volcanic rocks in the Abitibi greenstone belt, having slightly dipping REE patterns, weak negative Nb-Ta anomalies, and Th-enrichment. These rocks occur at the edge of the Niuafo'ou microplate where mantle flow is controlled by a well-known slab tear and STEP fault and the retreating subducting slab. Undepleted mantle is thought to flow around the edge of the subducting plate, introducing fertile mantle material into the back-arc.

The geology of the northern Lau Basin illustrates the complexity of modern microplate mosaics, with many similarities to Archean greenstone belts such as the Abitibi. Long-established subduction-zone related regimes elsewhere in the Western Pacific measure 1000s of km in length. Such a scenario seems to be a very unlikely analog for Archean greenstone belts, with increased heat flow resulting in an increased number of spreading centers. We have shown that increased numbers of spreading centers result in greater geochemical variability, more complex mantle flow regimes, and less organized plate motions that are seemingly identical to many interpretations of the Abitibi greenstone belt.

5.3 Future directions

The systematic analysis of modern submarine volcanic rocks show that their magmatic evolution is strongly affected by tectonic complexities at a range of different scales. Machine-learning applications developed in this study highlight conditions wherein enhanced magmatism and complex microplate-related regimes may contribute to highly diverse geochemical signatures. Mafic volcanic rocks that are most similar to samples from Archean greenstone belts include melts generated at the termination points of back-arc spreading centers, melts influenced by toroidal mantle flow at microplate edges, slab tears, and hotspots such as Iceland with thickened oceanic crust. The microplate mosaic, rift propagation, and localized mantle flow regimes seem the most promising modern analogs of Archean greenstone belt conditions. However, some important questions remain. For example:

Research question 1: Are particular stages of back-arc evolution associated with enhanced magmatism and therefore mineral endowment?

Research approach: Known mineralization and hydrothermal vent sites and other indicators of magmatic-hydrothermal activity need to be built into a machine-learning classifier to identify the relationship of whole-rock geochemistry to mineralization and better understand the underlying systematics.

Research question 2: How is crustal growth (and crustal thickness) reflected in the geochemical signatures?

Research approach: To explore underlying geochemical systematics, whole-rock geochemical data could be combined with gravity data to create a regression model trained to identify crustal thickness.

Research question 3: How common are the complex age relationships of the crust, like those found in the northern Lau Basin?

Research approach: Detailed geophysical mapping and sampling in other oceanic regimes may indicate similarly complex and unexpected age-relationships in other settings that can be compared to the geological record (e.g., in greenstone-belt assemblages).

Research question 4: What caused the exceptional preservation of FIIIb felsic volcanic rocks in Archean settings?

Research approach: Test whether hotter mantle that dominated the Archean favoured dry melting and preservation compared to colder regimes (e.g., in the Proterozoic) that favoured subduction and lack of preservation of the corresponding lithologies.

Table 5.1. Summary table of features in major Lau assemblages and similar AGB assemblages.

Lithotectonic assemblage	Descriptive rock formations	Geochemical signatures	Similar AGB assemblage
Central Lau Assemblage	Mafic dominated volcanic rock formations; depleted mid-ocean ridge like geochemical signatures	Low La/Sm; Low Nb/Yb; Low Th/Yb; Low Ba/Nb; No negative Nb-Ta anomaly	NA
East Lau Assemblage	Mafic dominated volcanic rock formations; occasional felsic volcanic rocks; strong arc-tholeiitic signature, transitioning into mid-ocean ridge like signature	Intermediate La/Sm; Intermediate Nb/Yb; Intermediate Th/Yb; Strong negative Nb-Ta anomaly	Tisdale assemblage; Val-d'Or group
Northwestern Lau Assemblage	Mafic dominated volcanic rock formations; occasional felsic volcanic rocks; enriched mid-ocean ridge like signature	Intermediate to high La/Sm; Intermediate to high Nb/Yb; Low Th/Yb; No negative Nb-Ta anomaly	Kidd-Munro assemblage
Fonualei Assemblage	Mafic dominated volcanic rock formations; strong arc-tholeiitic signature	Intermediate La/Sm; Intermediate Nb/Yb; Intermediate Th/Yb; Strong negative Nb-Ta anomaly	Tisdale assemblage; Val-d'Or group
Northeastern Lau assemblage	Mafic dominated volcanic rock formations; large felsic flow fields; enriched mantle signature; weak arc-related signature	High La/Sm; High Nb/Yb; High Th/Yb; Intermediate negative Nb-Ta anomaly	Blake River assemblage

Appendix A

Supplementary Information for Chapter 2: Geochemical Signatures of Felsic Volcanic Rocks in Modern Oceanic Settings and Implications for Archean Greenstone Belts

This document provides a detailed workflow for data analysis to accompany chapter 2: Geochemical Signatures of Felsic Volcanic Rocks in Modern Oceanic Settings and Implications for Archean Greenstone Belts. All data, figures and tables can be accessed online along with the main document. The complete workflow can be replicated within the open-source data mining software "KNIME" and R scripts within KNIME. The KNIME workflow is provided as Appendix workflow A1.knwf. To access the workflow, KNIME and R must be correctly installed from https://www.knime.com/ and https://www.r-project.org/. Additional plugins necessary for the analysis will be installed when the workflow document is started. A technical guide, with instructions on how to use KNIME, will appear within the KNIME work environment. A more detailed workflow is provided in this document.

Data QA/QC

A detailed description of data sources used in the study is provided in the text of the accompanying manuscript. In addition to our QA/QC on the compiled data, we examined the potential that metasomatic processes related to hydrothermal alteration and/or metamorphic processes could have altered the original compositions of the rocks. To identify potentially altered samples, we inspected the data in REE and immobile element plots and removed 11 samples that showed evidence of element mobility. The final database is given in **Appendix Table A1**. We further inspected all samples on a Pearce Element Ratio (PER) diagram, comparing the molar ratios of Al/Zr vs. (2Ca+Na+K)/Zr to unaltered feldspar (**Appendix Figure A1**). All modern oceanic felsic volcanic rocks in the final data set plot in a close array along the feldspar control line indicating little or no alteration (Stanley and Madeisky, 1996). We show a similar analysis of the samples from the Abitibi Greenstone Belt (AGB) that were used in this study. We removed 6 samples from the AGB data that showed evidence of Si, K and LREE mobility. We further tested the possible effects of element mobility in by comparing the principal components analysis (PCA) and random forest classification (RF) without the potentially mobile elements (Si, K, Ba). This yielded nearly identical PC1 and PC2 scores (**Appendix Figure A2**) and RF classifications (see below).

Data transformation

Prior to the PCA, all data were transformed using the centered-log transformation (CLR) to remove the effects of data closure (Aitchison, 1982). Because geochemical data sum to 100%, the element concentrations in a data table are not independent, possibly resulting in false correlations. To overcome this effect, all data were recalculated to elemental concentrations in ppm, and centered-log ratio transformations were applied. CLR divides the natural logarithm of each element by the geometric mean of all elements for each sample:

$$clr(x) = \left[ln\frac{x1}{g(x)} \ldots ln\frac{xD}{g(x)}\right]$$

Opening of the data in this way results in real numbers (e.g., containing positive and negative values) that are used in the PCA (see **Appendix Table A2**).

We further considered additive log ratio transformation (ALR) to remove the effects of data closure. However, using ALR transformed data yielded not as good results in the principal component analysis (i.e., less variance is covered in the first two principal components) and during the hierarchical clustering (i.e., less distinct separation of individual clusters) as CLR transformation.

Principal component analysis

The filtered and transformed data sets were used to carry out multivariate statistical analysis using 13 elements (Si, Ti, Al, K, Y, Zr, Nb, Ba, La, Sm, Eu, Yb, Th) as the variables. PCA reduces the variables into a limited number of components that account for the largest variance in the data set. Each principal component (PC) represents a fraction of the total variance that is affected by all the variables. **Appendix Table A3** lists the eigenvalues describing the weighting of each principal component in the total data set, the proportion of the variance represented by each component, and the cumulative variance. **Appendix Table A4** lists the loadings of each element on each component. The loadings of the principal components for each sample are given in **Appendix Table A5**.

Hierarchical clustering

The PCA results were used to perform an unsupervised agglomerative hierarchical clustering of the samples into distinct groups. The cluster analysis was performed with the R statistical software using the unsupervised hierarchical clustering function "HCPC" (Husson et al., 2009). HCPC uses a set of simple queries to group the samples into different and maximize the differences between the groups. This is done using Ward's criterion, which is the sum of the squared distances of individuals from the center of the cluster. In our study, we performed a cluster analysis on the first 3 principal components from the PCA. They account for ~90% of the variance and the most important geochemical features in the data set. The clustering results for each individual sample are given in **Appendix Table A5**. The clustering metadata describing standard deviation and mean

of each cluster and each element are given in **Appendix Table A6**. We further tested other clustering techniques such as k-means clustering with somewhat similar results. However, these techniques lack the crucial information of a data tree that can be retrieved from hierarchical clustering indicating the data structure and improving the decision-making process on deciding on the number of clusters.

Random forest classification

We used random forest (RF) to create a machine-learning classifier that sorts samples into known classes identified using hierarchical clustering and a "training" data set. The training is an iterative process by which random forest, learns what values are meaningful to achieve the best classification outcome and builds a model that can be used as a classification scheme. The application of the RF classifier is described in the text of the paper. To overcome differences in the number of samples in the target classes, we equalized the number of samples for each cluster prior to the training process using the synthetic minority oversampling technique (SMOTE: Chawla et al., 2002). SMOTE "creates" new samples by slightly altering the geochemical composition of original samples until each class contains the same number of samples as the largest class. The resulting artificial training set, with 1440 samples created by this process and the original data are given in **Appendix Table A7**.

Building and testing the RF classifier was done using KNIME, as described in the text. To validate the model, we used the subset of samples separated from the training dataset by a bootstrapping procedure (i.e., "out of bag" samples). **Appendix Table A8** shows the results of the classification of the "out of bag" samples in percentages for each target class; 100% of the samples were classified into the correct target class. **Appendix Table A9** lists the randomly selected samples from our original data set that were used in a blind test, which determines how well the classifier performs on new data. At least 4 samples were available for each target class in the blind test. **Appendix Table A10** shows the results of the blind test in which the samples were correctly classified in almost every case for all target classes, reaching an overall accuracy of 96%.

Comparison with Archean felsic volcanic rocks

We used the RF classifier developed in this study to compare modern oceanic volcanic rocks with Archean rhyolite samples from the Abitibi Greenstone Belt (AGB). The data sources are provided in **Appendix Table A11**. The outcome of the classification using all 13 elements (Si, Ti, Al, K, Y, Zr, Nb, Ba, La, Sm, Eu, Yb, Th) as the variables is provided in **Appendix Table A12**. For each sample, every target class receives a vote based on the trained decision trees. The assigned target class for each sample is based on the target class with the majority vote (>50%). We then retrained the RF classifier using only Al, Nb, Ti, Th, Y, Yb, and Zr (see workflow above) to remove the effect of potentially mobile elements. The results of this classification are presented in **Appendix Table A13** and are nearly identical to the analysis with the full suite of elements. More samples were classified in total (84 compared to 58 samples) and a number of samples originally identified in target class 5 were identified as target class 7. Using the immobile elements 4.6% of the samples in the blind test were misclassified, compared to our original RF classifier using all 13 elements that yielded a blind test error of 3.1%.

References

Aitchison, J., 1982: The statistical analysis of compositional data: Journal of the Royal Statistical Society, v. 44, issue 2, p. 139–160.

Chawla, N. V., Bowyer, K. W., Hall, L. O., and Kegelmeyer, W. P., 2002, SMOTE: Synthetic minority over-sampling technique: Journal of Artificial Intelligence Research, v. 16, p. 321–357.

Husson, F., Josse, J., Le, S., Mazet, J., 2009, FactoMinerR: Multivariate Exploratory Data Analysis and Data Mining with R. (http://factominer.free.fr).

R Core Team 2020, R: A language and environment for statistical computing: R Foundation for Statistical Computing, Vienna, Austria. (https://www.R-project.org).

Stanley, C.R. and Madeisky, H.E., 1996, Lithogeochemical exploration for metasomatic zones associated with hydrothermal mineral deposits using molar element ratio analysis: Lithogeochemical exploration for ore deposits using Pearce Element Ratio Analysis, v. 11. Geological Association of Canada, p. 193-212.

Figures

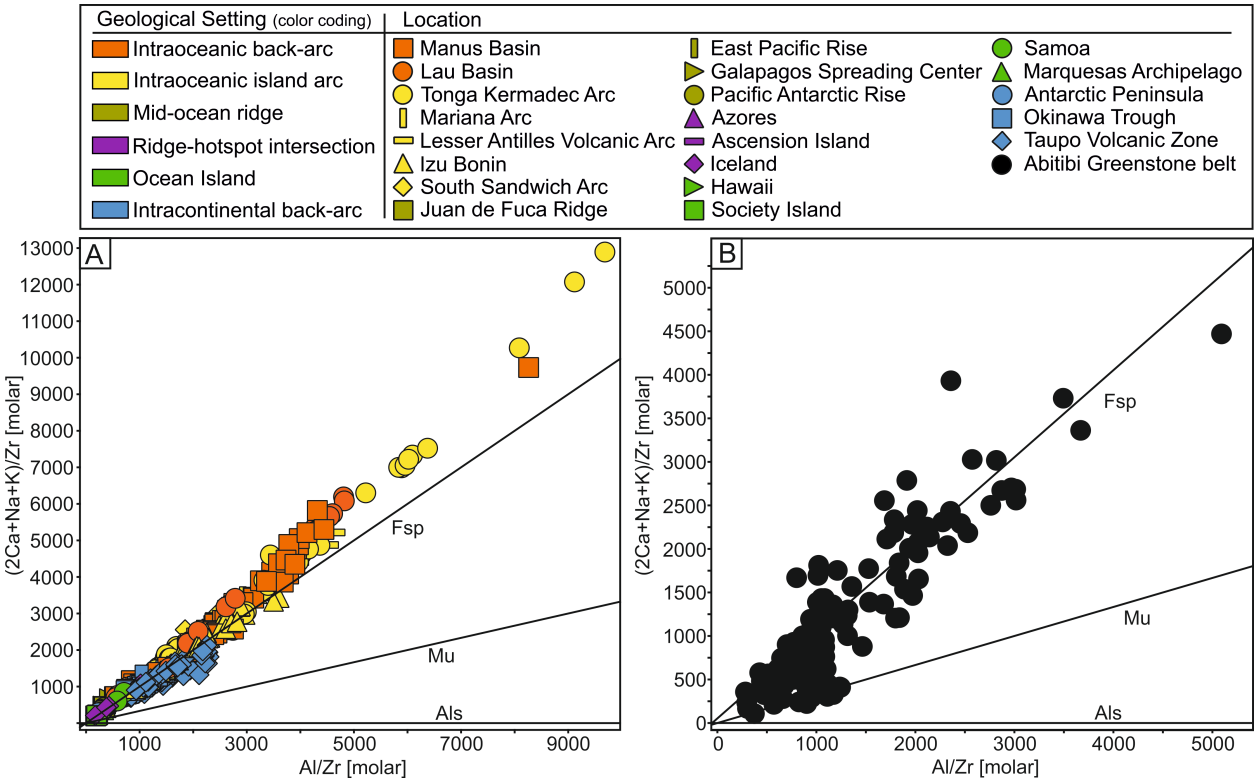


Figure A1. A) Pearce Element Ratio analysis of the least-altered samples of modern oceanic felsic volcanic rocks in Table A1, based on Al/Zr versus (2Ca+Na+K)/Zr molar ratios. The samples plot in a close array along the feldspar control line indicating no alteration. B) Pearce Element Ratio analysis of least-altered samples of Archean felsic volcanic rocks of the Abitibi Greenstone Belt (see Appendix Table A11). Most of the samples in the data set plot in a linear array with slight deviation from the feldspar control line indicating weak alteration for those samples.

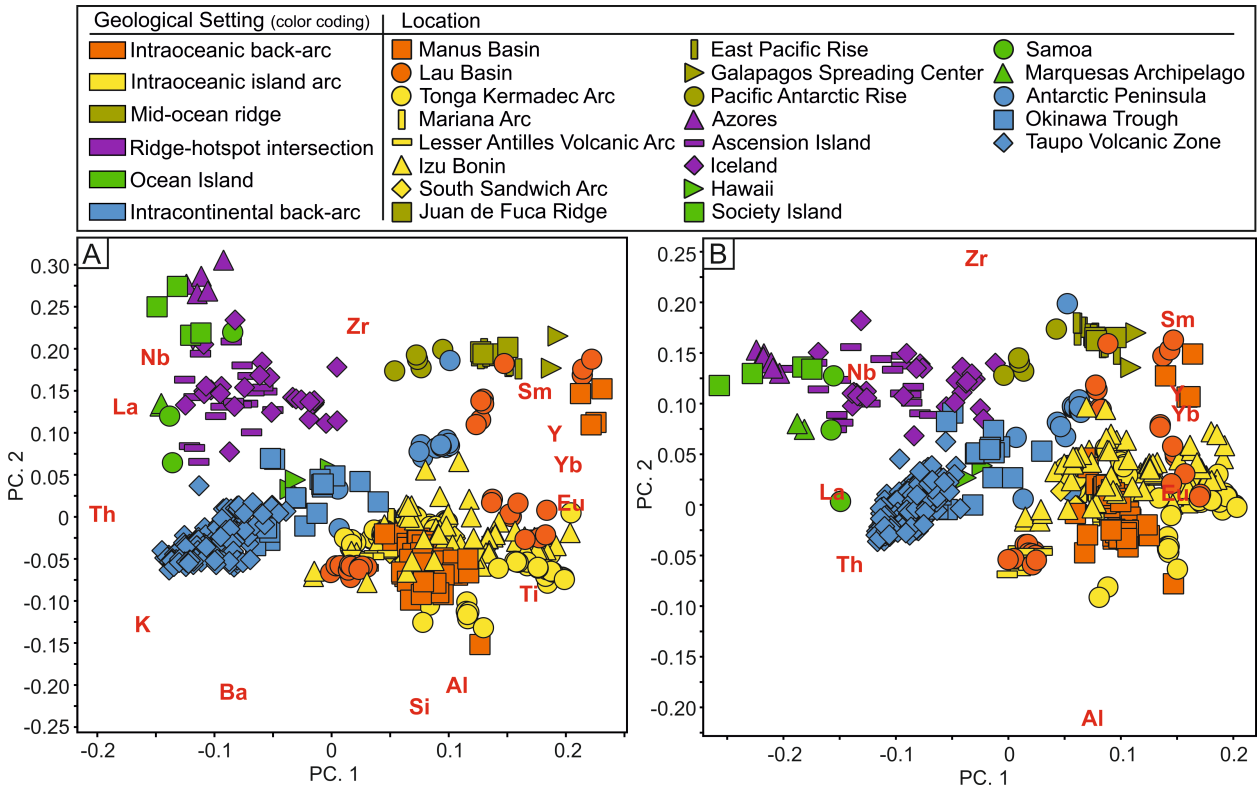


Figure A2. A) Principal components plot of the major and trace element geochemistry of modern oceanic felsic volcanic rocks using all 13 elements in the database (Si, Ti, Al, K, Y, Zr, Nb, Ba, La, Sm, Eu, Yb, Th). PC1 and PC2 account for 54% and 31%, respectively, of the total variance of the data set. The red element labels correspond to loadings for the entire data set; the symbols are the loadings for individual samples. PC1 has high loadings of Sm, Y, Yb, Eu, Ti and low loadings of Nb, La, Th, K while PC2 has high loadings of Zr, Nb, Sm and low loadings of Al, Ba, Si. Samples from ridge-hotspot intersections have high scores for PC1 and low scores for PC2. Samples from mid ocean ridge dacites have high scores for PC1 and high scores for PC2. Samples from intraoceanic arc-backarc systems have high scores for PC1 and low scores for PC2; and samples from the intracontinental arc-backarcs have low scores for PC1 and PC2. B) Principal components plot of the same samples using a subset of immobile elements. The analysis was conducted using 10 elements (Ti, Al, Y, Zr, Nb, La, Sm, Eu, Yb, Th) and excluding Si, K, and Ba. PC1 and PC2 account for 65% and 19%, respectively, of the total variance of the data set. PC1 has high loadings of Sm, Y, Yb, Eu, Ti and low loadings of Nb, La, Th, while PC2 has high loadings of Zr, Nb, Sm and low loadings of Al. As in the analysis using all 13 elements, samples from ridge-hotspot intersections have high scores for PC1 and low scores for PC2. Samples from mid-ocean

ridge dacites have high scores for PC1 and PC2. Samples from intraoceanic arc-backarc systems have high scores for PC1 and low scores for PC2; and samples from the intracontinental arc-backarcs have low scores for PC1 and PC2.

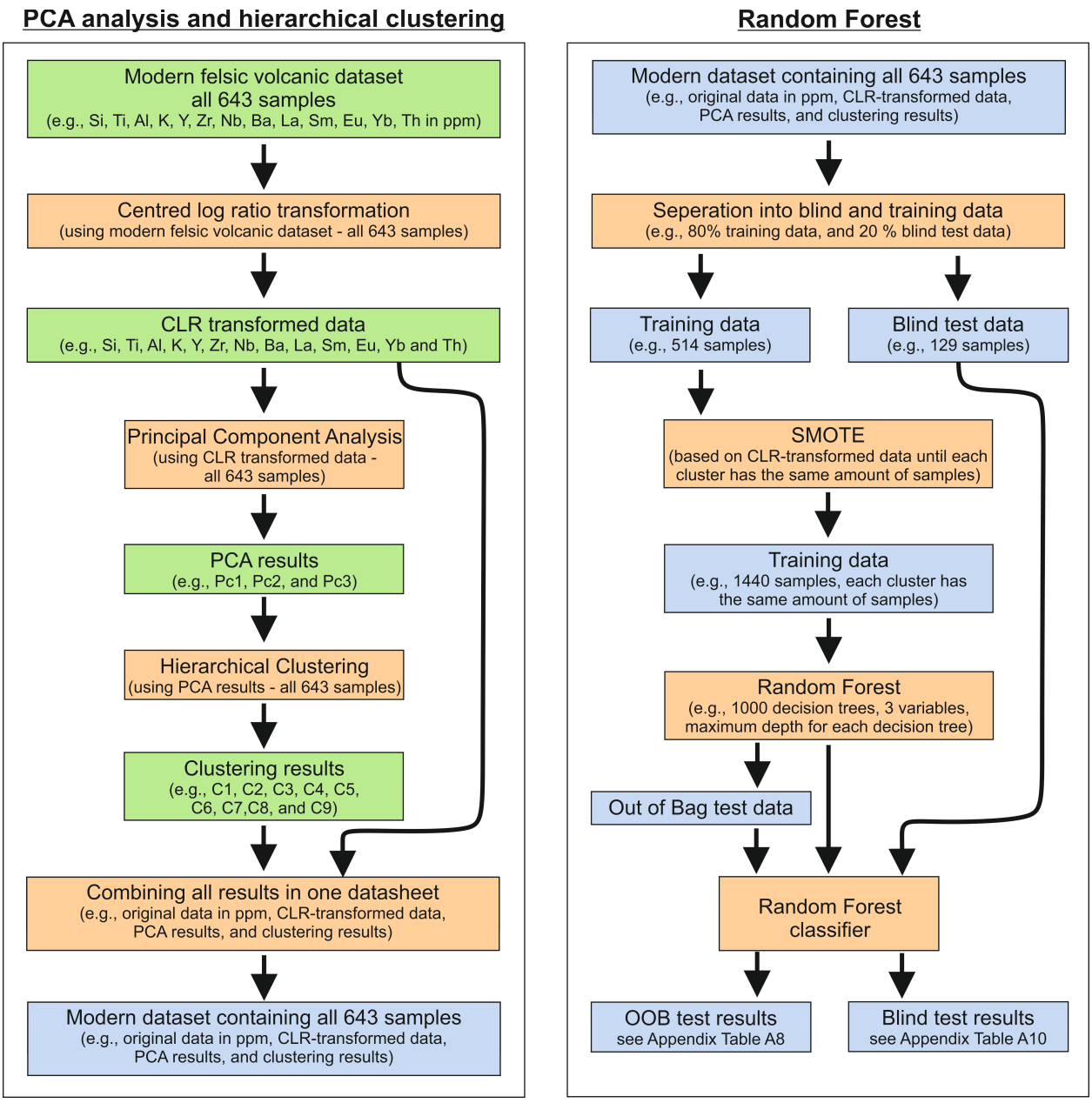
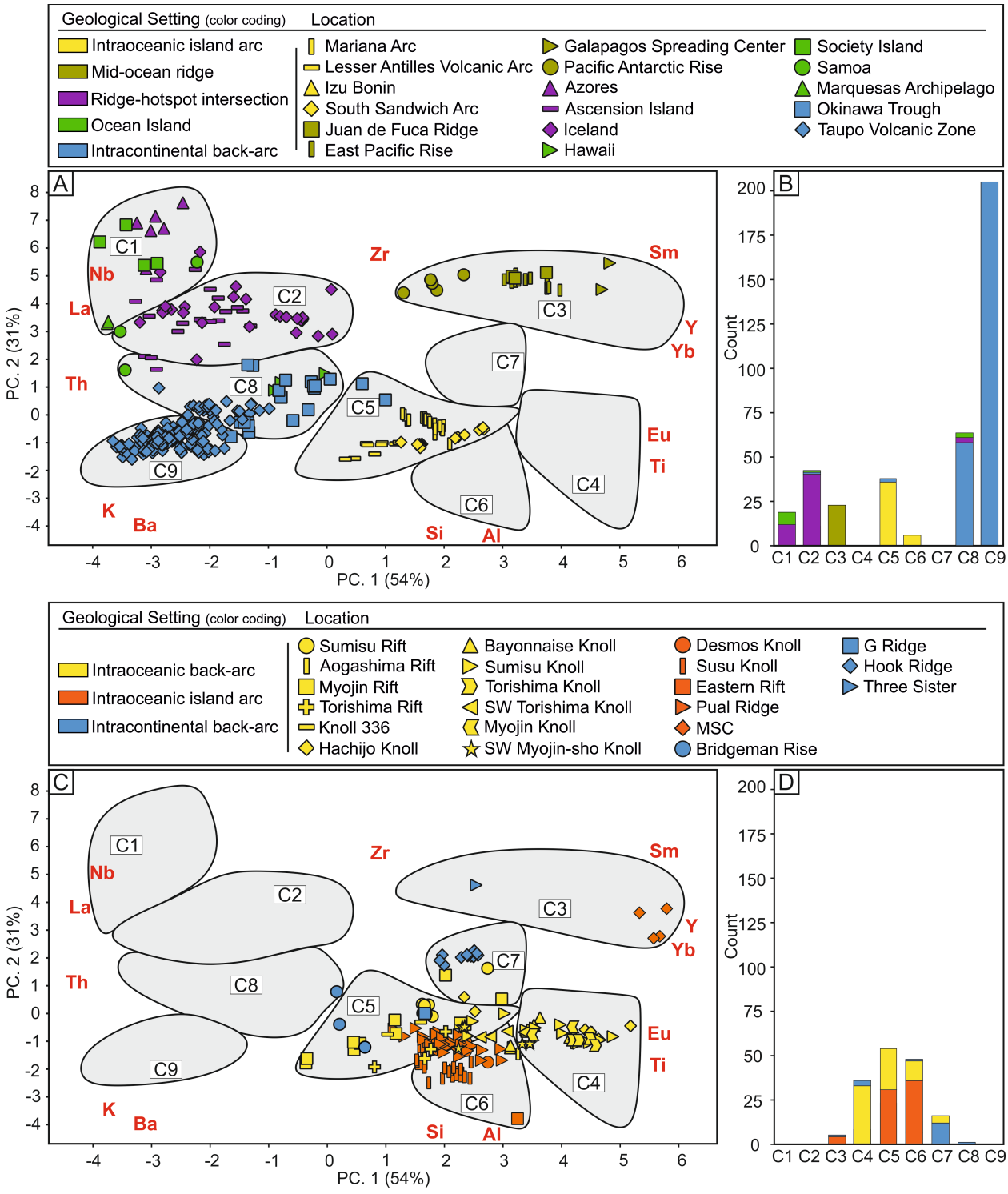


Figure A3. Illustration of the workflow used to compare felsic volcanic rock compositions in modern oceanic settings, showing the sequence of principal component analysis, hierarchical clustering and random forest classification.


Geological Setting (color coding)
Location
Intraoceanic island arc
Mid-ocean ridge
Ridge-hotspot intersection
Ocean Island
Intracontinental back-arc
Mariana Arc
Lesser Antilles Volcanic Arc
Izu Bonin
South Sandwich Arc
Juan de Fuca Ridge
East Pacific Rise
Galapagos Spreading Center
Pacific Antarctic Rise
Azores
Ascension Island
Iceland
Hawaii
Society Island
Samoa
Marquesas Archipelago
Okinawa Trough
Taupo Volcanic Zone
A
B
C1
C2
C3
C4
C5
C6
C7
C8
C9
Zr
Sm
Y
Yb
Nb
La
Th
Eu
Ti
K
Ba
Si
Al
PC. 2 (31%)
PC. 1 (54%)
Count
Geological Setting (color coding)
Location
Intraoceanic back-arc
Intraoceanic island arc
Intracontinental back-arc
Sumisu Rift
Aogashima Rift
Myojin Rift
Torishima Rift
Knoll 336
Hachijo Knoll
Bayonnaise Knoll
Sumisu Knoll
Torishima Knoll
SW Torishima Knoll
Myojin Knoll
SW Myojin-sho Knoll
Desmos Knoll
Susu Knoll
Eastern Rift
Pual Ridge
MSC
Bridgeman Rise
G Ridge
Hook Ridge
Three Sister
C
D

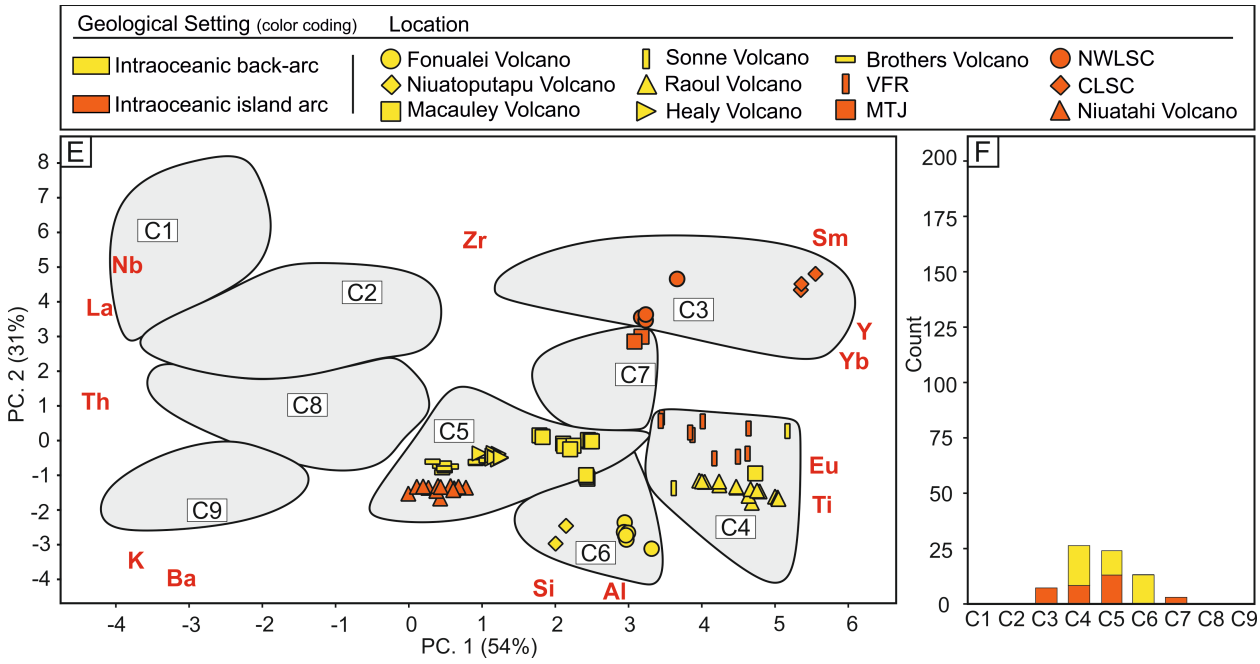


Figure A4. Detailed plots of the principal components analysis used to construct Table 3 and Figure 4A of the paper, showing the characteristics of each cluster and their relationship to specific lithotectonic assemblages. Cluster populations are shown in different plots for clarity. Principal components analysis (PCA) was conducted using 13 elements (Si, Ti, Al, K, Y, Zr, Nb, Ba, La, Sm, Eu, Yb, Th) for all samples in the data set (see Appendix Table A4). The loadings of each element on PC1 and PC2 are provided in Appendix Table A5. The red element labels correspond to loadings for the entire data set; the symbols are the loadings for individual samples. Using an iterative approach, the smallest number of clusters that represent the data was selected; nine clusters (C1-C9) were identified that show clear separation of the samples. The clustering results are given in Appendix Table A5, and the cluster metadata are given in Appendix Table A6. A) C1 = ocean islands (Society Islands, Marquesas Archipelago); C2 = ridge-hotspot intersections (Azores, Iceland, Ascension Island); C3 = mid-ocean ridges (Pacific-Antarctic Rise, East Pacific Rise, Galapagos Spreading Center, Juan de Fuca Ridge); C5 = intraoceanic arc volcanoes at the volcanic front of the Mariana Arc (Anatahan), Lesser Antilles Arc (Montserrat); C8 and C9 = intracontinental arc and back-arc related rifts (Okinawa Trough back-arc rift and the TVZ). B) Histogram of the sample distribution in A sorted by target class and geological setting. C) C3 = intraoceanic back-arc spreading centers (Manus Spreading Center) and one sample from continental margin setting (Three Sisters Volcano in the Bransfield Strait of the Antarctic

Peninsula); C4 = intraoceanic arc volcanoes (Hachijo Knoll, Sumisu Knoll, Torishima Knoll, Myojin Knoll, SW Torishima Knoll and Bayonnaise Knoll at the volcanic front of the Izu-Bonin Arc); C5 = intraoceanic arc rifts and knolls (Pual Ridge and Desmos in the Manus Basin, Myojin Rift, Torishima Rift, Sumisu Rift, Knoll 336 and Hachijo Knoll of the Izu volcanic arc), continental margin setting (G Ridge and Bridgeman Rise from the Bransfield Strait); C6 = intraoceanic arc rifts and knolls (Pual Ridge, Desmos and SuSu Knoll in the Manus Basin, Aogashima Rift and SW Torishima Knoll of the Izu volcanic) and continental margin setting (G Ridge from the Bransfield Strait); C7 = extending arc (Myojin Rift, Sumisu Rift and Hachijo Knoll of the Izu volcanic arc) and continental margin setting (Hook Ridge from the Bransfield Strait). D) Histogram of the sample distribution in C sorted by target class and geological setting. E) C3 = mature back-arc spreading centers (Central Lau Spreading Center and Northwest Lau Spreading Center from the Lau Basin); C4 = intraoceanic arc-related rift (Valu Fa Rift and Spreading Center from the Lau Basin) and arc volcanoes (Raoul Volcano, Sonne Volcano and Macauley Volcano on the Kermadec Arc); C5 = intraoceanic rear-arc volcanic complex (Niuatahi of the Tofua Arc in the northern Lau Basin) and volcanoes (Brothers Volcano, Healy Volcano and Macauley Volcano on the Kermadec Arc); C6 = intraoceanic arc volcanoes (Fonualei and Niuatoputapu volcanoes on the Tofua Arc); C7 = intraoceanic back-arc rift (Mangatolu Triple Junction in the northern Lau Back-arc basin). F) Histogram of the sample distribution in E sorted by target class and geological setting.

Description of Tables

Table A1. Selected high-quality geochemical analyses of submarine felsic volcanic rocks (>60 wt.% SiO_2) from different oceanic settings (N=643 samples). The data were selected from an original compilation of more than 2200 unique samples, removing duplicates, altered samples, and samples exceeding upper and lower detection limits or analyzed by inappropriate methods. The final database includes 404 high-quality analyses from modern oceanic settings plus a comprehensive data set of 239 samples from the well-studied TVZ. The table lists the literature resources (including DOI, title and publication year), location, sample type, analytical methods, laboratory, major elements as oxides (also converted to element concentrations in ppm), and trace elements in ppm. Location 1 refers to the general geographical region; location 2 refers to a specific location or volcanic complex. WR refers to whole rock samples; GL refers to glass analysis. Methods include X-ray fluorescence (XRF), electron microprobe analysis (EPMA), laser ablation – inductively coupled plasma – mass spectrometry (LA-ICP-MS), multi collector – inductively coupled plasma – mass spectrometry (MC-ICP-MS), inductively coupled plasma atomic emission spectroscopy (ICP-AES), thermal ionization mass spectrometry (TIMS), secondary-ion mass spectrometry (SIMS), instrumental neutron activation analysis (INAA), atomic absorption spectroscopy (AAS). The indicated laboratory refers to the facility where samples were processed and analyzed. FeO_t refers to total iron concentration reported as FeO.

Table A2. Centered-log ratio transformations of 13 elements in submarine felsic volcanic rocks and samples from the TVZ from Table A1 used in this study. The table lists location, sample ID and the values of the centered-log ratio transformations. Location 1 refers to the general geographical region; location 2 refers to the specific location or volcanic complex.

Table A3. Summary of PCA results in the analysis of submarine felsic volcanic rocks using 13 elements (Si, Ti, Al, K, Y, Zr, Nb, Ba, La, Sm, Eu, Yb, Th) as the variables (from Table A2). Eigenvalues describing the weighting of each principal component in the total data set are listed together with the proportion of the variance represented by each component and the cumulative variance.

Table A4. Loadings for each element on each principal component in the PCA of submarine felsic volcanic rocks using 13 elements (Si, Ti, Al, K, Y, Zr, Nb, Ba, La, Sm, Eu, Yb, Th) as the variables (all samples; data from Table A2). "Coordinates" refer to the centered-log ratio transformation of each element.

Table A5. Loadings of the principal components for each sample in the PCA of submarine felsic volcanic rocks using 13 elements (Si, Ti, Al, K, Y, Zr, Nb, Ba, La, Sm, Eu, Yb, Th) as the variables (data from Table A2). "Coord" refers to the position of each sample in a principal component plot. The clusters indicated are from the hierarchical clustering shown in Figure 4 of the paper.

Table A6. Summary statistics of samples belonging to the 9 target clusters identified by hierarchical clustering. The data are centered-log ratio transformations of the concentration (in ppm) of 13 elements used in the PCA. The sample clusters are those shown in Figure 4 of the paper and in Table A5. "Mean in category" refers to the mean of each element within each cluster. "SD in category" refers to Standard Deviation of each element within each cluster.

Table A7. Results of artificial sample creation to augment the training set by synthetic minority oversampling (SMOTE: Chawla et al., 2002). These data are generated to overcome differences in the number of samples in the target classes. SMOTE "creates" new data by slightly altering the geochemical composition of original samples until each class contains the same number of samples as the largest class. The "original samples" are samples from Appendix Table A1 selected for training, and the samples identified as "SMOTE" were created to address the class imbalances. The final balanced training set has 1440 samples. For samples created by SMOTE the sample ID refers to the original sample from which an artificial sample has been created. The data are centered-log ratio transformations of the concentrations (in ppm) of 13 elements used in the PCA.

Table A8. Results of validation of the RF classifier developed for modern submarine felsic volcanic rocks. To validate the model, a subset of samples was separated from the training dataset by a bootstrapping procedure (i.e., "out of bag" samples). 100% of these samples were correctly classified into the different target classes.

Table A9. Randomly selected samples from the original data set of submarine felsic volcanic rocks used in the blind test of the RF classifier. At least 4 samples were available for each target class in the blind test. The listed data are centered-log ratio transformations of the concentrations (in ppm) of 13 elements used in the PCA.

Table A10. Results of the blind test of the RF classifier of submarine volcanic rocks using the data in Table A9. The data listed are actual numbers of samples that were correctly (bold) or incorrectly (italics) classified. The x-axis indicates the actual class, and the y-axis indicates the prediction by random forest. The test samples were correctly classified in almost every case for all target classes, reaching an average accuracy of 96%.

Table A11. Selected high-quality geochemical analyses of Archean felsic volcanic rocks (>60 wt.% SiO_2) from 20 different locations in the Abitibi Greenstone Belt (N=145 samples). The data were selected from an original compilation of more than 160 unique samples created by Gaboury and Pearson (2008) and the MRD085 data set from the Ontario Geological Survey (2001), following the same QA/QC applied to the modern volcanic rocks. The table lists the literature resources (including DOI, title and publication year), location, analytical methods, laboratory, major elements and trace elements in ppm and centred-log ratio transformed. Location 1 refers to the general geographical region; location 2 refers to a specific location or volcanic complex; latitude and longitude refer to exact sample locations. Methods include X-ray fluorescence (XRF), inductively coupled plasma – mass spectrometry (ICP-MS). The indicated laboratory refers to the facility where samples were processed and analyzed.

Table A12. Results of the random forest classification of felsic volcanic rocks from the Abitibi Greenstone Belt using 13 elements (Si, Ti, Al, K, Y, Zr, Nb, Ba, La, Sm, Eu, Yb, Th) as the variables. 58 of the 145 AGB samples in the original database were classified into one of the 9 target clusters.

Table A13. Results of the random forest classification of felsic volcanic rocks from the Abitibi Greenstone Belt using only the immobile elements, Al, Nb, Ti, Th, Y, Yb, and Zr, as the variables. 84 of the 145 AGB samples in the original database were classified into one of the 9 target clusters.

Appendix B

Supplementary Information for Chapter 3: Geochemical Signatures of Mafic Volcanic Rocks in Modern Oceanic Settings and Implications for Archean Mafic Magmatism

This document provides a detailed workflow for data analysis to accompany the manuscript "Geochemical signatures of mafic volcanic rocks in modern oceanic settings and implications for Archean mafic magmatism". The complete workflow can be replicated within the open-source data mining software R. The R workflow is provided as Appendix workflow A1.R. To access the workflow, R must be correctly installed https://www.r-project.org/. A technical guide, with instructions on how to use R, will appear within the R work environment. A more detailed workflow is provided in this document.

Data QA/QC

A detailed description of data sources used in the study is provided in the text of the accompanying manuscript and in **Appendix Table A1**. As part of the QA/QC on the compiled data, we examined the potential that metasomatic processes related to hydrothermal alteration and/or metamorphism affected the original compositions of the rocks. To identify altered samples, we inspected REE and immobile element plots and removed samples that showed evidence of element mobility (e.g., unusual enrichment of K and Na). The final database is given in **Appendix Table A1**. We performed the same QA/QC on the available geochemical data from the Abitibi Greenstone Belt

(AGB) used in this study. Additionaly, we excluded ultramafic and felsic rocks based on major and trace element concentrations (e.g., exceptional Mg concentrations, SiO_2 concentrations, Zr/Ti ratios) and whole rock and petrographic descriptions such as spinifex textured komatiites.

Data transformation

Prior to the principal components analysis (PCA), all data were transformed using the centered-log transformation (CLR) to remove the effects of data closure (Aitchison, 1982). Because geochemical data sum to 100%, the element concentrations in a data table are not independent, possibly resulting in false correlations. To overcome this, all data were recalculated to elemental concentrations in ppm, and the centered-log ratio transformations applied. The CLR transformation divides the natural logarithm of each element by the geometric mean of all elements for each sample:

$$clr(x) = \left[ln^{x1}_{g(x)} \dots ln^{xD}_{g(x)}\right]$$

Opening of the data in this way results in real numbers containing both positive and negative values, that are used in the PCA (see **Appendix Table A2**).

We further considered additive log ratio transformation (ALR) to remove the effects of data closure. However, using ALR transformed data yielded not as good results in the principal component analysis (i.e., less variance is covered in the first two principal components) and during the hierarchical clustering (i.e., less distinct separation of individual clusters) as CLR transformation.

Principal components analysis

The filtered and transformed data sets were used to carry out multivariate statistical analysis using 9 elements (Ti, Al, Y, Zr, Nb, Ba, La, Yb, Th) as the variables. PCA reduces the variables into a limited number of components that account for the largest variance in the data set. Each principal component (PC) represents a fraction of the total variance affected by all the variables. **Appendix Table A3** lists the eigenvalues that describe the weighting of each principal component in the total

data set, the proportion of the variance represented by each component, and the cumulative variance. **Appendix Table A4** lists the loadings for each element on the first 7 principal components. The individual scores for each sample on the principal components are given in **Appendix Table A5**.

Hierarchical clustering

The centred log-ratio transformed data were used to perform an unsupervised agglomerative hierarchical clustering of the samples. The cluster analysis was performed with the R statistical software using the unsupervised hierarchical clustering function "hclust" (R Core Team 2020). Hclust uses a set of simple queries to group the samples and maximize the differences between the groups, identifying subtle geochemical differences in the mafic volcanic rocks. The separation of the clusters is done using Ward's criterion, which is the sum of the squared distances of individuals from the center of the cluster. Each sample is classified into one of the clusters and the final results are given in **Appendix Table A6**. We further tested other clustering techniques such as k-means clustering with somewhat similar results. However, these techniques lack the crucial information of a data tree that can be retrieved from hierarchical clustering indicating the data structure and improving the decision-making process on deciding on the number of clusters.

Random forest classification

Using the results of the hierarchical clustering and a "training" data set we created a machine-learning classifier that can sort unknown samples into the predetermined clusters. We chose random forest (RF) as the preferred machine-learning classifier, which learns what values are meaningful to achieve the best classification outcome. The classifier is trained in an iterative process using samples that were randomly selected from our database (2288 samples or 80% of the database: see **Appendix Table A7**); the remaining 20% (569 samples: see Appendix Table A8) was used for a blind test (see below). To overcome differences in the number of samples in the target classes identified in the hierarchical clustering, we equalized the number of samples for each cluster prior to the training process using the synthetic minority oversampling technique (SMOTE: Chawla et al., 2002). SMOTE "creates" new samples in target classes that are underrepresented by slightly altering the geochemical composition of original samples and

removes samples from target classes with too many samples until each class contains the same number of samples. The resulting artificial training set created by this process is given in **Appendix Table A9**. To validate the model, we used the subset of samples separated from the training dataset by a bootstrapping procedure (i.e., "out of bag" samples), as described in the text. **Appendix Table A10** shows the results of the classification of the "out of bag" samples for each target class. **Appendix Table A8** lists the randomly selected samples from our original data set that were used in a blind test. The blind test determines how well the classifier performs on new data. **Appendix Table A11** shows the results of the blind test in which the samples were correctly classified in almost every case for all target classes, reaching an overall accuracy of 96%. To exclude and inspect any potential control of Ba mobility on the random forest classification we created a second random forest classifier trained and tested on the same training and blind test datasets but excluding Ba from the training element. **Appendix Table A12** shows the results of the blind test in which the classifier yields almost identical results reaching an overall accuracy of 93%.

Comparison with Archean mafic volcanic rocks

We used the RF classifier developed in this study to compare modern oceanic volcanic rocks with Archean basalt samples from the Abitibi Greenstone Belt (AGB). The data sources are provided in **Appendix Table A13**. The outcome of the classification using all 9 elements (Ti, Al, Y, Zr, Nb, Ba, La, Yb, Th) as the variables is provided in **Appendix Table A14**. For each sample, every target class receives a vote based on the trained decision trees in the RF classifier. The assigned target class for each sample is based on the target class with the majority vote (>50%).

References

Aitchison, J., 1982: The statistical analysis of compositional data: Journal of the Royal Statistical Society, v. 44, issue 2, p. 139-160.

Barker, S.J., Wison, C.J.N., Baker, J.A., Millet, M.-A., Rotella, M.D., Wright, I.C., and Wysoczanski, R.J., 2013, Geochemistry and petrogenesis of silicic magma in the intra-oceanic Kermadec Arc: Journal of Petrology, v. 54, p. 351-391.

Beier, C., Turner, S.P., Sinton, J.M., and Gill, J.B., 2010, Influence of subducted components on back-arc melting dynamics in the Manus Basin: Geochemistry, Geophysics, Geosystems, v. 11, p. 1525-2027.

Beier, C., Bach, W., Turner, S., Niedermeier, D., Woodhead, J., Erzinger, J., and Krumm, S., 2015, Origin of silicic magmas at spreading centres – an example from the South East Rift, Manus Basin: Journal of Petrology, v. 56, p. 255-272.

Beier, C., Turner, S.P., Haase, K.M., Pearce, J.A., Münker, C., and Regelous, M., 2017, Trace element and isotope geochemistry of the northern and central Tongan Islands with an emphasis on the genesis of high Nb/Ta signatures at the northern volcanoes of Tafahi and Niuatoputapu: Journal of Petrology, v. 58, p. 1073-1106.

Bézos, A., Escrig, S., Langmuir, C.H., Michael, P.J., Asimow, P.D., 2009, Origins of chemical diversity of back-arc basin basalts: A segment-scale study of the Eastern Lau Spreading Center: Journal of Geophysical Research, v. 114, article B06212.

Caulfield, J., Turner, S., Arculus, R., Dale, C., Jenner, F., Pearce, J., Macpherson, C., and Handley, H., 2012, Mantle flow, volatiles, slab-surface temperatures and melting dynamics in the north Tonga arc-Lau back-arc basin: Journal of Geophysical Research, v. 117, article B11209.

Chauvel, C., Maury, R.C., Blais, S., Lewin, E., Guillou, H., Guille, G., Rossi, P., and Gutscher, M.-A., 2012, The size of plume heterogeneities constrained by Marquesas isotopic stripes: Geochemistry, Geophysics, Geosystems, v. 13, article Q0705.

Chawla, N. V., Bowyer, K. W., Hall, L. O., and Kegelmeyer, W. P., 2002, SMOTE: Synthetic minority over-sampling technique: Journal of Artificial Intelligence Research, v. 16, p. 321-357.

Escrig, S., Bézos, A., Langmuir, C.H., Michael, P.J., and Arculus, R., 2012, Characterizing the effect of mantle source, subduction input and melting in the Fonualei Spreading Center, Lau Basin: Constraints on the origin of the boninitic signature of the back-arc lavas: Geochemistry, Geophysics, Geosystems, v. 13, article Q10008.

Falloon, T.J., Malahoff, A., Zonenshain, L.P., and Bogdanov, Y., 1992, Petrology and geochemistry of back-arc basin basalts from Lau Basin spreading ridges at 15°, 18° and 19°S: Mineralogy and Petrology, v. 47, p. 1-35.

Falloon, T.J., Danyushevsky, L.V., Crawford, T.J., Maas, R., Woodhead, J.D., Eggins, S.M., Bloomer, S.H., Wright, D.J., Zlobin, S.K., and Stacey, A.R., 2007, Multiple mantle plume components invoved in the petrogenesis of subduction-related lavas from the northern termination of the Tonga Arc and northern Lau Basin: Evidence from the geochemistry of arc and backarc submarine volcanics: Geochemistry, Geophysics, Geosystems, v. 8, article Q09003.

Fretzdorff, S., Worthington, T.J., Haase, K.M., Hékinian, R., Franz, L., Keller, R.A., and Stoffers, P., 2004, Magmatism in the Bransfield Basin: Rifting of the South Shetland Arc?: Journal of Geophysical Research, v. 109, article B12208.

Fretzdorff, S., Schwarz-Schampera, U., Gibson, H.L., Garbe-Schönberg, C.-D., Hauff, F., and Stoffers, P., 2006, Hydrothermal activity and magma genesis along a propagating back-arc basin: Valu Fa Ridge (southern Lau Basin): Journal of Geophysical Research, v. 111, article B08205.

Fretzdorff, S., Livermore, R.A., Devey, C.W., Leat, P.T., and Stoffers, P., 2002, Petrogenesis of the back-arc East Scotia Rigde, South Atlantic Ocean: Journal of Petrology, v. 43, p. 1435-1467.

Freund, S., Beier, C., Krumm, S., and Haase, K.M., 2013, Oxygen isotope evidence for the formation of andesitic-dacitiv magmas from the fast-spreading Pacific-Antarctic Rise by assimilation-fractional crystallization: Chemical Geology, v. 347, p. 271-283.

Gale, A., Dalton, C.A., Langmuir, C.H., Su, Y., and Schilling, J.-G., 2013, The mean composition of ocean ridge basalts: Geochemistry, Geophysics, Geosystems, v. 14, p. 489-518.

Gibson, S.A., Geist, D.G., Day, J.A., and Dale, C.W., 2012, Short wavelength heterogeneity in the Galápagos plume: Evidence from compositionally diverse basalts on Isla Santiago: Geochemistry, Geophysics, Geosystems, v. 13, article Q09007.

Gill, J., Hoernle, K., Todd, E., Hauff, F., Werner, R., Timm, C., Garbe-Schönberg, D., and Gutjahr, M., 2021, Basalt geochemistry and mantle flow during early backarc basin evolution: Havre Trough and Kermadec Arc, Southwest Pacific: Geochemistry, Geophysics, Geosystems, v. 22, article e2020GC009339.

Haase, K.M., Worthington, T.J., Stoffers, P., Garbe-Schönberg, D., and Wright, I., 2002, Mantle dynamics, element recycling, and magma genesis beneath the Kermadec Arc-Havre Trough: Geochemistry, Geophysics, Geosystems, v. 3, article 1071.

Haase, K.M., Fretzdorff, S, Mühe, R., Garbe-Schönberg, D., and Stoffers, P., 2009, A geochemical study of off-axis seamount lavas at the Valu Fa Ridge: Constraints on magma genesis and slab contributions in the southern Tonga subduction zone: Lithos, v. 112, p. 137-148.

Haase, K. M., Gress, M.U., Lima, S.M., Regelous, M., Beier, C., Romer, R.L., and Bellon, H., 2020, Elemental composition from XRF and ICP-MS measurments of volcanic rocks of the Vate Trough and New Hebrides Island arc: PANGAEA.

Haase, K.M., Schoenhofen, M.V., Storch, B., Beier, C., Regelous, M., Rubin, K., and Brandl, P.A., 2022, Effects on the hydrous domain in the mantle wedge on magma formation and mixing at the Northeast Lau Spreading Center, SW Pacific: Geochemistry, Geophysics, Geosystems, v. 23, article e2021GC10066.

Haraguchi, S., Kimura, J.-I., Senda, R., Fujinaga, K., Nakamura, K., Takaya, Y., and Ishii, T., 2017, Origin of felsic volcanism in the Izu arc intra-arc rift: Contributions to Mineral Petrology, v. 172, p. 1-25.

Jenner, F.E., Arculus, R.J., Mavrogenes, J.A., Dyriw, N.J., Nebel, O., and Hauri, E.H., 2012, Chalcophile element systematics in volcanic glasses from the northwestern Lau Basin: Geochemistry, Geophysics, Geosystems, v. 13, article Q06014.

Jicha, B.R., Singer, B.S., and Valentine, M.J., 2013, $^{40}Ar/^{39}Ar$ Geochronology of subaerial Ascension Island and a re-evaluation of the temporal progression of basaltic to rhyolitic volcanism: Journal of Petrology, v. 54, p. 2581-2596.

Keller, R.A., Fisk, M.R., Smellie, J.L., Strelin, J.A., and Lawver, L.A., 2002, Geochemistry of backarc basin volcanism in Bransfield Strait, Antarctica: Subducted contributions and along-axis variations: Journal of Geophysical Research, v. 107, article B8, 2171.

Keller, N.S., Arculus, R.J., Hermann, J., and Richard, S., 2008, Submarine back-arc lava with arc signature: Fonualei Spreading Center, northeast Lau Basin, Tonga: Journal of Geophysical Research, v. 113, article B08S07.

Langmuir, C.H., Bézos, A., Escrig, S., and Parman, S.W., 2006, Chemical systematics and hydrous melting of the mantle in back-arc basins, in Christie, D.M., Fisher, C.R., Lee, S.-M., and Givens, S., ed., Back-arc Spreading Systems: Geological, Biological, Chemical, and Physical Interactions: Washington, D. C., American Geophysical Union, Geophysical Monograph 166, p. 87-146.

Lytle, M.L., Kelley, K.A., Hauri, E.H., Gill, J.B., Papia, D., and Arculus, R.J., 2012, Tracing mantle sources and Samoan influence in the northwestern Lau back-arc basin: Geochemistry, Geophysics, Geosystems, v. 13, article Q10019.

Myeong, B., Kim, J., Kim, J.H., and Jang, Y.D., 2020, Petrogenesis of subduction-related lavas from the southern Tonga arc: Journal of Asian Earth Sciences, v. 188, article 104089.

Park, J.-W., Campbell, I.H., Kim, J., and Moon, J.-M., 2015, The role of late sulfide saturation in the formation of a Cu- and Au-rich magma: Insights from the platinum group element geochemistry of Niuatahi-Motutahi lavas, Tonga Rear Arc: Journal of Petrology, v. 56, p. 59-81.

Pearce, J.A., Stern, R.J., Bloomer, S.H., and Fryer, P., 2005, Geochemical mapping of the Mariana arc-basin system: Implications for the nature and distribution of subduction components: Geochemistry, Geophysics, Geosystems, v. 6, Q07006, p.

Pearce, J.A., Kempton, P.D., and Gill, J.B., 2007, Hf–Nd evidence for the origin and distribution of mantle domains in the SW Pacific: Earth and Planetary Science Letters, v. 260, p. 98-114.

Peate, D.W., Kokfelt, T.F., Hawkesworth, C.J., v. Calsteren, P.W., Hergt, J.M., and Pearce, J.A., 2001, U-series isotope data on Lau Basin glasses: The role of subduction-related fluids during melt generation in back-arc basins: Journal of Petrology, v. 42, p. 1449-1470.

Price, A.A., Jackson, M.G., Blichert-Toft, J., Hall, P.S., Sinton, J.M., Kurz, M.D., and Blusztajn, J., 2014, Evidence for a broadly distributed Samoan-plume signature in the northern Lau and North Fiji Basins: Geochemistry, Geophysics, Geosystems, v. 15, p. 986-1008.

Price, A.A., Jackson, M.G., Blichert-Toft, J., Blusztajn, J., Conatser, C.S., Konter, J.G., Koppers, A.A.P., and Kurz, M.D., 2016, Geochemical evidence in the northeast Lau Basin for subduction of the Cook-Austral volcanic chain in the Tonga Trench: Geochemistry, Geophysics, Geosystems, v. 17, p. 1694-1724.

Price, A.A., Jackson, M.G., Blichert-Toft, J., Kurz, M.D., Gill, J., Blusztajn, J., Jenner, F., Brens, R., and Arculus, R., 2017, Geodynamic implications for zonal and meridional isotopic patterns across the northern Lau and North Fiji Basins: Geochemistry, Geophysics, Geosystems, v. 18, p. 1013-1042.

R Core Team 2020, R: A language and environment for statistical computing: R Foundation for Statistical Computing, Vienna, Austria. (https://www.R-project.org).

Sinton, J.M., Ford, L.L., Chappell, B., and McCulloch, M.T., 2003, Magma genesis and mantle heterogeneity in the Manus back-arc basin, Papua New Guinea: Journal of Petrology, v. 44, p. 159-195.

Tian, L., Castillo, P.R., Hilton, D.R., Hawkins, J.W., Hanan, B.B., and Pietruszka, A.J., 2011, Major and trace element and Sr-Nd isotope signatures of the northern Lau Basin lavas:

Implications for the composition and dynamics of the back-arc basin mantle: Journal of Geophysical Research: Solid Earth v. 116, B11201.

Todd, E., Gill, J.B., Wysoczanski, R.J., Hergt, J., Wright, I.C., Leybourne, M.I., and Mortimer, N., 2011, Hf isotopic evidence for small-scale heterogeneity in the mode of mantle wedge enrichment: Southern Havre Trough and south Fiji basin back arcs: Geochemistry, Geophysics, Geosystems, v. 12, article Q09011.

Yan, Q., Castillo, P.R., and Shi, X., 2012, Geochemistry of basaltic lavas from the southern Lau Basin: Input of compositionally variable subduction components: International Geology Review, v. 54, p. 1456-1474.

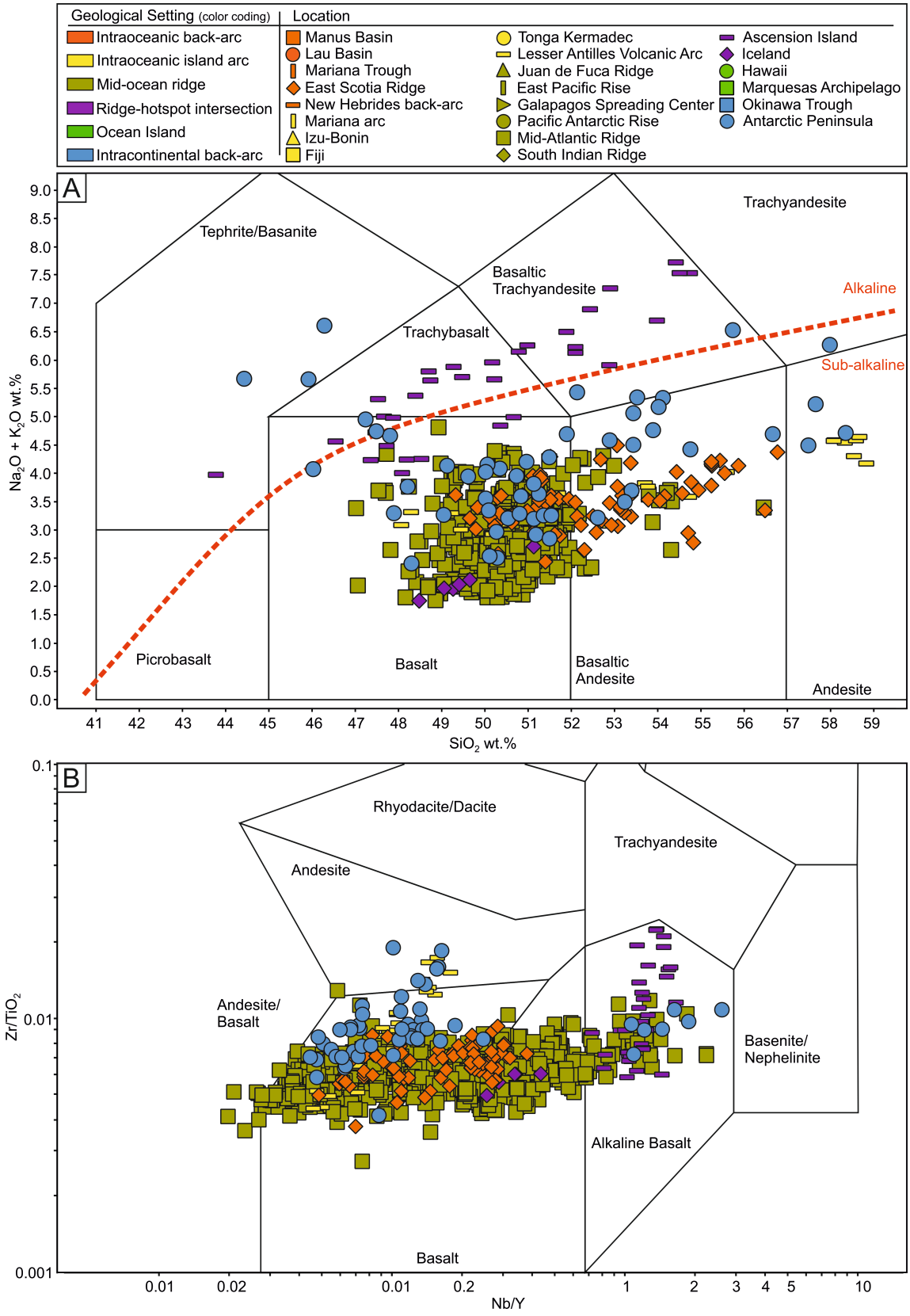
v.d. Zander, I., Sinton, J.M., and Mahoney, J.J., 2010, Late shield-stage silicic magmatism at Waianae volcano: Evidence for Hydrous Crustal Melting in Hawaiian Volcanoes: Journal of Petrology, v. 51, p. 671-701.

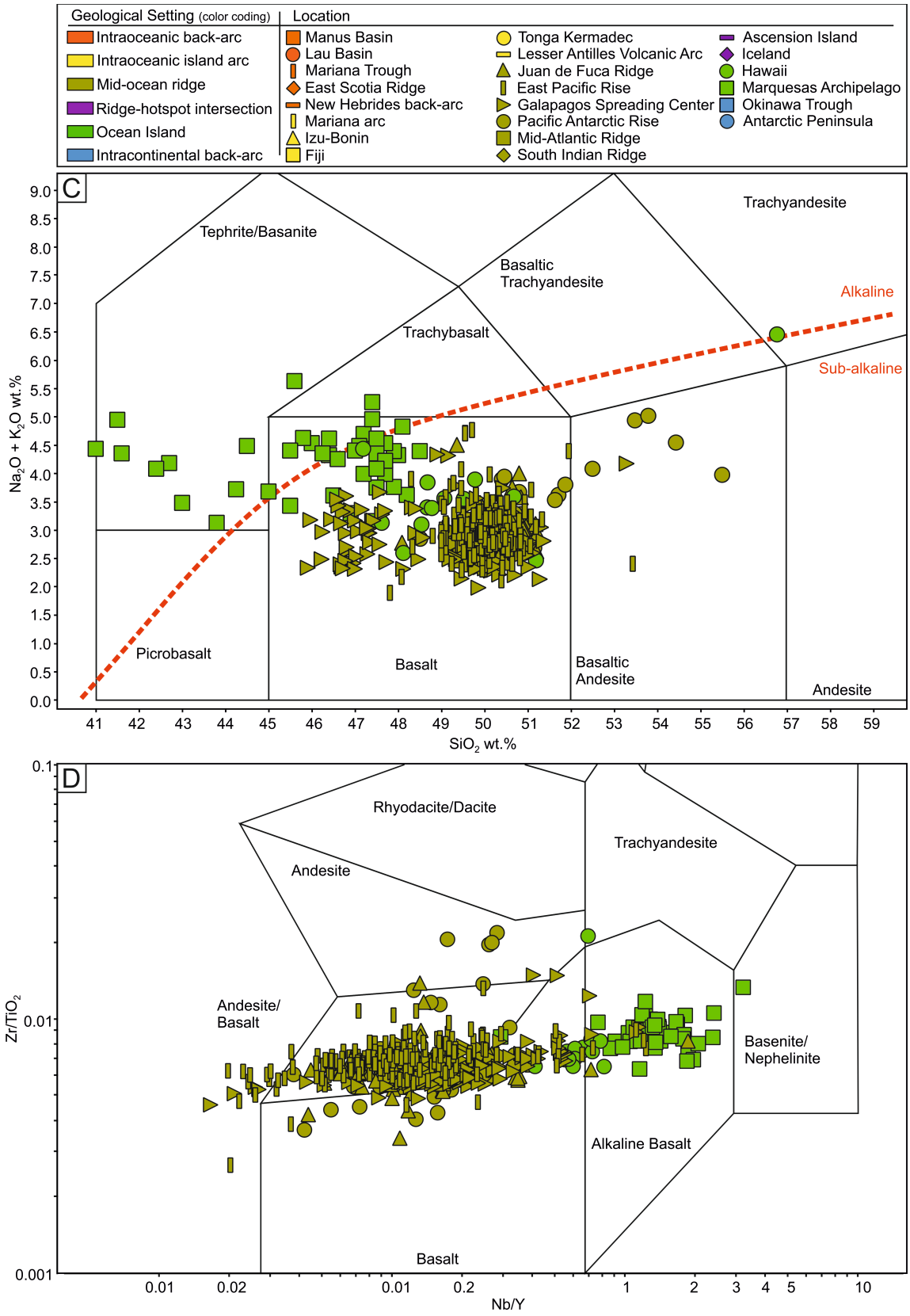
Zellmer, G.F., Rubin, K.H., Grönvold, K., and Jurado-Chichay, Z., 2008, On the recent bimodal magmatic processes and their rates in the Torfajökull-Veidivötn area, Iceland: Earth and Planetary Science Letters, v. 269, p. 388-398.

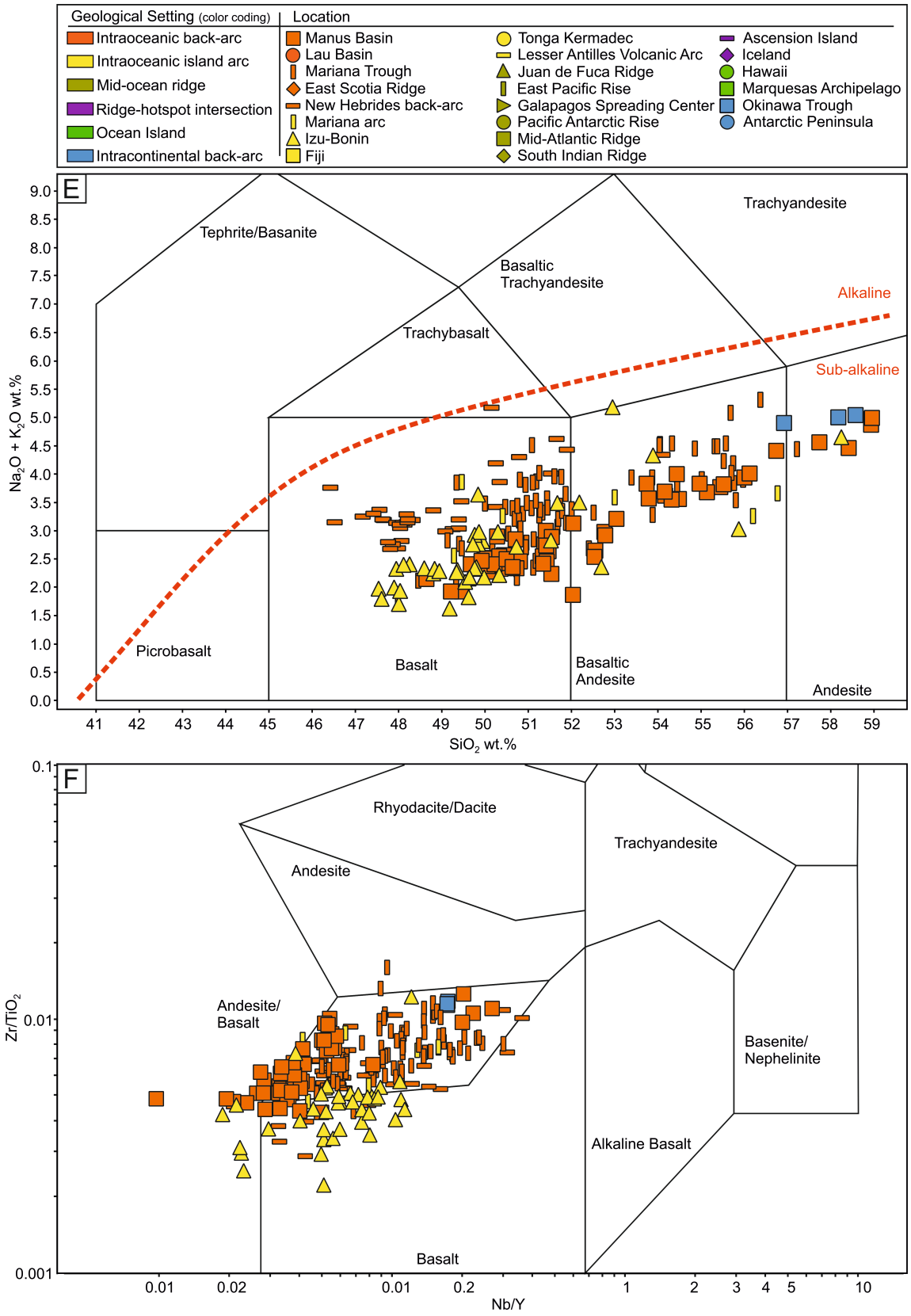
Zellmer, G.F., Hawkesworth, C.J., Sparks, R.S.J., Thomas, L.E., Harford, C.L., Brewer, T.S., and Loughlin, S.C., 2003, Geochemical evolution of the Soufrière Hills volcano, Montserrat, Lesser Antilles volcanic arc: Journal of Petrology, v. 44, p. 1349-1374.

Zhu, H., Du, L., Li, X., Zhang, Z., and Sun, W., 2020, Calcium isotopic fractionation during plate subduction: Constraints from back-arc basin basalts: Geochemica et Cosmochimica Acta, v. 270, p. 379-393.

Figures


Geological Setting (color coding)
Intraoceanic back-arc
Intraoceanic island arc
Mid-ocean ridge
Ridge-hotspot intersection
Ocean Island
Intracontinental back-arc
Location
Manus Basin
Lau Basin
Mariana Trough
East Scotia Ridge
New Hebrides back-arc
Mariana arc
Izu-Bonin
Fiji
Tonga Kermadec
Lesser Antilles Volcanic Arc
Juan de Fuca Ridge
East Pacific Rise
Galapagos Spreading Center
Pacific Antarctic Rise
Mid-Atlantic Ridge
South Indian Ridge
Ascension Island
Iceland
Hawaii
Marquesas Archipelago
Okinawa Trough
Antarctic Peninsula
A
Tephrite/Basanite
Trachyandesite
Basaltic Trachyandesite
Trachybasalt
Alkaline
Sub-alkaline
Picrobasalt
Basalt
Basaltic Andesite
Andesite
Na2O + K2O wt.%
SiO2 wt.%
B
Rhyodacite/Dacite
Andesite
Trachyandesite
Andesite/ Basalt
Basenite/ Nephelinite
Alkaline Basalt
Basalt
Zr/TiO2
Nb/Y


Geological Setting (color coding)
Intraoceanic back-arc
Intraoceanic island arc
Mid-ocean ridge
Ridge-hotspot intersection
Ocean Island
Intracontinental back-arc
Location
Manus Basin
Lau Basin
Mariana Trough
East Scotia Ridge
New Hebrides back-arc
Mariana arc
Izu-Bonin
Fiji
Tonga Kermadec
Lesser Antilles Volcanic Arc
Juan de Fuca Ridge
East Pacific Rise
Galapagos Spreading Center
Pacific Antarctic Rise
Mid-Atlantic Ridge
South Indian Ridge
Ascension Island
Iceland
Hawaii
Marquesas Archipelago
Okinawa Trough
Antarctic Peninsula
C
Tephrite/Basanite
Basaltic Trachyandesite
Trachyandesite
Trachybasalt
Alkaline
Sub-alkaline
Picrobasalt
Basalt
Basaltic Andesite
Andesite
Na2O + K2O wt.%
SiO2 wt.%
D
Rhyodacite/Dacite
Andesite
Trachyandesite
Andesite/ Basalt
Basenite/ Nephelinite
Alkaline Basalt
Basalt
Zr/TiO2
Nb/Y


Geological Setting (color coding)
Intraoceanic back-arc
Intraoceanic island arc
Mid-ocean ridge
Ridge-hotspot intersection
Ocean Island
Intracontinental back-arc
Location
Manus Basin
Lau Basin
Mariana Trough
East Scotia Ridge
New Hebrides back-arc
Mariana arc
Izu-Bonin
Fiji
Tonga Kermadec
Lesser Antilles Volcanic Arc
Juan de Fuca Ridge
East Pacific Rise
Galapagos Spreading Center
Pacific Antarctic Rise
Mid-Atlantic Ridge
South Indian Ridge
Ascension Island
Iceland
Hawaii
Marquesas Archipelago
Okinawa Trough
Antarctic Peninsula
E
Tephrite/Basanite
Trachyandesite
Basaltic Trachyandesite
Trachybasalt
Alkaline
Sub-alkaline
Picrobasalt
Basalt
Basaltic Andesite
Andesite
Na2O + K2O wt.%
SiO2 wt.%
F
Rhyodacite/Dacite
Andesite
Trachyandesite
Andesite/ Basalt
Basenite/ Nephelinite
Alkaline Basalt
Basalt
Zr/TiO2
Nb/Y

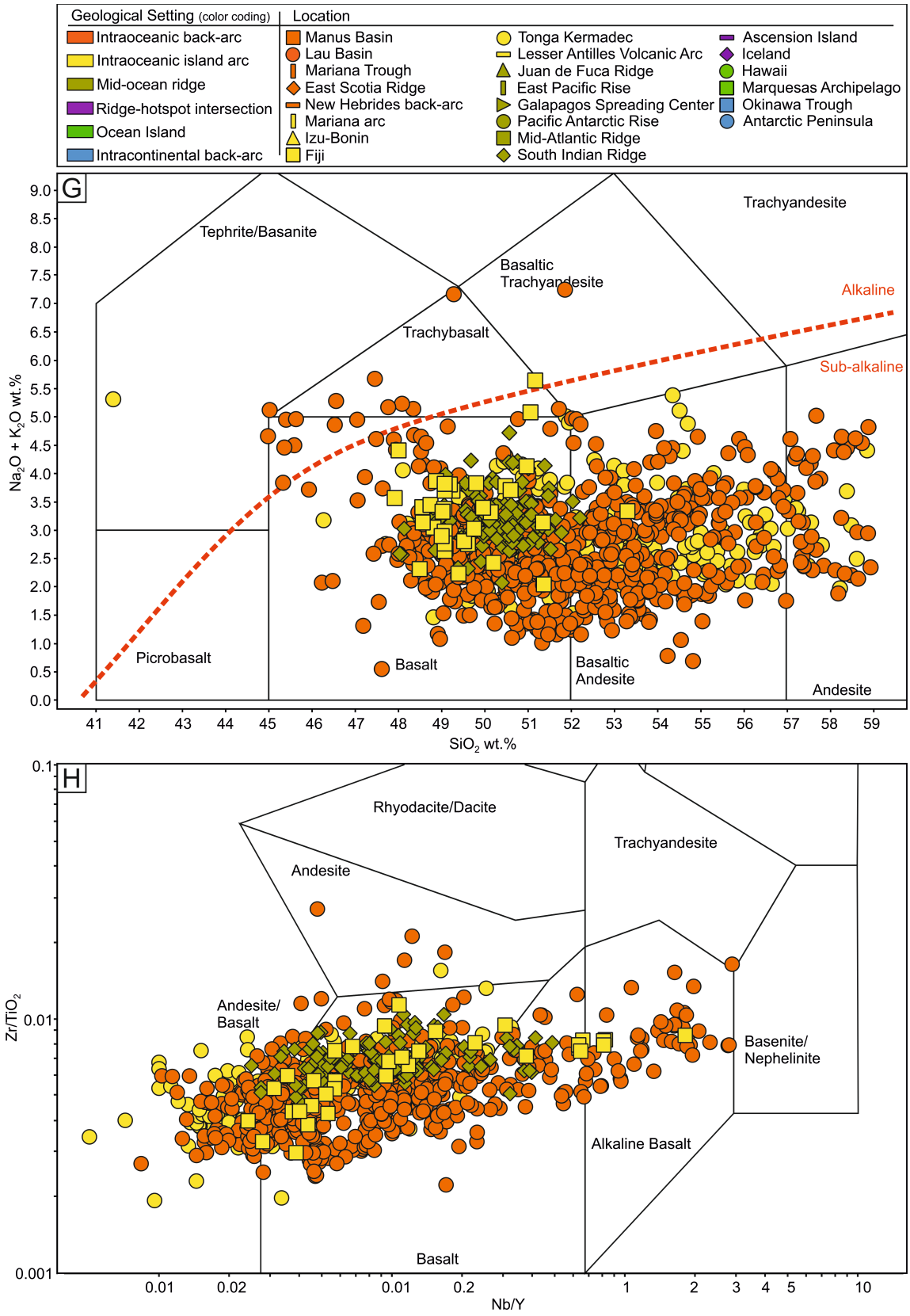

Geological Setting (color coding)
Intraoceanic back-arc
Intraoceanic island arc
Mid-ocean ridge
Ridge-hotspot intersection
Ocean Island
Intracontinental back-arc
Location
Manus Basin
Lau Basin
Mariana Trough
East Scotia Ridge
New Hebrides back-arc
Mariana arc
Izu-Bonin
Fiji
Tonga Kermadec
Lesser Antilles Volcanic Arc
Juan de Fuca Ridge
East Pacific Rise
Galapagos Spreading Center
Pacific Antarctic Rise
Mid-Atlantic Ridge
South Indian Ridge
Ascension Island
Iceland
Hawaii
Marquesas Archipelago
Okinawa Trough
Antarctic Peninsula
G
Tephrite/Basanite
Trachyandesite
Basaltic Trachyandesite
Trachybasalt
Alkaline
Sub-alkaline
Picrobasalt
Basalt
Basaltic Andesite
Andesite
Na2O + K2O wt.%
SiO2 wt.%
H
Rhyodacite/Dacite
Andesite
Trachyandesite
Andesite/ Basalt
Basenite/ Nephelinite
Alkaline Basalt
Basalt
Zr/TiO2
Nb/Y

Figure A1. A) Total alkali-silica plot (after Le Maitre, 1989) showing the distribution of modern oceanic mafic volcanic rocks from the Mid-Atlantic Ridge and Iceland, which are mostly subalkaline with low SiO_2 concentrations. Samples from Ascension Island are mostly alkaline with variable SiO_2 concentrations. Samples from the Lesser Antilles Volcanic Arc and the East Scotia Ridge are subalkaline with variable SiO_2 concentrations. Samples from the Antarctic Peninsula are subalkaline and alkaline and have a wide range of SiO_2 and $Na_2O + K_2O$ concentrations. B) Volcanic rock discrimination plot of Winchester and Floyd (1977) showing the distribution of modern oceanic mafic volcanic rocks from the Mid-Atlantic Ridge, which have variable Nb/Y and low Zr/TiO_2 and plot in the basalt and alkaline basalt fields. Samples from Iceland have intermediate to high Nb/Y and intermediate Zr/TiO_2 and plot in the basalt field. Samples from Ascension Island have high Nb/Y and intermediate to high Zr/TiO_2 and plot in the alkaline basalt field. Samples from the Lesser Antilles Volcanic Arc have low Nb/Y and low to high Zr/TiO_2. Samples from the East Scotia Ridge have intermediate Nb/Y and intermediate Zr/TiO_2. Samples from the Antarctic Peninsula have intermediate Nb/Y and intermediate to high Zr/TiO_2. C) Total alkali-silica plot (after Le Maitre, 1989) showing the distribution of-oceanic mafic volcanic rocks from the Juan de Fuca Ridge, East Pacific Rise, and Galapagos Spreading Center, which are subalkaline with low SiO_2 concentrations. Samples from the Pacific Antarctic Rise are subalkaline with variable SiO_2 concentrations. Samples from the Marquesas Archipelago are mostly alkaline with low to intermediate SiO_2 concentrations. Samples from Hawaii are subalkaline to alkaline with low SiO_2 concentrations. D) Volcanic rock discrimination plot of Winchester and Floyd (1977) showing the distribution of oceanic mafic volcanic rocks from the Juan de Fuca Ridge and East Pacific Rise, which have intermediate Nb/Y and low Zr/TiO_2 and plot mostly in the basalt field. Samples from the Galapagos Spreading Center and the Pacific Antarctic Rise have intermediate Nb/Y and variable Zr/TiO_2 and plot mostly in the basalt and andesite/basalt field. Samples from the Marquesas Archipelago and Hawaii have high Nb/Y and low Zr/TiO_2 plotting in the alkaline basalt field. E) Total alkali-silica plot (after Le Maitre, 1989) showing the distribution of oceanic mafic volcanic rocks from the Manus Basin, Mariana arc-backarc, New Hebrides, and Izu-Bonin arc-backarc systems, which are subalkaline with variable SiO_2 concentrations. Samples from the Okinawa Trough are subalkaline with high SiO_2 concentrations. F) Volcanic rock discrimination plot of Winchester and Floyd (1977) showing the distribution of mafic volcanic rocks from the Manus Basin and Mariana arc-backarc system, which have low to

intermediate Nb/Y and intermediate Zr/TiO_2 plotting mostly in the basalt and andesite/basalt field. Samples from the New Hebrides and Izu-Bonin arc-backarc systems have low to intermediate Nb/Y and low Zr/TiO_2 plotting mostly in the basalt field. Samples from the Okinawa have intermediate Nb/Y and high Zr/TiO_2 plotting in the andesite/basalt field. G) Total alkali-silica plot (after Le Maitre, 1989) showing the distribution of mafic volcanic rocks from Fiji, which are subalkaline with low to intermediate SiO_2 concentrations. Samples from the Tonga-Kermadec system are mostly subalkaline with highly variable SiO_2 concentrations. Samples from the South Indian Ridge are subalkaline with low SiO_2 concentrations. H) Volcanic rock discrimination plot of Winchester and Floyd (1977) showing the distribution of mafic volcanic rocks from Fiji and the Tonga-Kermadec system, which have variable Nb/Y and low to intermediate Zr/TiO_2 plotting mostly in the basalt field and andesite/basalt field. Samples from the South Indian Ridge have low to intermediate Nb/Y and intermediate Zr/TiO_2 plotting in the andesite/basalt field.

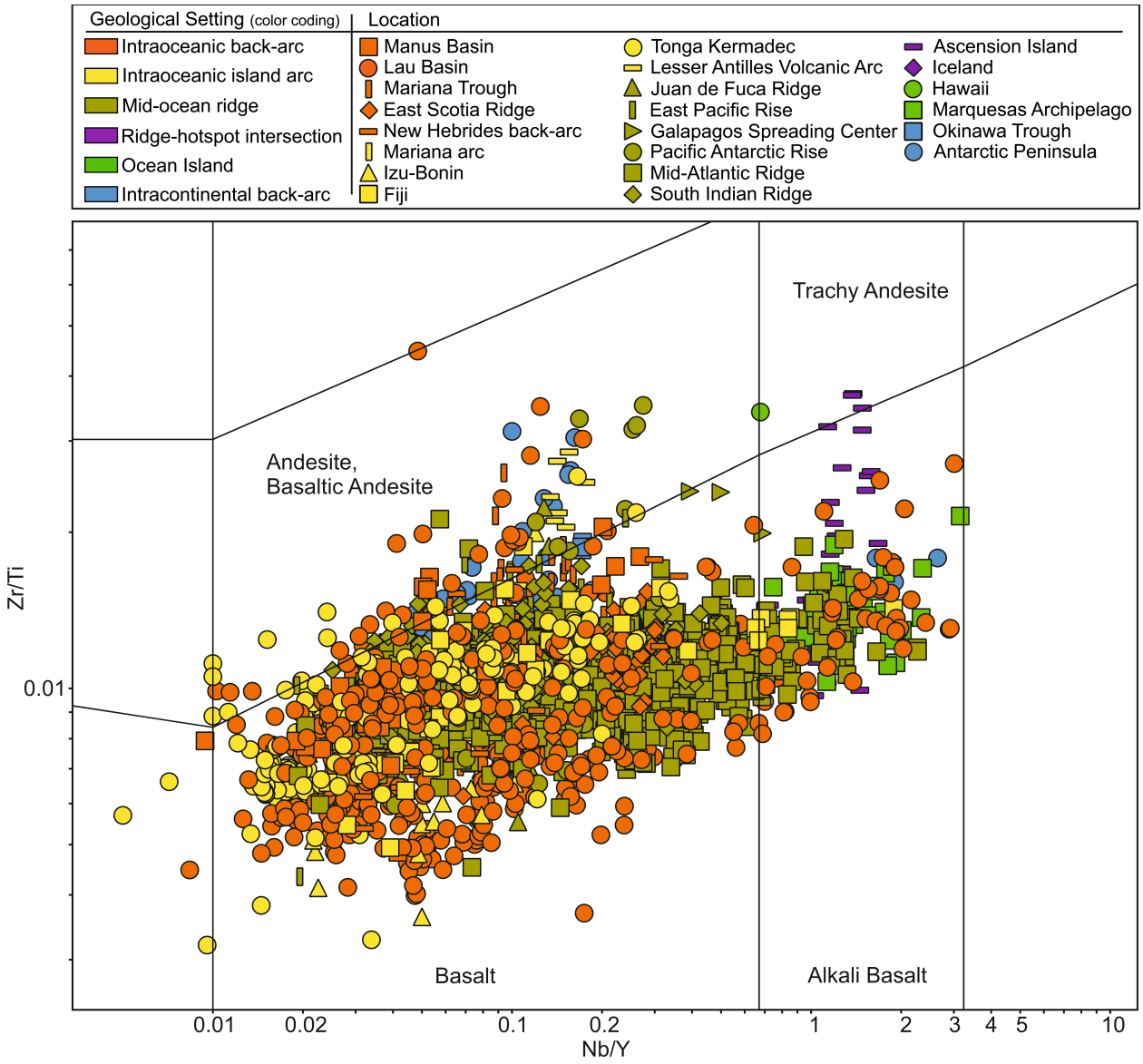


Figure A2. Immobile element plot of Winchester and Floyd (1977) modified by Pearce (1996), showing the range of mafic volcanic rock compositions in the database. The original Winchester and Floyd (1977) diagram is based on a limited number of samples, and so the full range of modern oceanic basalts is not well classified. Pearce (1996) used a more comprehensive dataset to define the boundaries; however, some of the modern oceanic basalts are still not well classified.

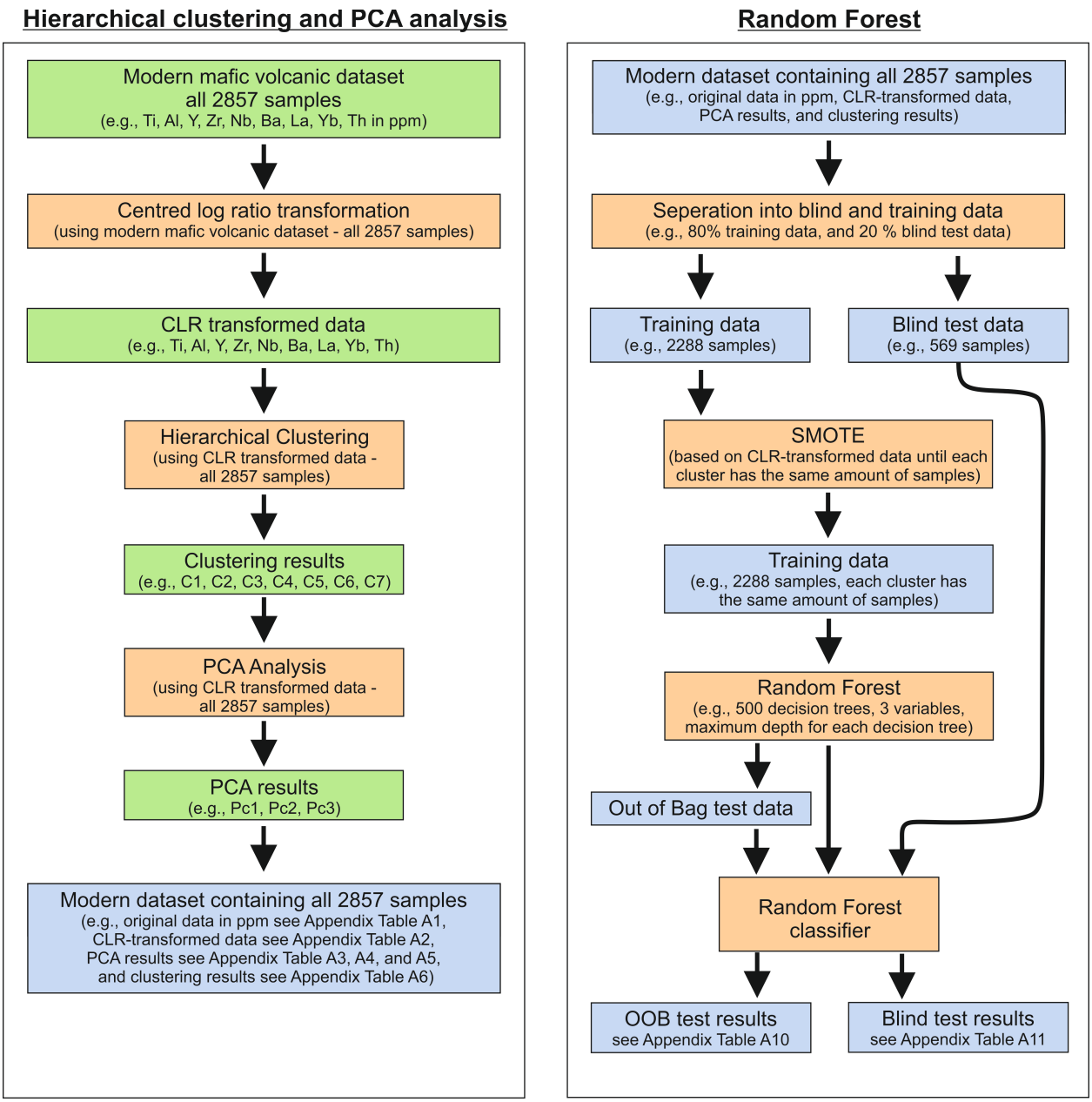


Figure A3. Illustration of the workflow used in the paper to compare mafic volcanic rock compositions in modern oceanic settings, showing the sequence of principal component analysis, hierarchical clustering and random forest classification.

Description of Appendix Tables

Table A1. Selected high-quality geochemical analyses of submarine mafic volcanic rocks (<60 wt.% SiO_2) from different oceanic settings (N=2857 samples). The data were selected from an original compilation of more than 3800 unique samples, removing duplicates, altered samples, and samples exceeding upper and lower detection limits or analyzed by inappropriate methods. The table lists the literature sources, location, sample type, analytical methods, laboratory, major elements as oxides (also converted to element concentrations in ppm), and trace elements in ppm. Location 1 refers to the general geographical region; location 2 refers to a specific location or volcanic complex. WR refers to whole rock samples; GL refers to glass analysis. Methods include X-ray fluorescence (XRF), electron microprobe analysis (EPMA), laser ablation – inductively coupled plasma – mass spectrometry (LA-ICP-MS), multi collector – inductively coupled plasma – mass spectrometry (MC-ICP-MS), inductively coupled plasma atomic emission spectroscopy (ICP-AES), thermal ionization mass spectrometry (TIMS), secondary-ion mass spectrometry (SIMS), instrumental neutron activation analysis (INAA). The indicated laboratory refers to the facility where samples were processed and analyzed as identified in the references. For simplicity, the concentrations are automatically formatted with 2 decimal places; the reader is referred to the original data sources for complete information on detection limits and reporting of significant figures.

Table A2. Centered log-ratio transformations of the concentrations (in ppm) of 9 elements in submarine mafic volcanic rocks from Table A1 used in this study. The table lists location, sample ID and the values of the centered-log ratio transformations. Location 1 refers to the general geographical region; location 2 refers to the specific location or volcanic complex.

Table A3. Summary of PCA results in the analysis of submarine mafic volcanic rocks using 9 elements (Ti, Al, Y, Zr, Nb, Ba, La, Yb, Th) as the variables (from Table A2). Eigenvalues describing the weighting of each principal component in the total data set are listed together with the proportion of the variance represented by each component and the cumulative variance.

Table A4. Loadings for each element on the first 7 principal components in the PCA of submarine mafic volcanic rocks using 9 elements (Ti, Al, Y, Zr, Nb, Ba, La, Yb, Th) as the variables (all samples; data from Table A2). "Coordinates" refer to the elements used in the PCA.

Table A5. Individual scores for each sample on the principal components in the PCA of submarine mafic volcanic rocks from Appendix Table A2. Loadings of the principal components for each sample in the PCA of submarine mafic volcanic rocks using 9 elements (Ti, Al, Y, Zr, Nb, Ba, La, Yb, Th) as the variables (data from Table A2). "Coord" refers to the position of each sample in a principal component plot.

Table A6. Results of the agglomerative clustering of submarine mafic volcanic rocks on the centred log ratio transformed data of 9 elements (Ti, Al, Y, Zr, Nb, Ba, La, Yb, Th) as the variables.

Table A7. Randomly selected samples from the original data set of submarine mafic volcanic rocks used in the training process of the RF classifier. The listed data are centered-log ratio transformations of the concentrations (in ppm) of 9 elements used in this study.

Table A8. Randomly selected samples from the original data set of submarine mafic volcanic rocks used in the blind test of the RF classifier. The listed data are centered-log ratio transformations of the concentrations (in ppm) of 9 elements used in this study.

Table A9. Results of artificial sample creation to augment the training set by synthetic minority oversampling (SMOTE: Chawla et al., 2002). These data are generated to overcome differences in the number of samples in the target classes. SMOTE “creates” new data by slightly altering the geochemical composition of original samples and removing samples of the target class with too many samples until each class contains the same number of samples. The final balanced training set has 2288 samples. The data are centered-log ratio transformations of the concentrations (in ppm) of 9 elements and associated clusters.

Table A10. Results of validation of the RF classifier using a subset of samples (i.e., “out of bag”) from the training dataset. See the text for a description of the procedure.

Table A11. Results of the blind test of the RF classifier of submarine volcanic rocks, using the data in Appendix Table A8. See the text for a description of the procedure.

Table A12. Results of the blind test of the RF classifier of submarine volcanic rocks, using the data in Appendix Table A8 excluding Ba. See the text for a description of the procedure.

Table A13. Selected high-quality geochemical analyses of Archean mafic volcanic rocks (<60 wt.% SiO_2) in the Abitibi Greenstone Belt (N=5746 samples). The data were selected from a compilation of volcanic rocks from Mole (2021), MRD 378, 292, 362, 377, 393, 355 and the MRD085 data set from the Ontario Geological Survey, open file 6623, OGS07, QUE09, GSC08 from the Geological Survey of Canada, and geochemical rock samples from SIGEOM Système d'information géominière of Québec, following the same QA/QC applied to the modern volcanic rocks. The table lists the literature sources, location, longitude, latitude, sample ID, major elements and trace elements in ppm. The location refers to the general geographical region; latitude and longitude refer to exact sample locations. For simplicity, the concentrations are automatically formatted with 2 decimal places; the reader is referred to the original data sources for complete information on detection limits and reporting of significant figures.

Table A14. Results of the random forest classification of mafic volcanic rocks from the Abitibi Greenstone Belt using 9 elements (Ti, Al, Y, Zr, Nb, Ba, La, Yb, Th) as the variables. 4681 of the 5746 AGB samples in the original database were classified into one of the 7 target clusters.

Appendix C

Supplementary Information for Chapter 4: Highly Episodic Growth of the Niuafo'ou Microplate, NE Lau Basin, from Ar-Ar Dating: Implications for Crustal Growth in Greenstone Belts

This document provides detailed information on the Ar-Ar analysis to accompany chapter 4: Highly Episodic Growth of the Niuafo'ou Microplate, NE Lau Basin, from Ar-Ar Dating: Implications for Crustal Growth in Greenstone Belts. All data, figures and tables can be accessed online along with the main document.

Descriptions of tables and techniques

All appendix tables contain results and analytical data for each individual sample provided in the digital appendix:

- **Table A1** contains all necessary information for sample SO267 DR 48
- **Table A2** contains all necessary information for sample SO267 DR 49
- **Table A3** contains all necessary information for sample SO267 DR 58
- **Table A4** contains all necessary information for sample SO267 DR 60
- **Table A5** contains all necessary information for sample SO267 DR 65
- **Table A6** contains all necessary information for sample SO267 DR 69
- **Table A7** contains all necessary information for sample SO267 DR 77

$^{40}Ar/^{39}Ar$ dating

The $^{40}Ar/^{39}Ar$ dating technique is a close relative of the K-Ar geochronology technique (Merrihue and Turner, 1966, Kelley, 2002). $^{40}Ar/^{39}Ar$ dates indicate when isotope exchange of ^{40}K and/or ^{40}Ar loss is closed, due to crystallization, alteration, or thermal diffusion, typically representing crystallization ages in young rapidly cooled volcanic rocks (Koppers et al., 2000). The radioactive parent isotope ^{40}K decays to the stable daughter isotopes ^{40}Ca and ^{40}Ar via beta emission and electron capture (Schaen, et al., 2020). The ^{40}Ar being produced is essentially the time measurement for this dating technique. Prior to this measurement, the sample is being placed in a nuclear reactor for irradiation with thermal and fast neutrons, producing nucleogenic ^{39}Ar from ^{39}K. The amount of ^{39}Ar produced from ^{39}K is depended on the initial amount of ^{39}K (Schaen, et al., 2020). The neutron flux is quantified by co-irradiating a sample with known age to define the irradiation parameter J. After irradiation the samples are being placed in an ultravacuum system where gasses are extracted using a furnace or a laser. During step heating the samples are being heated and the extracted gas (e.g., argon isotopes) is being measured at that temperature. Resulting in ages for each step, representing the degassing phase. The table for each sample includes all argon isotope measurement during this process as well as any metadata including J values,

extraction method, decay constants, instruments, lab and analyst. The ages are the results of the $^{40}Ar/^{39}Ar$ ratios, where ^{40}Ar reflects the insitu decay of ^{40}K and ^{39}Ar reflects the ^{39}Ar produced by neutron activation of ^{39}K. The J values are given in the tables and reflect the neutron flux constant. The decay constant λ is given in the table as well. The $^{40}Ar/^{39}Ar$ age equation is given below:

$$t = \frac{1}{\lambda} \ln \left(\frac{40Ar}{39Ar} J + 1\right)$$

Plateau ages were calculated and recommended by staff of the Oregon State University Argon lab that conducted the analysis. They provide the mean of individual ages and comprise at least 50% of the ^{39}Ar release and the majority of plateau steps do not have ascending or descending ages.

References

Kelley, S, 2002, K-Ar and Ar-Ar Dating: Reviews in Mineralogy and Geochemistry, v. 47, p.785-818.

Koppers, A.A.P., Staudigel, H., and Wijbrans, J.R., 2000, Dating crystalline groundmass separates of altered Cretaceous seamount basalts by the Ar-40/Ar-39 incremental heating technique: Chemical Geology, v. 166, p. 139-158.

Merrihue, C.M., and Turner, G., 1966, Potassium–argon dating by activation with fast neutrons: Journal of Geophysical Research, v. 71, p. 2852–2857.

Schaen, A.J., Jicha, B.R., Hodges, K.V., Vermesch, P., Stelten, M.E., Mercer, C.M., Phillips, D., Rivera, T.A., Jourdan, F., Matchan, E.L., Hemming, S.R., Morgan, L.E., Kelley, S.P., Cassata, W.S., Heizler, M.T., Vasconcelos, P.M., Benowith, J.A., Koppers, A.A.P., Mark, D.F., Niespolo, E.M., Sprain, C.J., Hames, W.E., Kuiper, K.F., Turrin, B.D., Renne, P.R., Ross, J., Nomade, S., Guillou, H., Webb, L.E., Cohen, B.A., Calvert, A.T., Joyce, N., Ganerod, M., Wijbrans, J., Ishizuka, O., He, H., Ramierz, A., Pfänder, J.A., Lopez-Martinez, M., Qui, H., and Singer, B.S., 2020, Interpreting and reporting 40Ar/39Ar geochronologic data: GSA Bulletin, v. 133, p.461-487.